THE UNIVERSITY *of* EDINBURGH

Hidden in Plain Light: High-Resolution Time-Resolved Fluorescence Modelling of Lung Cancer

Alexandra Adams

Doctor of Philosophy

THE UNIVERSITY OF EDINBURGH

2024

Abstract

Fibre-optic fluorescence lifetime-based devices are advanced spectroscopy techniques that can measure tissue autofluorescence (AF). The optical information AF offers provides insights into the tissue's metabolic and structural composition, as well as its surrounding environment. Therefore, these devices can be used to interrogate tissue. Conventional fluorescence lifetime-based devices typically measure the AF of tissue from broad emission channels. Or where multiple high-resolution channels are measured, the individual decay traces are often averaged into a single channel. Our research uses a novel in-house device, the Extensively Parallel Time-Resolved Fluorescence Spectroscopy (EP-TRFS) device which simultaneously measures high-resolution spectral and temporal fluorescence. We investigate device specific factors within the data collection, such as the instrument response function and sample specific factors such as photobleaching (Chapter 2).

We next present the paper titled "Simultaneous Spectral Temporal Modelling for a Time-Resolved Fluorescence Emission Spectrum", based on the Multichannel Fluorescence Lifetime Estimation (MuFLE) model (Chapter 3). MuFLE is an efficient computational model developed to explore the unique multi-channel spectroscopy data, simultaneously estimating the emission spectra and the spectral fluorescence lifetime in single and multi-exponential modes. We show the effectiveness of this approach in estimating the emission and spectral fluorescence lifetime of reference samples, and in un-mixing mixed reference samples.

We then present our initial findings of MuFLE when applied to *ex vivo* lung tissue data, presented in the paper titled "Fibre-optic based Exploration of Lung Cancer Autofluorescence using Spectral Fluorescence Lifetime", exploring the spectral information single-exponential fluorescence lifetime estimation provides (Chapter 4). The study demonstrates the sensitivity of the spectral fluorescence lifetime shape to the relative concentration of underlying fluorophores, independent of their environment. This study then explores the properties of the spectral fluorescence lifetime in paired *ex vivo* lung tissue deemed either abnormal or normal by pathologists.

When used in a multi-exponential mode, we finally show the performance of MuFLE in un-mixing endogenous fluorophores simultaneously in both the spectral and temporal domains of *ex vivo* lung samples from both non-cancerous and cancerous tissue (Chapter 5). We validate the presence of specific un-mixed endogenous fluorophores, using a commercial FLIM setup of paired samples. We also validate the spectral and temporal profile of the endogenous fluorophores when measured benchside and with the expected values estimated

in the literature. The identification of the fluorescence molecules responsible for AF changes in *ex vivo* samples, enable endogenous fluorophore specific label-free tracking. This, in turn, enhances our ability to assess individual fluorescence components contributing to the overall AF variation between non-cancerous and cancerous tissue *in vivo*.

In conclusion, we have developed and validated the results from a high-resolution fluorescence device, in combination with novel analytical models. This innovative approach when applied to lung tissue diagnosis enables us to gain a deeper understanding of the individual fluorescence components that contribute to the total AF of a tissue sample. By performing a comprehensive assessment of the AF, identifying the underlying sources of the individual signals, and their relative contributions becomes possible, better distinguishing fluorescence changes between cancerous and non-cancerous tissue. Consequently, the integration of this device and MuFLE, if applied *in vivo*, can potentially facilitate the instantaneous measurement of specific molecular and environmental properties associated with individual endogenous fluorophores in tissue. This approach can provide novel insights, offering a comprehensive understanding of the molecular dynamics in *in vivo* tissue, label-free and in real-time.

Lay Summary

Detecting lung cancer early is crucial for improving patients' chance of survival. At present, most machines which are used to detect lung cancer produce images. This limits the information available to make a diagnosis. The machines may also require the patients to change rooms which can disrupt them, particularly those who are critically ill. In addition, they expose patients to radiation during repeated screenings, which can be harmful.

On the other hand, new machines which use light, more specifically laser light, an alternative to radiation, may also detect lung cancer. Instead, the lasers stimulate properties of the lung to create a kind of 'optical fingerprint' of the tissue. The fingerprint gives us additional information about the tissue's growth and its surroundings, which is useful for understanding if it's healthy or not.

The early prototypes of these machines only assess one aspect of the light (called fluorescence) measuring how bright the tissue is and how long this brightness lasts. Scientists built new machines that can measure the light (fluorescence) in more detail and in different wavelengths.

This thesis uses data measured on these new machines and specialised mathematical models to analyse lung tissue. The data we collect is of lung tissue which has been surgically removed from patients with suspected lung cancer. The mathematical model when applied to the lung data is assessed to determine if it helps understand the source of the fluorescence, and what the light can tell us about the tissue. We show that our approach may be used to tell if the lung tissue is healthy or not, and why. In the end, this technology could be used in real-time during medical procedures and help doctors identify lung cancer more accurately.

Acknowledgements

This work was funded by the Medical Research Council [grant number MR/N13 166/1].

I would like to acknowledge and thank, first and foremost, my primary supervisor Dr Sohan Seth, whose dedication and commitment to my support as a scientist has and will continue to be invaluable. His meticulous attention to detail, kind encouragement and patience have played an instrumental role in shaping my journey as a PhD student. Without his mentorship and support, this thesis would not have been accomplished. I would also like to extend my gratitude to my second supervisors Professor Kev Dhaliwal and Dr Mohsen Khadem. To Kev, his technical guidance, advice, and positive encouragement have been a constant motivation throughout this journey. Additionally, to Mohsen for his unwavering support and technical contributions, particularly with Lynda the robot.

I would also like to extend my gratitude to Dr András Kufcsák for his comprehensive explanations, particularly in taking the time to elucidate the intricacies of fluorescence spectroscopy devices. I appreciate his dedication to providing clarity in complex concepts. I also wish to extend my appreciation to Dr Charles Lochenie for challenging hypotheses in an nonjudgmental, but curious perspective, fostering stimulating debates. I am also grateful for his expertise in photochemistry.

This thesis involves lots of crucial multi-disciplinary science. I extend my gratitude to Dr Ahsan Akram for providing patient samples and invaluable technical insights regarding tissue. Special thanks to Dr Katjana Ehrlich for her technical assistance, guidance, and introduction to various methodologies. I also want to express my appreciation to Dr Beth Mills, Dr Antonella Pellicoro, Dr Erin Gaughan, Dr Stuart Dickson and Dr Qiang Wang for their insightful discussions, encouragement, and advice. I want to express a special thank you to Dr Lilian Koppensteiner, Dr Layla Mathieson and Alex Kiang for their friendship, camaraderie, and company throughout this process, especially over coffee, beer, and lunch. My thanks also extend to my colleagues and friends in the THT group, SHaPE, the Vendrell group and my Frosé Friends. This work truly reflects the collaborative effort of a supportive community.

To my family, Mum, Dad, Matt and Soph, thank you for always believing in me and supporting me throughout my entire education, what a ride! Finally, to Kieran, thanks for always being there for me.

Declaration

I declare that this thesis was composed by myself, that the work contained herein is my own except where explicitly stated otherwise in the text, and that this work has not been submitted for any other degree or professional qualification except as specified.

Alexandra C. Adams

Contents

Abstract iii

Lay Summary v

Acknowledgements vi

Declaration vii

Figures and Tables xi

Nomenclature xiv

1 Introduction 1

1.1 Lung Cancer . . . 1

1.1.1 Fluorescence Advantage . . . 2

1.2 Overview of Fluorescence . . . 3

1.2.1 Fluorescence Excitation . . . 3

1.2.2 Fluorescence Emission . . . 3

1.2.3 Fluorescence Parameters . . . 6

1.3 Fluorescence Devices . . . 7

1.3.1 Single Photon Avalanche Diodes . . . 8

1.3.2 Time-Correlated Single Photon Counting . . . 8

1.3.3 Histogramming Mode . . . 9

1.3.4 Time Gated Techniques . . . 11

1.3.5 Pulse-Sampling Detection . . . 11

1.4 Fluorescence Detection . . . 11

1.5 Fluorescence Data Analysis . . . 13

1.5.1 Instrument Response Function . . . 13

1.5.2 Curve Fitting Methods . . . 14

1.5.3 Fit Free Methods . . . 15

1.5.4 Machine Learning . . . 16

1.6 Translational Fluorescence . . . 17

1.6.1 Smart Probes . . . 17

1.6.2 Autofluorescence for Lung Cancer Detection . . . 18

1.6.3 Tryptophan . . . 18

1.6.4 Pyridoxine . . . 20

1.6.5 Lipo-pigments . . . 21

1.6.6 Porphyrins . . . 21
1.6.7 Collagen and Elastin: The Extra Cellular Matrix . . . 21
1.6.8 Fluorescence and Metabolism . . . 23
1.6.9 Nicotinamide Adenine Dinucleotide . . . 24
1.6.10 Flavins . . . 26
1.6.11 Redox Ratios . . . 28
1.6.12 Autofluorescence for Cancer Detection in Tissue . . . 30
1.7 Research Aims . . . 32
1.8 Research Objectives . . . 33
1.9 Thesis Outline . . . 34

2 The EP-TRFS Device and Measurement Precision 36
2.1 The EP-TRFS Device . . . 37
2.1.1 Photon Detector . . . 37
2.1.2 Time Resolved Modes . . . 38
2.1.3 Temporal Jitter . . . 40
2.2 Lifetime Accuracy . . . 41
2.2.1 Photobleaching . . . 41
2.2.2 Sample Preparation . . . 42
2.3 The Instrument Response Function . . . 42
2.3.1 Tail Fitting . . . 42
2.3.2 Measured IRF . . . 44
2.3.3 Convolution with Quenched Fluorophores . . . 45
2.4 Sample Specific Alterations . . . 47
2.4.1 Concentration Dependent Lifetime . . . 49
2.4.2 Tissue Sample Preparation . . . 51
2.4.3 Photobleaching . . . 51
2.5 Discussion . . . 53
2.6 Conclusion . . . 55

3 Multichannel Fluorescence Lifetime Estimation 56
3.1 Multichannel Lifetime . . . 56
3.2 Limitations . . . 72
3.3 Conclusion . . . 72

4 Lung Cancer Discrimination using Spectral Fluorescence Lifetime 73
4.1 Spectral Fluorescence Lifetime Exploration . . . 73
4.2 Summary . . . 95
4.3 Additional Samples Analysis . . . 95
4.3.1 Sample Type Assessments . . . 99

4.4 Conclusion . . . 99

5 Towards Total Un-mixing 102
5.1 Introduction . . . 102
5.2 Methods . . . 106
5.2.1 Endogenous fluorophores . . . 106
5.2.2 *Ex vivo* lung resections . . . 106
5.2.3 EP-TRFS . . . 109
5.2.4 Fluorescence Lifetime Imaging Microscopy . . . 109
5.2.5 Analysis . . . 110
5.3 Results . . . 111
5.3.1 Simulated Data . . . 111
5.3.2 Multi-Exponential Tissue and Endogenous Fluorophores . . . 111
5.3.3 FLIM Data . . . 118
5.4 Discussion . . . 121
5.5 Conclusion . . . 126

6 Outlook and Conclusion 127
6.1 Results and Key Findings . . . 128
6.2 Towards Clinical Translation . . . 130
6.3 Limitations and Future Work . . . 132
6.3.1 Device Limitations . . . 132
6.3.2 Computational Limitations . . . 133
6.3.3 Data Collection Limitations . . . 134
6.4 Conclusion . . . 136

7 Appendix 137
7.1 Exponential Criteria . . . 137
7.2 Simulated Data . . . 139
7.3 EP-TRFS Sample Specific Components . . . 141
7.4 EP-TRFS vs FLIM Plots . . . 143
7.5 FLIM Plots . . . 150

8 List of Publications 157

Bibliography 158

Figures and Tables

Figures

1.1 Solitary pulmonary nodule. . . . 2
1.2 Adapted Jablonski diagram. . . . 4
1.3 The absorbance and fluorescence emission of an NBD die. . . . 5
1.4 Time domain device setups. . . . 10
1.5 Point-sampling fluorescence compared to fluorescence lifetime imaging microscopy. 12
1.6 Excitation and emission profiles of endogenous fluorophores. . . . 19
1.7 NADH fluorescence lifetime in different metabolic states. . . . 25
1.8 Chemical structure of flavins. . . . 26
1.9 Fluorescence lifetime changes of Flavins. . . . 28
1.10 Graphical objectives. . . . 33

2.1 A schematic of the EP-TRFS device. . . . 38
2.2 A diagram of the line sensor. . . . 39
2.3 The Instrument Response Function. . . . 40
2.4 Tail fitting. . . . 43
2.5 Detector instrument response functions. . . . 45
2.6 Different instrument response functions measured from quenched fluorophores. . 46
2.7 Single channel reference data. . . . 48
2.8 Concentration dependent lifetime. . . . 50
2.9 Transplant lung freeze thaw test. . . . 52
2.10 Tissue photobleaching. . . . 53

4.1 Simulated histograms . . . 96
4.2 Additional tissue samples analysed with MuFLE . . . 97
4.3 Additional samples MuFLE analysed using Procrustes . . . 98
4.4 Lifetime differences of samples with different features . . . 100

5.1 A schematic workflow of the setup. . . . 107
5.2 Components based on sample type. . . . 108
5.3 Average multi-exponential components from cancerous and non-cancerous lung tissue. . . . 112
5.4 Average multi-exponential components from lung tissue compared to fluorophores. 113
5.5 Sample specific single-exponential compared to multi-exponential components. . 117
5.6 Sample specific single-exponential compared to multi-exponential components. . 119

5.7 Fluorescence lifetime of lung tissue measured both on the EP-TRFS device and FLIM device. 120
5.8 Paired cancer and non-cancerous FLIM images. 122
5.9 Fluorescence intensity of lung tissue measured both on the EP-TRFS device and FLIM device. 123

7.1 Residual variance plots. 138
7.2 Multi-exponential MuFLE on simulated data. 140
7.3 Abnormal sample number 11 measured on MuFLE compared to FLIM. 144
7.4 Normal sample number 11 measured on MuFLE compared to FLIM. 145
7.5 Normal sample number 15 measured on MuFLE compared to FLIM. 146
7.6 Abnormal sample number 15 measured on MuFLE compared to FLIM. 147
7.7 Abnormal sample number 16 measured on MuFLE compared to FLIM. 148
7.8 Normal sample number 16 measured on MuFLE compared to FLIM. 149
7.9 FLIM images collection from the cancerous sample number 11 151
7.10 FLIM images collection from the non-cancerous sample number 11 152
7.11 FLIM images collection from the cancerous sample number 15 153
7.12 FLIM images collection from the non-cancerous sample number 15 154
7.13 FLIM images collection from the cancerous sample number 16 155
7.14 FLIM images collection from the cancerous sample number 16 156

Tables

1.1 Autofluorescence analysis of *in vivo* and *ex vivo* cancerous and non-cancerous tissue samples. 31

2.1 Fluorescence lifetime differences between two reference fluorophores, where two different measured IRF's are incorporated into the analysis routine. 47
2.2 Power output of the excitation laser following its attenuation with varying neutral density filters. 49
2.3 The average fluorescence lifetime of Rhodamine B following a serial dilution from 20 µM to 4 µM 49

4.1 Sample information of the additional *ex vivo* lung tissue assessed in this thesis. . 95

5.1 Tissue samples analysed alongside their respective features, with the number of components fitted using a multi-exponential MuFLE model displayed. Samples where t-tests were conducted are highlighted in blue. 108

5.2 The average fluorescence lifetime of a tri-exponential MuFLE model applied to both cancerous and non-cancerous *ex vivo* lung tissue. 111
5.3 Fluorescence lifetime values of the endogenous fluorophores excited at 485 nm as described in the literature. 113
5.4 The average fluorescence intensity of a tri-exponential MuFLE model applied to both cancerous and non-cancerous *ex vivo* lung tissue. 114
5.5 The average fluorescence lifetime of a bi-exponential MuFLE model applied to both cancerous and non-cancerous *ex vivo* lung tissue. 115
5.6 The average fluorescence intensity of a bi-exponential MuFLE model applied to both cancerous and non-cancerous *ex vivo* lung tissue. 115

7.1 Paired cancerous and non-cancerous *ex vivo* tissue samples with a tri-exponential MuFLE model fitted. T-tests conducted on the fluorescence lifetime values. . . . 142
7.2 EP-TRFS average lifetime components fitted using a bi-exponential model and compared using a t-test. 142
7.3 Paired cancerous and non-cancerous *ex vivo* tissue samples with a tri-exponential MuFLE model fitted. T-tests conducted on the fluorescence intensity values. . . . 142
7.4 Paired cancerous and non-cancerous *ex vivo* tissue samples with a bi-exponential MuFLE model fitted. T-tests conducted on the fluorescence lifetime values. . . . 142
7.5 Paired cancerous and non-cancerous *ex vivo* tissue samples with a bi-exponential MuFLE model fitted. T-tests conducted on the fluorescence intensity values. . . . 143
7.6 Fluorescence intensity of lung tissue analysed on a FLIM confocal microscope. Comparisons are drawn using a t-test. 150
7.7 Fluorescence lifetime of lung tissue analysed on a FLIM confocal microscope. Comparisons are drawn using a t-test. 150

Nomenclature

18F-FDG 18-Fluorodeoxyglucose
5-ALA 5-Aminolevulinic acid
AF Autofluorescence
ANN Artificial Neural Network
CM Time The Centre of Mass Time
CMOS Complementary Metal-Oxide Semiconductor
CT Computerised Tomography
DMSO Dimethylsulfoxide
ECM Extracellular Matrix
EP-TRFS Extensively Parallel Time-Resolved Fluorescence Spectroscopy
FADH Reduced Flavin Adenine Dinucleotide
FAD Flavin Adenine Dinucleotide
FI Fluorescence Intensity
FLIM Fluorescence Lifetime Imaging Microscopy
FLIRR Fluorescence Lifetime Induced Redox Ratio
Fluo Fluorescein Sodium
FL Fluorescence Lifetime
FMN Flavin Mononucleotide
FR-α Folate Receptor α
FS Fluorescence Spectroscopy
FWHM Full-Width Half Maximum
HistMode Histogramming Mode
ICG Indocyanine Green
IDH Isocritrate Dehydrogenase
IDO-1 Indoleamine 2, 3-dioxygenase 1
IHC Immunohistochemistry
IRF Instrument Response Function
LC Lung Cancer
LDH Lactate Dehydrogenase
LOX Lysyl Oxidase
MB Methylene Blue
ME-1 Malic Enzyme
MI Metabolic Index
MLE Maximum Likelihood Estimation
ML Machine Learning

MuFLE Multi-channel fluorescence lifetime estimation

NADH Reduced Nicotinamide Adenine Dinucleotide

NADPH Reduced Nicotinamide Adenine Dinucleotide Phosphate

NAD Nicotinamide Adenine Dinucleotide

ND Neutral Density

NLLS Non-linear Least Squares

NSCLC Non-small Cell Lung Cancer

OEM Optical Endomicroscopy

OR Optical Redox

OXPHOS Oxidative Phosphorylation

PCA Principal Component Analysis

PDXK Pyridoxal Kinase

PET Positron Emission Tomography

PMT Photon Multiplier Tubes

PpIX Protoporphyrin IX

RB Quenched Rose-Bengal

RhB Rhodamine B

RLD Rapid Lifetime Determination

ROS Reactive Oxygen Species

SCLC Small Cell Lung Cancer

SFL Spectral Fluorescence Lifetime

SPAD Single Photon Avalanche Diodes

SPN Solitary Pulmonary Nodules

TCA Tricarboxylic Acid Cycle

TCSPC Time-correlated Single Photon Counting

TDC Time-To-Digital Converters

TNM Tumour size, Nodes and Metastasis

TRES Time-resolved Emission Spectrum

TRFS Time-resolved Fluorescence Spectroscopy

Trp Tryptophan

UV Ultraviolet

Chapter 1

Introduction

1.1 Lung Cancer

For the diagnosis of lung cancer (LC) the following evaluations are likely to have been conducted: chest radiograph, computerised tomography (CT), positron emission tomography (PET), and tissue sampling through either a conventional biopsy or CT-guided needle aspiration [1, 2]. Histology is then used to assess the microscopic cellular structure, and genome sequencing identifies specific tumour related mutations of the sample. Given all the above information, patients are grouped into cancer type, i.e., non-small cell lung cancer (NSCLC) which represents 80 % of all cases and small cell lung cancer (SCLC), representing the rest. Within NSCLC, adenocarcinoma is a subset representing 40 % of all cases and squamous cell carcinoma represents 20 % [1]. Patients are also staged into prognostic risk groups i.e., NSCLC is staged according to TNM (tumour size, nodes and metastasis) staging [1].

Despite extensive work-ups available, LC remains the deadliest cancer worldwide, responsible for 1 in 5 cancer related deaths [3, 4]. Prognosis is largely influenced by the disease stage at diagnosis [5]. A diagnosis at stage 1 has an anticipated 5 year survival rate of 80 %, which decreases to 10 % with a stage 4 diagnosis [6]. However, only 16.6 % of patients diagnosed with lung cancer are diagnosed in the earliest stage 1 of the disease [7].

To increase early detection, low-dose CT scans for high-risk individuals are recommended (i.e., aged $>$ 50 and smoke). In this screening population, small, $<$3 cm spherical masses in the lung called solitary pulmonary nodules (SPN) in $>$ 50 % are detected (see Fig. 1.1)[8]. A proportion of SPNs are early stage LC, however, the differentiation between benign, pre-malignant and malignant SPNs remains elusive. Therefore, some SPNs are removed and some typically of smaller size (i.e., a diameter of $<$ 1 cm) are monitored using radiological surveillance [8].

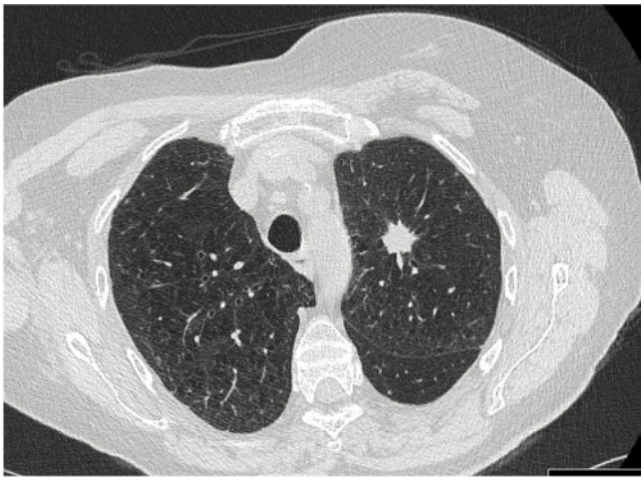

Figure 1.1: Solitary pulmonary nodule in the upper right lobe of a lung. Figure taken from [9].

1.1.1 Fluorescence Advantage

Pre-sampling clinical information of a lung available instantaneously is typically image based [2]. Recorded via radiograph or CT scans, these images are captured using potentially harmful ionising radiation, X-rays [10]. Using radiotracers, PET enables a comprehensive assessment of a tissue's function globally (i.e., when used with 18-fluorodeoxyglucose, PET measures tissue metabolism via glucose uptake) [11]. However, in addition to using radiation, PET provides images of low spatial resolution, therefore cancer margins and smaller areas of potential abnormalities (i.e., SPNs) are difficult to detect. In addition, PET is expensive [8]. Moreover, enriched clinical information from histology or genome sequencing is often slow and requires additional departmental coordination, skills and techniques. There is, therefore, an unmet need for tools that can instantly provide in-depth information on the tissue's metabolic state, structural composition, and environment, in addition to improving diagnostic certainty for patients presenting with SPNs. Fluorescence spectroscopy (FS), offering a cost-effective solution devoid of harmful radiation, may address this unmet clinical need by measuring light emitted from amino acids, structural proteins and metabolic proteins in pico- to nano- seconds [12].

Detailing and describing the application of fluorescence for diagnosis and monitoring requires, at first, the examination of the principles of fluorescence and how this physical phenomenon lends itself to this problem. We then discuss how fluorescence is monitored with specialised devices, including innovations into high resolution time-resolved fluorescence devices and the advantage these may bring. We finally provide evidence of fluorophores, both endogenous and exogenous, as effect diagnostic biomarkers.

1.2 Overview of Fluorescence

Fluorescence describes the phenomenon whereby following the excitation of specific molecules, i.e., **fluorophores**, light is emitted. Fluorescence was first adopted into clinic in 1948, whereby surgeons injected fluorescein, an organically synthesised molecule, or **exogenous fluorophore**, intravenously to define and locate brain tumour cells [13]. The adoption of fluorescence into clinic faded out until in 2005 a clinical trial using 5-aminolevulinic acid (5-ALA) a molecule metabolised by tumour cells, caused an accumulation of the naturally occurring, **endogenous fluorophore**, Porphyrin IX (PpIX) in malignant glioma cells. The illumination of this fluorophore in brain tissue enhanced intra-operative tumour and tumour margin detection doubling surgical resection success from 36 % without fluorescence to 65 % with fluorescence [14].

1.2.1 Fluorescence Excitation

Fluorescence is a radiative process originating predominantly from aromatic molecules [15, Chapter 1.1]. Fluorophores reside at room temperature in the ground electron energy state S0 [15, 16, Chapter 1.2]. Following the absorption of light, fluorophores become excited, entering into a higher energy state (S1 and above), a process which occurs in a matter of femtoseconds (10^{-15} s) (see Fig. 1.2) [17, 16, Chapter 11.11]. Within the excited state, molecular and environmental collisions occur causing vibrational relaxation, also known as internal conversion, whereby the molecules, in a matter of picoseconds (10^{-12} s), travel down to the lowest excited energy state of S1 [17, 16, Chapter 11.11]. Fluorescence occurs when, as the fluorophore exists the excited state, in a process called electronic relaxation (traveling back from S1 to S0), a photon is released (see Fig. 1.2)[18, Chapter 3.1.2].

1.2.2 Fluorescence Emission

When measuring fluorescence, there are specific aspects of a fluorophore which can be defined and assessed, including fluorescence **absorption**, **emission**, its **quantum yield**, **intensity** and **lifetime**. When measured across a wavelength range fluorescence absorption describes the absorption spectrum, i.e., the number of photons absorbed across a wavelength range, also corresponding to the energy absorbed [15, Chapter 1] (see Fig. 1.3 A). Fluorescence emission spectrum describes the number of photons emitted also across a wavelength range (see Fig. 1.3 A) [18, Chapter 3.3]. Due to a loss of energy in the higher energy states during vibrational relaxation the energy of the emitted photon is lower than the energy absorbed during excitation. This observation is termed 'Stokes Shift' and describes the shift across the wavelength region between the absorption and emission spectra [17, Chapter 11.11]

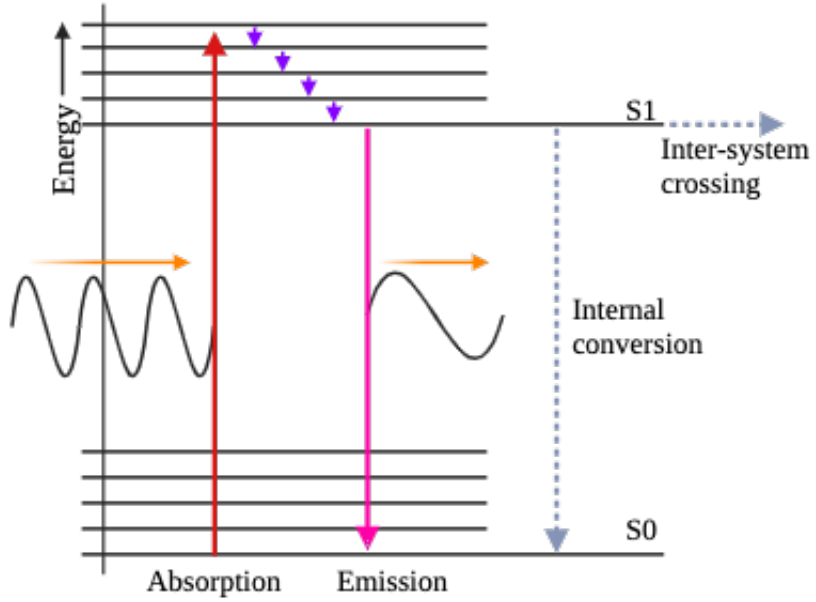

Figure 1.2: Molecules absorb light (orange), exciting the molecule from the lowest energy ground state (S0) to a higher energy state (S1) and above (red). Within the energy states, the molecules collide (inter-molecular collision) decreasing through the electronic states via vibrational relaxation (purple). When in the lowest vibrations state of S1, fluorescence (pink) occurs when the molecules exit the excited state (electronic relaxation) and a photon is emitted (orange). Due to the loss of energy during the relaxation processes in the higher energy states, the energy of the photon emitted during fluorescence is lower than the energy absorbed (represented by the waveforms). Alternative to fluorescence, a molecule may exit the excited state via other no radiative pathways, i.e., internal conversion, or undergo inter-system crossing leading to phosphorescence (grey dotted lines). Figure adapted from: [17, Fig. 11.21].

(see Fig. 1.3). Absorption and emission depend on a fluorophore's molecular structure and electronic configuration, factors which are also influenced by its environment [18, Chapter 3.4]. Therefore, fluorophores have their own environment dependent absorption and emission spectra.

In addition to absorption and emission, fluorophores exhibit a molecular brightness upon excitation at a particular wavelength [15, Chapter 1]. The molecular brightness is related to both the fluorophore's ability to absorb photons, its **extinction coefficient**, and its quantum yield [19]. The quantum yield can be described as the number of photons emitted (k_r) proportional to the number of photons being absorbed [18, Chapter 3.2]. De-excitation from alternative mechanisms, e.g., internal conversion from S1 to S0 without photon release, or inter-system crossing (e.g., spin conversion) leading to phosphorescence is possible (see Fig. 1.2). The de-excitation by alternative mechanisms is a non-radiative process which can be defined as

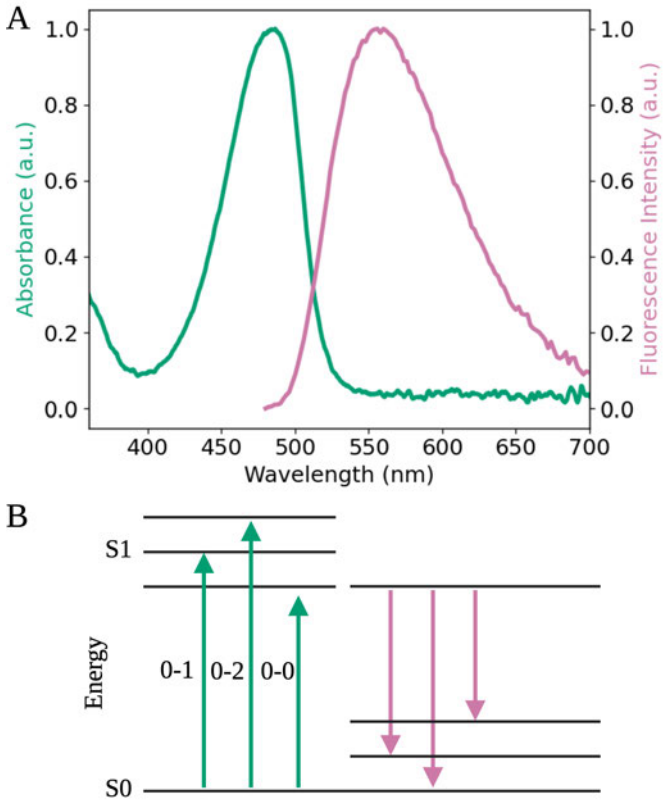

Figure 1.3: The absorbance (green) and fluorescence emission (pink) of an NBD dye **A)**. The relative fluorescence excitation (green) and emission (pink) of the fluorophores excited and an example of the vibrational energy states (labeled 0, 1, 2) in which they are likely to fall in to produce the absorbance and emission structure similar to the NBD fluorophore is also presented **B)**. Raw data of the fluorophore is supplied by Dr Charles Lochenie. Figure replicated from [15, Fig. 1.8]

k_{nr}. Therefore the quantum yield (θ) can be described as:

$$\theta = \frac{k_r}{k_r + k_{nr}} \tag{1.1}$$

[18, Equation 3.5]. In accordance's with Vavilov's rule the quantum yield is independent of the excitation wavelength [15, Chapter 1]. In addition, Kasha's rule states that the fluorescence emission of a photon typically originates from the lowest energy state of S1 and is therefore also independent of the excitation wavelength [15, Chapter 1]. Furthermore, given that the quantum yield describes the ratio between the number of photons absorbed vs emitted, the extinction coefficient and the quantum yield dictate the molecular brightness of a fluorophore [19]. Taken together this also suggests that fluorescence emission can be expected to occur from a fluorophore so long as the excitation wavelength of the excitation source falls within its absorption spectrum (i.e., fluorescence emission from fluorescein can be expected to occur following excitation between 400 nm-535 nm, depending on the aforementioned states

[20]). However, the emission also depends on the proximity of the fluorophore to a quencher. **Quenching**, a phenomenon where the fluorescence intensity (FI) of a fluorophore is reduced due to interactions with nearby molecules or environmental factors, can further alter the emitted fluorescence signal [15, Chapter 9]. Therefore the excitation wavelength, extinction coefficient, quantum yield, concentration, and the presence of quenching factors dictate the number of photons emitted and consequently the number of measurable photons at a particular wavelength.

1.2.3 Fluorescence Parameters

In a mixed system (e.g., in tissue), the **absorption** spectrum of individual fluorophores often overlap. Therefore from one excitation wavelength, multiple fluorophores can be excited. Spectral overlap of the corresponding fluorescence **emission** of the individual emitting fluorophores also ensues [21, Chapter 3]. Therefore estimating individual fluorophores based on intensity alone in mixed systems becomes challenging. **Fluorescence lifetime** (FL), in comparison, describes the time a fluorophore spends in the excited state, i.e., the time between excitation and photon emission, typically occurring in nanoseconds (see Fig. 1.2) [18, Chapter 3]. The formal definition of FL (τ) is the time of the intensity to decay to $1/e$, a radiative decay process (k_r). As molecules can also exit the de-excited state via non-radiative decay mechanisms (k_{nr}) [18, Chapter 3],

$$\tau = \frac{1}{k_r + k_{nr}}. \tag{1.2}$$

FL is (mostly) independent of FI, highly sensitive and fluorophore specific [15]. Additionally, it is influenced by the fluorophore's environment [15, Chapter 1]. Estimating this value is therefore useful for both specific fluorophore identification and environment sensing. FL follows the first order kinetics, in which the decay rate of a fluorophore is proportional to the concentration of fluorophores in the excited state. Therefore, FL can be modelled as an exponential decay where the intensity (γ) of photons measured across time (t) can be described by [18, Chapter 3]

$$f_t = \gamma \cdot e^{-\frac{t}{\tau}}. \tag{1.3}$$

Moreover, from a homogeneous single fluorophore population (e.g., a fluorophore in a single conformational state and constant physico-chemical environment), the FL is independent of the emission wavelength. Therefore, when estimated across the emission spectra the FL will remain constant [18, Chapter 3].

1.3 Fluorescence Devices

The fluorescence process can be measured using devices which assess the fluorescence emission (e.g., the steady-state mode of the FLS1000 Photoluminescence Spectrometer, Edinburgh Instruments), and/or time-resolved devices (e.g., the time domain mode of the FS5 Spectrofluorometer, Edinburgh Instruments), which assess fluorescence in either time-domain or frequency domain, capturing the FL [22]. The aforementioned devices have a bench-top microscopy set-up and therefore, aren't suitable for an *in vivo* assessment of lung tissue. Innovations into fibre based microscopy, such as confocal optical endomicroscopy (OEM), allow an *in vivo* fluorescence emission assessment of lung tissue at high spatial resolution (e.g, the Cellvizio system assesses FI with an image based field of view (600x600 µm) [23, 24]). Fibre-based time resolved techniques can be divided into image based devices, i.e., **fluorescence lifetime imaging microscopy** (FLIM), or point-based devices, i.e., point-based **time-resolved fluorescence spectroscopy** (TRFS). Since temporal-spectral devices are experimentally evaluated in this thesis, a description of their typical set-up ensues. FLIM is an image based technique which captures spatial, temporal, and often spectral information as well [25]. TRFS, in the absence of images, captures spectral and temporal information of a sample. To measure time-resolved fluorescence, devices generally require: a pulsed excitation light source, optical paths by which the emission and excitation passes, and detectors [21].

The origin of the excitation source has evolved over time, from Xenon lamps to ultrafast pico-/femto- second pulsed lasers [26, Chapter 3.1.1]. These advancements have been complemented by the progression of optical paths, which ensure excitation light effectively reaches the sample, distinguishes between excitation and emission light, and permits only the emission light to reach the detector, thereby minimising emission loss [26, 21, Chapter 3.1.2]. Within fibre-based optical paths the excitation light may be reflected, typically at 90° to the excitation source from specialized dichroic mirrors before reaching the sample [27]. The emission light travels back through the fibre, whereby the dichroic mirror permits the longer emission light (due to Stokes Shift as described in section 1.2.2), only, to travel through [27]. Bandpass filters may also be embedded within the optical path. These filters allow a central emission wavelength to pass, with a range or band width of wavelengths, e.g., a bandpass filter with a central wavelength of 470 nm$\pm$20 detects emission between 450-490 nm [27]. Bandpass filters can be used to both tune specific excitation light wavelengths and to determine the emission range allowing emission only of specific wavelengths to pass through [26, 21, Chapter 3.1.2]. Once the fluorescence emission passes through the optical path the emission then reaches a photon detector.

1.3.1 Single Photon Avalanche Diodes

Photon detectors' primary objective is to convert light into electrical signal. There are various types of detectors optimised for specific applications. E.g., photon multiplier tubes (PMT) and single photon avalanche diodes (SPADs) [15, Chapter 23.4]. SPADs employ an internal gain, in which detecting a single photon can result in a measurable electrical output. When coupled with timing electronics, time correlation can be established between the excitation light pulses and single photons emitted from the sample in the order of tens of picoseconds [28, 29]. The base of a SPAD contains a p-n semiconductor junction. An electric field is created across the junction by applying a voltage with higher potential on the n-side with respect to the p-side (i.e., reverse-biasing the junction). Photons are then absorbed by the semiconductor, stimulating free electron-hole pairs. The electric field allows the charge carriers to gain energy and move through the semiconductor crystal lattice. As the free charge carriers are swept through the junction by the electric field, they gain energy and create new electron-hole pairs upon colliding with the atoms of the semiconductor crystal structure [29]. The newly created electron-hole pairs create more and more free charge carriers in a chain reaction, which rapidly results in an avalanche current [15, 30, Chapter 23.4].

The avalanche current is then sensed by ancillary electronics and may be further processed, e.g., digitized and counted, or passed on to timing electronics [26]. To return the SPAD into an operational state, active or passive techniques are used to quench the avalanche current and restore the electric field over the junction. Semiconductor technologies, such as complementary metal-oxide semiconductors (CMOS) enable the manufacturing of highly integrated SPAD arrays [30, 29]. These allow a low power SPAD operating system, on-chip processing, and low noise. Following the detection of photons, different signal processing systems register their arrival times, allowing the time decay of the emitted photons to be built up over time [30, 29]. Sensing a photon may be followed by a high resolution measurement of time between photon absorption and the detection events marking laser emission (time-stamping) or conditional counting of photons based on when they arrived (time-gating). A common technique to observe the temporal shape of fluorescence signals through collecting and time-stamping single-photons is **time-correlated single photon counting** (TCSPC) [26, 31].

1.3.2 Time-Correlated Single Photon Counting

In TCSPC, a timing stop watch is started at the emission of light pulses from a high repetition rate pulsed laser. The stop watch is stopped upon the arrival of a photon emitted from the sample subsequent to excitation by a laser pulse, noting its stop time [31]. The difference in time between the two events can be measured and provided as digital numbers e.g., with time-to-digital converter (TDC) circuits. The timestamps are iteratively recorded from periodic excitation of the sample facilitated by a pulsed laser, building up a histogram of photon arrivals

across time (see Fig. 1.4 A and B). To ensure the distribution of the recorded time-stamps accurately represent the decay rate of the excited fluorophore, the rate of photon emission from the sample needs to remain below a certain level, typically between 0.1 and 0.001 photons per excitation cycle. Higher count rates can induce a measurement artifact called **early photon pile-up**. This occurs when several photons arrive to the sensor in a single excitation cycle (while recording the first one only), causing an over representation of photons with short time-of-arrival [31]. In early TCSPC devices the event starting the time measurement has been the laser emission and the detection of a photon has been the stopping event. A more efficient operation with less frequent initiation of the timing process is achieved performing a so-called reverse start-stop (or stop-start) approach. In this configuration, the photon detection starts the timer while the following laser pulse stops it. This approach enables the TDCs to run less frequently, matching the rate of photon emission, rather than at the higher frequency of the laser pulses [32, Fig. 2.3].

The clinical benefit of measuring fluorescence using TCSPC devices is their electronic sensitivity. This sensitivity is particularly relevant when measuring **autofluorescence** (AF) in samples. AF, described as the total emission of light from the endogenous fluorophores in biological tissue, typically arises from photons with lower quantum yields compared to exogenous fluorophores. Furthermore, the high sensitivity of TCSPC detection enables the use of lower powered lasers, minimising the effect of **photo-bleaching**, a phenomenon where prolonged light exposure irreversibly alters the chemical bonds of a fluorophore, leading to a permanent decrease in the overall fluorescence emission of a sample [33]. This is especially important in tissue samples, where the emission of dim fluorophores is often measured. In TCSPC, while the low excitation rate reduce the effect of pile-up, it contributes to a slower data collection time, which is a clinical disadvantage [34, Section 2].

1.3.3 Histogramming Mode

To address the slower fluorescence collection speed of the TCSPC method, other techniques have been developed, such as on-chip histogramming mode (HistMode) [35]. This setup consists of 512 individual **pixels**, each containing 16 SPADs. At each of the 512 pixels, individual SPADs detect photons, contributing to the construction of a histogram on the chip (see Fig. 1.4 C). This histogram categorises photons into 32 time bins, with a tunable temporal resolution from 51.20 ps-6.55 ns [35]. Photons with specific arrival times are directly stored at separate counters for each time bin, with up to 1 photon per laser cycle (as opposed to 1 photon per exposure time as in TCSPC). This speeds up the collection process, which may be more appropriate in a clinical setting. However, the 32 time bin restriction may prove to be a limitation, depending on the specific fluorophore(s) being identified (see Fig. 1.4 C).

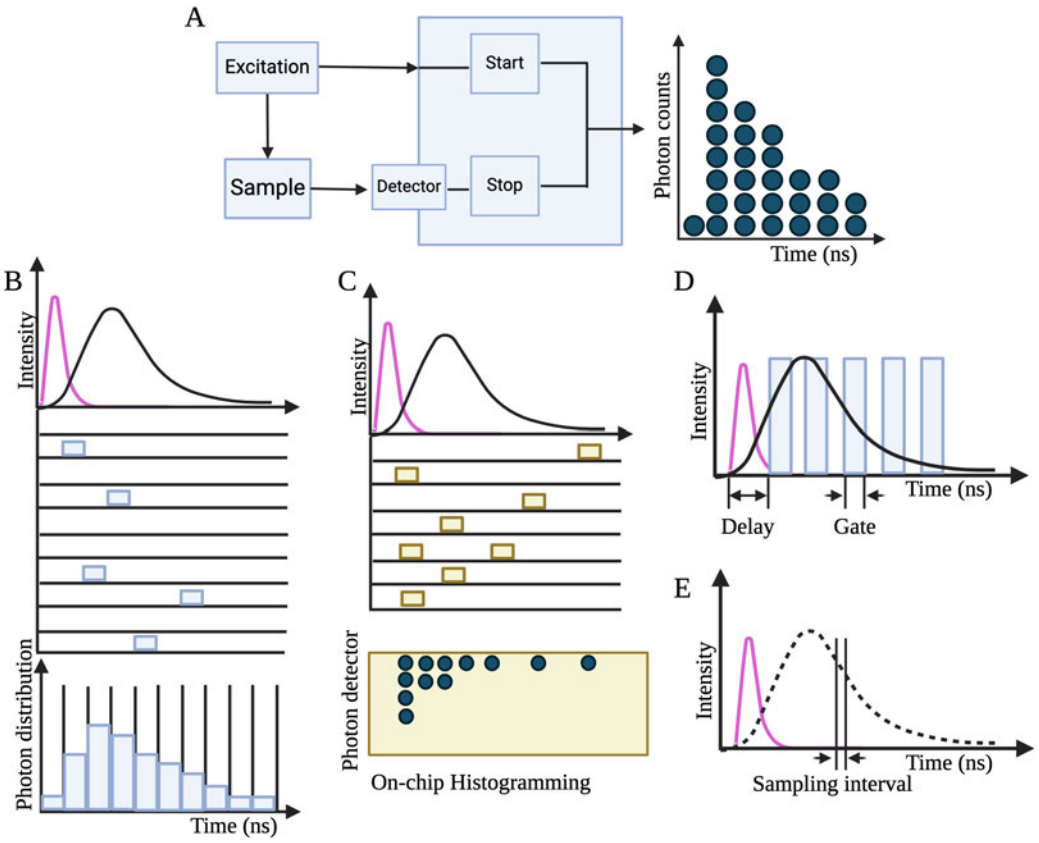

Figure 1.4: A schematic diagram showing the start-stop set-up of a typical time-correlated single photon counting (TCSPC) device to measuring the arrival time of photons emitted from a sample following excitation from a pulsed laser source **A)**. The photon counts are built up from arrival times to create a histogram of photon distributions over arrival times **B)**. An adaption to TCSPC mode called histogramming mode records the time of individual photons on an on-chip memory storage system within the photon detector **C)**. Allowing 1 photon per laser cycle to be recorded increasing the speed of collection compared to TCSPC [35]. Alternative to TCSPC devices, time gated techniques **D)** measure, following a short delay excluding excitation light, photons in set, or scanning, time gates. Another alternative photon detection technique is the pulsed sampling detection which measures photon counts in predefined sampling intervals **E)** to capture the photon decay over time. Figure adapted from [36, Fig.2].

1.3.4 Time Gated Techniques

For a more rapid estimation of FL, time-gated techniques measure fluorescence emission using specified time gates. This technique encompasses two main methods: one utilises fixed time gates ≥ 2, while the other involves scanning time gates across a timing axis during the emission process [34, Section 2]. In both approaches, photons emitted by the sample are detected and translated into voltages within these gates. Over successive excitation-emission cycles, a histogram of intensity versus time is constructed (see Fig. 1.4 C). However, this techniques lacks the temporal resolution of TCSPC and the specificity [34, see Fig. 3]. Despite this limitation, time-gating offers faster acquisition times, making it suitable for applications where rapid detection time is preferred [37, 38].

1.3.5 Pulse-Sampling Detection

Alternatively, for achieving faster detection times, pulse sampling techniques may be used. In pulse sampling, a high-powered excitation source generates a strong emission signal, which is then converted into an electrical signal. This method necessitates fast detectors capable of capturing the entire optical decay. The electrical signal is often connected to digitizers which measures the fluorescence decay at a high temporal resolution (see Fig. 1.4 D) [34, 39, Section 2]. As the decay signals are measured at a higher photon rate compared to other techniques, the rapid detection capability of the pulse-sampling method enhances its clinical advantage. However, the use of high-powered lasers also increases the risk of photo-bleaching which may limit its application in detecting dim AF samples [36].

1.4 Fluorescence Detection

Devices measuring temporal decay across the emission spectrum are also possible (i.e, spectral point-sampling TRFS or spectral FLIM). In these high-resolution multi-dimensional devices, the spectral width that the decay is measured in is called the **wavelength bandwidth resolution**. This differs depending on the optical setup, i.e., 1 - 500 individual spectral channels, with a wavelength bandwidth resolution as wide as 50 nm to as narrow as 0.5 nm. From these devices, multi-dimensional histograms can be built up consisting of the intensity of photon counts measured across a wavelength spectrum and time, this may prove particularly valuable for assessing AF. An innovative spectral FLIM device, as described in [40], details an optical scanning microscope device with an additional spectral-temporal component. This device enables the measurement of spectral and temporal fluorescence across a 256x256 image pixels. Photon counts are resolved across wavelengths ranging from 500-760 nm, with

a wavelength bandwidth resolution of 0.5 nm. Additionally, the decays are measured in 32 time bins, each with a temporal resolution of 50 ps at every spatial position. The results demonstrate unprecedented detail of the fluorescence of an *ex vivo* adenocarcinoma sample [40].

Due to a sampling area discrepancy in the spatial area of tissue measured by point-sampling TRFS compared to FLIM (e.g. FLIM measures 600x600 µm [40], whereas TRFS measures $\sim <100\,\mu m^2$) [41], spectral FLIM may be slower. For an *in vivo* assessment, spectral FLIM technology is therefore limited by speed and resolution (see Fig. 1.5 B). Although FLIM devices enhance tissue images and videos, assessing the global fluorescence profile of a sample, high-resolution point-sampling TRFS at equivalent speeds, provide detailed spectroscopic insights into microscale tissue areas (e.g. 30 µm) without the spatial reference [34] (see Fig. 1.5 A). Given that the origin of emission from the AF of a specific tissue area is fundamentally unknown, high resolution TRFS point-sampling technologies may be potentially better suited for *in vivo* assessment.

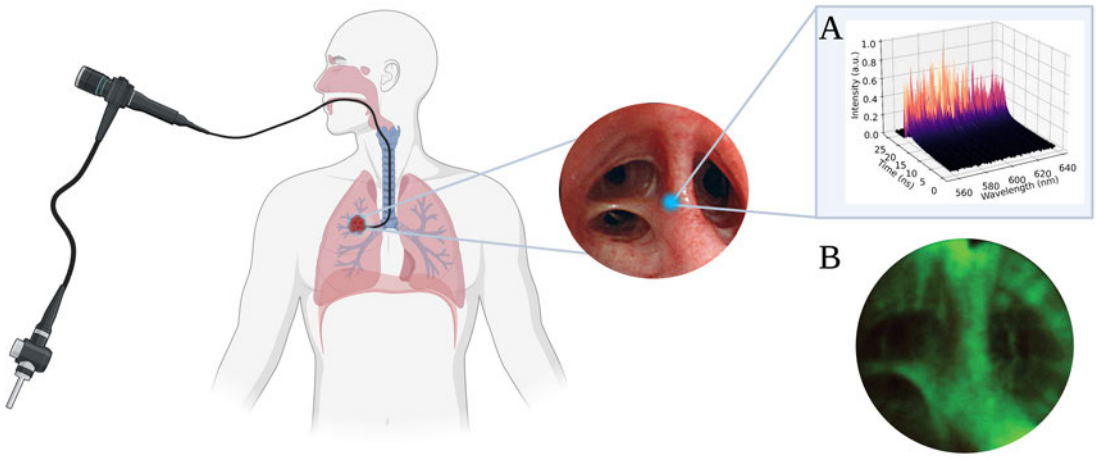

Figure 1.5: There are two broad categories of time-domain fluorescence spectroscopy (TRFS) devices that can be miniaturized and passed through the working channel of a bronchoscope to provide information on lung tissue. These devices are known as point-sampling TRFS devices or fluorescence lifetime imaging microscopy (FLIM). TRFS measures the fluorescence properties of a smaller tissue area in the absence of an image **A)**. However, FLIM devices not only measure the time-resolved decay properties but also capture the spatial architecture of the tissue **B)**.

1.5 Fluorescence Data Analysis

Time-resolved data from fluorescence devices is obtained from wavelength-defined channels, recording the intensity of the detected photons over time. Extracting biologically relevant parameters from the decay traces, particularly FI and FL, requires computational models. The choice of the analysis method depends primarily on the objective of the routine. Fitting routines can be categorised into distinct groups: fit-free methods, suitable for a quick contrast assessment; curve fitting approaches, ideal for more precise FL assessment and inverse machine learning models. Some account for device artifacts like the **instrument response function** (IRF), while others offer a broader overview of the inherent decay.

1.5.1 Instrument Response Function

The underlying fluorescence (f_t) of the fluorophores emitting in a sample, as aforementioned in equation 1.3, can be modelled by exponential decays. However, the observed decay traces (y_t), contain additional artifacts. The most well characterised artefact is the IRF, originating from distortions in the laser pulse, detector distortions and timing uncertainty. The signal of the IRF is typically characterised by its full-width at half maximum (FWHM) and can be incorporated into fitting routines to remove its effects using many different methods. The simplest method, known as tail fitting, assumes that the effect of the IRF is smaller than the overall decay of the measured fluorescence. Tail fitting, therefore, involves cropping the observed decay to start at the temporal peak. The estimated fluorescence signal over time, denoted by $f(t)$, and the time axis adjusted to start at the temporal peak (p) where $t > t_p$, can be described by the equation:

$$f_t = \gamma \cdot e^{-t/\tau} I(t > t_p). \tag{1.4}$$

The disadvantage of this method is that any fluorophore with a short FL, i.e., fluorophores with lifetimes that fall within the initial time bins, may be measured inaccurately. In cases where a single FL is estimated following a tail fitting approach, the final FL obtained from the sample may be overestimated if shorter FL components are measured. An alternative approach involves a deconvolution method, wherein the decay traces are deconvolved with a measured IRF within the fitting routine. These methods can all be estimated using curve fitting approaches.

1.5.2 Curve Fitting Methods

Curve fitting methods provide a direct assessment of the individual decay rates. The most common curve fitting method is the **non-linear least squares** (NLLS) method [42], where by the squared residuals of a loss function J are minimised between the observed decay (y_t) compared to the fluorescence decay (f_t),

$$J = \sum_{t=1}^{T} (f_t - y_t)^2. \tag{1.5}$$

A disadvantage of the NLLS method is in the least squared function which assumes the noise is Gaussian. However, where photon counts are sparse, Poisson noise can be observed. Therefore, the NLLS method in these settings may not provide the most accurate lifetime estimation. An alternative method with a different noise distribution, is the **maximum likelihood estimation** (MLE) [43]. Optimal parameters are fit through maximising the equation, instead of minimising the residuals, where the likelihood function is given by:

$$L(\gamma, \tau; y_t) = \prod_{t=0}^{T} \frac{f_t^{y_t}}{y_t!} e^{-f_t}. \tag{1.6}$$

[44, Equation. 2]. Both curve fitting methods can be adapted to represent equation 1.4, or be incorporated into a deconvolution function. I.e.,

$$s_t = (f * h)[t]. \tag{1.7}$$

In this method, f_t represents the underlying fluorescence from the sample, s_t the estimated decay, and h_t the measured IRF. Here, f_t can also be adapted into a multi-exponential decay, therefore, samples containing a mixture of fluorophores, and therefore, a mixture of decay components, can be individually estimated. The overall decay trace can be modelled as a summation of the individual fluorescence components, such as:

$$f_t = \sum_{l=1}^{L} \gamma_l \cdot e^{-t/\tau_l}. \tag{1.8}$$

In this instance l represents the fluorescence decays of individual fluorophores. However, these approaches are limited by the accuracy of the measured IRF, which itself may be challenging to capture. Moreover, the goodness of fit using the curve fitting methods is often expressed with a chi squared close to 1 [45]. However, where mixed systems, i.e., in tissue where multiple unknown fluorophores are estimated, and multi exponential decay models are used, the number of components as an *a prior* are required. Moreover, these methods are computationally slower, potentially limiting an instantaneous FL assessment which may be required in clinic.

1.5.3 Fit Free Methods

Fit-free methods provide an alternative rapid assessment of samples and are particularly advantageous for contrast objectives, such as rapidly distinguishing between diseased and healthy tissues without the need for additional information. One of the most common fit-free methods is rapid lifetime determination (RLD). This method calculates integral differences of signal across a broad time range, splitting the observed decays into two temporal windows y_0 and y_1 of width $\hat{T}$, allowing for quick and efficient analysis [46]. The time bins the decay is recorded in is denoted as m and the total time bin M, therefore

$$\hat{y}_0 = \sum_{m=m_{\text{peak}}}^{(m_{\text{peak}}+M)/2} y_m \text{ and } \hat{y}_1 = \sum_{m=(m_{\text{peak}}+M)/2+1}^{M} y_m \tag{1.9}$$

where m_{peak} is the time bin containing the highest photon count, and $M' = M - m_{\text{peak}}$. RLD can then be described as:

$$RLD = \frac{\hat{T}}{\log \hat{y}_0/\hat{y}_1}. \tag{1.10}$$

In this equation, y_0 represents the observed fluorescence decay in the first time window and y_1 the observed fluorescence decay in the subsequent time window [46, equation 1a] [47, equation 15]. RLD is typically not employed with an IRF, potentially impacting the interpretability of the data, particularly when measurements are taken on different days with slightly varied optical setups.

The centre of mass time (CM time) offers an alternative fit-free approach. In this method, decay traces are summed over time, represented by the equation:

$$CMtime = \frac{\sum_{m=1}^{M}((m-1)M + T/2)y_m}{\sum_{m=1}^{M} y_m}. \tag{1.11}$$

Here, y_m describes the observed decay traces in time bin m, with a total of M time bins and temporal resolution T [48, 49]. This method can incorporate a measured IRF, potentially providing a more accurate decay rate estimation compared to the RLD method. Both methods, however, consider fluorescence decay as a single decay component. Therefore, in mixed systems with complex decay rates (e.g., tissue), there is a risk of oversimplification.

An alternative fit-free approach is the Phasor method. Within this approach, fluorescence decays are Fourier transformed into Phasor specific G-S coordinates of a 2D space [34, Fig. 6 B]. Of single exponential decays, values are plotted on the outside region of the 2D space, with short decays appearing towards the right of the plot, and longer decays towards the left. Moreover, a particular advantage of this method is that, without any *a priori* information, decays containing multiple fluorophores i.e., in mixed systems such as in tissue, the different FL components are plotted towards the inside of the 2D space, differentiated also into their specific longer and shorter components. This may be advantages when different parameters

within the total decay become biologically relevant. This method is also rapid, commonly used in FLIM settings, co-coloring different FLs in the spatial location on the images. However, to convert Phasor values into actual FL values, a re-conversion is required. Additionally, implementing Phasor analysis is more complex compared to alternative fit-free methods [34]. Moreover, this method does not include additional distortions from the detector and optical system (i.e., the IRF). These factors may perturb the interpretation of the analysis.

An alternative method for calculating the average FL, and incorporating the IRF into the analysis, is the Laguerre deconvolution method [50]. This method estimates 12 base pairs of Laguerre polynomials within the fitting routines, typically using a NLLS method to determine optimal parameters. It provides a more accurate FL assessment than fit-free models, incorporates IRF deconvolution within the calculation, and is computationally faster than multi-exponential fitting methods. However, since the 12 base pairs are used to estimate the total decay, it is not possible to determine specific lifetimes, corresponding to individual fluorescence species or decay rates, within a sample using this method. More recently, machine learning (ML) methods have been deployed to extract FL from the decay traces alone. These models provide a rapid estimation of FL from multiple components, without requiring information from the IRF.

1.5.4 Machine Learning

Inverse ML techniques, including deep learning models, have been explored for rapid and specific FL assessment [51]. For instance, [52] employed an artificial neural network (ANN) to estimate a bi-exponential decay model from FLIM data, achieving FL estimation within 0.2 s However, this method was less efficient for samples with low photon counts. An alternative approach involved Laguerre deconvolution to estimate fluorescence decays outwith the IRF, followed by principal component analysis (PCA) and random forest regression for FL and amplitude estimation [53]. This model's performance was validated on real-world datasets, including cell lines and *ex vivo* liver samples. In an alternative approach, a feed-forward ANN estimated the fractional contributions of multiple fluorophores in a mixed system [54]. This method focused on determining the relative concentration of > 2 fluorophores, rather than specific FL values, making it suitable for complex systems like tissues. In summary, these methods provide a rapid alternative for estimating FL without requiring a measured IRF. However, in these methods, similar to curve fitting approaches, the predetermined number of exponentials must be known *a priori*. Furthermore, all analysis routines described only consider individual fluorescence decays. Therefore, in cases where high-resolution multi-dimensional devices are used, multiple decays recorded across the emission spectrum are considered independent of each other.

ML has also been deployed for the classification and segmentation of fluorescence [51]. Trained on labeled fluorescence parameters from both cancerous and non-cancerous samples, these classifiers can provide a probability score as to whether the sample is cancerous or not. However, they are limited by both the accuracy of the FL calculations and the samples used for training.

1.6 Translational Fluorescence

1.6.1 Smart Probes

The diagnostic and prognostic potential of FS ultimately depends on the biological relevance of the specific fluorophore(s) being detected. As mentioned, two types of fluorophores exist, **endogenous** and **exogenous** fluorophores. However, only a specific subset of endogenous fluorophores is discoverable in tissue following excitation at certain wavelength ranges, which may limit the diagnostic potential of AF (see Fig. 1.6). Moreover, these fluorophores frequently have low quantum yields and overlapping spectral regions, therefore, can be difficult to both detect and analyse.

Exogenous fluorophores can be administered either unmodified, or altered to enhance biological specificity, i.e., bound to an epitope, known as a smart probe. Exogenous fluorophores have a higher quantum yield than endogenous fluorophores, known specific spectral bands, can be administered at a higher concentration and may provide disease specific detection. Exogenous fluorophores in the context of biomarkers can be defined in different categories. Exogenous fluorophores administered alone, as **small molecule agents**, such as methylene blue (MB) and 5-ALA [55]. These have been FDA approved, have low toxicity and can be measured in the visible light range. MB has a peak absorbance at 665 nm and emission at 685 nm. MB accumulated in metastatic neuroendocrine tumours when intravenously injected, showing 93 % specificity when administered in 17 patients with small intestinal neuroendocrine tumours [55, 56]. 5-ALA on the other hand, as a precursor to the endogenous fluorophore PpIX, when metabolised simulates an accumulation of PpIX. PpIX has a maximum absorption range of 405-420 nm [57, Fig. 4] and an emission range of 620-700 nm [58]. 5-ALA has a higher metabolic turnover in certain tumour cells, therefore, when administered, a tumour specific increase in the endogenous fluorophore can be observed. This method has been applied to detecting diffusely infiltrating gliomas in 22 patients, specifically enhancing the visualisation of low grade glioma tissue [55, 59].

Small molecule agents, however, have lower specificity and may accumulate throughout the body, including in non-cancerous regions. Smart probes, exogenous fluorophores altered to detect specific biomarkers, provide an enhanced alternative. These probes can be categorised based on their targeted features, including cell surface marker identification, extracellular pH monitoring, protease detection, and protein receptor identification [55].

An example of a pH-sensitive smart probe is ONM-100, which consists of an indocyanine green (ICG) exogenous fluorophore activated in acidic environments [60]. When administered to 30 patients with solid tumours, including head and neck, breast, oesophageal, and colorectal cancers, this probe provided clear delineation of tumour margins [60]. Another type of smart probe, VGT-309, is designed to detect cathepsin, a protease often overexpressed in tumors. Following phase 1 and 2 clinical trials, VGT-309 successfully identified pulmonary tumours, including occult and non-palpable ones [61]. Additionally, smart probes targeting specific protein receptors, such as the folate receptor α (FR-α), have been developed. An example is folate-FITC, which binds to FR-α, a receptor often overexpressed in solid tumours such as LC, with high affinity to folate. The folate portion of folate-FITC binds to FR-α, causing the FITC portion to fluoresce. This fluorophore has shown promise in detecting ovarian cancer [55].

Fibre based spectroscopy setups used in conjunction with smart probes allow real-time detection of the specified epitope. However, high levels of inter- and intra- patient heterogeneity render a generic cancer specific probe difficult to achieve. Moreover, the uniform fluorescence of the administered probes are also difficult to achieve. In addition, smart probes may alter the biological signalling processes, require regulatory approval, and increase the cost of the procedure [62, 63]. Therefore, despite endogenous fluorophores lower quantum yield/extinction coefficients, these may be more applicable in early stage LC diagnosis and prognosis.

1.6.2 Autofluorescence for Lung Cancer Detection

At present, a number of known endogenous fluorophores are excited at a specific excitation wavelength. These molecules have different biological connotations and therefore, have different biological implications when used as diagnostic markers. Moreover, as from one excitation wavelength, more than one endogenous fluorophore is excited, the potential for AF to contribute to diagnostics and monitoring is enhanced by information from multiple markers simultaneously (see Fig. 1.6).

1.6.3 Tryptophan

The fluorophore excited at the shortest wavelength range (ultra-violet (UV)), tryptophan (Trp), is an essential, aromatic amino acid. This has a reported excitation maxima of 280 nm and emission maxima of 350 nm [66]. Trp is one of the most abundant fluorophores in tissue, at an estimated 1 mol % in proteins in proteins in the cytosol, and 3 mol % in proteins in cell membrane proteins [66]. Trp has 3 reported lifetime values, dictated by environmental factors: 0.5 ns, 3 ns and when in serum albumin (blood plasma) proteins 6 ns - 9 ns. Its quantum yield has also been reported to vary, from 0.35 to 0.01, again dictated by the environment. In addition, an emission maximum in the blue-shift direction has been reported in non-polar

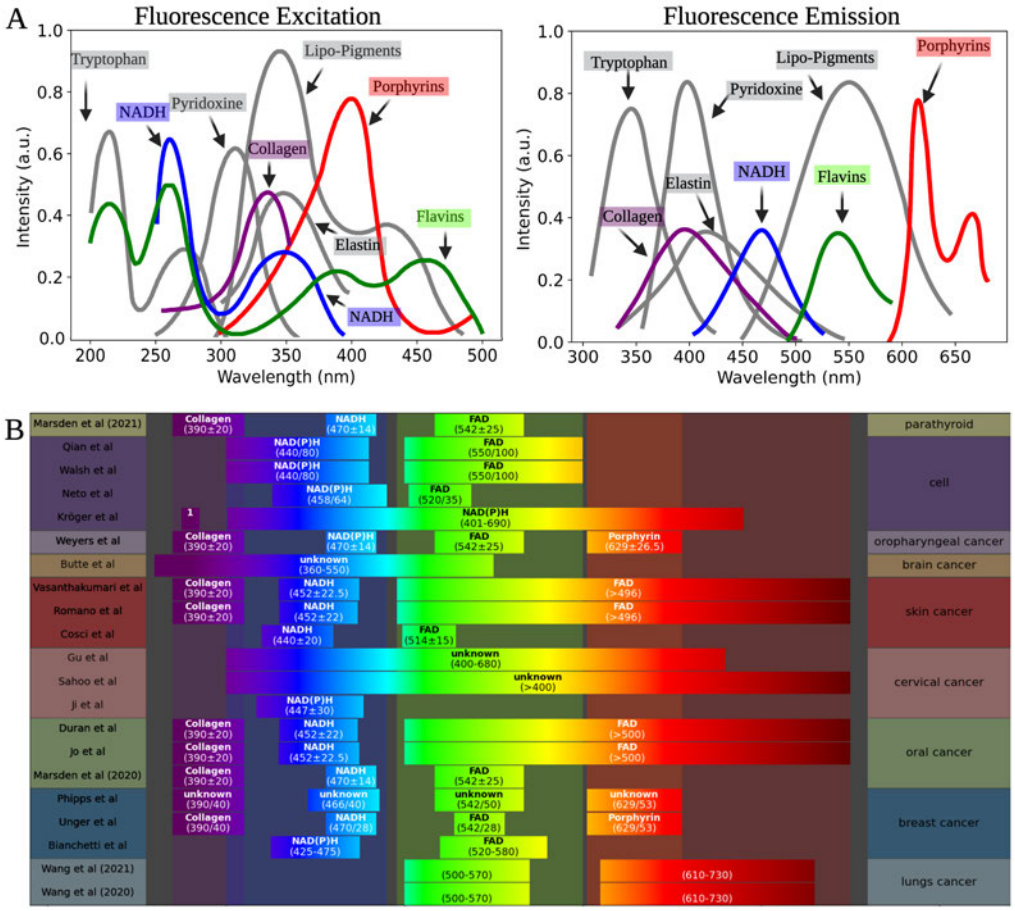

Figure 1.6: The excitation and emission profiles of endogenous fluorophores, in addition to devices used to assess their autofluorescence when used with specific emission filters. **A)** shows the excitation (left) and subsequent emission (right) of endogenous fluorophores. Specific fluorophores commonly assessed in tissue, label free have been coloured, however, the fluorophores which may also contribute to the overall tissue fluorescence (grey) have been highlighted. The figures are adapted from [64]. **B)** shows the specific wavelength channels and the corresponding fluorophores measured from different tissue in cancerous settings. From A, despite a subset of fluorophores mentioned being detected in the channels, other fluorophores may also be present perturbing the interpretation. This figure is adapted from [65].

environments, and a red-shift in polar environments, i.e., environments consisting of a pull factor between negatively and positively charged molecules. Therefore, although difficult to interpret, the overall spectroscopic information that an emission measurement of Trp gives is rich in information of both the proteins and their environment [66].

Trp, along with being an efficient, natural, fluorophore, has connotations in LC. Trp, in the lung and other organs, is metabolised by indoleamine 2, 3-dioxygenase 1 (IDO-1), an enzyme in the kynurenine cycle. IDO-1 activity has also been linked to increases in oxidised nicotinamide adenine dinucleotide (NAD+) [67]. IDO-1, is produced in response to inflammation, limiting T cell function and immune tolerance; in addition to assisting in tumour immune evasion.

Moreover, Trp metabolism in LC has been shown to indicate tumour immune escape. Specifically, lower levels of Trp have been observed in LC compared to normal controls, particularly in NSCLC. With $\geq$ 92 % specificity as a diagnostic marker in some studies [67]. Even lower levels of Trp were reported in patients with adenocarcinoma, compared to squamous cell cancer types. In addition, low levels of Trp specifically in LC cells have been linked to the chemotherapy cisplatin resistant cell types, highlighting the potential of this amino-acid as both a predictive and prognostic biomarker, and its use in precision medicine (i.e., identifying drug resistant tumours) [67]. Taking both the LC relevance of Trp, and its effectiveness as a fluorophore, including the sensitivity of the fluorescence profile of Trp in conjunction with its microenvironment Trp is an ideal endogenous fluorophore to detect oncogenic changes. However, Trp excitation is in the UV-B range (280 nm), which may be problematic for inducing DNA damage to cells [68]. Therefore consideration needs to be taken for harm-free excitation of Trp in diagnostics and monitoring applications.

1.6.4 Pyridoxine

Vitamin B6, also known as pyridoxine, is phosphorylated by pyridoxal kinase (PDXK) [69]. The family of vitamin B6 metabolites are associated with $>$140 enzyme reactions and are estimated to be essential in at least 4 % of all enzymatic activities in the genome [69]. These molecules are specifically related to the metabolism of amino acids, carbohydrates, fatty acids and some neurotransmitters, therefore, are essential in many normal biological functions and may have implication in oncogenesis [69]. The role of vitamin B6 in cancer has been explored. In *in vitro*, including in cell line models these molecules have been shown to inhibit proliferation and enhance chemotoxicity [69]. However, there has been conflicting results when investigated in animal models. In NSCLC specifically, studies investigated vitamin B6 in A549 cell lines, concluding that pyridoxin increased the intracellular uptake of the chemotherapy drug cisplatin [69]. An alternative study showed that PDXK is an accurate positive NSCLC prognostic marker [70]. With elevated levels of circulating vitamin B6 associated with improved disease outcome, however, cancer patients typically display reduced levels of circulating vitamin B6 [70]. In summary, the relationship between vitamin B6 and cancer is complex, however, some evidence shows that it may be appropriate as an accurate prognostic marker in NSCLC.

The fluorescence of vitamin B6 is well documented [71]. With a broad absorbance range of 245 nm-326 nm and emission range of 336 nm-393 nm depending on multiple environmental factors [71]. The quantum yield changes in varying pH levels from 0.028 in a pH of 9.5, to 0.15 in a pH $<$6.2 [71]. Moreover, the lifetime is also influenced by both the environment and solvent, often displaying a single exponential lifetime of 1.6 ns in aqueous solutions, dropping

to 0.37 ns in ethanol and increasing to 2.1 ns in dimethylformamide [71]. The majority of the fluorescence of pyridoxamine is reported in solution, extrapolating the fluorescence findings of this molecule to an *in vivo* interpretation would require a more in depth assessment, however, given its implications in NSCLC, it may act as an effective biomarker.

1.6.5 Lipo-pigments

Lipo-pigments, or lipofuscins, brown granules containing cellular waste products, accumulate over time in certain tissue types including in the kidney, liver, brain and heart [72]. These are known to exhibit AF in specific tissues, i.e., an excitation of 330 nm-380 nm and emission of 540 nm-570 nm in the brain [73]. However, there is limited evidence that these are found in lung tissue, or have implications in LC [72].

1.6.6 Porphyrins

Porphyrins are a group of heterocycle (5 ringed) compounds which make up the essential components of hemoproteins. The most abundant porphyrin is PpIX [74]. This specific molecule binds to iron, making up heme. Heme plays essential roles in oxygen transport, cellular oxidation and reduction reactions and in drug metabolism [74]. As previously mentioned, PpIX is converted into heme by mitochondrial enzymes within the mitochondrial matrix by an 5-ALA. During regular heme synthesis, this process is quick, however, cancerous cells often display a deregulated heme metabolism [75]. This results in an accumulation of PpIX in cancer specific cells, acting as a natural smart probe.

A range of FL values of PpIX have been identified, from and average of 16.4 ns in DMSO, to between 6.3-3 ns in cell lines following 5-ALA incubation [76]. However, in both mouse and human tissue, the FL of PpIX has been reported to range from 0.8-2 ns [75]. Moreover, the red emission window of this fluorophore allows a higher spectral specificity of its identification in complex systems like tissue (see Fig. 1.6). In addition, as the specificity of PpIX is induced following the administration of 5-ALA, it less efficient and cost effective compared to alternative fluorophores.

1.6.7 Collagen and Elastin: The Extra Cellular Matrix

LC tumours both in primary and metastatic stage are often characterised by a tissue stiffness, particularly in the stroma, the extracellular compartment of tissue [77]. The majority of the stroma is made up of a specialised matrix called the extracellular matrix (ECM). The ECM, is a large network of proteins, structural and functional, providing tissue with stability and elasticity. The ECM has been described as a regulator of the cellular response which underlines cancer hallmarks [77]. Studies have shown that SCLC patients presenting with tumours surrounded

by extensive stroma have shortened survival times. Furthermore, binding of SCLC cells to the ECM has been shown to protect cancer cells from chemotherapy-induced apoptosis [77]. The ECM, therefore, has major implications in cancer progression, including supporting chemoresistance [77].

The two most abundant proteins in the ECM are collagen and elastin [77]. Enzymatic cross-linking of collagen and elastin fibres are catalysed by enzymes in the lysyl oxidase (LOX) family and the transglutaminase family. Genetic mutations in LOX enzymes has been indicative of poor LC prognosis [78]. In addition, covalent cross-linking of collagen via specialised linker proteins (i.e., pyridinoline) contributes to stroma stiffening [79]. Studies have observed the increase in pyridinoline cross linking mediates an increase in tissue stiffness [80]. An increase in tissue stiffness has shown to favour tumour cell invasion and metastasis. This has been investigated in both early and late stage LC development [80].

Elastin, a polymer-like gel, in addition to its flexibility, provides extension resilience in tissue structures. It is, therefore, a major protein in the lung making up over 30 % of its dry weight [81, 82]. Elastin is comprised of precursor molecules called tropoelastin produced by surrounding specialised cells such as fibroblasts [81]. These modular precursor molecules are cross linked together with cross linker proteins desmosine and isodesmosine, catalysed by LOX enzymes into elastin fibres. Damage to fibre structures facilitates a thinner elastin matrix and an accumulation of elastin fragments [81]. Elevated levels of elastin protein fragments are observed in adults diagnosed with LC [81]. Furthermore, structural changes in elastin in certain types of LC (i.e. Adenocarcinoma) have also been observed [83].

Evidence suggests the ECM matrix and its constitutes are often deregulated within cancerous tissue. Moreover, the ECM has distinct fluorescence properties, providing the basis of the biology behind fluorescence discrimination observed between normal and cancerous ECM at specific excitation wavelengths [84]. I.e., the major fluorescence contributor of OEM emission (when excited at 488 nm in the lung) has been shown to originate from elastin fibres [85]. The distinct fluorescence profile of elastin have been shown to originate from both the overall structure, and the cross-linkers pyridinoline (both the hydroxylysine or lysyl forms of the molecule). Pyridinoline has a FL range of between 1.5-2 ns [86], an absorbance peak of 325 nm [87, 88], and an emission peak of 350 nm depending on the pH. The elastin structure has an absorption range of between 300-400 nm, although as the OEM results suggest, an excitation of 488 nm has also been shown to excite a significant proportion of elastin. An elastin FL range has been reported, from 0.38 ns in tissue [21], to bovine neck ligament of between 1.72 ns-1.83 ns [89]. However, given the broad range of FL and emission from both the elastin cross-linkers and the structure, interpreting the AF of these may be complex. In addition to fluorescence from the hydroxylysic pyridinoline and lysyl pyridinoline linkers of collagen, the structure has a reported FL of between 2.84 ns-2.94 ns [89]. The absorption and emission peaks have been reported at 339 nm and 380 nm respectively [90]. Given the specificity of

the fluorescence profiles of molecules within the ECM, and that the tumour ECM provides aberrant microenvironment cues favouring proliferation and metastasis, inhibiting apoptosis of tumour cells. An assessment of this matrix, and the major components may provide additional insight into drug resistances, prognosis and tumour aggression prediction.

1.6.8 Fluorescence and Metabolism

One of the 10 revised hallmarks of cancer is a deregulated metabolism [91, 92]. Specifically, a tumour related effect was identified called the Warburg effect, originating from the observation that tumour cells consume glucose and excrete lactate at a higher rate than normal [93]. Studies have shown this is due to a shift in metabolic processes, whereby tumours increase their rate of **glycolysis**, a metabolic process which occurs typically in hypoxic environments even when oxygen is available, also known as aerobic glycolysis. [94]. This effect has been shown to support sustained and increased cancer cell proliferation and invasion [94]. Glycolysis occurs in the cytosol whereby in a 10 step reaction process glucose is converted into pyruvate and lactate [94, Fig. 1]. During this process one glucose molecule is converted into 2 NADH molecules, 2 ATP molecules and 2 pyruvate molecules. Furthermore this reaction supplies several metabolic intermediates that are required for macromolecule biosynthesis to support continued proliferation of cancer cells [95]. Pyruvate is then transformed into lactate, catalysed by an enzyme called lactate dehydrogenase (LDH), lactate is then exported from the cells via MCT4 transporters [94, Fig. 1]. Initially considered a waste product, the secretion of lactate to the extracellular media is now considered a key characteristic of the Warburg effect, because it leads to an **acidic** microenvironment that triggers immunosuppression and angiogenesis, all contributing to tumour survival [96, 97].

Counter to the Warburg effect, some tumours and cells within the tumour microenvironment display a reverse Warburg effect [98]. These cells consume lactate at a higher rate, which is converted into pyruvate and transferred into the mitochondria resulting in an increase in **oxidative phosphorylation (OXPHOS)** favouring a tricarboxylic acid (TCA) cycle skewed metabolism [98]. Within the TCA cycle in the mitochondria during OXPHOS a molecule of glucose is efficiently converted into around 32 ATP molecules [94]. The by product of this reaction is also carbon dioxide and water. Moreover during this process **NAD** and flavin adenine dinucleotide (**FAD**) act as electron donors and acceptors in specific steps of the reaction cycle [94, Fig. 1]. These are essential in generating ATP in the TCA cycle. Studies have shown that both the Warburg and reverse Warburg effect can happen in different tumour cells of the same cancer, a phenomenon known as metabolic symbiosis [99, 100]. A subset of hypoxic cells favouring glycolysis, consumes glucose at a higher rate, excreting more lactate [98]. The alternative subset of normoxic cells favouring OXPHOS then absorb the lactate, converting more lactate into pyruvate to be used in the TCA cycle for a more efficient glucose free ATP generation.

Studies have shown that LC is not exempt from this metabolic symbiosis, displaying either a glycolysis or OXPHOS skewed metabolism [94]. Moreover, during a glycolysis skewed metabolism, not only is an increase of glucose observed, but an increase in glucose-6-phosphate. This glucose analogue is phosphorylated and therefore unable to leave the cell, this is the basis of the biology behind PET imaging, tagging a phosphorylated glucose analogue (^{18}F-FDG) with radiotracer markers [94]. Favoring a glycolysis metabolism pathway, these LC cells have increased levels of the radiotracer. However, more recent studies investigating the metabolic transformation of 80 LC cell lines have shown there is a large variety in metabolic plasticity, concluding that a consistent Warburg shift is not always observed across an entire cell cohort [101]. Therefore, despite metabolic changes being a hallmark of cancer, heterogeneity exists.

OXPHOS and glycolysis rely on the electron donation and acceptance of two specific molecules, NAD and FAD in producing ATP. These molecules also naturally fluoresce (see Fig. 1.6 A), exhibiting different photo-physical properties in various reduced and oxidative steps, in addition to when in different protein bound stages. Although it is important to note that in the reduced forms neither molecule is fluorescent. As these metabolic cycles are directly implicated in LC, these fluorophores may contribute significantly to LC AF.

1.6.9 Nicotinamide Adenine Dinucleotide

NAD has different forms, a reduced form (NADH) and an oxidised form (NAD^+). When bound to an additional phosphate, this molecule is known as nicotinamide adenine dinucleotide phosphate (NADP) which also has an oxidised ($NADP^+$) and reduced form (NADPH). The different forms of NAD(PH) have different biological functions. NAD(H) is responsible for catabolic reactions, i.e., the breakdown of larger molecules into smaller sub-units, which either release energy or are oxidised [102]. NADP(H) has anti-oxidative effects (involved in regulating reactive oxygen species, amongst other functions) and implications in anabolic reactions. Both molecules are found in the cytosol and in mitochondria [102]. The homeostasis and function of NAD(PH) is dependent various metabolic signalling pathways [102]. Overexpression of NADKs, which synthesise NADPH, enhance LC activity [102]. Moreover, overexpression of malic enzymes (ME1), located within the cytosol, induce NADPH production. This overexpression is associated with poor LC progression [102]. Overexpression of isocitrate dehydrogenase (IDH) 1 generating NADPH from $NADP^+$ is also linked to poor NSCLC prognosis. Hence this molecule is significant in LC indicating its utility in routine diagnostic and monitoring procedures [102].

NAD molecules are endogenous fluorophores, and, despite functioning differently, NAD(H) and NADP(H) have identical absorption and emission spectra. Therefore, their fluorescence is reported as NAD(P)H [104, 105]. The emission, FL, and quantum yield of these molecules is largely influenced by its environment [104]. The molecules have a general excitation range

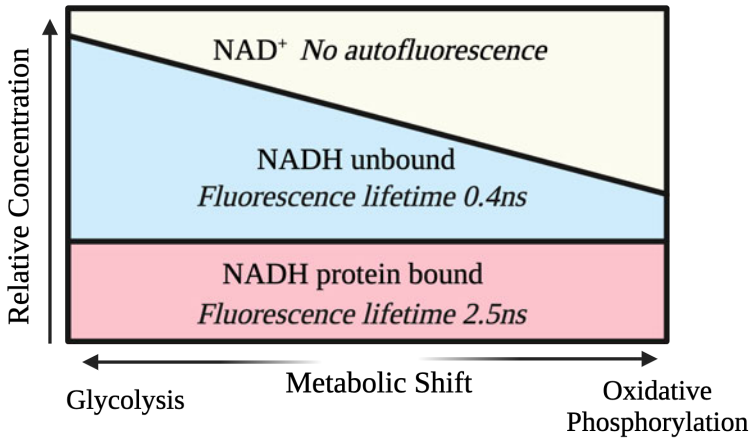

Figure 1.7: The fluorescence lifetime of NAD(H)/(+) in different metabolic switches and relative concentrations. Figure adapted from [103].

of 320 nm-380 nm (see Fig. 1.6 A). More specifically, NAD^+ has an excitation maximum of 260 nm, with no further excitation above 320 nm reported. NAD(P)H, has two excitation peaks, one at 260 nm and another at 340 nm. The quantum yield of NADH varies, increasing when bound to melate dehydrogenase and LDH, but decreasing when bound to glyceraldehyde 3-phosphate dehydrogenase [104]. A general emission range of 420 nm-480 nm has been reported, however, a shift towards the blue spectrum when bound to LDH or octopine dehydrogenase by between 25-30 nm can be observed. However, these measurements were conducted of the molecule in solution [104]. A double exponential FL in different variations has been observed. Influenced by the protein binding, solvent component, pH and temperature. These have been reported in cell lines, *in vitro*, and *in vivo* [104]. Specifically, the lifetime of NAD(P)H changes depending on whether its bound or unbound to protein. Bound to protein NAD(P)H has a lifetime of around 2.5 ns, unbound to protein NAD(P)H has a lifetime of around 0.4 ns [103] (see Fig. 1.7). Moreover, in different metabolic conditions as the relative concentration of bound and unbound NAD(P)H changes, the overall lifetime of this fluorophore changes, increasing in OXPHOS and decreasing in glycolysis (see Fig. 1.7). Due to the structural differences of NADH bound and NADPH bound to proteins, studies investigating the lifetime difference of these compartments was conducted [105]. Following chemical and genetic manipulation of cell lines, the longer lifetime from the bound compartment of NAD(P)H fluorescence (4.4 ns $\pm$ 0.2) was attributed to NADPH and the shorter bound compartment (1.5 ns $\pm$ 0.2) was attributed to NADH [105]. Given tumour heterogeneity (both functional, mutational and environmental), interpreting and translating the fluorescence of NAD(P)H is, therefore, complex [104] (see Fig. 1.7).

1.6.10 Flavins

The final group of endogenous fluorophores to be discussed in this review are flavins. Flavins exist in different forms with a range of functions. The most common flavin is FAD and its precursor riboflavin (also known as vitamin B2) [106] (see Fig. 1.8). As aforementioned in section 1.6.8, FAD has implications in the metabolism, acting as a co-factor in the TCA cycle during OXPHOS [107]. Flavoproteins are specific proteins which bind, often covalently, to FAD or flavin mononucleotide (FMN) [106]. Within cell lines, riboflavins are the most abundant in 14.0-3.1 mol per cell, FAD is also present in high concentrations of 17.0-2.2 mol per cell and FMN is reported in lower concentrations at 3.4-0.46 mol per cell. These levels vary within cell and tissue type [108].

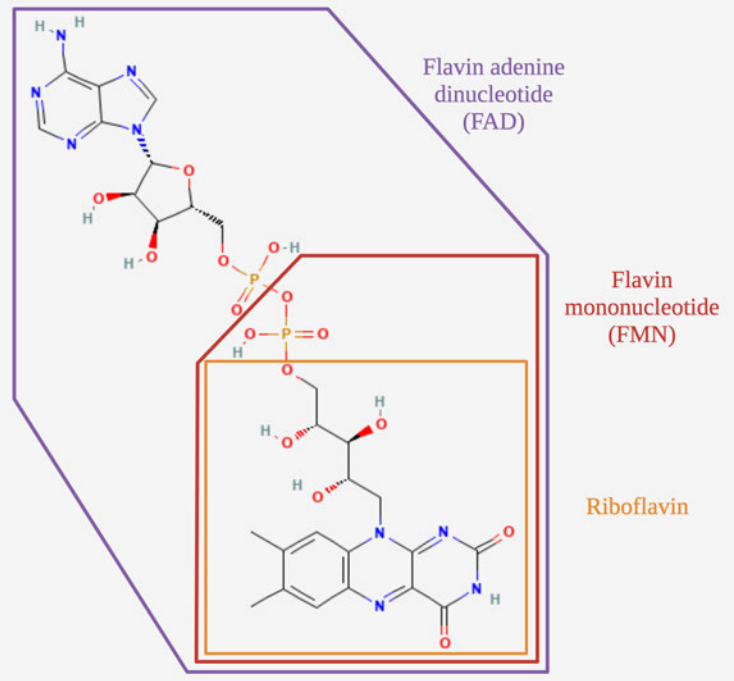

Figure 1.8: The chemical structure of flavins, with riboflavin as the core molecule (yellow), which when an additional nucleotide group is bound, is adapted into flavin mononucleotide (FMN) (red). This can then also be adapted into flavin adenine dinucleotide (FAD) with the addition of a further nucleotide and adenine group (purple). The chemical structure was from [109] and the Figure was adapted from [110].

Deficiency in riboflavin has implications in different diseases including LC, although the differences in its implication have been reported [111]. I.e., cancer specific riboflavin implications have found to increase the toxicity of cisplatin resistant cells and reduce apoptosis in healthy tissue [111, fig. 5]. On the other hand, studies assessing riboflavin in LC and LC cell lines *in vitro*, concluded that elevated riboflavin contributes to increased tumour cell proliferation and metastasis [112].

FMN and FAD exist in different oxidised and reduced states. FAD exists in three main forms, an oxidised form (FAD), a semi-reduced form (FADH) and a reduced form ($FADH_2$) [113]. The forms dictate the electron donation or acceptance potential, i.e., FAD can be reduced into $FADH_2$, FADH can be oxidised by FAD, or reduced by $FADH_2$ [114]. These function mostly in the mitochondria where FAD has a strong reduction potential (electron gaining function). The most prominent function of FAD is within the TCA cycle, where by when covalently bound to an enzyme called succinate dehydrogenase (complex II), the oxidation of this enzyme (loss of electron) into fumarate is catalysed [115, Fig. 1]. This is a key step within the TCA cycle, converting FAD to $FADH_2$ for electron storage. $FADH_2$ then reverts to FAD and produces ATP.

Flavins are also fluorescent and exhibit similar fluorescence profiles. As a result, their fluorescence emission is commonly regarded collectively (see Fig. 1.6 A (green) and Fig. 1.8). However, variations within the fluorescence of the flavins arise during interactions with different environments (particularly in different pH's), and when bound to proteins (i.e., flavoproteins) [113]. Typically FAD (although in higher abundance), has a lower quantum yield than FMN and riboflavin: 0.04, 0.22 and 0.27 respectively [113]. Moreover, in a lower pH of 2-4, FAD quantum yield increases to 0.12, matching the quantum yield of FMN until a pH 2 [113, Fig. 4]. The absorption spectrum is also similar with peaks around 370 nm and 450 nm [113, 116, 64]. The fluorescence emission of flavins peaks at around 550 nm and ranges from 480-600 nm [117, 64] (see Fig. 1.6 A). The FL of flavins is also diverse, riboflavin has been reported between 4-12 ns [36]. The FL of different oxidative states overlap, although, $FADH_2$ is not fluorescent. However, FAD and FMN FL is considered dependent on whether they are in bound or unbound states [118].

The fluorescence of FAD bound to proteins is quenched, decreasing the FL from its unbound state of around 2.3-2.9 ns, to as low as 0.1 ns in some reported cases [118]. Studies suggest that a significant proportion of protein bound FAD fluorescence originates from lipoamide dehydrogenase (around 50 %) and electron transfer flavoprotein (around 20 %). The contribution of FAD bound to complex II is debated, some studies suggest its negligible [118], however, other studies find it influential [110, 119]. Despite the debate regarding the origin of bound FAD fluorescence, evidence suggests the ratios of the two lifetimes serve as valuable indicators of metabolic switches, particularly when assessed with the FL of NAD(P)H [110]. Moreover, studies investigating metabolic specific FL changes of FAD in lung cells, found an increase in FL when glycolysis was inhibited (2.49 ns), and a decrease when OXPHOS was inhibited (1.81 ns), compared to the control (2.13 ns) [120, Fig. 5]. These results demonstrate metabolic FL sensitivity of FAD, enhancing FL interpretation [110] (see Fig.1.9).

The FL of FMN has been reported. Similar to FAD, two lifetime components relating to either its protein bound or unbound state have been observed. However, the directional behaviour of FMN FL is different to FAD, with a bound FL of around 4.7 ns and an unbound FL of around 1.5 ns [110, Fig. 1] (see Fig.1.9). Moreover, studies show in glycolysis, an increase in the

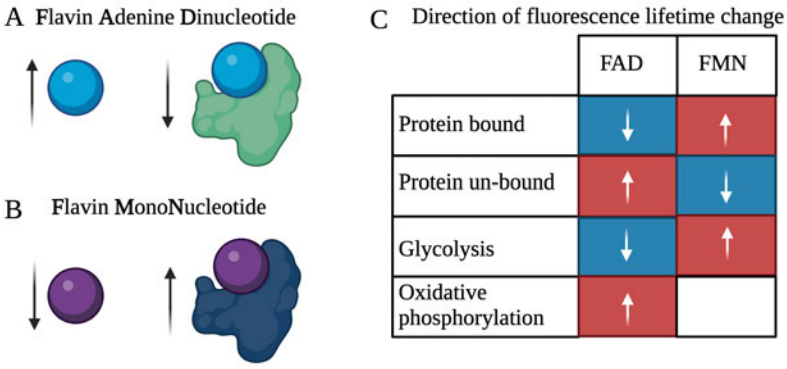

Figure 1.9: The fluorescence lifetime change of flavin adenine dinucleotide (FAD) and flavin mononucleotide (FMN) when bound or unbound to proteins **A)** & **B)**. In addition the change of the fluorescence lifetime when in different metabolic properties of tissue **C**.

fluorescence of FMN can be observed, evident by an increase in a long FL in the flavin region in brain tumours [121]. Due to the structural similarities of both FAD, FMN and riboflavins, and the similarity of the long (and short) FL, differentiating them is complex. Often the FL component is referred to as FAD and collected in a broad emission band around the peak of the emission (i.e., in [120] the emission of FAD was considered in channels 545-595 nm following excitation of 750 nm) (see Fig.1.9).

1.6.11 Redox Ratios

Redox describes the levels of cellular oxidation and reduction (originating from reactions which facilitate the transfer of electrons) [122]. A disruption in the redox balance of tissue results in oxidative stress. Many different external factors may cause oxidative stress, including cancer. Studies have demonstrated that oxidative stress, induced by elevated levels of reactive oxygen species (ROS), leads to an increase in genomic mutations, instability, and cancer development [123]. Additionally, oxidative stress can originate from various factors including phosphorylation events involving proteins within the mitochondria (i.e., NAD(P)H) [123]. Considering the sensitivity of fluorescence parameters associated with molecules within the mitochondria (NAD(P)H and FAD), fluorescence studies aimed to determine whether these fluorescence parameters may serve as indicators of cellular (and tissue) redox status, known as the optical redox ratios [118, 121, 110]. One of the first optical redox ratios developed, also known as the metabolic index (MI), is often described as:

$$MI = \frac{NAD(P)H_{bound}\alpha_1\%}{NAD(P)H_{unbound}\alpha_2\%} \tag{1.12}$$

where the amplitudes (α_1 and α_2) of the corresponding bi-exponential decay characterises of NAD(P)H provide metabolic insights (see Fig. 1.7) [110]. This calculation has been expanded describing the fluorescence emission of both NAD(P)H and FAD, known as either the optical redox (OR) ratio, or the fluorescence lifetime induced redox ratio (FLIRR) which includes FAD as:

$$FLIRR = \frac{NAD(P)H_{unbound}\,\alpha_2\%}{FAD_{unbound}\,\alpha_1\%}. \tag{1.13}$$

Where the ratio of unbound NAD(P)H and FAD provides further indications of the redox potential of cells/tissue. [124] investigated the OR of prostate cancer cells. Observing an increase in mitochondrial OR when the cells switched to OXPHOS as doxorubicin (chemotherapy) was administered. To compare the relative emission of the two fluorophores, emission channels for the peak emission of either flavins and NAD(P)H are used. I.e., [110] used channels 542-582 nm for FAD and 426-446 nm for NAD(P)H. However, variations in the redox ratio calculation remain [125].

Traditionally, bi-exponential decay's have been fit from the distinct emission channels to account for the ratios of bound/unbound NAD(P)H and FAD. However, the emission of FMN within the FAD channel (and potentially riboflavin) is also present. Therefore, [110] argues without accounting for the additional decay components of FMN, the redox calculation may be difficult to interpret. [110] fit a tri-exponential decay to the FAD channel, and observed an elevated significance of the redox potential between tumour and non-tumour cells (a p value of 0.007 was observed between two different cellular co-cultures) [110]. The results were conducted on cell lines. Therefore, extrapolating this to tissue becomes complex due to the influence of additional fluorophores within these emission bands (see Fig. 1.6 A). In lung tissue, most prominently, elastin and collagen may also contribute to the FL in these channels (see Fig. 1.6). Moreover, due to the influence of environmental factors such as pH (especially considering the acidic feature of lactate produced during glycolysis as mentioned in section 1.6.8), in addition to considering the presence of riboflavins (the highest abundant intracellular Flavin (see section. 1.6.10)), interpreting the redox calculations from AF in tissue using bi-, or tri- exponential fitting routines of broad emission channels may be a simplification.

1.6.12 Autofluorescence for Cancer Detection in Tissue

The endogenous fluorophores discussed above and their deregulation provide the basis of the biology behind AF discrimination. Coupled with the sensitivity and specificity of fluorescence measurements, a photo-physical difference between normal and cancerous tissue at different excitation wavelengths persist [84] (see Table 1.1). Differences in both optical setups and analysis methods used to differentiate fluorescence decay traces into interpretable results also impacts the translation of these studies. At present FL devices have shown the potential to detect cancer from different tissue, including breast, oral, skin, cervical, brain and lung tissue [126, 127, 128, 129, 130]. Given the specificity of FL these devices have the potential to greatly improve the diagnostic accuracy, particularly in early stage LC [131, 8] (see Table. 1.1).

The most common setup for measuring tissue AF involves using devices with large wavelength bandwidth resolution, optimised to detect various endogenous fluorophore emission peaks (see Table. 1.1). These devices typically employ rapid pulse-sampling methods, enabling a reliable, point-based assessment of the entire tumor profile in a short time frame. Alternatively, some devices record fluorescence across multiple channels with higher wavelength bandwidth resolution, but frequently marginalise the fluorescence decays into a single decay [141]. Furthermore, the analysis of fluorescence decays often employs Laguerre deconvolution models or bi- (sometimes tri-) exponential fitting routines. However, most frequently the average FL is calculated. While this metric offers a rapid, real-time overview of endogenous fluorophores within the tissue, its ability to capture nuanced biological features that could enhance tumour diagnosis may be limited. Therefore, to better characterise tissue, understanding the total fluorescence profiles of specific endogenous fluorophores *in vivo* may enhance the fluorescence translation, allowing a more sensitive and specific cancer interpretation.

In summary, the literature review presents the photo-physical properties of fluorophore specific alterations, such as brightness and excitation time. Additionally, it provides an overview of both time-resolved devices and data analysis methods. Following this overview, an in-depth assessment of the biological function of certain endogenous fluorophores implicated in LC deregulation is conducted, elucidating the underlying biology behind fluorescence discrimination. Finally, the literature review concludes with an examination of current methods for analysing *ex/in vivo* FL for tissue discrimination.

Table 1.1: Autofluorescence analysis of *in vivo* and *ex vivo* cancerous and non-cancerous tissue samples.

Tissue Type	Excitation (nm)	Emission (nm)	Lifetime Analysis Method	Number of Lifetimes	Number of Patient Samples	Tissue Type	Reference
Breast	355	390/40, 466/40, 542/50, 629/53	Constructed least-squares deconvolution and Laguerre expansion method	Average lifetime and intensity ratios	20	*Ex vivo*	[132]
Breast	355	390/40, 470/28, 542/28, 629/53	Constraint Laguerre model	Average lifetime and intensity, and intensity ratios	18	*Ex vivo*	[133]
Oral	355	396/20, 452/22.5, >500	Non-linear least squares iterative reconvolution	Bi-exponential	34	*In vivo*	[134]
Oral	355	390/20, 452/22.5, >500	Deconvolution	Bi-exponential, intensities and redox ratio	73	*In vivo*	[135]
Oral	355	390/20, 470/14, 542/25, 629/26.5	Laguerre based deconvolutions	Average lifetime and intensity ratios	53	*In vivo* & *Ex vivo*	[136]
Skin	378 & 445	440/20, 514/*15*	Reconvolution	Bi-exponential	14	*In vivo*	[137]
Cervical	405	>430	SPCImage software	Bi-exponential, average lifetime	31	*Ex vivo*	[138]
Gioblastoma	355	390/40, 470/28, 540/50, 629/53	Non-negative least squares and Laguerre expansion method	Average lifetime and intensity	15	*In vivo*	[139]
Lung	405	>430	SPCImage software	Bi- or Tri- exponential, weighted mean	31	*Ex vivo*	[120]
Lung	405	>430 & 510-550, 600-640	Non-linear least squares reconvolution	<= tri-exponential and weighted mean	11	*In vivo*	[140]

1.7 Research Aims

Patients with LC are most commonly diagnosed with late-stage disease resulting in a poor prognosis. Current clinical diagnostic strategies although extensive, are either image-based or have slow processing times (e.g., histology following a biopsy) and can be uncertain in early stage detection. Moreover, there is a lack of an *in vivo* instantaneous detection tool of an abnormal mass in the lung.

TRFS is a sensitive tool for detecting the excitation of endogenous fluorophores. When used in the visible light region this technique has low cellular toxicity capturing metabolic, structural, and environmental tissue properties *in vivo* instantaneously. FS devices have detected cancer, early-stage benign vs malignant, and tumor margin discrimination both in excised tissue and *in vivo* (see Table 1.1). However current devices although rapid, either detect fluorescence at low spectral resolutions measuring decays in broad emission channels (e.g., [139]), or, where multiple channels at a higher wavelength bandwidth resolution are assessed, often the multiple decays are marginalised into one decay (i.e., [141]). Traditional analysis tools then often calculate the average spectroscopy parameters from these measurements (see Table 1.1). Therefore, due to the sensitivity of endogenous fluorophores, and the influence of the environment on their fluorescence properties, current methods may miss factors that provide greater insight into abnormal lung tissue.

Innovations in detector technology (i.e., Ra-II) allow rapid, high-resolution collection of fluorescence from a single excitation wavelength. When integrated into a fiber-based device, these can be passed down the working channel of a bronchoscope, providing a detailed *in vivo* assessment of fluorescence from tissue. The device used in this thesis excites samples at 485 nm and contains a Ra-II CMOS SPAD line sensor, detecting fluorescence emission in 512 individual wavelength channels, with a wavelength bandwidth resolution of 0.5 nm. Each channel has an independent timing circuit and a temporal resolution of 50 ps. The resulting fluorescence emission from 485 nm excitation of lung tissue predominantly originates from elastin fibres and flavins (see Fig. 1.6). In LC damaged and elevated levels of elastin fibres have been observed, particularly in Adenocarcinomas. Moreover, fluorescence specific properties of flavins (both FAD and FMN) also provide an indication of the metabolic status of tissue, with cancer favouring a glycolytic metabolism to support increased and sustained proliferation, often exhibited by both LC cells and the surrounding tumour environment (the Warburg effect). Riboflvains have also been found to contribute to enhanced LC specific cisplatin toxicity, in addition to proliferation and metastasis.

By leveraging innovative TRFS detector technology and our understanding of specific endogenous fluorophores, the primary aim of this thesis is to investigate whether a more detailed assessment of the decay profiles of fluorophores from lung tissue can enhance our understanding of both the photo-physical properties of endogenous fluorophores and the diagnostic potential of high-resolution time-resolved devices.

1.8 Research Objectives

The primary research objective of this thesis is to develop a computational model capable of comprehensively interpreting the complex time-resolved fluorescence data generated by the TRFS device. This tool aims to capture both the fluorescence emission and FL from individual channels and neighboring channels. It will offer two distinct analysis modes (see Fig 1.10 F):

- A single exponential mode able to track overall changes in the spectral and temporal emission profile across the entire histogram. This mode assumes no underlying features of fluorescence, thus requiring no *a priori* assumptions.
- A multi-exponential mode able to simultaneously un-mix spectral and temporal profiles from any number of components, reflecting specific fluorophores within the histogram from mixed samples.

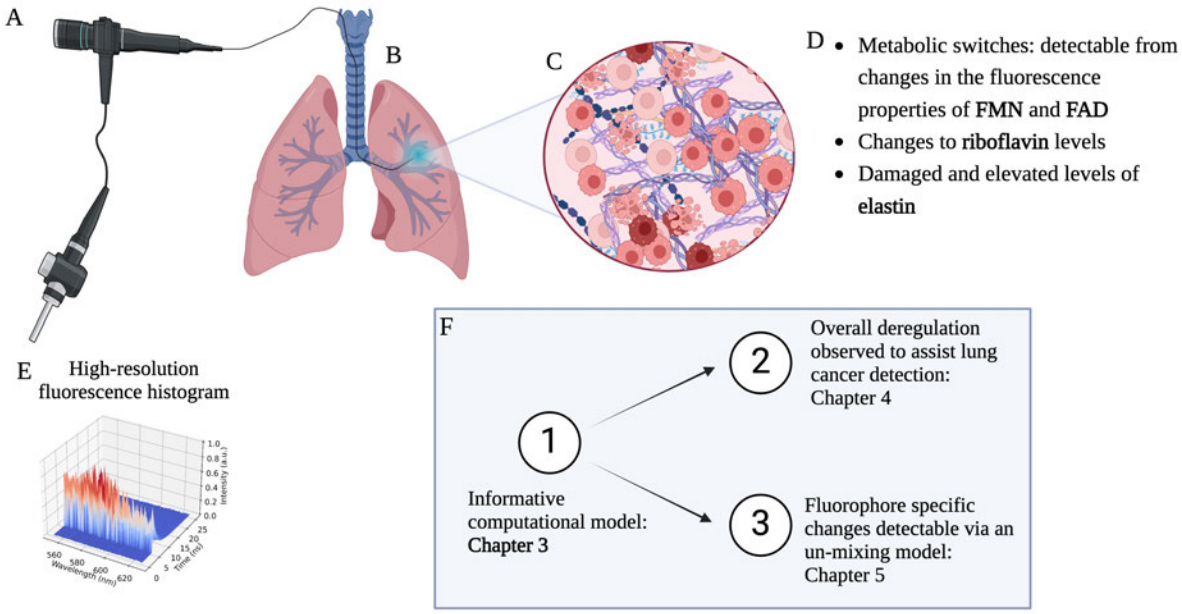

Figure 1.10: A schematic diagram of a time-resolved fluorescence spectroscopy (TRFS) device is shown, passed down the working channel of a bronchoscope and into a lung **A)** & **B)**. The fluorescence spectroscopy device excites endogenous fluorophores naturally occurring within the lung tissue **C)**. Specific fluorophores implicated in lung cancer include flavin mononucleotide (FMN), flavin adenine dinucleotide (FAD), riboflavin, and elastin. Changes in these fluorophores are detectable using TRFS **D)**. The devices produce high-resolution fluorescence histograms **E)**. The research objectives of this thesis **F)** first involve developing an informative computational model and then assessing different modes of the model on TRFS of lung tissue.

In addition to the development of the computational model, the application of this on assessing lung tissue AF will be analysed. The objectives of this are as follows:

1: Accuracy

The accuracy of both modes of the model using exogenous fluorophores measured benchside which have been well documented in the literature will be explored. The emission profiles will be compared to the emission profiles of the same fluorophores measured on an emission reader, and the FL values will be compared to the expected FL values within the literature.

2: The Single Exponential Mode

The next objective is to investigate the single exponential mode on mixed samples from simulated data, and endogenous fluorophores measured benchside. The endogenous fluorophores will be measured in different concentrations and environmental conditions. The model will then be applied to paired normal and abnormal lung tissue to assess its proficiency in LC detection, and in whether additional insights into the fluorescence profile of these samples can be obtained.

3: The Multi Exponential Mode

The final objective of this thesis is to assess whether a multi-exponential mode of this computational model can be used to un-mix specific endogenous fluorophores of lung tissue, using both spectral and temporal profiles. Prior to being applied to the lung tissue, the objective is to assess whether, using simulated data, the model is able to un-mix individual fluorophores with both distinct and overlapping emission profiles. The presence of the un-mixed endogenous fluorophores will be validated using FLIM confocal microscopy providing a spatial fluorescence assessment at cellular resolution, although not a tool viable for *in vivo* use.

The Overarching Objective

The overarching objective of this thesis is, in combining our knowledge of biology and photo-physical properties of tissue, to determine the potential for a fluorophore specific label-free detection of endogenous fluorophores in lung tissue, providing deeper insight into both structural and metabolic changes, advancing our understanding of the photo-physical properties of diseased tissue, and the diseased tissue itself (see Fig.1.10).

1.9 Thesis Outline

The thesis is structured as follows.

Chapter 2: The EP-TRFS Device and Measurement Precision

First, details of *Flamingo*, the Extensively Parallel Time-Resolved Fluorescence Spectroscopy (EP-TRFS) device is explored. Device specific alterations are investigated within the data collection, such as the IRF. Sample specific perturbations are also investigated such as photobleaching. This chapter was reviewed by Dr András Kufcsák who provided the device details. Additionally, Dr András Kufcsák conducted the IRF laser experiment and generously provided data for Fig 2.4.

Chapter 3: Multichannel Fluorescence Lifetime Estimation

In the third chapter, we present the paper titled: *Simultaneous Spectral Temporal Modelling for a Time-Resolved Fluorescence Emission Spectrum*, based on the Multichannel Fluorescence Lifetime Estimation (**MuFLE**) model. In addition, the limitations of the model are discussed. The mathematical framework of MuFLE was conceptualised by Dr Sohan Seth. Alexandra Adams led the implementation, data collection and analysis. Dr András Kufcsák, Dr Katjana Ehrlich, and Professor Kev Dhaliwal proofread the manuscript.

Chapter 4: Lung Cancer Discrimination using Spectral Fluorescence Lifetime

In the fourth chapter we present the paper titled: *Fibre-optic based Exploration of Lung Cancer Autofluorescence using Spectral Fluorescence Lifetime*, exploring the spectral information single-exponential fluorescence lifetime estimation using the MuFLE model provides, revealing additional fluorescence details of the samples. The contributions of this paper are as follows: Alexandra Adams conceptualised the study, and led the experimental design, and data collection, with support from Dr Sohan Seth, Dr András Kufcsák , Dr Mohsen Khadem, Dr Ahsan Akram, Dr Charles Lochenie.

Chapter 5: Towards Total Un-mixing

In the fifth chapter, we explore the un-mixing potential of the MuFLE model. We show results of the multi-exponential MuFLE model when applied to endogenous fluorophores and tissue data, validating the identification of the fluorescence compartments. We conclude this chapter with the results of multi-exponential estimates taken on some of the same samples using a FLIM confocal microscope. The estimated fluorophores with MuFLE, are co-identified from the FLIM confocal device, with an additional imaging parameter to assess their spatial location.

Chapter 6: Summary and Conclusion

The research of the thesis are summarised in the final chapter. In addition, areas of future work are discussed, including a second version of the MuFLE model, further validation un-mixing experiments, and optical alterations to enhance the diagnostic potential of this setup.

Chapter 2

The EP-TRFS Device and Measurement Precision

The optimal optical setup using AF for cancer detection can be defined by a device adjusted to collect the maximum number of photons, however, this may not coincide with exciting the maximum number of potential endogenous fluorophores (as the brightness is determined by the individual extinction coefficients, quantum yields and concentration of the molecule in the tissue of interest) (see Fig. 1.6 in section 1.2.2). Moreover, which fluorophores are excited, may also alter the diagnostic potential of the device when used for particular tissue, due to the biological significance of the fluorophores excited and their specific tissue relevance. This chapter details the TRFS device used for data collection in this thesis. It also evaluates device-specific and sample-specific modifications that could alter fluorescence measurements of the sample independently of changes in fluorescence due to the diseased state of the tissue.

Common time-resolved devices used to collect AF from *ex vivo* and/or *in vivo* tissue excite at around 355 nm, and collect the resulting fluorescence emission in 3-4 emission channels covering a broad spectral emission range (i.e., 390 nm $\pm$ 20, 452 nm $\pm$ 22.5, 542 nm $\pm$ 25 & 629 nm $\pm$ 26.5) [142] (see Table 1.1). Due to the specific excitation wavelength and broad emission channels, these devices allow for a rapid FL and FI based assessment from a broad range of fluorophores (i.e., NAD(P)H, FAD, collagen, porphyrins), however at the expense of the wavelength bandwidth resolution. Fibre based OEM devices, without a time domain feature, have been shown to discriminate lung tissue from a longer excitation of 488 nm [143]. The majority of the AF emission from this setup originates from elastin and elastin fibres which become visible in their images [143, Fig. 1]. The time resolved setup used in this thesis is called **Flamingo**, or, the **Extensively Parallel Time-Resolved Fluorescence Spectroscopy (EP-TRFS)** device. This device, similar to OEM devices, has an excitation wavelength of 485 nm and has been optimised to collect high resolution AF histograms predominating in the visible light range from elastin and flavins (see Fig. 1.3). This allows a FL based assessment of the structural composition of lungs (via the emission of elastin), and a functional metabolic assessment (via the emission of flavins, encompassing FAD, FMN and riboflavins) in addition to their environmental changes.

2.1 The EP-TRFS Device

The EP-TRFS device is an epi-fluorescence system where excitation and emission are collected through the same optical path [27] (see Fig. 2.1). The device is also fibre based and small enough to be passed down the working channel of a bronchoscope (fibre outer diameter of 285 µm, a coating diameter of 350 µm and a core diameter of 35 µm). The fibre field of view is $<100\,\mu m^2$ and samples are collected with 0 working distance between the fibre tip and the respective sample. The optical path contains coupling and collection optics and spectrometer optics (see Fig. 2.1). The 485 nm pulsed excitation laser is primarily used with a pulsed repetition rate of 20 MHz when used in TCSPC mode, and a power range of between 175 µW-200 µW. Excitation light travels first through the coupling and collection optics, collimated by asperic lenses (f=11 mm, aspheric lens, Thorlabs) and filtered by an excitation filter (FITC-Ex01-Clin-25, Semrock). A dichroic beam splitter (Single band dichroic, FITC-Di01-Clin-25x36, Semrock) reflects the excitation light through the sensing fibre (see Fig. 2.1 D). The emission light then travels back through the sensing fibre, reaching the coupling and collection optics where by lenses collimate the emission. An emission filter filters the light (long pass emitter, FITC-LP01-Clin-25, Semrock) and the dichroic beam splitter then permits the emission to travel into the spectrometer optics. The emission in the spectrometer optics is collimated by doublet lenses (achromat doublets, Thorlabs) and dispersed into wavelength constituents by a dispersion grating (600 grooves/mm, Wasatch Photonics) (see Fig. 2.1 G). Following its dispersion and refocusing, the emission reaches the spectrometer which is composed of a CMOS SPAD line sensor [35], covering a total spectral range of 470-720 nm, centered at 590 nm. Due to the emission filtering and dichroic beam splitter, light <512 nm is prevented from reaching the detector (see Fig. 2.1).

2.1.1 Photon Detector

The line-sensor (Ra-II) consists of 512 individual **pixels** [35] (see Fig. 2.2). A pixel can be defined as a single photon detection element with an independent timing circuit to measure fluorescence decays. The grating disperses light over the line sensor, such that each pixel detects a certain wavelength of light, hence forming wavelength **channels**. The emission is detected with a wavelength bandwidth resolution of 0.5 nm per channel. Each pixel consists of 16 SPADs arranged in a stacked column of 2x8 blue and 2x8 red SPADs. Moreover, pixels are ordered with an independent timing circuit, incorporating 5x clock trees, TDCs and 32-bin/11-bit/bin histogram memory (see Fig. 2.2 A) [35]. The geometry of the line sensor in proximity to the grating, allows at each pixel, wavelength constituent photons to be detected. Therefore, the total spectral-temporal profile of a fluorophore excited at 485 nm and emission range between 512-720 nm can be captured. Optical spectra detected with the line sensor are subject to variations across the channels. This is attributed to different behaviour of the sensor pixels, as well as a wavelength dependent photon detection efficiency [35]. The former comes

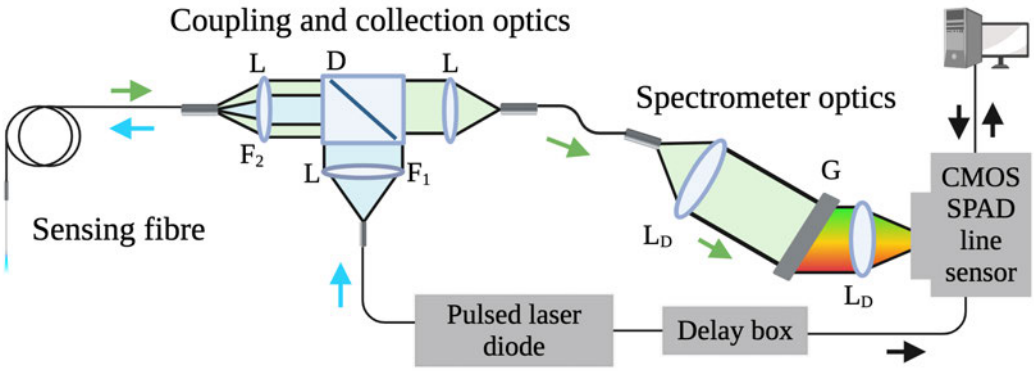

Figure 2.1: The extensively parallel time-resolved fluorescence spectroscopy (EP-TRFS) device is an epi-fluorescence device where by the excitation (blue) and emission (green) is collected from the same optical path. Within the coupling and collection optics, the excitation light is collimated by aspheric lenses **L)** and filtered through an excitation filter **(F_1)** where it is reflected off a dichroic beam splitter **D)** before travelling through the sensing fibre reaching the sample. Emission light travels back through the sensing fibre, filtered through an emission filter **(F_2)** and passing through the dichroic beam splitter, also collimated by aspheric lenses (L) before reaching the spectrometer optics. Emission is then collimated by doublet lenses **(L_D)** and then dispersed via a dispersion grating element **G)**. The emission light is further collimated by another doublet lens before reaching the complementary metal oxide semiconductor (CMOS) single photon avalanche diode (SPAD) line sensor for detection.

from semiconductor process variations. For the latter, multiple reflections between surfaces of the sensor's semiconductor structure lead to constructive or destructive interference. In essence, light is amplified or attenuated depending on its wavelength and the distance between reflecting surfaces [35]. The individual pixels also have different photon sensitivities, therefore, a **spectral sensitivity** can be observed defined as a marginal shift in the maximum number of photon counts per channel, independent of the emission spectrum at each channel. Process variations in the timing electronics lead to per pixel variations in the timing properties, such as the time resolution and timing uncertainty or **jitter**. Therefore, for accurate measurements using this device, when incorporated into the analysis pipeline, an accurate measurement of the IRF at each channel is essential.

2.1.2 Time Resolved Modes

The device has two time resolved modes, a TCSPC mode and a mode in which photon arrival times are directly stored in histograms on chip (on-chip), here denoted as HistMode (see section. 1.3.3)[35]. A unique TDC architecture supports both HistMode and TCSPC mode. In TCSPC mode, the arrival time of the first photons of an exposure are stored as 11-bit timestamps. This architecture is prone to counting loss and pile-up, as the TDCs cannot process additional photon arrivals until the readout finishes (at the end of the exposure).

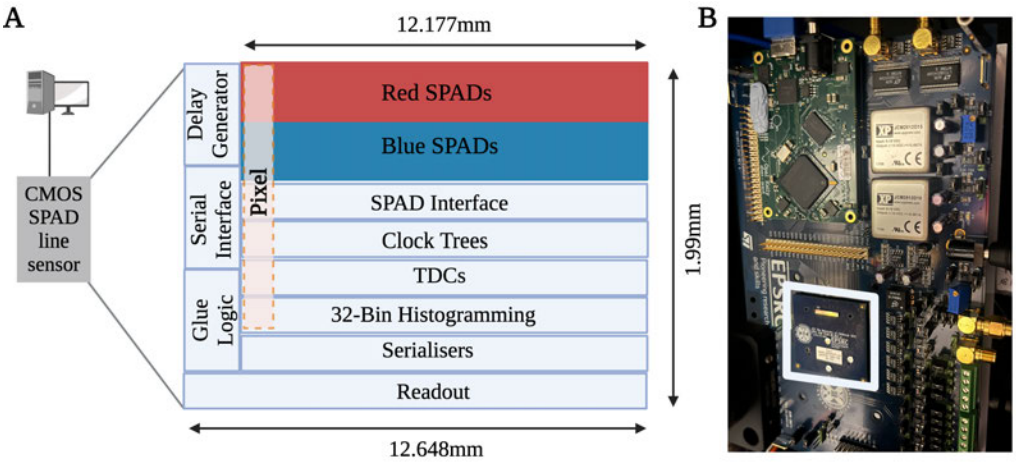

Figure 2.2: A schematic diagram of the Ra-II line sensor **A)** and an image showing the entire sensor, including the circuit board and the line sensor highlighted in the blue box **B)**. The Ra-II line sensor comprises 512 pixels (orange), each housing 16 red SPADs (optimised to collect light at 600-900 nm) and 16 blue SPADs (optimised to collect light at 450-550 nm) organised in two columns. Independent timing circuits for each pixel allows simultaneous measurements of photon time-of-arrival over a range of wavelengths. The diagram is adapted from [35, Fig. 1].

In HistMode, the underlying architecture allows multiple photon arrivals per exposure to be recorded and stored in an on-chip memory setup within 32 time bins. This process allows the recording of up to one photon per excitation cycle, enabling more rapid detection. However, in this setup, the maximum number of photons that can be recorded in each time bin is limited, and the total observable time span is limited by the number of bins (32) and their time-resolution [35, section. 3]. Therefore, HistMode is optimised for rapid photon collection, applicable for a real time assessment. However, TCSPC mode is more suitable for sampling longer decay periods with high resolution, favouring AF sampling. In TCSPC mode the arrival time of photons are collected in 50 ps time bins (see section 1.3 for more detail). In HistMode, photons are built into histograms with an interchangeable timing resolution (50 ps - 1500 ps) and a corresponding time range, however in a fixed number of 32 time bins [35]. In TCSPC mode, the time range in which photon arrivals are expected is determined by the laser repetition rate. With a laser repetition rate at 20 MHz, and a consequent time period of 50 ns between pulses, and a bin resolution of $\sim$50 ps, histograms are built with 1200 bins. In this thesis most measurements are collected in TCSPC mode where 3 repeats of each sample are collected and summed for analysis.

2.1.3 Temporal Jitter

The decay traces recorded from fluorescence in individual channels are constructed into histograms of intensity, wavelength and time. These observed histograms are built from the fluorescence of the measured samples, but altered by other effects as well (e.g., from the sensor). As mentioned in section 1.5.1 and above, the IRF describes the system's response to an infinitely sharp excitation, and involves the laser pulse width, the transit time of the pulses travelling along the fibre, and the detector timing uncertainty. The IRF may change in slightly different setups of the same system, i.e., by different fibre lengths, altering the rise time of the decay (see Fig. 2.3). Therefore, where this is to be incorporated into the analysis pipeline, an accurate measurement of the IRF is required. Traditional methods to measure the IRF involve reflecting the excitation light back through the detector, or using scattered light [144]. However, this often results in a measured IRF at a shorter wavelength than the measured signal. Alternative methods involve using quenched fluorophores with shorter FWHM than the exciting light source. Specifically, Erythosine B in water, Rhodamine 6G with iodine, Erythrosine B with potassium iodide (FL of 25 ps) and Rose-Bengal in potassium iodide (a FL of 16 ps) [144]. As long as the decay properties of these quenched fluorophores are shorter than the laser pulse, so as to ensure the timing measurement is not also influenced by the photo-physical properties of the fluorophore, an accurate IRF can be captured. However, there are spectral limitations in using these fluorophores as the spectral range is restricted to their distinct emission spectra [144]. Failure to accurately account for the IRF will cause errors within the fitting routine leading to a miss interpretations of the estimated parameters [144].

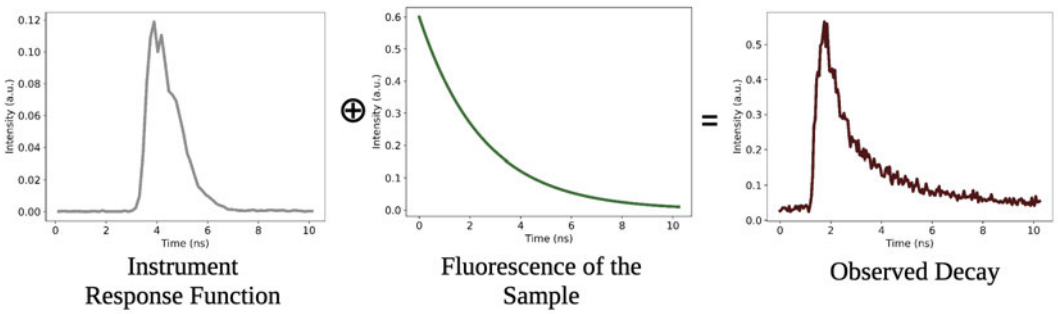

Figure 2.3: A schematic diagram of an instrument response function (IRF) convolved with the fluorescence measured from a sample, which together makes up the observed decay. The IRF is a convolution of distortions from the laser pulse, detector jitter, timing uncertainty and spectral grating uncertainty.

2.2 Lifetime Accuracy

To assess whether the device is able to record accurate FL measurements, reference exogenous fluorophores can be used with well documented FLs. The concentration of these fluorophores can be altered to also test the stability and accuracy of the FL recorded from the device in lower concentrations, and so in subsequent lower photon counts. This is particularly relevant where the objective of the device is to accurately record the fluorescence of tissue, as endogenous fluorophores are typically dim with lower quantum yields than exogenous fluorophores.

2.2.1 Photobleaching

Alternative factors effecting the recorded fluorescence which do not originate from the diseased state of tissue exist within sample preparation methods and data collection. In addition, a recognised alteration is an photo-chemical effect called photobleaching. Photobleaching, most commonly observed following either prolonged or high power excitation, describes a permanent drop in the FI of fluorophores, due either to covalent bond cleavage or from undefined photo-chemical factors in its environment [145]. Different fluorophores have different photobleaching sensitivities, however, the most pronounced effect is a drop in FI. A fluorophore's photobleaching rate depends on the fluorophore's structure, its environment and the excitation power of the laser [145]. Some fluorophores described as photostable are minimally effected by photobleaching (e.g., Rhodamine B) [145]. However some endogenous fluorophores can be particularly sensitive. Moreover, photobleaching effects different fluorophores at different rates. Consequently, in the context of a mixed system such as tissue, photobleaching may alter the overall FL of a sample.

Studies have investigated the effect of photobleaching on human tissue [146, 147]. Particularly on the FL in different spectral channels. [146] showed that at a lower wavelength of between 498-560 nm there was no change in the FL following prolonged laser exposure [146]. However at 560-720 nm a 10 % reduction of FL was observed. This effect was thought to be negligible compared to the change in FL when comparing between healthy and diseased tissue [146]. An alternative study investigated the effect of photobleaching in the arterial wall. Following an excitation of 337 nm three purified endogenous fluorophores: elastin, collagen and cholesterol were assessed at three different emission wavelengths 390 nm, 430 nm and 470 nm. Elastin exhibited the smallest change in FI and no variation in FL was observed. However, bleaching was most pronounced at 390 nm where the FL of collagen dropped from 5.9 ns to 5.5 ns [147]. Photobleaching also affected the FI and FL of cholesterol.

2.2.2 Sample Preparation

Differences in sample preparation ranging from storage practices to collection methods may also influence the cellular composition of tissue. To assess this impact on the photo-physical properties of tissue, and ensure accurate data is collected and assessed, it is necessary to investigate these.

2.3 The Instrument Response Function

To incorporate detector artefacts within the fitting routine, avoiding errors where possible, the IRF can be accounted for within the analysis pipeline. The method of this incorporation depends on the overall objective of the fluorescence interpretation (as mentioned above and in section 1.5.1). I.e., where the primary objective is to assess an overall fluorescence contrast between sample types, a tail-fitting approach may be appropriate. Under the assumption that the IRF represents the detector's response to an infinitely short FL, the effect of the IRF may be considered negligible in the analysis routine, given that the FL of measured fluorophores typically ranges from 2-6 ns. The tail-fitting approach involves initiating the fitting from the temporal bin containing the peak number of photon counts. However, this reduces the number of data points available to the fitting routine, potentially leading to a decrease in accuracy. Moreover, where the IRF is wider, the effect of the IRF may still be observed in the time bins around the peak, particularly when fluorophores with shorter FL are assessed. Where the precise FL from a sample is a priority, an accurate IRF is required to be incorporated into a deconvolution model. This section assesses both the tail-fitting and deconvolution model of two well characterised reference fluorophores Rhodamine B (RhB) and Fluorescein Sodium (Fluo). This section also assesses two different fluorophores quenched and measured for an accurate IRF estimation.

2.3.1 Tail Fitting

Two reference fluorophores were measured with the EP-TRFS device in TCSPC mode, with the same laser repetition rate as previously detailed (20 MHz), and arrival times built at each channel from 1.5×10^6 exposures, each with an exposure time 5 µs. RhB (Sigma-Aldrich: 102 406 918) measure in a concentration of 10 µM, dissolved in methanol and Fluo (Sigma-Aldrich: F6377-100G) in a concentration of 1 µM, dissolved in PBS. We first consider the analysis of the observed decay trace in the tail fitting regime using the least squares method. Here, a single exponential decay is estimated from the peak of the temporal decay, minimising a squared loss function as:

$$f(t-t_p) = \gamma \cdot e^{-t-t_p/\tau} \text{ and } J = \sum_{t-t_p=1}^{T} (f(t)-y(t))^2. \tag{2.1}$$

The least squares solution used in this chapter is computed using the Levenberg-Marquardt algorithm, SciPy LMFit [148].

The spectral emission peak of Fluo is 519.39 nm, and the average FL estimated between the emission range of 512.76 nm-623.43 nm is 3.91 ns $\pm$ 0.37 (see Fig. 2.4 A and B). The spectral emission peak of RhB is 579.57 nm, and the average FL estimated between the emission range of 552.03 nm-649.95 nm is 2.33 ns $\pm$ 0.15 (see Fig. 2.4 C and D). The FL and emission from the tail fitting routine is in an agreeable range with the literature (with a FL of Fluo estimated at around 4.1 ns[149] and RhB in methanol at 2.41 ns $\pm$ 0.07[150]) (see Fig. 2.4). However, the tail fitting method impairs accurate estimation of fluorophores with short FLs, which may be problematic when the FL from tissue is to be estimated (with expected FL ranges from 0.1 ns-4 ns, see section 1.6). This is due to interference from the first few time bins which contain photons perturbed by the IRF along with photons from the fluorescence of the measured sample.

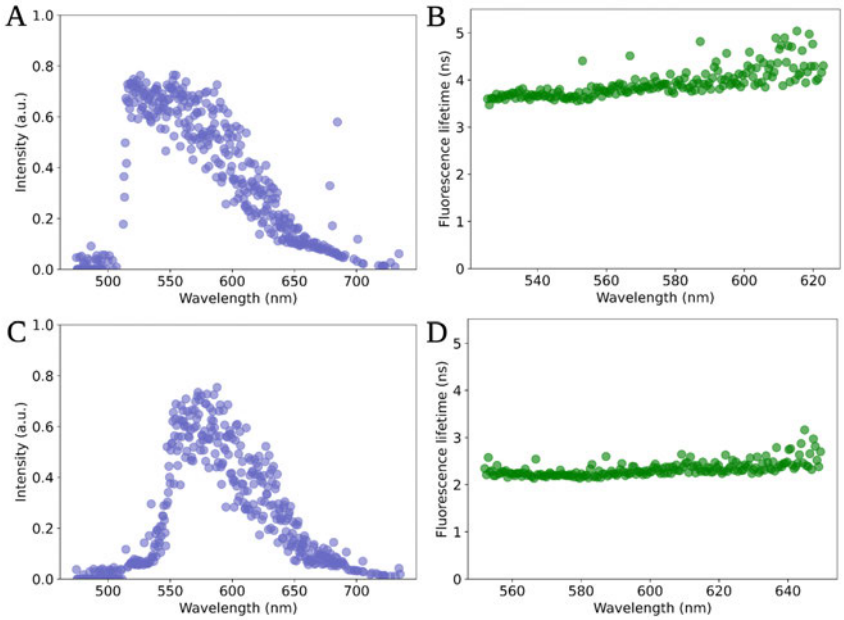

Figure 2.4: Plots to show reference fluorophores, Fluorescein Sodium dissolved in PBS at a concentration of 1 µM, and Rhodamine B dissolved in methanol at a concentration of 10 µM. The data was analysed using a tail fitting non-linear least squares method. **A)** shows the intensity plots of the Fluorescein, **B)** shows the corresponding fluorescence lifetime fitted across a cropped wavelength region between 512.76 nm-623.43 nm. **C)** shows the intensity plots of the Rhodamine B, **D)** shows the corresponding fluorescence lifetime fitted across a cropped wavelength region between 552.03 nm-649.95 nm

2.3.2 Measured IRF

For an accurate representation of the FL from samples, a measured IRF, convolved with the observed decay trace is anticipated to yield a more precise estimation. The IRF measured, however, must represent the instrument distortions so that additional biases are not considered within the fitting routine. To characterise the IRF in our device and the correct timing delay time (or jitter, as mentioned above), associated with each channel using the same optical path used for data collection, quenched fluorophores are used. The fluorophores are required to have a FWHM shorter than both the FWHM of the excitation laser pulses (PicoQuant LDH-P-C-485: laser width 30 ps), and the jitter of the SPADs (162 ps) [35, Fig. 15]. This is to ensure that the FWHM only captures the characteristics of the IRF without confounding influences of the FL from the measured fluorophores.

In the first instance, two fluorophores were quenched and assessed. Quenched Rose-bengal (RB) with an expected FL of 16 ps was used (see Fig. 2.7 A - D)[144]. RB was measured at a concentration of 1 M (ACROS Organic: 632-69-9) in 6.03 M potassium iodide (Sigma-Aldrich: 30 315-100G) at a pH of 9.8 [144]. Quenched Fluo (Sigma-Aldrich: F6377-100G), with an expected FL of 17 ps, was also used, measured at a concentration of 1 M in sodium iodide (at 12.2 M) [151]. Fluo has an expected emission range of 480 nm-600 nm [151], RB has an expected emission range of 540 nm-610 nm, although this is solvent dependent [144, 152].

To compare the accuracy of the IRF measured using quenched fluorophores, the IRF was also measured shining the excitation source directly onto the detector (see Fig. 2.5). This method does not account for the emission path from the fibre to be incorporated into the measurement, bypassing the internal optics of the device. Therefore, is not appropriate to be incorporated into the fitting routines. However, it provides an accurate estimation of the FWHM from both the laser and the detector (see Fig. 2.3). The average FWHM of the IRF measured from the laser was 0.49 ns (see Fig. 2.5 C). Moreover, the temporal jitter in arrival times of photons across channels is observed to be accounted for in this IRF (see Fig. 2.5 B).

When evaluating the IRF measured using quenched fluorophores, in the time domain the IRF is captured, however, in the spectral domain the emission spectrum of the fluorophores remains (see Fig. 2.6 A & C). The observed IRF also includes a detector property called dark counts, recorded detection outwith light, which is assumed to be constant across the time bins. For each channel, we therefore, first subtract the dark counts measured by averaging the counts within the first 2 time bins at each channel. We then normalise the IRF by the area normalisation method, such that the influence of the emission spectrum of the fluorophores is removed (see Fig. 2.6 B & D).

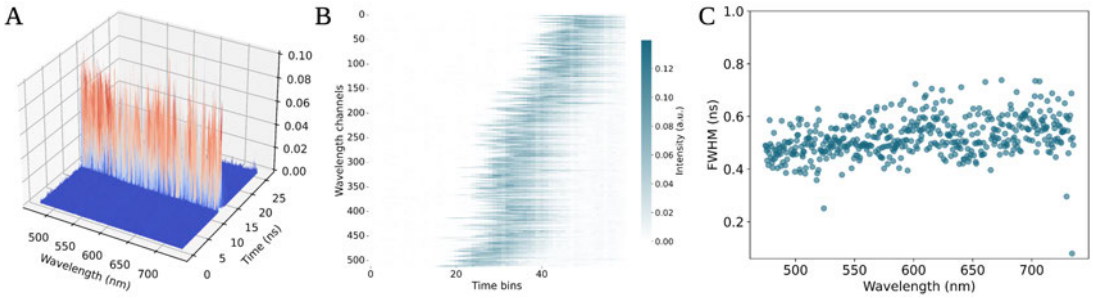

Figure 2.5: An instrument response function (IRF) measured by shining the laser at the detector. The captured histogram represents the IRF recorded across wavelength, intensity, and time **A)**. The heatmap of the recorded decays highlights the temporal variability of this feature across different time intervals **B)**. The full width at half maximum (FWHM) illustrates the variation of the IRF widths across channels **C)**.

We observed that the measured IRF decay traces at each channel, similar to the IRF measured from the excitation source, is not aligned in the temporal domain (Fig. 2.6 E & G) [35]. However, the arrival times of both measured IRFs, and the IRF from the excitation source are observed to be in alignment with each other (Fig. 2.5 B & Fig. 2.6 E & G). As aforementioned, filters and a beam splitter within the optical path of the setup prevents light below 512 nm entering the detector, therefore, measurements were assessed from emission here after. When assessing the FWHM of the two measured IRFs they align in similar regions with an average of 0.49 ns observed of RB, and 0.53 ns of Fluo (Fig. 2.6 F & H). In addition, we hypothesise due to the different fluorescence emission signals (and the spectral location of emission peaks), the FWHM of quenched Fluo has more variation (standard deviation of 0.06 ns, compared to RB 0.04 ns), and has a higher than average FWHM compared to both the measured IRF with the laser and the quenched RB (Fig. 2.6 F & H).

2.3.3 Convolution with Quenched Fluorophores

To compare the difference between using either quenched Fluo or quenched RB, the FI and FL was assessed using reference exogenous fluorophores (as aforementioned in section 2.3.1). The FL and FI of these decay traces were calculated using the NLLS method, as described above, with equations 1.8 and 1.7 representing the model function.

A higher average FL of Fluo was observed when analysed using quenched RB as the IRF (3.35 ns) compared to using quenched Fluo (3.20 ns) (see Table. 2.1). In addition, a shift in the spectral emission peak is observed when estimating the FI with the different IRFs (523.47 nm with quenched RB and 515.82 nm with quenched Fluo) (see Fig. 2.7 A, B, E & F) (see Table.2.1). A higher average FL of RhB was also observed when analysing the decays using quenched RB compared to using quenched Fluo (2.20 ns and 2.07 ns respectively). In addition, a blue shifted emission peak is observed with a quenched RB IRF compared to with a quenched Fluo (562.74 nm and 587.73 nm respectively) (see Fig. 2.7 C, D, G &

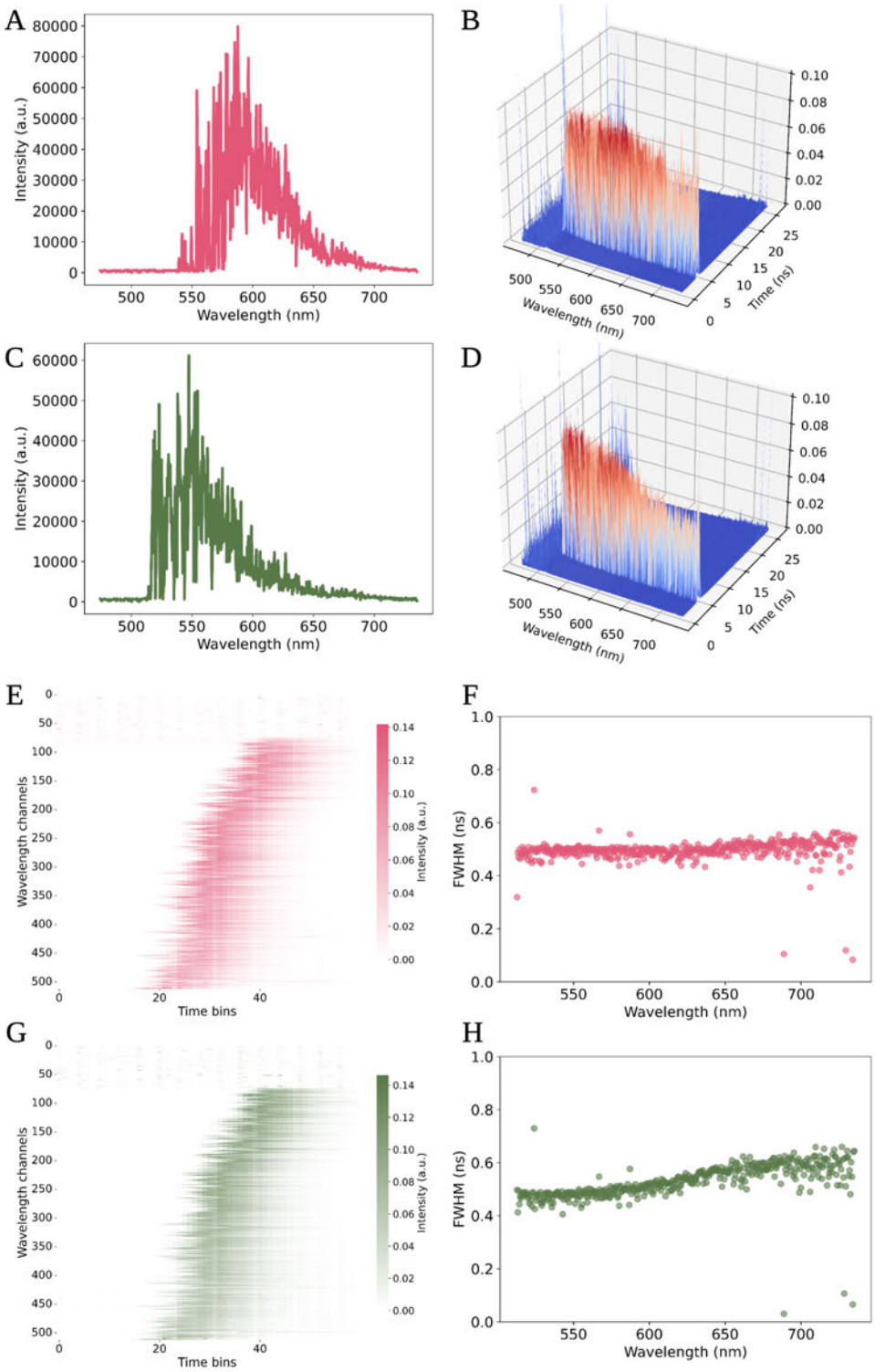

Figure 2.6: Comparison of an instrument response function measured either from quenched rose-bengal or quenched fluorescein sodium. **A)** shows the emission spectrum of quenched rose-bengal, **B)** show the corresponding histogram following normalisation by the area, mitigating the emission shape. **C)** shows the emission spectrum of quenched fluorescein sodium, **D)** shows the corresponding histogram following normalisation by the area. **E)** shows the temporal delay of the arrival of the individual photons in each channel from an IRF measured of quenched rose-bengal. **F)** shows the full width at half maximum (FWHM) of the signal from the quenched rose-bengal IRF. **G)** also shows the arrival time of the individual photons in each channel from an IRF measured from quenched fluorescein sodium, and **H)** shows the FWHM.

Table 2.1: Fluorescence lifetime differences between two reference fluorophores, where two different measured IRF's are incorporated into the analysis routine.

	Rhodamine B average lifetime (ns)	Rhodamine B emission peak (nm)	Fluorescein Sodium average lifetime (ns)	Fluorescein Sodium emission peak (nm)
Quenched Rose-bengal IRF	2.20	562.74	3.35	523.47
Quenched Fluorescein Sodium IRF	2.07	587.73	3.20	515.82

H) (see Table.2.1). The FL and FI from both measured IRFs are within the expected range of these fluorophores from the literature [47, Table 2]. However, a decrease in the FL of both fluorophores is observed with the Fluo IRF. A hypothesis for this is that the FWHM is marginally wider than that of the detector. Therefore, the IRF captures both the IRF from the device as well as photons from Fluo. This results in lower FL values of the measured samples during the deconvolution process.

The primary objective for selecting an IRF is to provide an accurate deconvolution of FL values from the measured fluorophores in a sample. As the average FWHM is in agreement with the FWHM when estimating an IRF from shining the laser directly onto the detector, quenched RB is used to capture the EP-TRFS's IRF in this thesis. However, the use of RB limits the analysis across the spectral region, particularly $<$550 nm and above 630 nm as the spectral region of this fluorophore does not provide significant decays outwith these wavelengths (see Fig. 2.6 A). This is a major limitation to the results collected in this thesis.

2.4 Sample Specific Alterations

Sample specific alterations include factors affecting the measured FI and FL of a sample independent of the composition of fluorophores changing due to the diseased status of tissue. Therefore, three main features of data collection are explored. First, the concentration limit of the detector is examined to assess the stability of FL with varying photon counts. Next, the photo-physical effects of different tissue storage methods prior to data collection are investigated. The chapter concludes with experiments testing whether photobleaching alters the FL of the measured samples.

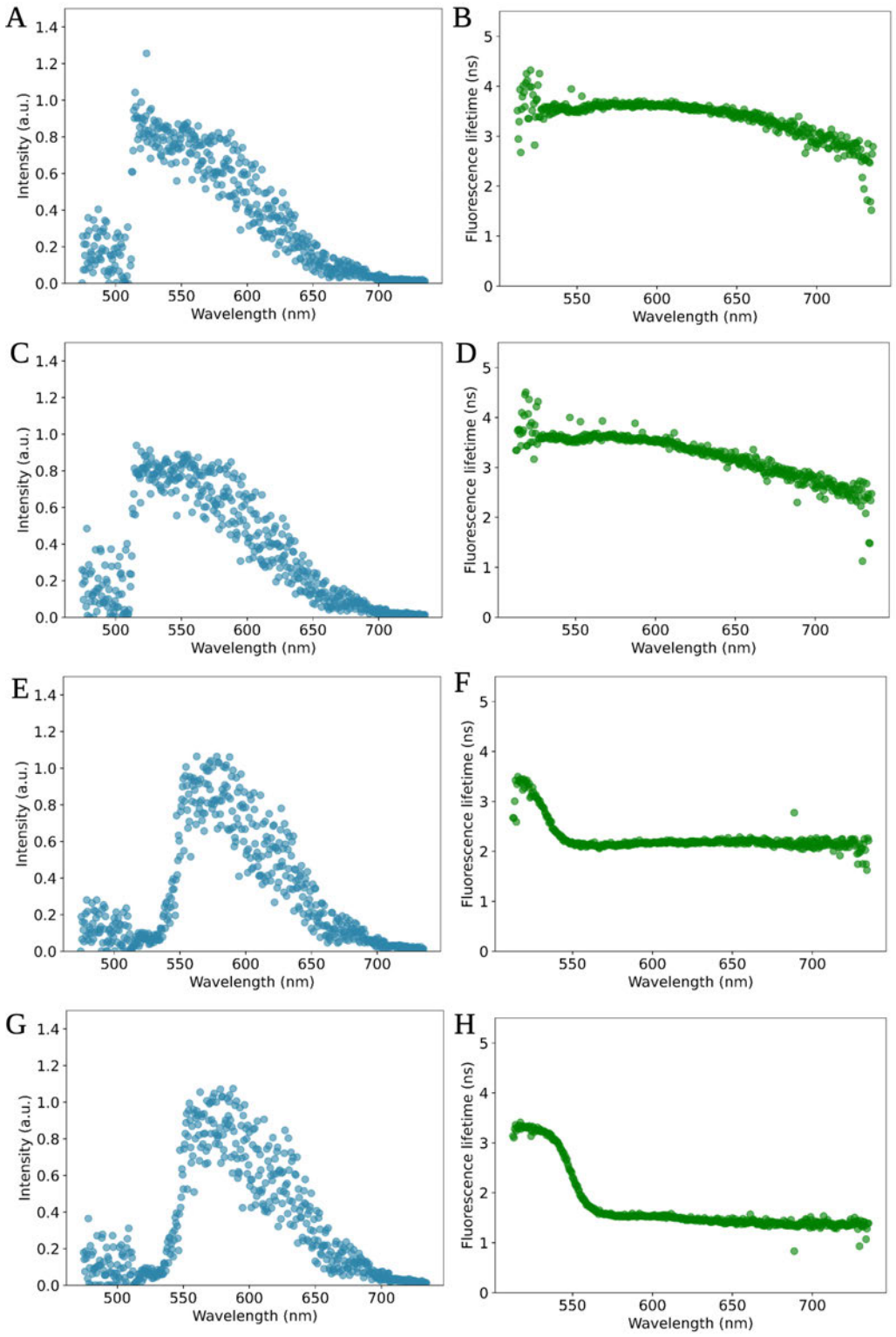

Figure 2.7: Fluorescence intensity (FI) and fluorescence lifetime (FL) estimations of Fluorescein dissolved in PBS at a concentration of 1 µM (**A)**, **B)**, **C)**, & **D)**) and Rhodamine B dissolved in methanol at a concentration of 10 µM (**E)**, **F)**, **G)**, & **H)**). The FI and FL values were estimated using the least squares method, deconvolved with a measured instrument response function (IRF). A, B, E & F were deconvolved with an IRF measured with quenched rose-bengal. C, D, G & H were deconvolved with an IRF measured with quenched fluorescein sodium.

Table 2.2: Power output of the excitation laser following its attenuation with varying neutral density filters.

ND filter	0	5	10	11	12	14	15	16
Laser power (µW)	184	54	17	12	11	6	5	3

Table 2.3: The average fluorescence lifetime of Rhodamine B following a serial dilution from 20 µM to 4 µM

Concentration (µM)	Fluorescence lifetime (ns)
4	1.49 ± 0.10
6	1.50 ± 0.06
8	1.49 ± 0.05
10	1.46 ± 0.04
12	1.47 ± 0.04
14	1.42 ± 0.04
16	1.37 ± 0.03
18	1.28 ± 0.03
20	1.17 ± 0.03

2.4.1 Concentration Dependent Lifetime

In the context of tissue AF, the range of FL as mentioned is expected to vary from 0.1 ns-$<$10 ns. Therefore, to assess the accuracy and stability of FL in decreasing concentrations RhB (Sigma-Aldrich: 102 406 918), dissolved in water, with an anticipated FL of 1.52 ns $\pm$ 0.1 [153], was measured two fold, with the same aforementioned TCSPC setup (i.e., matching exposure time and laser repetition rate). In the first instance a serial dilution was performed. RhB was mixed up in a range of different concentrations from 20 µM-4 µM and a 2 µM step size. To mitigate the impact of different concentrations on the FL of the fluorophore, in parallel RhB at a fixed concentration (20 µM) measured using neutral density (ND) filters with various attenuation was assessed. 8ND filters were used reducing the laser power from 184 µW - 3 µW (see Table. 2.2). As aforementioned, quenched RB is used as the IRF, therefore the spectral range of this fluorophore analysed is 550 nm-630 nm.

As anticipated, the photon count of the peak spectral intensity dropped from 3624.0 to 667.0 in a declining concentration of RhB from 20 µM to 4 µM (see Fig. 2.8 A). The average FL changed when RhB is estimated in different concentrations ranging from 1.50 ns-1.17 ns (see Fig. 2.8 C, and Table 2.3). The standard deviation of the FL between 4 µM-14 µM decreased from 0.1-0.04, but the FL remained within the expected region of 1.52 ns $\pm$ 0.1 [153]. However, the average FL dropped below the expected region with increasing concentrations between 16 µM-20 µM (see Fig.2.8 C, and Table 2.3). We hypothesise this drop in FL is an artefact

observed in TCSPC mode known as early photon pile-up. In pile-up during each repetition rate of the laser pulses >1 photon arrives at the detector, overemphasizing photons with shorter arrival times and skewing the detection, resulting in an artificial drop in the FL of the recorded decay traces [34, Section 2]. Therefore, RhB samples <16 µM are used in the thesis.

The peak spectral intensity also dropped with increasing ND filters, attenuating the signal (from 2963.0 to 450.0) (see Fig. 2.8 B). Moreover, the peak of the spectral emission remained in at 587.73 nm when all ND filters were used (see Fig.2.8 B). In comparison to the serial dilution of RhB, the average FL when estimated from ND filters is relatively stable, but a slight increase from 1.57 ns with an ND of 5 to 1.60 ns with an ND of 16 is observed (see Fig. 2.8 D). The average FL is also marginally greater than when a serial dilution of RhB is estimated. However, all values are within the expected range of the fluorophore (1.52 ns $\pm$ 0.1), even in particularly low photon counts and a low excitation laser power of 3 µW. These results suggest that the FL and spectral range of fluorophores measured on the EP-TRFS device in low photon counts and concentrations remains stable and accurate.

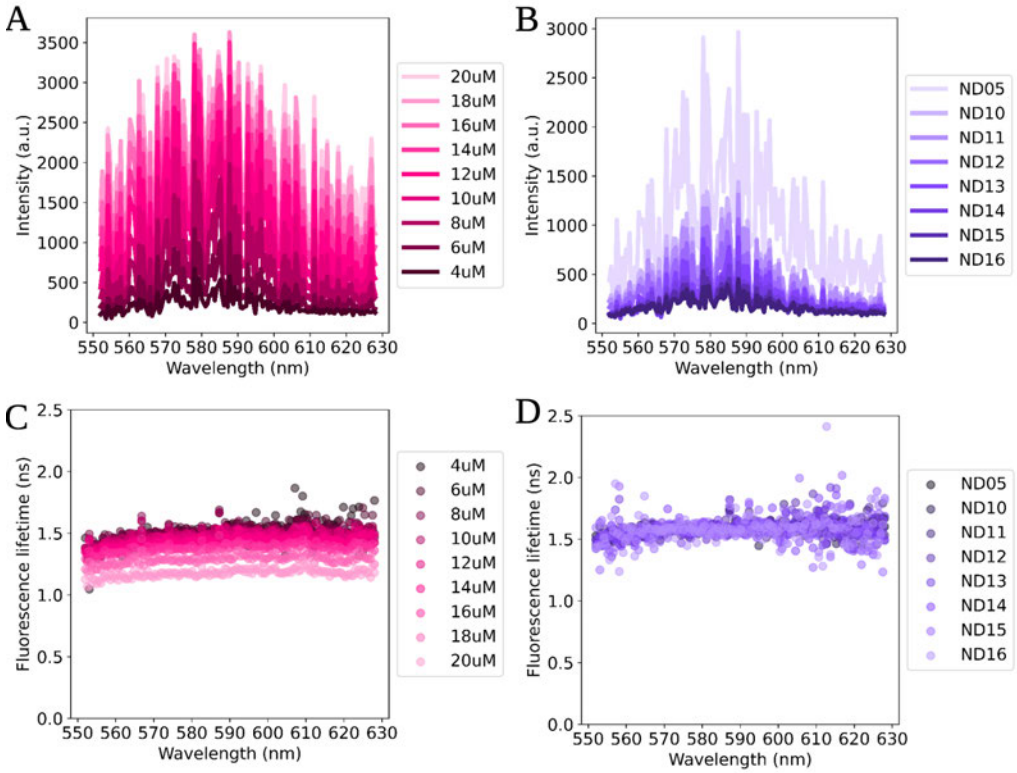

Figure 2.8: Comparison of the fluorescence profile of Rhodamine B dissolved in water, from a serial dilution (**A)** and **C)**) and following the attenuation of a laser with neutral density (ND) filters (**B)** and **D)**

2.4.2 Tissue Sample Preparation

The final set of sample-specific experiments conducted evaluates variations in sample preparation methods of tissue. This assessment is essential to determine if differences in the measured signal arise from the tissue preparations alone. All tissue measurements are collected with the fibre of the system integrated into a Cartesian robot. This allows control of the fibre on a precise location of tissue in the X Y and Z axis. The tissue samples are also pinned onto a foam board for stability. Between each sample change (including samples from the same patient), the fibre tip is cleaned with non-fluorescence 80 % ethanol.

Depending on the collection time of the tissue, fresh measurements are not always possible. To assess whether tissue storage altered the fluorescence profile of samples, lung tissue declined for transplant is tested (AJEQ226). The tissue was measured fresh after being placed in a cold unit at 4 ℃ (see Fig. 2.9 A & B). The sample is then left in a -80 ℃ freezer for a week and reassessed, using the robot to direct the fiber into the same location as the fresh measurement. Note that variation in the placement of the tissue on the analysis board may have resulted in a slight difference in the precise location. However, a negligible difference between both the FI and FL can be observed between either sample (see Fig. 2.9), with an average FL of 0.90 ns in the fresh sample and an average FL of 0.92 ns following the freeze/thaw. These results align with previous results comparing the FL of frozen and fresh tissue [154]. Therefore, depending on the sample collection time the samples are collected, the tissue samples are either measured fresh or thaw following a brief incubation period in a -80 ℃ freezer.

2.4.3 Photobleaching

The final sample-specific experiment conducted is the effect of photobleaching. The photobleaching effect of tissue is endogenous fluorophore specific, and subsequently dependent on the optical setup of the device as aforementioned, determining which fluorophores are excited and detected. Three different locations of lung tissue declined for transplant are assessed (AJJG174) using HistMode of the EP-TRFS device. In HistMode, multiple histograms are collected in 32 time bins with a temporal resolution of 800 ps, each with a 20 ms exposure time at location 1 and 30 ms at location 2 and 3, with negligible timing between histogram acquisitions. Samples are exposed to the excitation source, collecting tissue fluorescence for 120 s at each location, with the same excitation power as when used in TCSPC mode (192 µW) (see Fig. 2.10). TCSPC data collection in our system is not optimised for high speed and involves an overhead in data collection time, resulting in a total runtime of 10 s while the sample is being exposed to light, even though the actual exposure time while photons are collected is shorter for acquiring data with 1.5×10^6 exposures and an exposure time of 5 µs for a single histogram. Therefore, any photobleaching measured using TCSPC can be approximated to any photobleaching observed in HistMode during a total exposure of 120 s.

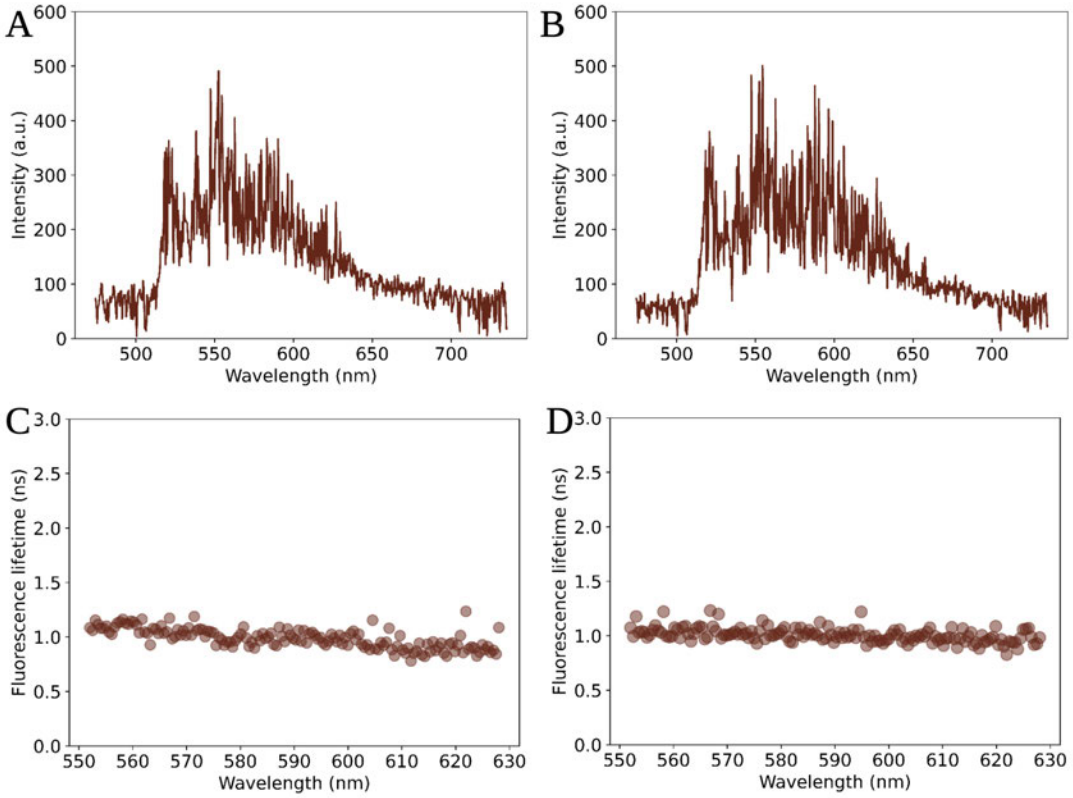

Figure 2.9: The estimated fluorescence intensity and fluorescence lifetime of a lung declined for translated and prepared either fresh following a brief incubation in a cold room **A)** and **C)**, or thaw after storage in a -80 freezer **B)** and **D)**.

A drop in FI is observed in in all locations over the 120 s when sampled every 20 or 30 ms (i.e, the exposure time of each histogram measurement) (see Fig. 2.10 A-C). From 737-264 in location 1, 1194-375 in location 2 and 1057-344 in location 3. In addition, a slight shift in the average FL is observed from 1.75 ns $\pm$ 0.6 to 1.42 ns $\pm$ 0.5 in location 1, 0.92 ns $\pm$ 0.28 to 1.16 ns $\pm$ 0.40 in location 2 and 1.82 ns $\pm$ 0.47 to1.38 ns $\pm$ 0.49 in location 3. Despite the differences in the FL values, the change in direction between all samples is different (a slight increase in FL is observed between 0-120 s at location 2, however, a decrease at location 1 and 3). Moreover, the range of values is large and overlap in all cases (see Fig. 2.10 D-F). As mentioned, the collection time when used in TCSPC mode is around 10 s per histogram, therefore, following repeated measurements, we can conclude that photobleaching of tissue 485 nm although influencing the FI, only minimally effects the FL.

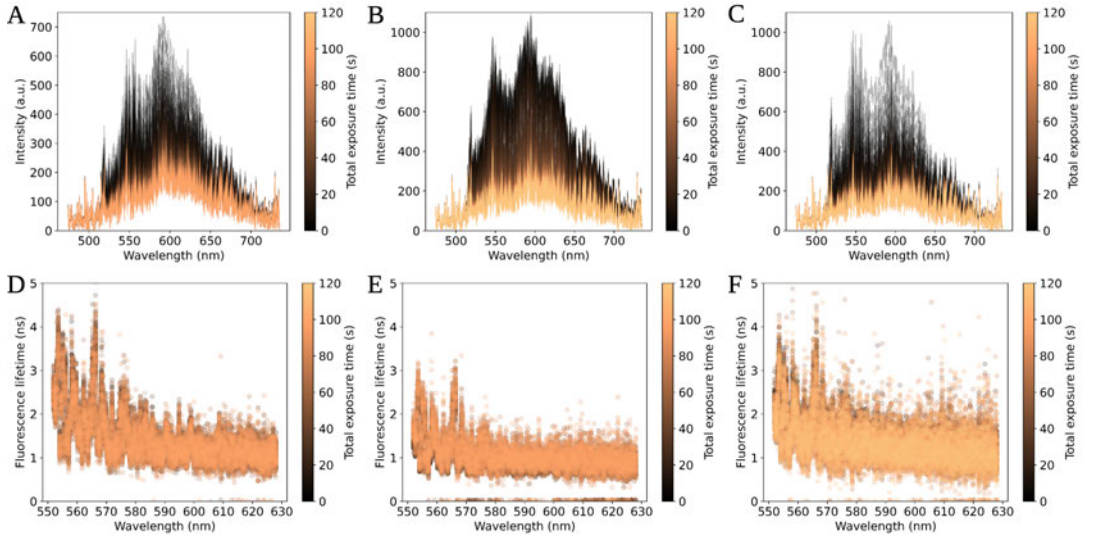

Figure 2.10: Tissue measured following prolonged exposure to an excitation source was assessed. Three different sampling locations were used for data collection. **A)**, **B)** and **C)**, show the emission profile of the sample locations. **D)**, **E)** and **F)** show the estimated fluorescence lifetime.

2.5 Discussion

This chapter evaluates potential data artifacts from the EP-TRFS and variations within the measured sample which can occur independently of changes to the underlying fluorophores. We aim to identify effective strategies for addressing these variations to ensure accurate interpretation of the results here after.

Various methods for for handling temporal decay features are first presented, either by removing the temporal jitter from the observed decay (tail fit), or incorporating an IRF into the analysis pipeline. Initially, we demonstrate results obtained using a tail fitting approach applied to known reference fluorophores RhB and Fluo. This highlights an increase in FL compared to where a deconvolution approach is applied, attributed to photons in the initial time bins perturbed both by the IRF and the measured sample. Subsequently, we examine two quenched fluorophores, RB and Fluo. These are considered suitable for integration into a deconvolution analysis model as the measured IRF due to short expected FL values. We compare these quenched fluorophores to an IRF obtained by shining the excitation laser directly onto the detector. Furthermore, the performance of the two measured IRFs are assessed when incorporated into an analysis model, focusing on accurately estimating both FL and FI of RhB and Fluo.

Despite covering a red shifted spectral range compared to Fluo, quenched RB exhibits a FWHM matching that of the optical setup. Consequently, it is concluded that quenched RB is the most suitable fluorophore. Using fluorophores to measured the IRF, whilst accurately capturing the time-resolved features, presents a significant limitation only capturing the spectral range of the fluorescence emission. Therefore the appropriate spectral analysis range using a deconvolution method with this setup and quenched RB is between 550 nm-630 nm (see Fig.2.6 A). This allows a greater spectral bandwidth resolution analysis of fluorescence following the excitation at 485 nm compared to previous devices used to assess tissue. However, prevents the potential full spectrum to be analysed, which is a significant limitation. One potential improvement could involve evaluating an IRF from erythrosine B, with an emission range of 500-620 nm, this may allow fluorophores with emission peaks around 520 nm (such as FAD) to be assessed. An alternative method is to develop an analysis tool which is able to simultaneously extract the fluorescence from both the sample and the IRF. This is something we save for future work.

Specific to the EP-TRFS device, as mentioned in the introduction, and observed in Fig.2.7, a jitter across both the timing range of incoming photons, and a sensitivity across the emission spectra, independent of the number of photons collected per pixel is observed. Whilst the temporal jitter is accounted for with the IRF, the spectral sensitivity remains unaddressed. The spectral sensitivity is observed by a difference in photon sensitivity at individual neighbouring pixels (see Fig.2.7). This spectral sensitivity may limit the devices potential to delineating multiple individual fluorophores, as the emission at each channel is influenced both by the emission from the fluorophores and the spectral sensitivity. Characterising the feature and incorporating this into the analysis routine is also something we leave to characterise in future work.

Sample specific alterations are also explored within this chapter, focusing initially on the sensitivity of FL in low photon counts. Initially, we compared a serial dilution of RhB with measurements taken after an attenuation of the laser through a series of ND filters. Our initial observations indicate that the FL and peak intensity of RhB following laser attenuation remain relatively constant, suggesting the device is sensitive even when lower photon counts are captured. Moreover, in the samples from a serial dilution, the average FL matches the expected values of RhB in water from 4 µM-14 µM, with decreasing variance as the concentration increases (and so the subsequent number of photons increases) (see Table 2.3). However, a drop in FL is observed between 16 µM-20 µM which we attribute to early photon pile-up. Therefore, RhB when used as a reference sample in TCSPC mode is recorded in concentrations $<$16 µM. The likelihood of pile-up from endogenous fluorophores in tissue is reduced as these fluorophores are generally dimmer than exogenous fluorophores. They are also present in lower concentrations and have lower quantum yields, reducing the likelihood of this issue when measuring tissue AF. Given the stability of the FL, and the overlap between the

values compared to the expected values in the literature, it can be concluded that the device is accurate in estimating the FL in various photon levels. However, these measurements were conducted with an exogenous fluorophore, which has a different photo-physical property compared to endogenous fluorophores in tissue.

The experiments conducted on tissue preparation include measuring the same sample following different preservation methods. This experiment shows neither method perturbs the photo-physical proprieties of the tissue, therefore, both storage methods are used prior to tissue collection. The final photobleaching experiments conducted in this chapter show the photo-chemical properties of tissue following prolonged exposure to the excitation source (between 0-120 s). The results show marginal changes in the FL of tissue, suggesting that when TCSPC mode is used, and a maximum exposure time of $<$30 s is applied, the overall FL change is minimal. However, the tissue experiments conducted in this chapter are conducted on lung tissue which has been rejected for transplantation. The photo-chemical properties both between these lung tissues assessed and from lung tissue of patients with suspected cancer may also be different. To provide an enhanced understanding of both the effect of sample preparation methods and photobleaching, more samples are required. This is a limitation to these results, however, due to limitations in lung availability was not possible during this thesis but something we save for future work.

2.6 Conclusion

In summary, this chapter comprehensively evaluated both device and sample specific alterations. Initially, various quenched solutions for measuring an accurate IRF ensued. Our findings indicate that quenched RB is the most suitable option for this device. This determination is supported by its average FWHM of 0.49 ns, aligning well with the FWHM of the IRF measured using the excitation laser, and its emission peak positioned towards the center of the detector channels. Furthermore, the investigation into concentration-dependent FL, both through serial dilution of RhB and the use of ND filters revealed a consistent accuracy in FL even at lower laser powers (3 µW). Additionally, we explored variations in tissue preparation methods, particularly in different tissue storage techniques to ascertain their impact on fluorescence data quality. Our results indicate that neither of these factors significantly influences fluorescence quality. Lastly, we investigated the effects of photobleaching on tissue data obtained using the EP-TRFS device. Our analysis revealed no significant variation in FL with increasing exposure time to the excitation source. Thus, we conclude that the observed photobleaching effect on tissue using this setup is negligible.

Chapter 3

Multichannel Fluorescence Lifetime Estimation

Analysis techniques for assessing FL, traditionally rely on channel specific measurements, often analysed using devices that collect the temporal emission in large wavelength bandwidth resolutions. However, the underlying fluorescence emission of a fluorophore tends to have a broad peak and emit over a wide-ranging wavelength range.

The device used to measure time resolved fluorescence in this thesis collects high-resolution spectral-temporal histograms of the resulting fluorophores. Therefore, the initial aim of this thesis is to develop an analysis tool which is able to incorporate the fluorescence across the wavelength range to simultaneously estimate both the total emission spectrum and corresponding FL. This chapter presents the computational model called **MuFLE**, the **Multichannel Fluorescence Lifetime Estimation model**. The results of this chapter are published in IEEE Transactions of Biomedical Engineering titled: Simultaneous Spectral Temporal Modelling for a Time-Resolved Fluorescence Emission Spectrum, therefore, the exact format of the published paper is included.

Simultaneous Spectral Temporal Modelling for a Time-Resolved Fluorescence Emission Spectrum

Alexandra C. Adams, András Kufcsák, Katjana Ehrlich, Kevin Dhaliwal and Sohan Seth

***Abstract*— Innovations in complementary metal-oxide semiconductor (CMOS) single-photon avalanche diode (SPAD) technology has featured in the development of next-generation instruments for point-based time-resolved fluorescence spectroscopy (TRFS). These instruments provide hundreds of spectral channels, allowing the collection of fluorescence intensity and fluorescence lifetime information over a broad spectral range at a high spectral and temporal resolution. We present Multichannel Fluorescence Lifetime Estimation, MuFLE, an efficient computational approach to exploit the unique multi-channel spectroscopy data with an emphasis on simultaneous estimation of the emission spectra, and the respective spectral fluorescence lifetimes. In addition, we show that this approach can estimate the individual spectral characteristics of fluorophores from a mixed sample.**

***Index Terms*— Fluorescence lifetime, time-resolved fluorescence spectroscopy, B-splines, non-linear least squares,**

I. Introduction

Fluorescence spectroscopy (FS) is an analytical tool used to measure the spectral characteristics of fluorescence emission detected from molecules (*fluorophores*) following their excitation with monochromatic light [1, Chapter 2.3]. The spectroscopy of endogenous fluorophores, when assessed in tissue, allows for the differentiation between certain tissue conditions and disease status [2], [3]. FS analyses the distribution of fluorescence intensity (FI) over wavelengths, i.e., the *emission spectrum*. FI measures the relative 'brightness' of the fluorophore related to its quantum yield, i.e., the proportion of photons emitted following absorption, and its concentration [4].

FS has several limitations, e.g., the emission spectrum depends on the concentration of individual fluorophores when multiple fluorophores are present. This can be overcome by measuring the fluorescence lifetime (FL) [1, Chapter 1]. FL describes the average time a fluorophore spends in its excited state [1, Chapter 1], it is fluorophore specific and sensitive to the environment. Therefore, analysing both FL and FI together can provide detailed optical information of a sample, e.g., tissue [5].

Recent technological advancements and improvements in signal processing have seen FL devices entering clinical studies [6]. FL devices have shown the potential to discriminate cancerous and non-cancerous tissue in head and neck surgery [6], [7]; in the detection of brain [8] and gastrointestinal tumours, [9] and in the detection of early stage lung cancer [10]. Given the specificity of FL, these devices have the potential to greatly improve the diagnostic accuracy where uncertainty in the diagnosis remains [11], [12]. However, to enable the diagnostic potential of these devices, dedicated data analysis methods are needed to improve their sensitivity, specificity and the inter- and intra-patient variability [13].

Traditionally, two types of devices allow FL to be measured, frequency-domain based and time-domain based [3]. We focus on the latter in this study. These devices capture the fluorescence emission as a function of time delay following pulsed excitation. There two are main spectroscopic setups for time-domain based devices: an imaging setup, either via scanning or wide-field microscopy, referred to as the fluorescence lifetime imaging microscopy (FLIM), or a point based setup, referred to as the time-resolved fluorescence spectroscopy (TRFS) [3], [5], [13]. Both these setups can have either a time-correlated single-photon counting (TCSPC) based detector or a time gated (TG) detector, and can measure emission at either a single wavelength or multiple wavelengths.

Commercially available devices with a scanning monochromator and a single detector can assess FLs in a single channel. To achieve a multi-channel assessment using this set up, repeated measurements over the selected wavelength range is required. These devices achieve good signal-to-noise ratios due to their high stray light rejection, however, recording repeated measurement is inefficient, likely to induce photobleaching and motion artefacts [1, chapter 2]. Alternative multi-channel devices developed in research include the multispectral (ms-) TRFS device. ms-TRFS utilises band pass filters that segregate the fluorescence signal into four distinct channels matched to the fluorescence emission maxima of specific endogenous fluorophores, NADH, FAD, elastin and porphyrin, with coarse wavelength bandwidths between 40 nm and 53 nm [14]. Here each channel arrives at the detector consecutively via optical fibres of different lengths, the fibres allow a time delay of 45 ns between the signal. The number of wavelength specific fibres used in this setup dictates the number of channels the fluorescence decays are segregated into, e.g., 3 channels are

A. A., A. K., K. D., and S. S. are with the Translational Healthcare Technology Group, Centre for Inflammation Research, Queen's Medical Research Institute, University of Edinburgh, 47 Little France Crescent, Edinburgh, EH16 4TJ, UK. (e-mails: ,{A.Kufcsak, Kev.Dhaliwal.). S. S. is with the School of Informatics, University of Edinburgh. K. E. is with the Scottish Universities Physics Alliance (SUPA), Institute of Photonics and Quantum Science, Heriot-Watt University, Edinburgh, EH14 4AS, UK. (email:).
A. A. was supported by the Medical Research Council [grant number MR/N13 166/1]. K. E. was supported by EP/V6185/1.

used in [15] and 4 channels are used in [6]. This device allows a rapid multi-spectral assessment, but is limited in the wavelength bandwidth resolution.

Recently, highly integrated devices composed of complementary metal-oxide semiconductor (CMOS) single-photon avalanche diode (SPAD) arrays, has enabled extensively parallel point-based TRFS (EP-TRFS) measurements based on TCSPC, which allows for both FI and FL to be resolved spectrally [16]–[19] (see Fig. 1A). Following spectral dispersion with a grating, these devices enable photons of known wavelengths to be recorded in *hundreds* of individual wavelength channels with independent timing circuits recording respective photon arrival times. The recorded photon arrival times can be converted into a two-dimensional histogram of photon counts over wavelength channels and time bins to build a *time-resolved emission spectrum* (TRES) (see Fig. 1B) [18]. The advantage of these EP-TRFS devices is a multi-channel, spectral (see Fig. 1C) and temporal assessment of the sample providing extremely information-rich profiles. In addition, it allows the spectral FL, i.e., the FL value of the individual channels across a wavelength spectrum, of a heterogeneous sample to be assessed in high resolution (see Fig. 1D).

Existing computational tools are designed to process time-resolved data from a single channel, and there exists many approaches to estimate the FL with varying complexity and accuracy. For a rapid assessment, fit-free approaches are most common, specifically the centre of mass (CM) calculation [20], [21] and rapid lifetime determination (RLD) [22], [23]. However, these approaches are limited to estimating a single (average) FL. To resolve multi-exponential decays at a wavelength channel, other curve fitting methods such as the maximum likelihood estimation [24], the Laguerre polynomials expansion [25] and least squares approach are preferable [26]. These methods can estimate both the FI and FL, for each fluorophore at each channel. These techniques, however, are limited considering they are applied to each channel separately. In addition, where TRES is available, existing approaches often reduce the high resolution channel information into a single, or a few channels of low resolution (by marginalizing the histogram) and thus, losing crucial information on the emission spectra as well as any potential variation of FL over the channels.

We propose that the high-resolution, time-resolved data generated by EP-TRFS requires dedicated algorithms to fully explore their information content. We present **Multichannel Fluorescence Lifetime Estimation (MUFLE)**, a computational framework to analyse TRES that simultaneously captures the fluorescence emission spectra and the FLs of individual fluorophores in a sample. In MUFLE, we estimate one or more FIs and FLs at each channel using a least squares approach by fitting either a single or multi-exponential decay model, and we simultaneously utilise the information within the spectral context by allowing the fitted FI and FL values to vary smoothly across the channels. We hypothesise that MUFLE can better capture the fluorescence characteristics of a sample encompassing all data points in the spectral and temporal domain of TRES simultaneously.

The contribution of the paper is three fold: first, we present a novel approach, MUFLE, to analyse multi-channel time resolved fluorescence spectroscopy data for simultaneously estimating the FIs and FLs of underlying fluorophores along with the associated uncertainties, second, we experimentally show that MUFLE can effectively capture the FIs and FLs of single fluorophores using three reference solutions, and third, we experimentally show that MUFLE can reliably un-mix two fluorophores using two mixed solutions.

II. METHODS

We denote a function over continuous variables, e.g., t or ω (for time and wavelength respectively) as $x(t)$ or $x(\omega, t)$ while we denote its corresponding discrete representations as $x[m] = x(t_m)$ and $x[p, m] = x(\omega_p, t_m)$, respectively. Given a function over two variables $x[p, m]$, we denote one dimensional *slice* of the function at an index p as $(x[p])[m]$. We denote by $\mathbf{x}$ (lower case bold) a M-dimensional vector $[x[1], \ldots, x[M]]^\top$, and similarly by $\mathbf{X}$ (upper case bold) the $P \times M$ sized matrix with entries $x_{pm} = x[p, m]$. We denote the observed histogram of photon counts as $\mathbf{Y}$, the photon count at time bin m and wavelength channel p as $y[p, m]$. Note that photon arrival times are quantised by the detector's time resolution, and therefore, y_m denotes the photon count over the interval $[t_{m-1}, t_m]$, rather than an instantaneous photon count at t_m. Although we assume this to be instantaneous when the binwidth is sufficiently small, e.g., of 50 ps. We denote the observed instrument response function (IRF) over time and wavelength as $\mathbf{H}$, and denote the IRF at a specific wavelength index p as $(h[p])[m]$. See supplementary table IV for the notations used in this paper.

A. Standard least squares fitting

Let us model the decay trace at a single channel with $s(t)$. The fitted signal $s(t)$, in the continuous domain is usually expressed as a composition of multiple exponential decay traces, one for each fluorophore present in the sample, convolved with the IRF and an additional bias, i.e.,

$$s(t) = (f * h)(t) + b \text{ and } f(t) = \sum_{l=1}^{L} \gamma_l \exp(-t/\tau_l)\mathbb{H}(t) \quad (1)$$

where γ_l and τ_l are the relative FI and FL of the l-th fluorophore, b is the bias due to the dark counts of the detector and the fibre background, $h(t)$ is the IRF at a single channel, $*$ denotes convolution, and $\mathbb{H}$ is the Heaviside function. Eq. (1) can also be expressed in the discrete domain as

$$s[m] = (f * h)[m] + b \text{ and } f[m] = \sum_{l=1}^{L} \gamma_l \exp(-t_m/\tau_l) \quad (2)$$

with $m \in \{1, \ldots, M\}$ under the assumption that the time bin width is sufficiently small. Let $y[m]$ be the observed signal at the m-th bin, then FI and FL values can be found by minimizing the loss function

$$J_1 = \sum_{m=1}^{M} (y[m] - s[m])^2 \quad (3)$$

with respect to γ_ls, τ_ls and b given $h[m]$ is known.

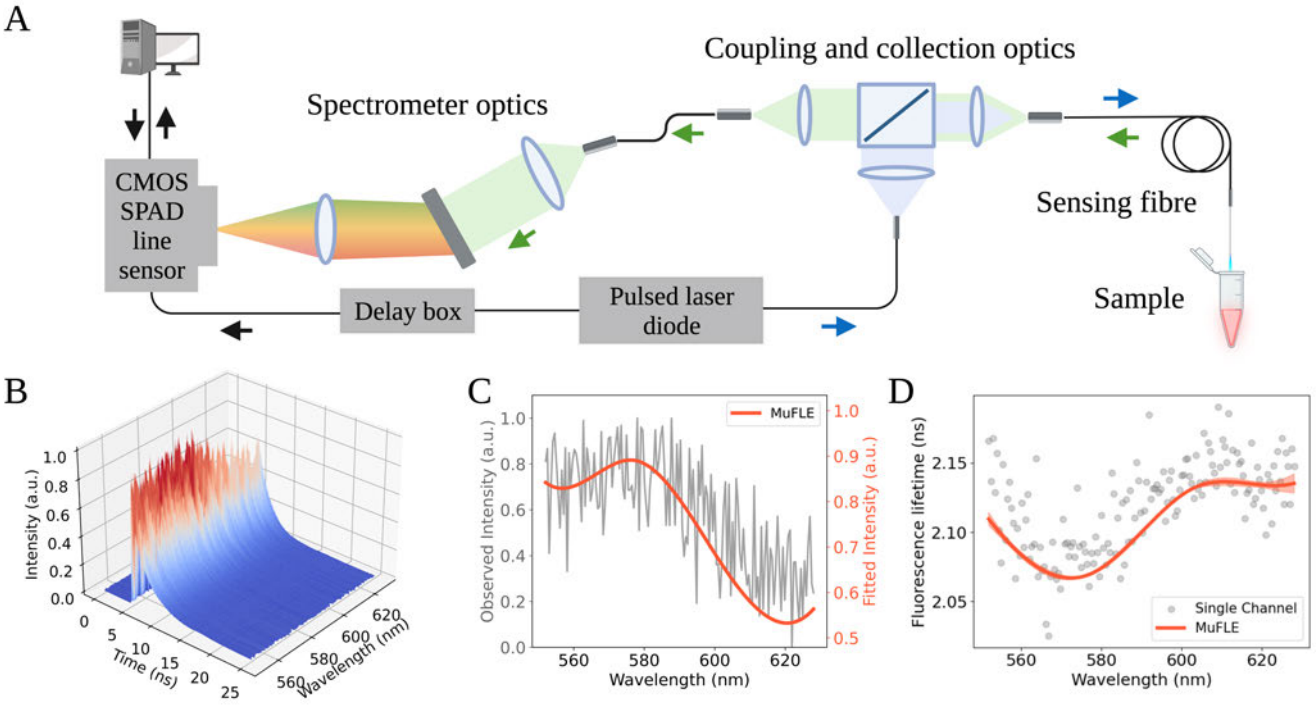

Fig. 1. **A)** Illustration of the EP-TRFS instrument device used in this study, including a pulsed laser, coupling and collection optics, a spectrometer and a complementary metal-oxide semiconductor (CMOS) single-photon avalanche diode (SPAD) line sensor. The black arrows represent the direction of the electrical signals, while the coloured arrows represent the direction of the optical signals going to (blue) or from (green) the sample. **B)** The pre-processed histogram of RHB-ME in a truncated spectral range of 552.03 nm - 628.02 nm. Results from RHB-ME showing **C)** the fluorescence intensity and **D)** the fluorescence lifetime. Lines represent the estimated intensity and fluorescence lifetime (orange) using the MUFLE algorithm (C,D). The gray line represents the underlying intensity from the histogram following its normalisation (C). Dots represent the fluorescence lifetime (grey) for single channel fits (D). Figure created with BioRender.com.

B. Multichannel least squares fitting

In the EP-TRFS system (Fig. 1), the observed decay trace is not only recorded over time, but also across wavelength resulting in TRES. If the relative FI and FL over the spectral domain vary as $\gamma_l(\omega)$ and $\tau_l(\omega)$ respectively, then we can express the TRES histogram as

$$s[p,m] = (f[p] * h[p])[m] + b[p] \tag{4}$$

with

$$f[p,m] = \sum_{l=1}^{L} \gamma_l(\omega_p) \exp(-t_m/\tau_l(\omega_p)) \tag{5}$$

where we assume that $b(p)$ is the bias that varies across the channels, and $(h[p])[m]$ is the IRF at channel p. Then FI and FL spectra can be found by minimizing the following loss function

$$J_2 = \sum_{p=1}^{P} \sum_{m=1}^{M} (y[p,m] - s[p,m])^2, \tag{6}$$

given $h[p,m]$.

C. Fluorescence intensity and B-splines

Given a sequence of knots $\mathbf{\Omega} = [\Omega_1, \ldots, \Omega_{n+1}]$, B-splines basis functions of order k are composed of polynomials of degrees up to $k-1$ where the higher order basis functions are defined recursively using the lower order basis functions (also known as *Cox-de Boor recurrence relation* [27]) such that for $n \geq k \geq 2$: $B_{i,k}(\omega) = \frac{\omega - \Omega_i}{\Omega_{i+k-1} - \Omega_i} B_{i,k-1}(\omega) + \frac{\Omega_{i+k} - \omega}{\Omega_{i+k} - \Omega_{i+1}} B_{i+1,k-1}(\omega)$ $\forall i = 1, \ldots, n-k+1$ where $\Omega_i < \omega \leq \Omega_{i+k}$ (and the function is zero elsewhere), and where $B_{i,1}$ is defined as $B_{i,1}(\omega) = 1$ for $\Omega_i < \omega \leq \Omega_{i+1}$, and 0 otherwise, $\forall i = 1, \ldots, n$.

We use open uniform knot sequences such that between $[\Omega_1, \Omega_{n+1}]$, $\Omega_i = \Omega_1$ $\forall i \leq k$, $\Omega_{i+1} - \Omega_i = \frac{\Omega_{n+1} - \Omega_1}{n-2k+2}$, $\forall k < i < n-k+2$, $\Omega_i = \Omega_{n+1}$, $\forall i \geq n-k+2$ and we refer to the knot sequences $k < i < n-k+2$ as the internal knots. See supplementary Fig. 5 for 6 B-spline basis functions of $k = 4$ between $[0,1]$ with knot sequences $[0,0,0,0,1/3,2/3,1,1,1,1]$. Given the basis functions we approximate an unknown function as $f(\omega) = \sum_{i=1}^{I} a_i B_{i,k}(\omega)$ where a_i are coefficients to be estimated, and $I = n-k+1$.

To capture the variation of FI over wavelengths, we assume that the respective emission spectrum for each fluorophore is smooth, and approximate them using B-splines as $\gamma_l(\omega) = \sum_{i=1}^{I_\gamma} a_{li}^{\gamma} B_{i,k_\gamma}(\omega)$ where a^γs are the coefficients with a given order k_γ for the l-th fluorophore. Notice that although the emission spectrum is assumed to be smooth, the observed spectrum can have jitter between consecutive channels due to different channel sensitivities. However, we ignore this in the formulation for simplicity.

D. Spectral Fluorescence Lifetime

The EP-TRFS system enables the collection of FL information across several channels, and although FL of a single fluorophore is expected to be constant over wavelengths [28, Chapter 3.4], this can vary in practice for several reasons. For example, if we consider a multi-exponential decay trace with two fluorophores (a and b) with single exponential decays and constant FLs (τ_a and τ_b) then:

$$f(\omega, t) = \gamma_a(\omega)\exp(-t/\tau_a) + \gamma_b(\omega)\exp(-t/\tau_b). \quad (7)$$

As the intensities, reflecting the individual emission spectrum of the fluorophores ($\gamma_a(\omega)$ and $\gamma_b(\omega)$) change across the wavelength, FLs when estimated by a single exponential will also vary across the channels.

To capture this change of FL across the wavelength range, we consider several parameterisation schemes. Particularly, while estimating a single exponential fit over the channels, we approximate the variation of FL over wavelengths using B-splines as $\tau_l(\omega) = \sum_{i=1}^{I_\tau} a^\tau_{li} B_{i,k_\tau}(\omega)$. However, while estimating a multiexponential fit over the channels, we approximate the variation of FL for each fluorophore as a linear function of wavelength as $\tau_l(\omega) = a^\tau_{l1}\omega + a^\tau_{l2}$ to reduce the computational complexity but to yet allow flexibility for accommodating model mismatch in terms of the number of fluorophores L.

E. Optimization

Our goal is to find coefficients a^γ's, a^τ's and biases b's by minimizing the loss function (Eq.6). Although $\gamma(\omega)$ and $\tau(\omega)$ are both positive, we do not use these constraints explicitly to simplify our optimization. We use a gradient descent algorithm to find the parameters. The first-order derivatives of the cost function with respect to the parameters are as follows.

$$\frac{\partial J}{\partial a^\gamma_{l'i'}} = -2\sum_{p=1}^{P}\sum_{m=1}^{M} o[p,m]\nu[p,m,l']B^\gamma_{i'}[p] \quad (8)$$

$$\frac{\partial J}{\partial a^\tau_{l'i'}} = -2\sum_{p=1}^{P}\sum_{m=1}^{M} o[p,m]\varsigma[p,m,l']\frac{\gamma_{l'}[p]}{\tau_{l'}[p]^2}B^\tau_{i'}[p] \quad (9)$$

$$\frac{\partial J}{\partial \hat{b}[p']} = -2\exp(b[p'])\sum_{m=1}^{M} o[p',m] \quad (10)$$

where

$$o[p,m] = y[p,m] - s[p,m] \quad (11)$$

$$\nu[p,m,l] = \exp(-m/\tau_l[p]) * (h[p])[m] \quad (12)$$

$$\varsigma[p,m,l] = (m\exp(-m/\tau_l[p])) * (h[p])[m] \quad (13)$$

and $\hat{b}[p'] = \exp(b[p'])$ is reparameterzied to make it positive. The computation of the gradient scales linearly with P, L, and I, and log-linearly with M.

F. Implementation

To compute the least squares solution using the Levenberg-Marquardt algorithm, SciPy optimize.least_squares is used [29]. We initialise the intensity coefficients a^γ_{li} as a random number generated uniformly between $(0, 1)$, such that the emission spectra is initialised as a constant across the channels. While for each l, we initialize FL coefficients a^τ_{li} as a random number generated uniformly between $(0, 4)$, such that FLs are constant over the channels but different for different fluorophores. We choose this range of initial FL values since it is in the expected FL range for the fluorophores used in our study, but this can easily be adapted. To find the B-splines basis functions, SciPy version 1.8.0 interpolate package, specifically BSpline basis_element is used [29].

G. Estimating uncertainty

We estimate the uncertainty of the estimated parameters using Cramèr-Rao bound, i.e., the covariance matrix of the estimated parameters $\mathbf{\Sigma}$ is approximated as the inverse information matrix. We estimate the information matrix as $\sigma_r^2\mathbf{H}$ where σ_r^2 is the variance of the residual, and $\mathbf{H}$ is the Hessian matrix of the cost function. Given the covariance matrix of the estimated parameters, we use the delta method to compute the error band around the estimated emission spectra and spectral FL [30]. For example, let $\mathbf{\Sigma}^\gamma_l$ be the covariance of the estimated intensity coefficients for the l-th fluorophore then $var(\gamma_l(\omega)) = \mathbf{B}^\top(\omega)\mathbf{\Sigma}^\gamma_l\mathbf{B}(\omega)$ where $\mathbf{B}(\omega) = [B_{1,k}(\omega), \ldots, B_{I,k}(\omega)]^\top$.

We estimate the Hessian matrix in closed form (Eq. 16-24). Notice that although we report confidence interval in the Figures and Tables presented in the result section, the respective confidence interval can be very narrow (see Fig. 1D).

H. Selecting hyper-parameters

MuFLE requires choosing hyperparameters for the splines fitting, i.e., the sequence of knots and the splines order for both FI and FL. Given the complexity and shape of both FI across the spectrum, and the spectral FL for the single exponential fit (i.e., $L = 1$), a cubic spline (4th order) is selected. To choose the two knot parameters, i.e., I_γ and I_τ, we use cross-validation. At random, 90 % of the time bins are selected as the training set, and the remaining 10 % are selected as the validation set. Cross validation was trialed over a grid for differing number of *internal* knots (i.e., $n - 2k + 1 = 1, 2, 3$) with random starting parameters (as previously stated in Section. II-F), and the best performing parameters were chosen (see supplementary Tables V, VI, and VII for cross-validation results of experiments performed in section IV and see supplementary Figs. 6, 7 and 8 for FI and FL fits achieved by different hyper-parameter choices).

I. Fit-free methods and Multi-channel comparison

To compare the results of MuFLE with other traditional fit-free approaches (in addition to using the least squares method across the individual channels (as stated in Section. II-A)), the CM [20], [31] and (RLD) [22] are implemented and applied across the individual channels. The CM is calculated as:

$$\psi = \frac{\sum_{m=1}^{M}((m-1)M + T/2)y_m}{\sum_{m=1}^{M} y_m} \quad (14)$$

where T represents time bin width. We report $\psi_S - \psi_{\text{IRF}}$ as the estimated CM, incorporating the CM from observed signal (ψ_S) and the CM of the IRF (ψ_{IRF}) [20].

For a single decay trace, FL is calculated using RLD method by splitting the decay into two windows, such that

$$\hat{y}_0 = \sum_{m=m_{\text{peak}}}^{(m_{\text{peak}}+M')/2} y_m \text{ and } \hat{y}_1 = \sum_{m=(m_{\text{peak}}+M')/2+1}^{M'} y_m \quad (15)$$

where m_{peak} is the time bin containing the highest photon count, and

$$M' = \begin{cases} M \text{ if } M - m_{\text{peak}} \text{ is even} \\ M-1 \text{ otherwise .} \end{cases}$$

It should be noted that the bin number containing the highest photon count varies across the spectrum. Each window has a width of $\hat{T}$ which is calculated by $\hat{T} = T\frac{M'-m_{\text{peak}}}{2}$. Therefore, FL [22] can be calculated as RLD $= \frac{\hat{T}}{\ln \hat{y}_0/\hat{y}_1}$.

To compare the results from the EP-TRFS device used in this study, to devices that calculate the spectral lifetime from a single channel with large spectral bandwidth, multiple channels were marginalised by summing the decays across the wavelength axis, in a 20.39 nm wavelength window. The window was selected such that the middle channel contained the peak emission. Following this 'smoothing' of the decay traces across the wavelength window, the lifetime of the smoothed decay trace was computed using single exponential least squares model, CM and RLD.

III. Data Collection

A. TRFS System

The EP-TRFS system used for data collection is comprised of a pulsed laser (laser diode head (LDH-P-C-485, PicoQuant, Germany) and laser driver (PDL 800-D, PicoQuant, Germany)) with an excitation wavelength of 485 nm and repetition rate of 20 MHz, coupling and collection optics (aspheric lenses of 11 mm focal length and numerical aperture (NA) of 0.3 for focusing and collimating (Thorlabs, UK) and dichroic beam splitter (FITC-LP01-Clinical-000, Semrock, US)), a bespoke, multi-mode optical fibre of 35 µm core diameter [32] to transport the excitation light and fluorescence emission to and from the sample (Fig. 1A), and a spectrometer (with a volume phase holographic grating (600 grooves / mm, Wasatch Photonics, US), acrhomatic lens doublets of 30 mm and 50 mm focal lengths (Thorlabs, UK) for collimating and focusing the light, respectively, and a bespoke CMOS SPAD line sensor, [33]). Light was delivered to the spectrometer with a fibre patch cable of 50 µm core diameter and a NA of 0.22 (M42L01, Thorlabs, UK). A wavelength range of 474.51 nm - 735.12 nm was covered by 512 pixels of the line sensor (i.e., channels), with 0.509 nm covered by a single channel. This was confirmed by detecting the spectrum of a fluorescent lamp with known emission spectrum. The CMOS SPAD line sensor was used in time-correlated single photon counting (TCSPC) mode with a temporal resolution of 50 ps, collecting data in 1200 time bins at each channel [33]. Histograms of photon arrival times at each channel were built using 1.5×10^6 exposures, each with a 5 µs exposure time (Fig. 1B). The highest photon count along a single channel of the histograms (i.e., the channel with peak intensity from the solution with strongest fluorescence emission) was 1 311 868, which relates to an average photon detection rate of 175 kHz for this channel. Notice that we crop the time bins (see section III-D). The optical power from the probe was 175 µW, which was measured by a power meter (PM100D with S130C, Thorlabs, UK).

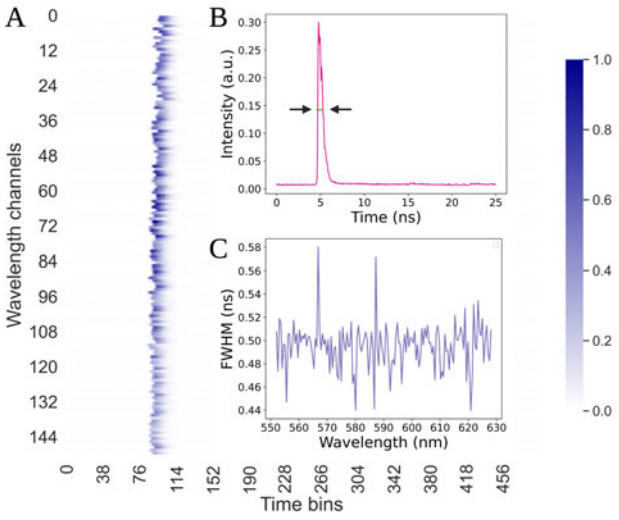

Fig. 2. **A)** The intensity heatmap of the measured instrument response function (IRF) across a selected number of wavelength channels and time bins. **B)** A specific single channel IRF with the full width half maximum (FWHM) (arrow) plotted. **C)** The FWHM of all the individual IRF measurements across the spectral window.

B. Instrument Response Function

A common method for measuring the IRF is to record the detector's response to the excitation laser, e.g., by shining the laser at the detector directly [34], under the assumption that the uncertainty of the timing electronics (i.e., jitter) is the major contributor to the IRF. However, to achieve this, the optical path involving the fiber optic used (which introduces a delay) to collect data from a sample is removed. Therefore, to characterise the IRF in our device, or timing uncertainty, associated with each channel using the same optical path used for data collection, quenched rose-bengal with an expected negligible lifetime of 16 ps was used [35]. The rose-bengal (ACROS Organic: 632-69-9) was measured at a concentration of 1 M in 6.03 M potassium iodide (Sigma-Aldrich: 30 315-100G), at a pH of 9.8 [35]. In the spectral domain the IRF captures the emission spectra of the rose-bengal while in the time domain it captures the IRF at each channel. The observed IRF also includes the dark counts, and the background baseline is assumed to be constant across the time bins. For each channel, we first subtract the dark counts and then normalize the IRF by the total photon count at each channel to remove the influence of the emission spectrum of the rose-bengal. The IRF observed in the EP-TRFS device is shown in Fig. 2. We observe that, first, the measured IRF decay traces are not aligned across the wavelength channels demonstrating a jitter in arrival times of photons across channels [33], and second, the full width half maximum (FWHM), i.e., the width of the impulse response

TABLE I
ABBREVIATIONS OF SAMPLES USED IN THIS PAPER.

Notation	Fluorophore
RHB-ME	Rhodamine B in Methanol
RHB-H2O	Rhodamine B in Water
FLUO	Fluorescein Sodium in PBS
RHB-ME-FLUO	Rhodamine B in Methanol and Fluorescein mixed
RHB-H2O-FLUO	Rhodamine B in Water and Fluorescein mixed

TABLE II
A SUMMARY OF REPORTED LIFETIME VALUES IN THE LITERATURE.

Fluorophore	Expected Lifetime (ns)
RHB-ME	2.15 ns [36], 2.41 ns [37], 2.50 ns [38]
RHB-H2O	1.35 ns [39], 1.52 ns [38], 1.74 ns [36]
FLUO	3.60 ns [40], 4.00 ns [41], 4.11 ns [42]

at half of its intensity, varies across channels for this CMOS SPAD line sensor.

C. Samples

Two fluorophores, Rhodamine B (Sigma-Aldrich: 102 406 918) and Fluorescein Sodium (Sigma-Aldrich: F6377-100G), were analysed in homogeneous and mixed samples. Rhodamine B was prepared at a concentration of 10 µM in methanol (ACROS Organics: 167 835 000) (RHB-ME) and in (double-distilled) water (RHB-H2O), and Fluorescein Sodium was prepared at a concentration of 1 µM in phosphate-buffered saline (PBS) (FLUO) (Table I). Additionally mixed samples of Fluorescein Sodium in PBS at 0.5 µM with Rhodamine B at a concentration of 5 µM in methanol (RHB-ME-FLUO) and in water (RHB-H2O-FLUO) were prepared. Three replicates were taken of all samples (see supplementary Fig. 10) but we presented the results from the first replicate only since they agree with each other. All samples were measured at room temperature, with the Rhodamine B in a pH of 6 and Fluorescein Sodium in a pH of 7.4. The expected lifetime of the samples from the literature is presented in Table II. The samples were analysed on a Synergy H1 Hybrid plate reader for spectral reference. In addition, the bias terms of all samples were computed using MUFLE and we observe them to fall into a similar range and trend over different measurements (see supplementary Fig. 9).

D. Data Pre-processing

The time span and spectral range over which the fluorescence emission was observed were cropped in the time domain to only include a region with the complete rise and fall of the decay traces. To achieve this the first 710 bins not containing any fluorescence signal were removed. Thus, the timing axis was adjusted with time bins starting from 1 at bin 711. Each time bin was then multiplied with the time-bin resolution to estimate the timepoint assigned to the bins. The timebin resolution was measured separately. Additionally, in the spectral domain, channels with intensities that were less than 20 % of the maximum intensity were excluded from the analysis to reduce noise level. A further spectral limitation in the data restricts the wavelength range to above 520 nm as the EP-TRFS device has a bandpass filter removing the laser line below this range. For samples that contained Rhodamine B, the spectral channels between 552.03 nm - 628.02 nm were analysed, decided by the 20 % rule and the bandpass filter. For samples that contained FLUO alone, the spectral channels between 519.39 nm - 620.88 nm were analysed. These wavelength ranges are in good agreement with the expected fluorescence spectra from the fluorophores [37]. In addition, the data was normalized by the maximum intensity.

IV. RESULTS

We compare the estimated emission spectra of the three reference samples, RHB-ME, RHB-H2O and FLUO against the emission peaks recorded using a plate reader (Table. VIII). We compare the lifetimes against their expected values in the literature (Table II) and from other methods (section IV-B). In addition, we show the un-mixing potential of MUFLE in separating two fluorophores in RHB-ME-FLUO and RHB-H2O-FLUO (section IV-C).

A. Accuracy of the estimated emission spectrum

Fig. 3A, B and C show the difference in the single channel intensity estimates, using the least squares method, to MUFLE, as well as the spectral emission recorded from a Synergy H1 Hybrid plate reader for all three individual solutions, i.e., RHB-H2O, RHB-ME and FLUO, respectively. For single channel estimates, a large variation can be observed in the estimated intensities even for neighbouring channels. This can be attributed to individual channel sensitivities and their respective SPAD noise levels [33]. MUFLE, on the other hand, accounts for this 'jitter' and provides a smooth estimate of the emission spectrum. We also observe that the estimated emission spectrum using MUFLE follows a similar trend to the emission spectrum when recorded from a plate reader. However, their dynamic range and peak positions differ from each other. Table VIII shows the peak locations from these measurements, and we observe a mean red shift deviation of ∼2-4 nm. This may occur due to the difference in readout characteristic (e.g. resolution, gain differences and differences in emission readout methodology) of the plate reader and EP-TRFS, however, the differences are all within an agreeable range.

B. Accuracy of the estimated fluorescence lifetime values

Fig. 3 D, E and F show the spectral FLs of the three individual fluorophores estimated using MUFLE, compared to the expected values from the literature. We observe that all three FLs fall within their expected range (Table II). FLs in the literature are not captured across such a broad spectral range, and therefore, we compared the MUFLE fitted FLs with the FLs estimated from the individual channels using the least squares method. We observe that MUFLE estimates agree with the single channel estimates well and provide a smooth approximation similar to its FI counterpart. The FLs from MUFLE were also compared to the RLD and CM methods on individual (narrow) channels (see supplementary Fig. 11). We observe that MUFLE exhibits less channel-to-channel variation.

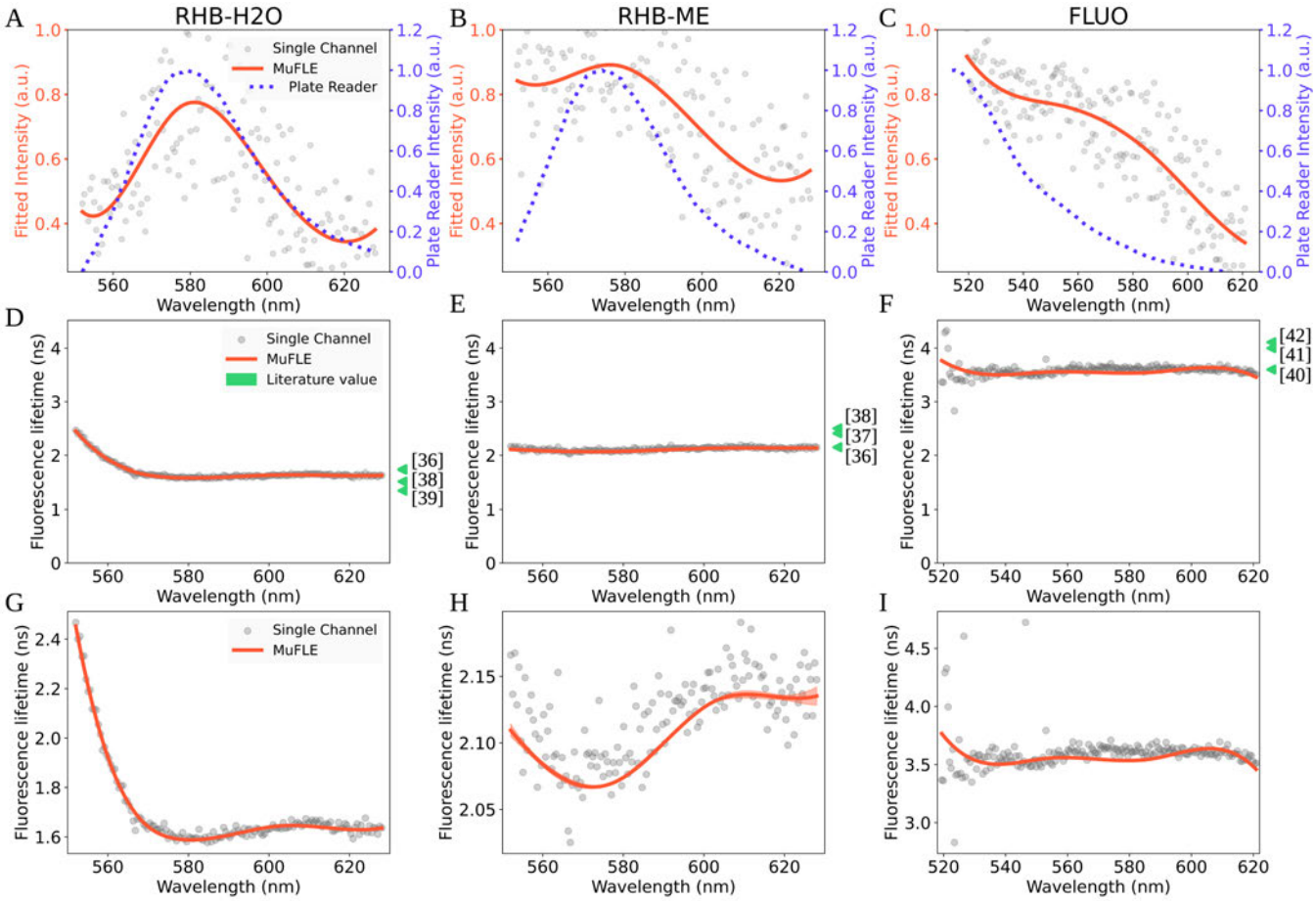

Fig. 3. Single exponential MuFLE model showing the fluorescence emission and spectral fluorescence lifetime of reference fluorophores. The intensity plots across a wavelength spectrum of 552.03 nm - 628.02 nm for both RHB-H2O **A)** and RHB-ME **B)** and for FLUO **C)** across a wavelength spectrum of 519.39 nm - 620.88 nm of MuFLE (orange) are compared to both the single channel fit (grey dots) and the emission of the fluorophore following its measurement on a plate reader (purple). The spectral fluorescence lifetime of RHB-H2O **D)**, RHB-ME **E)**, and FLUO **F)** estimated using MuFLE (orange) are compared to the lifetime results of the individual channels estimated using a least squares method (grey dots). The fluorescence lifetime values reported in the literature are also shown (green arrows). **G)**, **H)** and **I)** show a close up of the fit of RHB-H2O, RHB-ME and FLUO respectively, of the spectral fluorescence lifetime of MuFLE (orange) compared to the lifetime results of the individual channels using the least squares method (grey dots).

TABLE III
LIFETIME COMPARISON OF THE MARGINALISED CHANNEL USING DIFFERENT LIFETIME METHODS.

	RHB-H2O	RHB-ME	FLUO
RLD	2.12 ns	1.70 ns	2.10 ns
CM	2.57 ns	2.41 ns	3.41 ns
LS	1.61 ns	2.09 ns	3.59 ns

Finally, we compared the FLs with the (broad) multichannel estimates. We observe that the MuFLE estimates agree with the LS fit from marginalized histogram counts well but differ from the CM and RLD estimates (Table III). This agrees with our overall observation that LS provides more stable estimates than alternative fit-free methods.

C. MuFLE un-mixing potential

Fig. 4 shows the estimated FI and FL from mixed samples RHB-H2O-FLUO and RHB-ME-FLUO, respectively. We observe that no prevailing feature of either fluorophore was captured in both cases for MuFLE fitted with single exponential, i.e., $L = 1$ (Fig. 4 A-D). Un-mixing the fluorophores using double exponential decay is presented in Fig. 4 E and F for RHB-H2O-FLUO and G and H for RHB-ME-FLUO where we use a linear spectral FL trend to allow flexibility in fitting. The two estimated emission spectra and corresponding spectral FLs resemble the fluorescence characteristics of the respective homogeneous samples in Fig. 3 well. In addition, they match the spectral shapes of the individual fluorophores when measured on the plate reader. The longer FL in both cases can be attributed to the longer FL of the FLUO compared to the shorter FLs of Rhodamine B, dominant at longer wavelengths (Fig. 4 F and H). However, in both cases, the second shortened lifetime component corresponding to the Rhodamine B signal does not exactly reflect the lifetimes recorded from these fluorophores when measured in a homogeneous solution e.g., in RHB-ME 2.10 ns versus 1.39 ns. These values are shorter

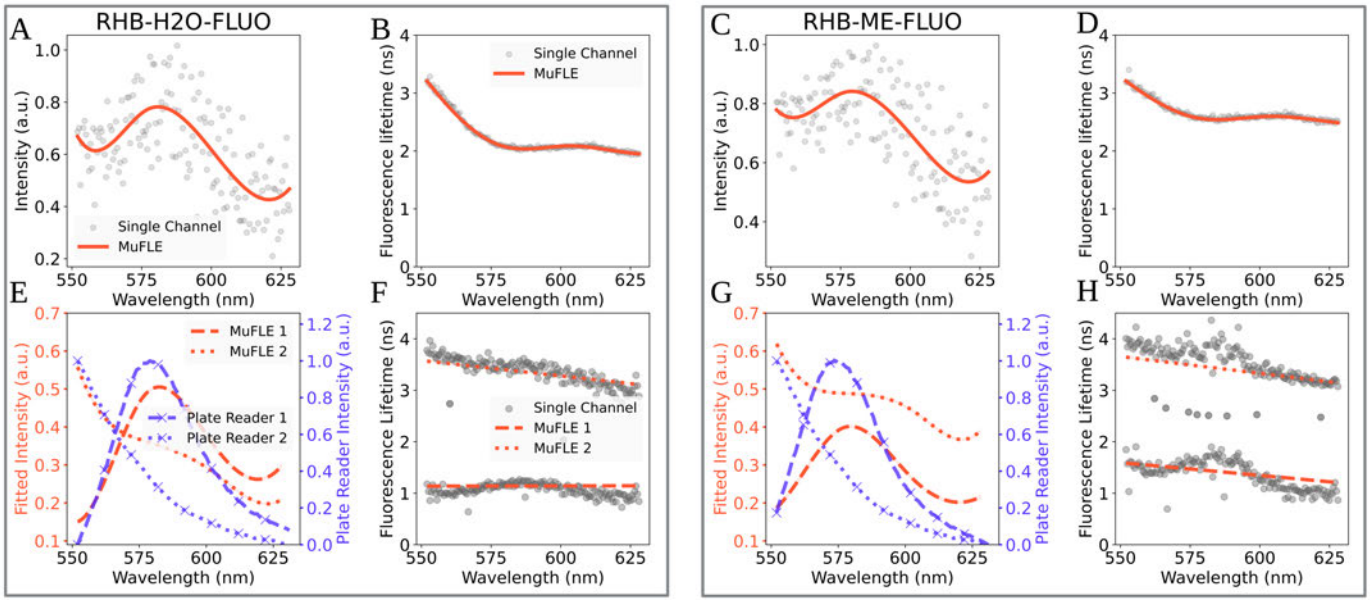

Fig. 4. MuFLE model showing the fluorescence emission and fluorescence lifetime of mixed reference fluorophores, highlighting the applicability of MuFLE un-mixing two mixed samples. **A)** and **C)** show the fluorescence intensity from a single exponential MuFLE model of RhB-H2O-Fluo and RhB-Me-Fluo (orange) compared to the individual channel estimates using the least squares method (grey dots) across a wavelength channel of 519.39 nm - 620.88 nm. **B)** and **D)** show the fluorescence lifetime from a single exponential MuFLE model of RhB-H2O-Fluo and RhB-Me-Fluo (orange) compared to the individual channel estimates using the least squares method (grey dots). **E)** and **G)** show the fluorescence intensity from a double exponential MuFLE model of RhB-H2O-Fluo and RhB-Me-Fluo respectively (orange), compared to the emission of the individual fluorophores following their measurement from a plate reader (purple, with x markers). The dotted lines compare MuFLE's un-mix of Fluo (orange) with the plate reader emission measurement (purple with x markers). The dashed lines compare MuFLE's un-mix of RhB-H2O (E) (orange) and of RhB-Me (G) (orange) with the plate reader emission measurement (purple with x markers). **F)** and **H)** show the fluorescence lifetime from a double exponential MuFLE model of RhB-H2O-Fluo and RhB-Me-Fluo (orange) compared to the individual channel estimates of a double exponential least squares model (grey dots). The dotted lines show MuFLE lifetime value that best matches both the intensity and lifetime value of Fluo. The dashed lines show MuFLE lifetime value that best matches both the intensity and lifetime value of RhB-H2O (F) and RhB-Me (H) alone.

than expected, and we anticipate this to be true as the solvents are also mixed, which would alter the lifetime values (e.g., in all cases, the Rhodamine B solvent is mixed in Fluorescein Sodium phosphate buffer saline solvent, possibly altering the protonation as well as the aqueous nature of the solution) [40]–[43].

V. Discussion

Multi-channel EP-TRFS devices, such as the one used in this study, produce high resolution TRES that requires tailored techniques to fully interrogate the spectral profiles of the underlying fluorophores. We present MuFLE, a novel method that utilises the entire TRES histogram collected from these devices, simultaneously analysing the FIs and FLs of individual fluorophores in a sample over all wavelength channels. This is different from standard approaches that estimate either the wavelength dimension (emission spectrum) or the time dimension (exponential decay trace) exclusively.

We show that MuFLE is able to estimate the underlying FIs and FLs and increases the total precision of both the intensity spectrum and lifetime across the wavelength, decreasing the intra-channel variation. Using Rhodamine B and Fluorescein Sodium as reference samples, we show that MuFLE captures the underlying emission spectrum and lifetimes reliably, where the emission spectrum resembles the emission spectrum collected using a plate reader and the lifetime value is in the range of values reported in the literature.

To accurately characterise fluorescence from complex heterogeneous samples, for example tissue fluorescence, devices that allow a full spectral and temporal interrogation of the fluorescence profile are preferred. These, in turn, require novel devices and methods that fully capture this information. Through the use of EP-TRFS and MuFLE, both the emission spectrum and the spectral fluorescence lifetime becomes accessible, thus moving away from individual channel assessment and into a greater understanding of the fluorescence components of the heterogeneous samples. Using two mixed solutions, we show that MuFLE can reliably un-mix two fluorophores to provide their individual fluoreschence lifetimes and intensities.

While MuFLE shows promise, the method can be improved in several ways. One of the directions is to include the photon sensitivities of the individual spectral detectors in the computational model. The variation of photon sensitivities leads to intensity variation in the consecutive channels in the observed spectrum, and that in turn, leads to model mismatch since MuFLE assumes the estimated emission spectrum to be smooth. We believe that this modification will further improve the performance of MuFLE in un-mixing fluorophores in a heterogeneous sample. The other direction is to improve the convergence and speed of the optimization when un-mixing multiple fluorophores for noisy measurements and

in presence of device artifacts. We also show that the true environment of individual fluorophores in a mixed solution can be difficult to assess and therefore further experimentation is needed to establish adequate individual *ground-truth* lifetime values of fluorophores in a mixed sample, and to ascertain the performance of MUFLE in un-mixing.

In summary, as MUFLE utilises information within the spectrum, the accuracy of fluorescence lifetime estimates at each channel are increased, and as MUFLE simultaneously estimates the spectral and temporal components of the fluorescent sample individual fluorophores can be identified with greater confidence, increasing the potential to investigate more fluorophores. This is particularly relevant for *in vivo* applications since intrinsic tissue fluorescence is expected to be highly complex with several overlapping fluorophores [3]. The emission of many endogenous fluorophores have been well characterised (i.e. FAD, riboflavin etc), and this can facilitate unmixing [5].

REFERENCES

[1] J R Lakowicz. *Principles of fluorescence spectroscopy*. SSBM, 2013.

[2] Nirmala Ramanujam. Fluorescence spectroscopy of neoplastic and non-neoplastic tissues. *Neoplasia*, 2(1-2):89–117, 2000.

[3] M Y Berezin and S Achilefu. Fluorescence lifetime measurements and biological imaging. *Chem. Rev.*, 110(5):2641–2684, 2010.

[4] C Würth, M Grabolle, J Pauli, et al. Relative and absolute determination of fluorescence quantum yields of transparent samples. *Nat. Protoc*, 8(8):1535–1550, 2013.

[5] L Marcu. Fluorescence Lifetime Techniques in Medical Applications. *Ann Biomed Eng* ., 40(2):304–331, February 2012.

[6] M Marsden, T Fukazawa, Y Deng, et al. Flimbrush: dynamic visualization of intraoperative free-hand fiber-based fluorescence lifetime imaging. *Biomed. Opt. Express*, 11(9):5166–5180, 2020.

[7] A Alfonso-Garcia, J Bec, B Weyers, et al. Mesoscopic fluorescence lifetime imaging: Fundamental principles, clinical applications and future directions. *J. Biophotonics*, 14(6):e202000472, 2021.

[8] L Marcu, R C Thompson, S Garde, et al. Time-resolved fluorescence spectroscopy of human brain tumors. In *Optical Biopsy IV*, volume 4613, pages 183–187. International Society for Optics and Photonics, 2002.

[9] Z Nie, S A Yeh, M LePalud, et al. Optical biopsy of the upper gi tract using fluorescence lifetime and spectra. *Front. Physiol.*, 11:339, 2020.

[10] Q Wang, M Vallejo, and J Hopgood. Fluorescence lifetime endomicroscopic image-based ex-vivo human lung cancer differentiation using machine learning. *TechRxiv*, 2020.

[11] J A Kim, D J Wales, and G Yang. Optical spectroscopy for in vivo medical diagnosis—a review of the state of the art and future perspectives. *Prog. biomed. eng*, 2(4):042001, 2020.

[12] S Fernandes, G Williams, E Williams, et al. Solitary pulmonary nodule imaging approaches and the role of optical fibre-based technologies. *Eur. Respir. J.*, 57(3), 2021.

[13] R Datta, T M. Heaster, J T. Sharick, et al. Fluorescence lifetime imaging microscopy: fundamentals and advances in instrumentation, analysis, and applications. *J. Biomed. Opt*, 25(07):1, May 2020.

[14] D Ma, J Bec, D Gorpas, et al. Technique for real-time tissue characterization based on scanning multispectral fluorescence lifetime spectroscopy (ms-trfs). *J. Biomed. Opt.*, 6(3):987–1002, 2015.

[15] Y Sun, Y Sun, D Stephens, et al. Dynamic tissue analysis using time- and wavelength-resolved fluorescence spectroscopy for atherosclerosis diagnosis. *Opt. Express*, 19(5):3890–3901, 2011.

[16] C Bruschini, H Homulle, I M Antolovic, et al. Single-photon avalanche diode imagers in biophotonics: review and outlook. *Light Sci. Appl.*, 8(1):1–28, 2019.

[17] A Kufcsák, A Erdogan, R Walker, and et al. Time-resolved spectroscopy at 19,000 lines per second using a cmos spad line array enables advanced biophotonics applications. *Opt. Express*, 25(10):11103–11123, 2017.

[18] G OS Williams, E Williams, N Finlayson, et al. Full spectrum fluorescence lifetime imaging with 0.5 nm spectral and 50 ps temporal resolution. *Nat. Commun.*, 12(1):1–9, 2021.

[19] J L Lagarto, F Villa, S Tisa, et al. Real-time multispectral fluorescence lifetime imaging using single photon avalanche diode arrays. *Sci. Rep.*, 10(1):1–10, 2020.

[20] S P Poland, A T Erdogan, N Krstajić, et al. New high-speed centre of mass method incorporating background subtraction for accurate determination of fluorescence lifetime. *Select highlightSelect highlightOptics express*, 24(7):6899–6915, 2016.

[21] J Xu, J Qiao, K Nie, et al. Calibration method for the center of mass method to enlarge the solvable range of fluorescence lifetime. *JOSA A*, 33(10):1961–1969, 2016.

[22] R M Ballew and JN Demas. An error analysis of the rapid lifetime determination method for the evaluation of single exponential decays. *Anal. Chem.*, 61(1):30–33, 1989.

[23] M Wang, F Tang, X Pan, et al. Rapid diagnosis and intraoperative margin assessment of human lung cancer with fluorescence lifetime imaging microscopy. *BBA clinical*, 8:7–13, 2017.

[24] J Kim and J Seok. Statistical properties of amplitude and decay parameter estimators for fluorescence lifetime imaging. *Opt. Express*, 21(5):6061–6075, 2013.

[25] A S Dabir, C Trivedi, Y Ryu, et al. Fully automated deconvolution method for on-line analysis of time-resolved fluorescence spectroscopy data based on an iterative laguerre expansion technique. *J. Biomed. Opt.*, 14(2):024030, 2009.

[26] N Periasamy. Analysis of fluorescence decay by the nonlinear least squares method. *Biophys. J.*, 54(5):961–967, 1988.

[27] M G Cox. The numerical evaluation of b-splines. *IMA J Appl Math*, 10(2):134–149, 1972.

[28] B Valeur and M N Berberan-Santos. *Molecular fluorescence: principles and applications*. John Wiley & Sons, 2012.

[29] P Virtanen, R Gommers, T E. Oliphant, et al. SciPy 1.0: Fundamental Algorithms for Scientific Computing in Python. *Nat. Methods*, 17:261–272, 2020.

[30] G W Oehlert. A note on the delta method. *Am. Stat*, 46(1):27–29, 1992.

[31] D U Li, D Tyndall, R Walker, et al. Video-rate fluorescence lifetime imaging camera with cmos single-photon avalanche diode arrays and high-speed imaging algorithm. *J. Biomed. Opt.*, 16(9):096012, 2011.

[32] H Wood, K Ehrlich, S Yerolatsitis, et al. Tri-mode optical biopsy probe with fluorescence endomicroscopy, raman spectroscopy, and time-resolved fluorescence spectroscopy. *Journal of biophotonics*, page e202200141, 2022.

[33] A T Erdogan, R Walker, N Finlayson, et al. A cmos spad line sensor with per-pixel histogramming tdc for time-resolved multispectral imaging. *IEEE J. Solid-State Circuits*, 54(6):1705–1719, 2019.

[34] R Luchowski, Z Gryczynski, P Sarkar, J Borejdo, M Szabelski, P Kapusta, and I Gryczynski. Instrument response standard in time-resolved fluorescence. *Rev. Sci. Instrum*, 80(3):033109, 2009.

[35] M Szabelski, R Luchowski, Z Gryczynski, et al. Evaluation of instrument response functions for lifetime imaging detectors using quenched rose bengal solutions. *Chem. Phys. Lett.*, 471(1-3):153–159, 2009.

[36] Noël Boens, Wenwu Qin, Nikola Basarić, et al. Fluorescence lifetime standards for time and frequency domain fluorescence spectroscopy. *Analytical chemistry*, 79(5):2137–2149, 2007.

[37] A S Kristoffersen, S R Erga, B Hamre, et al. Testing fluorescence lifetime standards using two-photon excitation and time-domain instrumentation: rhodamine b, coumarin 6 and lucifer yellow. *J. Fluoresc.*, 24(4):1015–1024, 2014.

[38] D Magde, E Rojas, and P G Seybold. Solvent dependence of the fluorescence lifetimes of xanthene dyes. *Photochem. Photobiol.*, 70(5):737–744, 1999.

[39] F López Arbeloa, T López Arbeloa, MJ Tapia Estévez, and I López Arbeloa. Photophysics of rhodamines: molecular structure and solvent effects. *J. Phys. Chem. A*, 95(6):2203–2208, 1991.

[40] P G Seybold, M Gouterman, and J Callis. Calorimetric, photometric and lifetime determinations of fluorescence yields of fluorescein dyes. *Photochem. Photobiol.*, 9(3):229–242, 1969.

[41] M Hammer, D Schweitzer, S Richter, et al. Sodium fluorescein as a retinal ph indicator? *Physiol*, 26(4):N9, 2005.

[42] Xian-Fu Zhang, Jianlong Zhang, and Limin Liu. Fluorescence properties of twenty fluorescein derivatives: lifetime, quantum yield, absorption and emission spectra. *Journal of fluorescence*, 24(3):819–826, 2014.

[43] SJ Strickler and R A Berg. Relationship between absorption intensity and fluorescence lifetime of molecules. *Chem. Phys.*, 37(4):814–822, 1962.

Supplementary Information

TABLE IV
THE TABLE DESCRIBES NOTATIONS USED IN THIS PAPER.

Notation	Meaning
L	Number of fluorophore components
M	Number of histogram time bins
P	Number of histogram wavelength channels
t_m	Right edge of the m-th time bin
T	Time bin resolution
l	Index for fluorophore components $\in \{1, \ldots, L\}$
m	Index for histogram time bins $\in \{1, \ldots, M\}$
p	Index for histogram wavelength channels $\in \{1, \ldots, P\}$
γ_l	Unnormalized intensity for l-th component
τ_l	Fluorescence Lifetime of exponential decay for l-th component

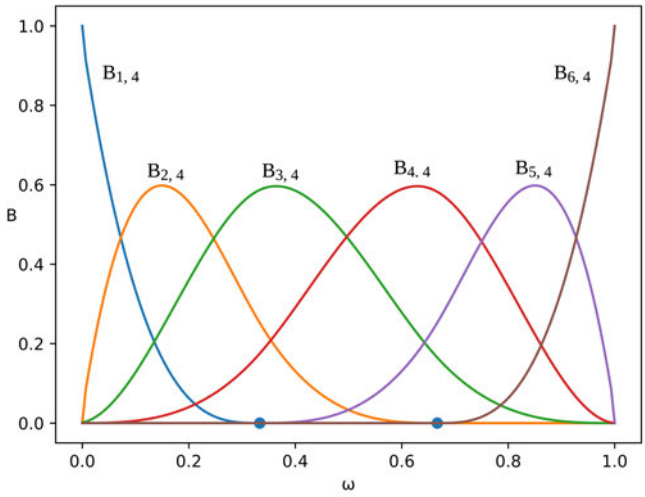

Fig. 5. Examples of the B-splines basis functions labeled B with equidistant internal knots (blue dots) at 0.333 and 0.666 and an order of 4.

VI. Second order derivatives

$$\frac{\partial^2 J}{\partial a^{\gamma}_{l''i''}\partial a^{\gamma}_{l'i'}} = 2\sum_{p=1}^{P}\sum_{m=1}^{M}\nu[p,m,l'']B^{\gamma}_{i''}[p]\nu[p,m,l']B^{\gamma}_{i'}[p] \tag{16}$$

$$\frac{\partial^2 J}{\partial a^{\tau}_{l''i''}\partial a^{\gamma}_{l'i'}} = 2\sum_{p=1}^{P}\sum_{m=1}^{M}\varsigma[p,m,l'']\frac{\gamma_{l''}[p]}{\tau_{l''}[p]^2}B^{\tau}_{i''}[p]\nu[p,m,l']B^{\gamma}_{i'}[p] \quad l\neq l' \tag{17}$$

$$\frac{\partial^2 J}{\partial a^{\tau}_{l''i''}\partial a^{\gamma}_{l''i'}} = 2\sum_{p=1}^{P}\sum_{m=1}^{M}\varsigma[p,m,l'']\frac{\gamma_{l''}[p]}{\tau_{l''}[p]^2}B^{\tau}_{i''}[p]\nu[p,m,l'']B^{\gamma}_{i'}[p] - 2\sum_{p=1}^{P}\sum_{m=1}^{M}o[p,m]\varsigma[p,m,l'']\frac{B^{\tau}_{i''}[p]}{\tau_{l''}[p]^2}B^{\gamma}_{i'}[p] \quad l=l' \tag{18}$$

$$\frac{\partial J}{\partial a^{\tau}_{l''i''}\partial a^{\tau}_{l'i'}} = 2\sum_{p=1}^{P}\sum_{m=1}^{M}\varsigma[p,m,l'']\frac{\gamma_{l''}[p]}{\tau_{l''}[p]^2}B^{\tau}_{i''}[p]\varsigma[p,m,l']\frac{\gamma_{l'}[p]}{\tau_{l'}[p]^2}B^{\tau}_{i'}[p] \quad l''\neq l' \tag{19}$$

$$\begin{aligned}\frac{\partial J}{\partial a^{\tau}_{l''i''}\partial a^{\tau}_{l''i'}} &= 2\sum_{p=1}^{P}\sum_{m=1}^{M}\left[\varsigma[p,m,l'']\frac{\gamma_{l''}[p]}{\tau_{l''}[p]^2}\right]^2 B^{\tau}_{i''}[p]B^{\tau}_{i'}[p]\\ &\quad - 2\sum_{p=1}^{P}\sum_{m=1}^{M}\left[o[p,m]\varrho[p,m,l'']\frac{B^{\tau}_{i''}[p]}{\tau_{l''}[p]^2}\frac{1}{\tau_{l''}[p]^2} - o[p,m]\varsigma[p,m,l'']\frac{2B^{\tau}_{i''}[p]}{\tau_{l''}[p]^3}\right]\gamma_{l''}[p]B^{\tau}_{i'}[p] \quad l''=l'\end{aligned} \tag{20}$$

$$\frac{\partial J}{\partial b[p']\partial b[p'']} = -2\exp(b[p'])\sum_{m}o[p',m] + 2\exp(b[p'])\exp(b[p'])) \quad p'=p'' \tag{21}$$

$$\frac{\partial J}{\partial b[p']\partial b[p'']} = 0 \quad p'\neq p'' \tag{22}$$

$$\frac{\partial^2 J}{\partial a^{\gamma}_{l'i'}\partial b[p']} = 2\exp(b[p'])\sum_{m=1}^{M}\nu[p',m,l']B^{\gamma}_{i'}[p'] \tag{23}$$

$$\frac{\partial J}{\partial a^{\tau}_{l'i'}\partial b[p']} = 2\exp(b[p'])\sum_{m=1}^{M}\varsigma[p',m,l']\frac{\gamma_{l'}[p']}{\tau_{l'}[p']^2}B^{\tau}_{i'}[p']. \tag{24}$$

where

$$\nu[p,m,l] = \exp(-m/\tau_l[p]) * (h[p])[m] \tag{25}$$

$$\varsigma[p,m,l] = (m\exp(-m/\tau_l[p])) * (h[p])[m] \tag{26}$$

$$\varrho[p,m,l] = \left(m^2\exp(-m/\tau_l[p])\right) * (h[p])[m] \tag{27}$$

TABLE V
THE CROSS VALIDATION RESULTS FOR DIFFERING NUMBER OF INTERNAL KNOTS.

Fluorophore	Intensity Parameter Internal Knot	Lifetime Parameter Internal Knot	Cost Function
RHB-H2O	3	1	2.39
	2	1	2.45
	1	1	2.66
	3	2	2.39
	2	2	2.45
	1	2	2.56
	3	**3**	**2.39**
	2	3	2.42
	1	3	2.53
RHB-ME	3	1	2.54
	2	1	2.55
	1	1	2.59
	3	2	2.54
	2	2	2.55
	1	2	2.57
	3	**3**	**2.54**
	2	3	2.55
	1	3	2.57
FLUO	3	1	3.81
	2	1	3.83
	1	1	3.87
	3	2	3.81
	2	2	3.83
	1	2	3.84
	3	**3**	**3.81**
	2	3	3.82
	1	3	3.83

TABLE VI
THE CROSS VALIDATION RESULTS FOR DIFFERING NUMBER OF INTERNAL KNOTS, OF A SINGLE EXPONENTIAL MODEL OF THE MIXED SOLUTIONS.

Fluorophore	Intensity Parameter Internal Knot	Lifetime Parameter Internal Knot	Cost Function
RHB-H2O-FLUO	3	1	2.54
	2	1	2.52
	1	1	2.74
	3	2	2.51
	2	2	2.55
	1	2	2.67
	3	**3**	**2.51**
	2	3	2.55
	1	3	2.67
RHB-ME-FLUO	3	1	2.42
	2	1	2.43
	1	1	2.52
	3	2	2.42
	2	2	2.43
	1	2	2.48
	3	**3**	**2.42**
	2	3	2.42
	1	3	2.48

TABLE VII
THE CROSS VALIDATION RESULTS FOR DIFFERING NUMBER OF INTERNAL KNOTS, OF A DOUBLE EXPONENTIAL MODEL OF THE MIXED SOLUTIONS.

Fluorophore	Intensity Parameter Internal Knot	Cost Function
RHB-H2O-FLUO	**3**	**3.37**
	2	3.38
RHB-ME-FLUO	**3**	**3.37**
	2	3.39

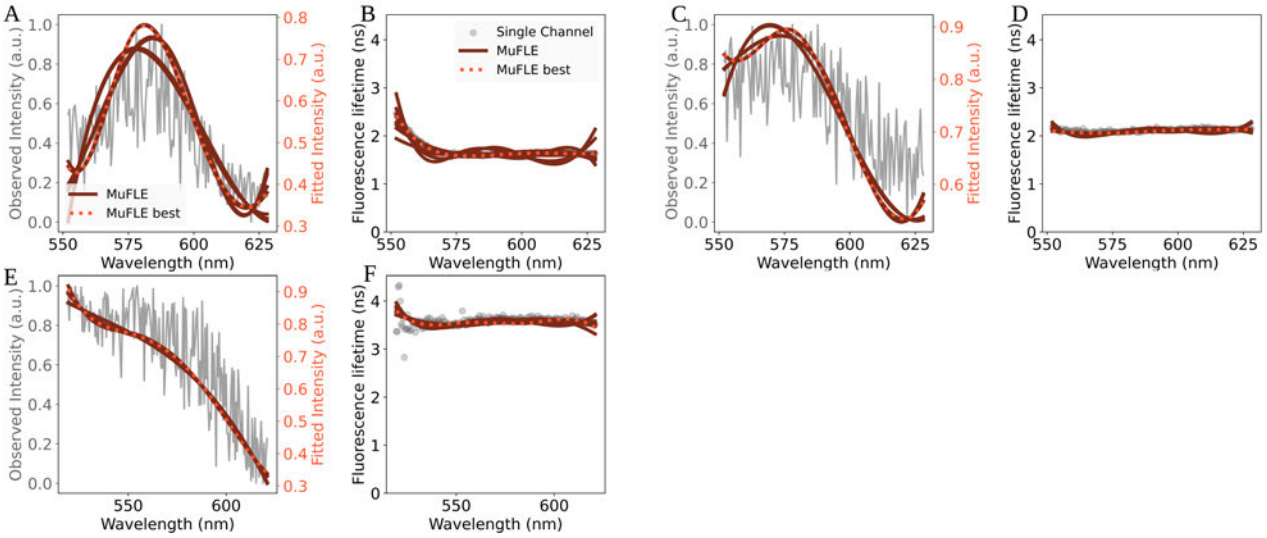

Fig. 6. Hold-out cross validation results of a single exponential MuFLE model on the individual fluorophores, varying different internal knots over a grid. **A)**, **C)** and **E)** show the fluorescence intensity plots of RhB-H2O, RhB-Me and Fluo respectively of MuFLE (orange) compared to the normalised observed intensity (grey lines). A and C show the results across a wavelength spectrum of 552.03 nm-620.88 nm and E shows results across a wavelength spectrum of 519.39 nm-620.88 nm. The dark orange MuFLE show the fluorescence intensity from different internal knot values, and the dotted orange MuFLE shows the fluorescence intensity from the knot values which returned the lowest cost function. **B)**, **D)** and **F)** show the lifetime plots of RhB-H2O, RhB-Me and Fluo respectively of MuFLE (orange) compared to the fluorescence lifetime results of the individual channels estimated using a least squares method (grey dots). B and D show the results across a wavelength spectrum of 552.03 nm-620.88 nm and F shows results across a wavelength spectrum of 519.39 nm-620.88 nm. The dark orange MuFLE show the fluorescence lifetime from different internal knot values, and the dotted orange MuFLE shows the fluorescence lifetime from the knot values which returned the lowest cost function.

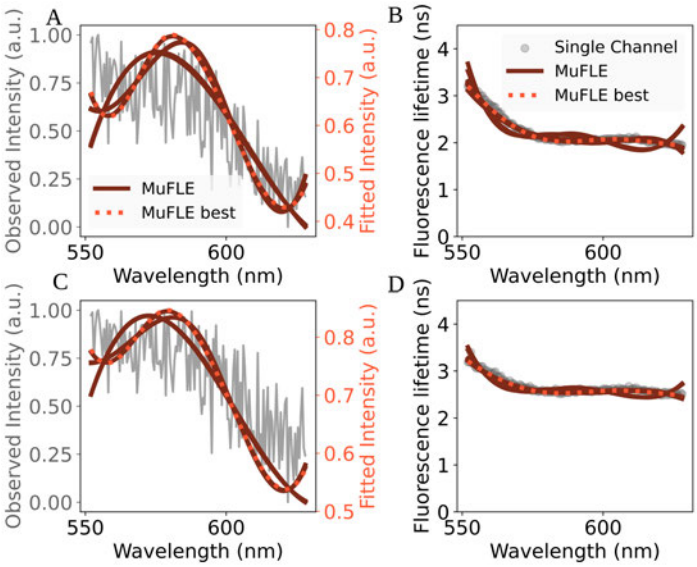

Fig. 7. Hold-out cross validation results of a single exponential MuFLE model on samples that contain a mixture of two fluorophores, varying different internal knots over a grid. **A)** and **C)** show the fluorescence intensity plots of RhB-H2O-Fluo and RhB-Me-Fluo respectively of MuFLE (orange) compared to the normalised observed intensity (grey lines) across a wavelength spectrum of 552.03 nm-620.88 nm. The dark orange MuFLE show the fluorescence intensity from different internal knot values, and the dotted orange MuFLE shows the fluorescence intensity from the knot values which returned the lowest cost function. **B)** and **D)** show the lifetime plots of RhB-H2O-Fluo and RhB-Me-Fluo respectively of MuFLE (orange) compared to the fluorescence lifetime results of the individual channels estimated using a least squares method (grey dots), across a wavelength spectrum of 552.03 nm-620.88 nm. The dark orange MuFLE show the fluorescence lifetime from different internal knot values, and the dotted orange MuFLE shows the fluorescence lifetime from the knot values which returned the lowest cost function.

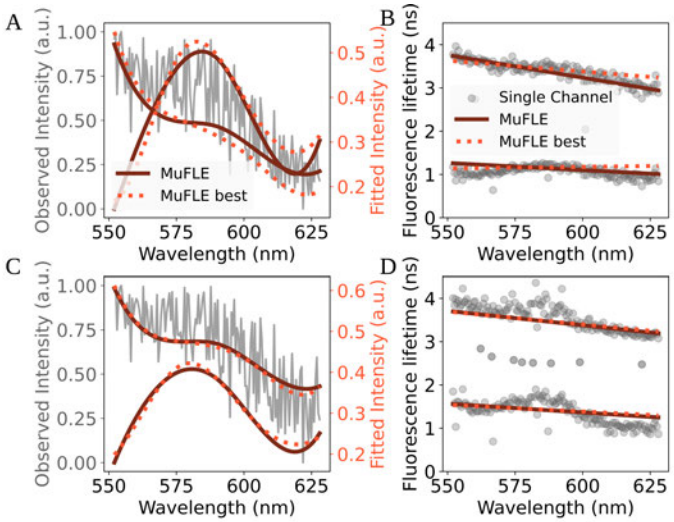

Fig. 8. Hold-out cross validation results of a double exponential MuFLE model on samples that contain a mixture of two fluorophores, varying different internal knots over a grid. **A)** and **C)** show the fluorescence intensity plots of RhB-H2O-Fluo and RhB-Me-Fluo respectively of MuFLE (orange) compared to the normalised observed intensity (grey lines) across a wavelength spectrum of 552.03 nm-620.88 nm. The dark orange MuFLE show the fluorescence intensity from different internal knot values, and the dotted orange MuFLE shows the fluorescence intensity from the knot values which returned the lowest cost function. **B)** and **D)** show the lifetime plots of RhB-H2O-Fluo and RhB-Me-Fluo respectively of MuFLE (orange) compared to the fluorescence lifetime results of the individual channels estimated using a double exponential least squares method (grey dots), across a wavelength spectrum of 552.03 nm-620.88 nm. The dark orange MuFLE show the fluorescence lifetime from different internal knot values, and the dotted orange MuFLE shows the fluorescence lifetime from the knot values which returned the lowest cost function.

TABLE VIII
COMPARISON BETWEEN THE PEAK LOCATION FROM FLUOROPHORES MEASURED ON BOTH THE EP-TRFS AND A PLATE READER.

	RhB-H2O	RhB-Me	Fluo
Plate Reader	578.00 nm	574.00 nm	515.00 nm
MuFLE	581.10 nm	576.00 nm	519.39 nm

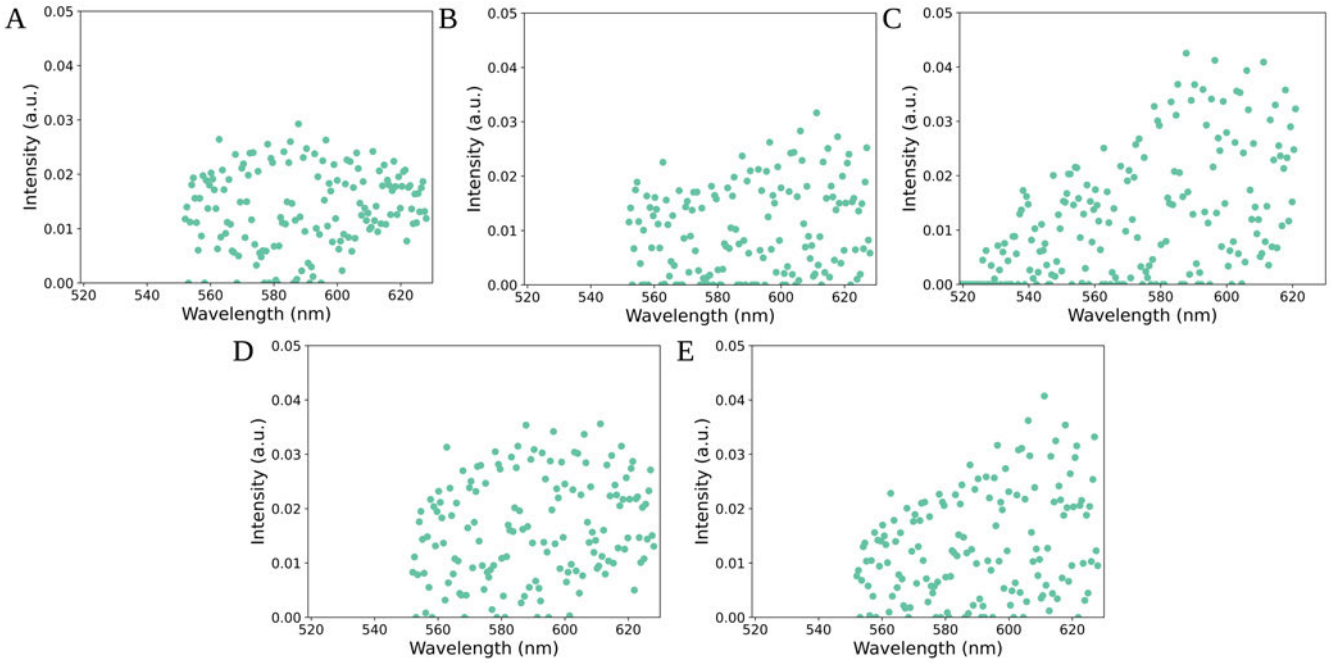

Fig. 9. The estimated bias parameters for individual channels from RhB-H2O **A)**, RhB-Me **B)**, Fluo **C)**, and from mixed samples of RhB-H2O-Fluo **D)** and RhB-Me-Fluo **E)** respectively.

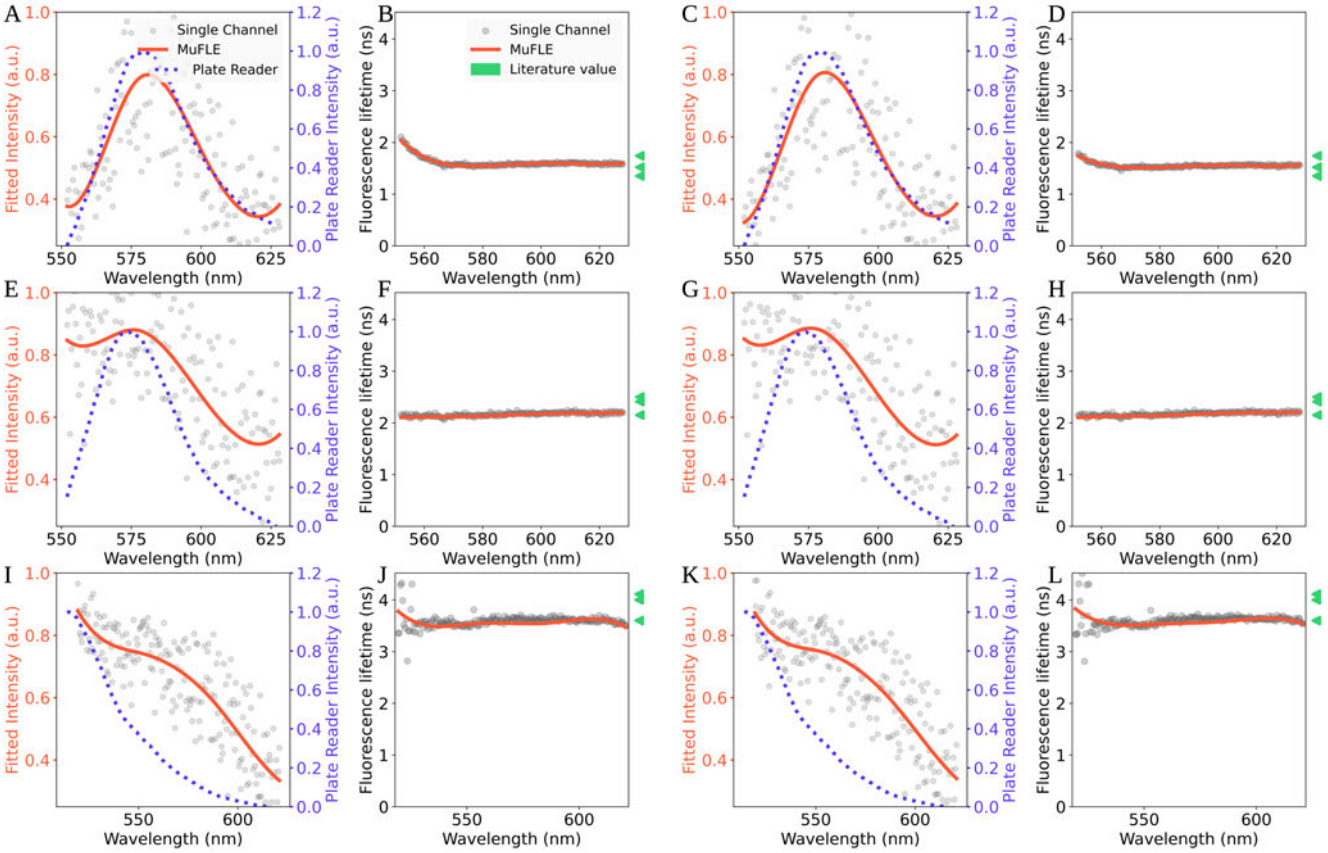

Fig. 10. Single exponential MuFLE model shows the fluorescence emission and spectral fluorescence lifetime of repeated measurements taken of the reference fluorophores. The fluorescence intensity plots across a wavelength spectrum of 552.03 nm - 628.02 nm for both RhB-H2O repeats 1 and 2, **A)** and **C)**, and repeats 1 and 2 of RhB-Me, **E)** and **G**, of MuFLE (orange) are compared to both the single channel fit (grey dots) and the fluorescence emission of the fluorophore following its measurement on a plate reader (purple). The fluorescence intensity plots across a wavelength spectrum of 519.39 nm - 620.88 nm for repeats 1 and 2 of Fluo, **I)** and **K)**, of MuFLE (orange) are compared to both the single channel fit (grey dots) and the emission of the fluorophore following its measurement on a plate reader (purple). The spectral fluorescence lifetime of RhB-H2O , repeats 1 and 2, **B)** and **D)**, and RhB-Me, repeats 1 and 2, **F)** and **H)**, and repeats 1 and 2 Fluo **J)** and **L)** estimated using MuFLE are compared to fluorescence lifetime results of the individual channels estimated using a least squares method (grey dots). The fluorescence lifetime values reported in the literature are also shown (green arrows).

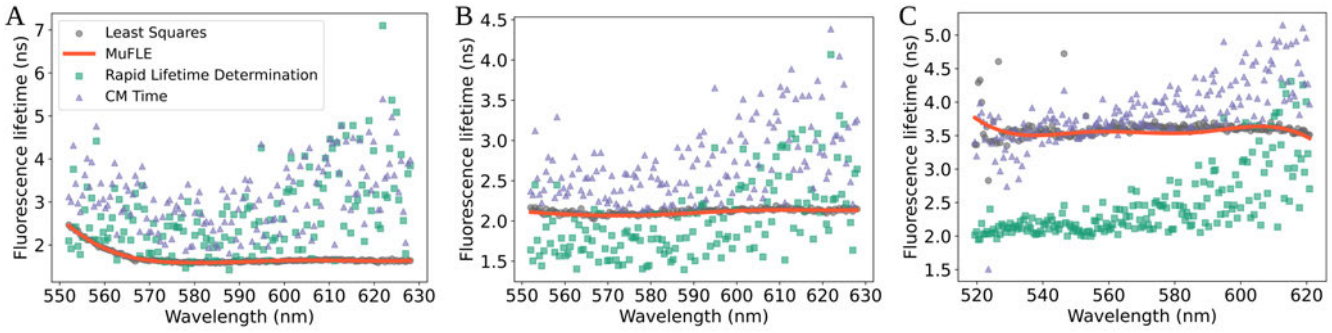

Fig. 11. A comparison of the fluorescence lifetime values estimated using different computational models. The single channel, fit-free lifetime results of the Centre of Mass Time (blue triangle), Rapid Lifetime Determination (green squares) are compared to the Least Squares fit (grey dots) and MuFLE (orange) of RhB-H2O **A)** and RhB-Me **B)** and Fluo **C)** are shown.

3.2 Limitations

Although demonstrating its ability to capture the total spectral and temporal emission profiles of individual fluorophores, and of fluorophores from a mixed system, a major limitation of MuFLE is that it does not incorporate different channel spectral sensitivity observed across the emission spectrum (as mentioned in section 2). The spectral profile of MuFLE includes the average spectral sensitivity from the observed signal originating from detector artefacts. A failure to capture spectral sensitivity, particularly when multiple components of MuFLE are estimated (i.e., > 3) may also pose a bottleneck in accurately estimating these fluorophores as the spectral range, in its current setup, contains both the spectral sensitivity and the spectral profiles from the underlying fluorophores. A simple solution to incorporating the spectral sensitivity in MuFLE is to increase the dimensions of the model to estimate multiple histograms simultaneously. Therefore, the fluorescence of different samples can be identified from features which change, and the spectral sensitivity can be delineated from the features which do not change, simultaneously. However, this is something we save for future work. Furthermore, the clinical translation of MuFLE, when used with the EP-TRFS device is currently limited by its computational efficiency. An adaption of the model to a more computationally efficient system, such as a neural network, may address this.

3.3 Conclusion

In conclusion, we present, to the best of our knowledge, a novel model capable of simultaneously estimating the emission spectrum and SFL of underlying fluorophores in both single and mixed systems. Our study demonstrates that MuFLE accurately estimates the average emission and average FL of exogenous fluorophores, which are well-characterised in the literature. Furthermore, we illustrate MuFLE's proficiency in accurately un-mixing two fluorophores in both the spectral and temporal domains when measured in a mixed system.

Chapter 4

Lung Cancer Discrimination using Spectral Fluorescence Lifetime

One of the key advantages of MuFLE, particularly when employed in a single exponential mode, lies in its capability to discern variations in both the total spectral FI and spectral FL (SFL) of a sample across a broad wavelength range and with high wavelength bandwidth resolution. The single exponential MuFLE model assumes no underlying features within the data, such as the precise location of emission peaks of fluorophores or the number of components fluorescing in a sample. Furthermore, the high resolution feature of the EP-TRFS device allows nuances in the photo-physical properties of the underlying fluorophores to be captured within the MuFLE model.

The following chapter explores additional features observed in the SFL of simulated data, endogenous fluorophores mixed benchside, and paired normal and abnormal LC samples. The analysis is published in Biomedical Optics Express titled "Fibre-optic based Exploration of Lung Cancer Autofluorescence using Spectral Fluorescence Lifetime". Following the presentation of the paper, additional tissue analysis is conducted on both the tissue presented in the paper and additional tissue samples collected. This chapter illustrates how the relative concentration of endogenous fluorophores effects the magnitude and shape of the SFL, offering a more in-depth insight into tissue AF compared to the assessment of a single FL value of marginalised histograms

Fibre-optic based Exploration of Lung Cancer Autofluorescence using Spectral Fluorescence Lifetime

ALEXANDRA C. ADAMS,[1,*] ANDRÁS KUFCSÁK,[3] CHARLES LOCHENIE[1], MOHSEN KHADEM[1,2], AHSAN R. AKRAM[1], KEVIN DHALIWAL[1] AND SOHAN SETH[1,2]

[1]*Translational Healthcare Technology Group, Institute for Regeneration and Repair, 5 Little France Dr, Edinburgh EH16 4UU, UK.*
[2]*School of Informatics, University of Edinburgh*
[3]*Institute of Photonics and Quantum Sciences, Heriot-Watt University, Edinburgh, EH14 4AS*
*

Abstract: Fibre-optic based time-resolved fluorescence spectroscopy (TRFS) is an advanced spectroscopy technique which generates sample-specific spectral-temporal signature, characterising variations in fluorescence in real-time. As such, it can be used to interrogate tissue autofluorescence. Recent advancements in TRFS technology, including the development of devices which simultaneously measure high-resolution spectral and temporal fluorescence, paired with novel analysis methods extracting information from these multidimensional measurements effectively, provide additional insight into the underlying autofluorescence features of a sample. This study demonstrates, using both simulated data and endogenous fluorophores measured bench-side, that the shape of the *spectral fluorescence lifetime*, or fluorescence lifetimes estimated over high-resolution spectral channels across a broad range, is influenced by the relative abundance of underlying fluorophores in mixed systems and their respective environment. This study, furthermore, explores the properties of the spectral fluorescence lifetime in paired lung tissue deemed either abnormal or normal by pathologists. We observe that, on average, the shape of the spectral fluorescence lifetime at multiple locations sampled on 14 abnormal lung tissue, compared to multiple locations sampled on the respective paired normal lung tissue, shows more variability; and, while not statistically significant, the average spectral fluorescence lifetime in abnormal tissue is consistently lower over every wavelength than the normal tissue.

1. Introduction

Lung cancer, the leading cause of cancer-related deaths worldwide [1], has a diagnostic deficit. Only 16.6 % of patients are diagnosed with the disease at an early stage with an anticipated 5-year survival rate of 80 % [2]. This drops to 10 % for diagnoses made at an advanced stage. Thus, we need new diagnostic strategies that enable early and accurate diagnoses. The development of non-surgical radiation-free diagnostic alternatives, such as Fluorescence Lifetime Imaging Microscopy (FLIM) and Time-Resolved Fluorescence Spectroscopy (TRFS) have been shown to discriminate diseased tissue and, additionally, can be available bed-side [3–5]. When used in a label-free setting, these devices produce a detailed molecular profile of tissue autofluorescence (AF), potentially facilitating a more informed and rapid diagnosis [3, 6].

AF describes the fluorescence of naturally occurring molecules, i.e., *endogenous fluorophores* [7]. Endogenous fluorophores, due to their intrinsic molecular structures, have distinct absorption and emission profiles when measured across a suitable wavelength range [8, Fig. 1] [9, Fig. 2]. In addition to the spectral emission, the average time the fluorophore spends in an excited state, known as the *fluorescence lifetime*, can be measured. This value is fluorophore specific and sensitive to the environment [7]. Therefore, in a given physico-chemical environment (i.e., with a set temperature, pH, viscosity, media dielectric constant, free or enzyme-bound), *a single*

fluorophore will exhibit a specific fluorescence lifetime and emission profile [10].

Interpreting AF in lung tissue presents challenges arising from the overlapping excitation and emission profiles, similarities in lifetimes, and the unknown environments of endogenous fluorophores [10]. Depending on the optical setup, various devices measure the emission spectrum at distinct wavelength locations, also referred to as *channels* [11]. Each channel has a *bandwidth* (with smaller bandwidths implying higher *resolution*) within which photons are accumulated, collectively covering a specific wavelength *range*. Therefore, both the range and bandwidth dictate which fluorophores the device can measure, and, in the context of tissue delineation, this variability can lead to different conclusions (see Table. 1 and supplementary Table. S2). In addition, the systems previously employed for measuring AF collected fluorescence in a limited number of parallel spectral channels. For example, the ms-TRFS device [12], utilised in detecting oral and oropharyngeal cancer [13], assessed fluorescence across 4 spectral channels with resolutions ranging from 14 nm to 26.5 nm. In these setups, the underlying signal is essentially marginalised into distinct, low-resolution spectral bins, thereby limiting the detection of subtle yet potentially significant changes in the tissue being explored. Moreover, lung cancer is often characterised by structural deregulation [14], and consequently, alterations may manifest not only in the physical-chemical changes of lung AF but also in the relative abundance of distinct endogenous fluorophores. This insight could provide additional information about the variations in lifetime between normal and abnormal lung tissue.

Table 1. Reported lifetime changes in different cancer and normal samples.

Cancer type	Excitation wavelength	Emission channel	Lifetime change	Reference
Lung	485 nm	557.13 nm-638.22 nm	No significant difference	This paper
Lung	405 nm	510 nm-550 nm & 600 nm-640 nm	No significant difference	[15]
Lung	405 nm	430 nm	Decrease (by 0.55 ns)	[16]
Lung	488 nm	498 nm-570 nm	Decrease (by 0.32 ns)	[17]
Breast	780 nm & 890 nm	350 nm-720 nm, 16 channels, 10 nm wide	Increase (by 0.229 ns)	[18]
Breast	415 nm	No mention	Decrease (by 0.119 ns)	[19]
Cervical	405 nm	430 nm	Increase (by 1 ns)	[20]
Thyroid	298 nm-300 nm	340 nm & 450 nm	Increase (340 nm) No significant difference (450 nm)	[21]
Colon	355 nm	375 nm	Increase (by 0.6 ns)	[22]
Gastrointestinal	355 nm	375 nm	Increase (by 0.44 ns)	[22]
Skin	435 nm	390 nm-600 nm, 16 channels	Decrease (by 0.620±0.340 ns)	[23]

Development in TRFS technology has allowed for alternative devices which assess multichannel AF profiles across a large wavelength range and at a higher resolution (i.e., smaller bandwidth for individual channels) [11, 24, 25]. This allows for the interrogation of both the emission spectrum and *spectral fluorescence lifetime* (SFL), i.e., the variation of *average* fluorescence lifetimes in consecutive channels over a broad range. As discussed in [26] and [27, Chapter 3.2.1], given a single fluorophore, we expect SFL to be constant over wavelengths, but in the context of tissue, where multiple fluorophores are excited simultaneously, we expect SFL to vary, depending on the respective emission spectra of the underlying fluorophores and their relative prevalence in the sample (see section 3.1). The relative abundance of underlying fluorophores can also be estimated through fitting multiple exponentials [18] and spectral-temporal un-mixing. This approach, however, requires assuming that the number of underlying fluorophores are known *a priori*, and we consider SFL to be a proxy for this information. SFL may, therefore, provide additional discriminating information between a diseased and normal tissue sample, than when

comparing the fluorescence over a single channel [28, 29].

Previously, we reported on the extensively-parallel (EP-TRFS) device providing a high resolution fluorescence profile of a sample *over hundreds of channels* [26]. When used in time-correlated single-photon counting (TCSPC) mode, this device constructs a high-resolution histogram of fluorescence concurrently in the temporal and spectral domains. This device excites tissue at 485 nm. Notably, an excitation at 488 nm has been shown to differentiate lung cancer from normal tissue *in vivo* using an optical endomicroscopy (OEM) setup [30–32]. However, while OEM measures spatial fluorescence without a temporal assessment (thus restricting the fluorescence analysis to emission spectra), our approach evaluates lung AF through high-resolution spectral-temporal profiles.

In addition, a computational tool designed to interrogate the acquired high-resolution histograms, named Multichannel Fluorescence Lifetime Estimation or MuFLE, was suggested to provide detailed insights into fluorescence characteristics over multiple channels [26]. A FLIM setup with an excitation of 475 nm has also exhibited lung cancer discrimination using high-resolution spectral-temporal profiles, however, these lung profiles were assessed without a multi-channel analysis tool [24, 33]. Therefore, using these recent developments, we assess the characteristics and applicability of SFL modeled from MuFLE in tissue delineation. Our assumption is that the relative abundances of endogenous fluorophores change in abnormal tissue compared to normal, due to the deregulation of tissue structure in neoplastic samples, thus, changing both the magnitude and shape of SFL, something which low resolution channel devices and conventional analysis tools are unable to capture.

Our overarching goal is to explore the utility of SFL, compared to alternative methods, i.e., *Aggregated Fluorescence Lifetime* (AFL) estimating fluorescence over marginalised histograms, in investigating mixed systems with multiple underlying fluorophores. Particularly in paired normal and abnormal lung tissue, e.g., in the context of delineating them. The contribution of the paper are as follows: first, we observe that the shape of the SFL is influenced by the relative abundance of underlying fluorophores when assessed in a mixed system. We show this to be true both when altering the relative abundance of simulated fluorophores and endogenous reference fluorophores while the physical-chemical environment (i.e., pH, temperature and viscosity of the solvent) remain unchanged, and *despite their emission spectra remaining similar* (see section. 3.1 and section. 3.2). Second, we show the shape of SFL, on average, shows more variability in abnormal tissue compared to normal tissue suggesting a more unpredictable alteration of fluorescence changes in suspected cancer tissue (see section. 3.3). However, we observe that there is considerable inter- and intra-sample heterogeneity between and within SFL of both normal and abnormal tissue in both magnitude and shape (see section. 3.3) limiting statistical significance where $n = 14$ paired samples are investigated (i.e., 28 tissue sections from lobe resections or 90 spectral histograms in total). Third, we observe that although the AFL and SFL perform similarly in delineating lung tissue, the latter provides additional information that is not preserved when aggregating the fluorescence decays across all channels. To the best of our knowledge, this study is the first to explore the characteristics and utility of SFL in simulated data, bench-side fluorophores, and lung tissue.

2. Data and Methods

2.1. EP-TRFS Device

The EP-TRFS device is a fibre based setup which was used in time-correlated single photon counting (TCSPC) mode. In addition, the device was comprised of a pulsed laser (laser diode head (LDH-P-C-485, PicoQuant, Germany) and laser driver (PDL 800-D, PicoQuant, Germany) used at a repetition rate of 20 MHz with a complementary metal oxide semi-conductor (CMOS) single photon avalanche diode (SPAD) line sensor, as detailed in [26] (see Fig. 1 A). This allows high resolution histograms of photon arrival times measured at all channels in parallel using

1.5×10^6 exposures, each with a 5 µs exposure time and an optical laser output power of 175 µW. Furthermore, we excite the sample such that we remain within the accepted photon detection rate of between 1 and 5 % of laser pulses so as to mitigate pile-up risk [34]. Fluorescence spectroscopy measurements in both the temporal and spectral domain, across a broad spectral region between 474 nm-720 nm may be collected. The samples were excited at 485 nm, at this wavelength, as aforementioned, OEM devices have shown through exciting elastin, discrimination between normal and cancerous lungs are visible [30]. Due to the unique fibre-based setup, and spectral-temporal profile of the device, the instrument response function was measured using a quenched form of rose-bengal [35] (see section 4 for more details). Due to the narrower emission profile of rose-bengal, and the emission peaks of the endogenous fluorophores estimated to be excited by a laser of 485 nm, the total fluorescence spectral window the data was analysed in was between 557.13 nm-638.22 nm which consisted 160 individual spectral channels at a wavelength resolution of 0.5 nm.

2.2. Reference fluorophores

Three reference endogenous fluorophores: Flavin Adenine Dinucleotide (Sigma-Aldrich: F8384-100MG), Riboflavin (Sigma-Aldrich: R9504-25G) and Elastin (Sigma-Aldrich: E4527-1G) were measured on the EP-TRFS device. To standardise the environment of the fluorophores, the fluorophores were dissolved in ${}_{dd}H_2O$ made up by the addition of buffer to a pH of 7. The fluorophores were collected at room temperature. Elastin was measured at a concentration of 500 µM, FAD was measured at a concentration of 100 µM and riboflavin was measured at a concentration of 100 µM. To assess the fluorescence profile of mixed endogenous fluorophores in the same environment, 3 samples, referred to as MIX 1, MIX 2 and MIX 3, containing the endogenous fluorophores at varying concentrations, at a pH of 7 were measured (see supplementary material Table. S1). To compare changes of SFL in different mixes, to that of different environments, MIX 2 was made up in 2 more pHs, referred to as MIX 2A and MIX 2B. MIX 2A at a pH of 4 with the addition of 1 M hydrochloric acid, and MIX 2B at a pH of 9 following the addition of sodium hydroxide. To validate the intensity profiles and excitation wavelengths of all samples, the emission (see section. 3.2) was measured using the bottom read out of a plate reader (biotek, cytation 3 imaging reader).

2.3. Ex vivo lung tissue fragments

Tissue data from *ex vivo* lobectomy specimens, ranging from 50 mm-3 cm in diameter were taken. Samples were obtained from patients undergoing lobe resections between January 2022 to January 2023, for suspected lung cancer (NHS Lothian BioResource, Scotland Research Ethics Service, reference 15/ES/0094). 14 lung samples, paired clinically as non-cancerous and cancerous, which we denote in the paper as normal and abnormal. Samples have been assessed and defined by type, stage and age (see Table. 2). The pathological profile of the tissue samples vary. Depending on the size of the tissue sample, 3-6 locations per sample were assessed using our device, with a point sampling approach (fibre core diameter of 32 µm). At each location 3 repeated spectroscopy measurements were taken, with the same device setup as detailed in [26]. Data was collected using a 3 axis Cartesian robot [36] (see Fig. 1 B and C) to allow repeated measurements in the same X, Y and Z plane to be collected. The 3 repeated histograms were summed together before further assessment (see Fig. 1 D) to improve signal-to-noise ratio. Moreover, summed histograms with a peak intensity of below 300 were excluded from the analysis due to poor signal-to-noise.

2.4. Analysis

The data from the EP-TRFS device was analysed using two different approaches.

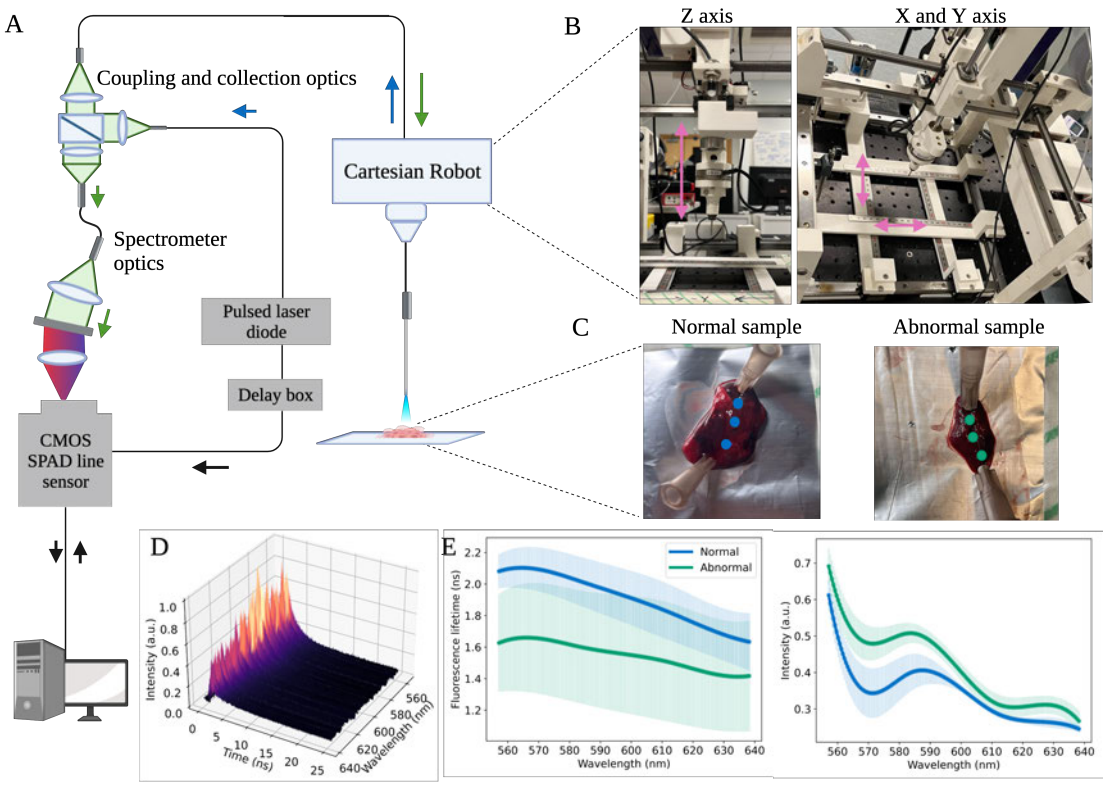

Fig. 1. Illustration of the tissue data collection set up used in this study. **A)** The extensively parallel time-resolved fluorescence spectroscopy system used to collect high resolution spectral-temporal data across 512 wavelength channels across a wavelength range of 474.51 nm-735.12 nm with a resolution of 0.5 nm. The device has a pulsed laser with an excitation of 485 nm, coupling and collection optics, a spectrometer and a complementary metal-oxide semiconductor (CMOS) single photon avalanche diode (SPAD) line sensor. **B)** Cartesian robot is used to collect repeatable, accurate tissue data. The sensing fibre is mounted into the robot and moved across an X, Y and Z axis with 0.5 mm precision. **C)** Paired normal and abnormal, as decided by histopathology following lobe resection, samples were measured on the device. These samples were mounted on a collection board and pinned to prevent movement during the data collection process. **D)** An example of a preprocessed histogram of tissue data collected from the device. The device collects fluorescence data in the form of a histogram of fluorescence intensity over time and wavelength. **E)** An example of the different fluorescence profiles between a normal (blue) and abnormal (green) paired sample. Fluorescence intensity across the wavelength and the SFL of the samples were estimated using Multichannel Fluorescence Lifetime Estimation [26].

2.4.1. Aggregated Fluorescence Lifetime

To compare signal measured in the EP-TRFS device with signal from systems measuring autofluorescence in the more traditional low resolution channel method, the 160 channels histogram was aggregated into two distinct channels of 40 nm each (see supplementary material sec. 1.B and supplementary Fig. S1), and single lifetime, referred to as AFL, was estimated using

Table 2. Sample information of the *ex vivo* lung tissue used in this study.

Sample label	Cancer type	Stage	Age	Sex
1	Adenocarcinoma	1B	63	F
2	Adenocarcinoma	1B	63	M
3	Adenocarcinoma	2B	73	F
4	Adenocarcinoma	1A	74	F
5	Adenocarcinoma	2A	77	M
6	Adenocarcinoma	3A	86	M
7	Adenocarcinoma	n/a	83	F
8	Squamous cell	3A	77	M
9	Squamous cell	3A	66	M
10	Squamous cell	3A	67	M
11	Squamous cell	3A		F
12	Squamous cell	2B	77	F
13	Large cell neuroendocrine	3A	81	M
14	Malignant melanoma	n/a	83	M

least squared fitting. The single exponential fluorescence decay is modelled as follows:

$$s[m] = (f * h)[m] + b \text{ and } f[m] = \gamma \exp(-t_m/\tau). \tag{1}$$

where γ and τ are the average intensity and fluorescence lifetime, b is the bias due to the dark counts of the detector and the fibre background, $h[m]$ is the IRF at the channel, and $*$ denotes convolution. Given $y[m]$ as the observed signal at the m-th bin, γ and τ can be estimated by minimising the loss function

$$J_1 = \sum_{m=1}^{M} (y[m] - s[m])^2 \tag{2}$$

assuming $h[m]$ is known.

2.4.2. Spectral Fluorescence Lifetime

In the second approach, each channel is analysed either separately with least squares fitting or simultaneously with MuFLE. Given multiple channels, MuFLE, simultaneously estimates the fluorescence intensity and lifetimes over these channels [26]. Here, the fluorescence decay is modelled as

$$\begin{aligned} s[p,m] &= (f[p] * h[p])[m] + b[p] \text{ and} \\ f[p,m] &= \gamma[m] \exp(-t_m/\tau[m]) \end{aligned} \tag{3}$$

where $\gamma[p]$ and $\tau[p]$ are spectral intensity and lifetime over channels, and $h[p][m]$ is the IRF at the p-th channel. In MuFLE, both $\gamma[p]$ and $\tau[p]$ are modelled using B-splines basis functions (B_i) as described in [26]. We find the optimal coefficients (a_i) for the emission spectrum and SFL given $\gamma(\omega) = \sum_{i=1}^{I_\gamma} a_i^\gamma B_i(\omega)$ and $\tau(\omega) = \sum_{i=1}^{I_\tau} a_i^\tau B_i(\omega)$. Following [26], we use cubic splines with 3 equidistant internal knots to generate the spline basis functions. Given $y[p,m]$ as the observed signal at the m-th bin and p-th channel, the spline coefficients can be estimated by

minimising the loss function

$$J_2 = \sum_{p=1}^{P} \sum_{m=1}^{M} (y[p,m] - s[p,m])^2 \tag{4}$$

assuming $h[p,m]$ is known.

2.4.3. Simulated data

Simulated data was generated to validate the hypothesis that SFL is sensitive to variation in the relative prevalence of fluorophores, even if the emission intensities are very similar to each other, i.e., without distinct peaks. A similar situation arises in the EP-TRFS system and lung tissue since the selected emission wavelength range only captures the tail end of emission spectra of the fluorophores of interest (see Fig. 2). Three hypothetical fluorophores were simulated using the model described in equation. (3) with different intensity and lifetimes. Exponential and hyperbolic functions were used to model the emission intensities, i.e., $\gamma[p]$, of the individual fluorophores. These functions were chosen to replicate the tail of the emission profile of real fluorophores excited at 485 nm. Across the wavelength range, the lifetime was simulated to be fixed for each fluorophore, i.e., $\tau[m] = \tau$.

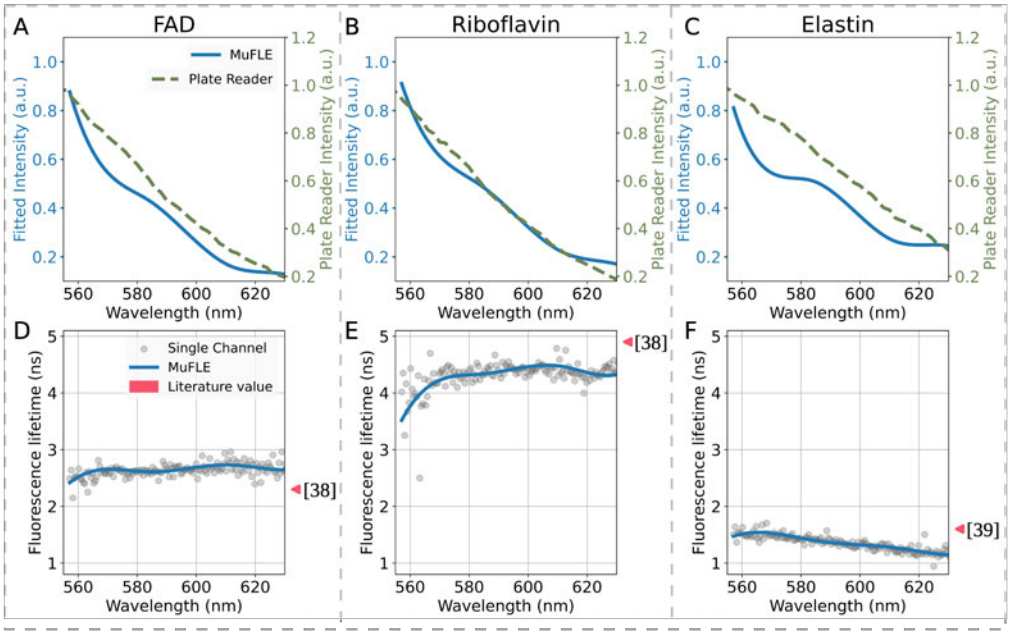

Fig. 2. Spectral fluorescence profiles of 3 reference endogenous fluorophores: FAD **(A and D)**, Riboflavin **(B and E)** and Elastin **(C and F)**. (A), (B) and (C) show the fluorescence emission of the fluorophores measured on the EP-TRFS device modeled using MuFLE (blue) compared to the fluorescence emission measured on a plate reader (green dashed). (D), (E) and (F) show the spectral fluorescence lifetime of the fluorophores measured on the EP-TRFS device modeled using MuFLE (blue), compared to the single channel lifetime estimation (grey dots) modeled using the least squares method assessing the individual channels alone, and the values reported in the literature (pink triangles). The measurements were collected in a wavelength window between 557.13 nm-628.02 nm

The temporal resolution was set to 0.05 ns to match the real data and a total of $M = 490$ time bins were simulated. The number of channels was set to $P = 160$ to match the real data. To simulate mixed samples, the histograms of the individual fluorophores were summed together and convolved with a simulated IRF. The simulated IRF was assumed to be exponential with a lifetime of 0.378 ns, matching the average lifetime of the IRF when fitted with a single exponential decay, recorded in the EP-TRFS device. The intensity at each channel and bin were perturbed using a Poisson noise.

3. Results

3.1. Simulation

It is expected that both the shape and magnitude of the SFL profile is influenced by the relative concentration of the underlying fluorophores with different but constant lifetimes. In the simplest model, we can consider a multi-exponential decay (y) of two fluorophores, in the same environment, a and b as

$$y(\omega, t) = \gamma_a(\omega) \exp(-t/\tau_a) + \gamma_b(\omega) \exp(-t/\tau_b) \tag{5}$$

where ω represents the wavelength, t represents time, and τ represents lifetime. As the intensities, reflecting the individual emission spectrum of the individual fluorophores, change across the wavelengths, the *average* lifetime, when approximated by a single exponential will also vary over the wavelengths. When $\gamma_a(\omega) < \gamma_b(\omega)$, the average lifetime will be closer to τ_b, and when $\gamma_a(\omega) > \gamma_b(\omega)$, the average lifetime will be closer to τ_a.

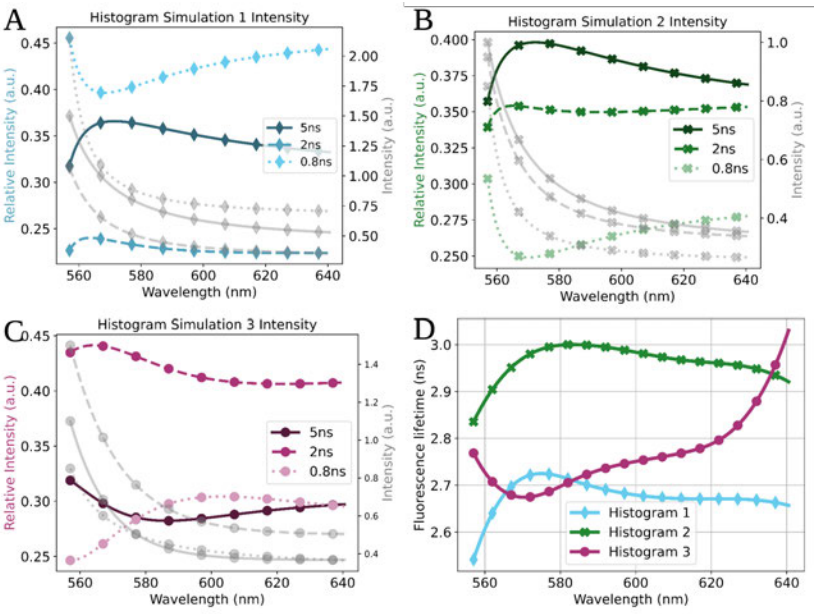

Fig. 3. The relative intensity (coloured), individual intensity (grey) and estimated single exponential lifetime MuFLE results from simulated histograms. **A), B) and C)** represent the underlying relative intensity and emission spectra of 3 individual fluorophores which make up the final observed histograms in the simulated data. **D)** represents the single exponential estimated spectral fluorescence lifetime using the MuFLE model of the 3 different simulated histograms.

The 3 individual simulated fluorophores had similar spectral intensity profiles to that of the endogenous fluorophores used, i.e., they drop monotonically at longer wavelengths (see section 2.4.3). In addition, they also had similar fixed lifetime values to that of the endogenous fluorophores. We observe that the shape of SFL reflects the relative abundance of fluorophores. For example, a dip is observed in the SFL in histogram 3 just before 580 nm (see Fig. 3 D), this aligns with the wavelength range where the fluorophore corresponding to the highest lifetime is declining (see Fig. 3 C), in addition, it aligns with the wavelength range where the fluorophore with the lifetime of 2 ns has started to decline, and the fluorophore with a lifetime of 0.8 ns has started to rise (see Fig. 3 C). In both simulated histograms 1 and 2, a similar trend in the SFL shape is also observed that reflects the relative abundance of the fluorophores (see Fig. 3). In particular, the peaks seen in both SFL lifetime ranges between 560 nm-580 nm, reflect the decline in relative abundance of the fluorophore with a lifetime of 0.8 ns and increase in relative abundance of both fluorophores with a lifetime of 5 ns and 2 ns.

3.2. Endogenous fluorophores

We replicate the same experiment in the simulated data using three endogenous fluorophores bench-side. We select three endogenous fluorophores known to be excited at 485 nm in lung tissue, and are therefore also likely to be present in the tissue samples. We first validated the absorption (to confirm the excitation at 485 nm) and emission spectra of 3 endogenous fluorophores (see Fig. 2). The emission profiles from a plate reader were in agreement with the single exponential MuFLE intensity results of the individual fluorophores (see Fig. 2 A, B, C). The magnitude of SFL estimated using MuFLE was also in agreement with the *ground truth* values reported in the literature while the shape remained broadly constant [37, 38] (see Fig. 2 D, E, F).

Following the validation, the mix of these fluorophores were analysed (see section 2.2 and supplementary material Table. S1). In all cases, similar intensity profiles of the samples were observed (see Fig. 4 ii-iv). When the environment of the sample was altered, a significant increase in the absolute lifetime value (average of 3.38 ns±0.18) of MIX 2B (Mix 2 made up to a pH of 9 as mentioned in section. 2.2) was observed, compared to when measured in MIX 2 or MIX 2A (Mix 2 made up to a pH of 4 as mentioned in section. 2.2) (with an average lifetime value of 2.99 ns±0.15 and 2.95 ns±0.15 respectively) (see Fig. 4 Ai). When the relative concentration of the individual fluorophores was altered, independent of the environment (see supplementary material Table. S1), both the absolute value of the fluorescence lifetime (average lifetime: MIX 1: 2.89 ns±0.12, MIX 2: 2.99 ns±0.15 and MIX 3: 3.33 ns±0.11), and the spectral fluorescence shape of the lifetime across the wavelength changed (see Fig. 4 Bi). The most notable spectral shape change was observed in MIX 3 which reached a plateau across the wavelength between 570 nm-610 nm, instead of a decline in value. The higher lifetime of MIX 3 is expected from higher abundance of riboflavin and lower abundance of elastin compared to MIX 1 and 2, while the slight lower lifetime of MIX 1 compared to MIX 2 is expected due to higher abundance of FAD.

3.3. Ex vivo *lung tissue autofluorescence*

The tissue samples were analysed both in terms of AFL and SFL. We assessed their characteristics both in normal and abnormal tissue samples in individual patients separately (INDV), and normal and abnormal tissue samples pooled together across all individuals (POOL).

3.3.1. AFL:

POOL Despite no significant difference, a slight decline is observed between the average lifetime of both channels from all normal samples (shorter wavelength channel: average lifetime of 1.49 ns±0.47, longer wavelength channel: average lifetime of 1.35 ns±0.41) compared to

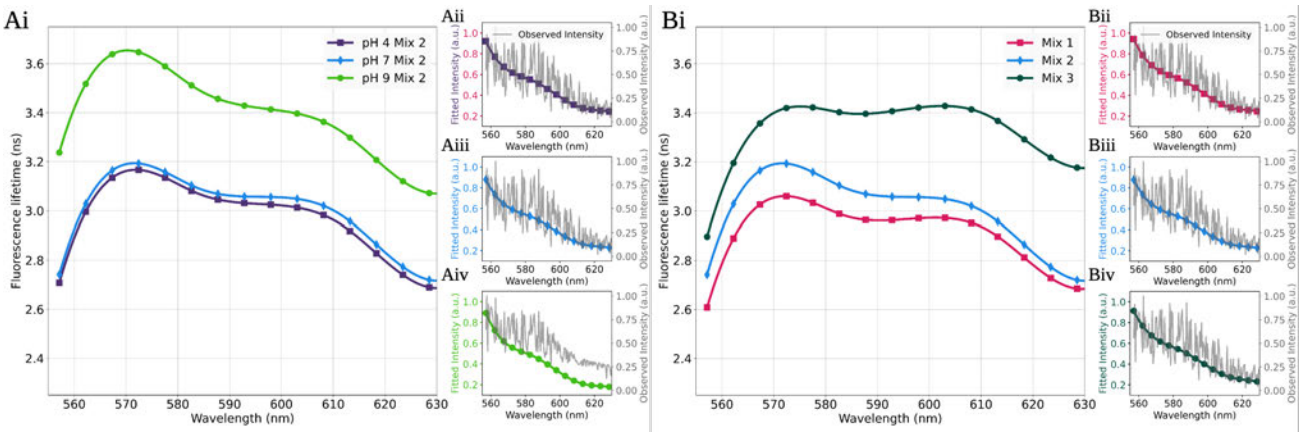

Fig. 4. **A)** shows spectral fluorescence profiles of 3 samples which contain the same concentration of reference endogenous fluorophores: FAD, Riboflavin and Elastin, however, the pH of the solvent has been altered changing the environment of the fluorophores. **B)** shows spectral fluorescence profiles of 3 different mixes of the reference endogenous fluorophores: FAD, Riboflavin and Elastin all measured in a pH of 7 at room temperature. Mix 1 (pink squares) is comprised of 500 µM of elastin, 50 µM of riboflavin and 100 µM of FAD. Mix 2 (blue diamonds) is comprised of 500 µM of elastin, 50 µM of riboflavin and 50 µM of FAD. Mix 3 (green dots) is comprised of 400 µM of elastin, 100 µM of riboflavin and 100 µM of FAD. **i** shows the spectral fluorescence lifetime estimated using the MuFLE model, of the 6 different mixed samples. **ii), iii) and iv)** show the emission profile of the mixed solutions, estimated using the MuFLE model, compared to the observed intensity when measured from the EP-TRFS device (grey line). The measurements were collected in a wavelength window between 557.13 nm-628.02 nm.

the abnormal samples (shorter wavelength channel: average 1.37 ns±0.48, longer wavelength channel: average of 1.30 ns±0.40) (see supplementary Fig. S1 D).

INDV In the shorter wavelength channel (see Fig. 5 A) no significant difference was observed between any paired sample. In the longer wavelength channel (see Fig. 5 B), a significantly higher lifetime value of the abnormal lifetime compared to the normal lifetime between one sample (sample number 12, p-value 0.03) was observed.

3.3.2. SFL: Magnitude

POOL A consistent decrease in the average SFL is observed in abnormal samples compared to normal samples at each channel (see Fig. 6 A). A t-test at each channel between pooled normal and pooled abnormal samples reveal that the drop in lifetime is not significant. When considering the average SFL of all samples, the most prominent difference is observed in the lower wavelength region (between 560 nm - 580 nm) (see Fig. 6 A). Furthermore, a declining trend in the value of lifetime across the wavelength range is observed, independent of sample type (see Fig. 6 A). These observations align with some reported in the literature, i.e. [23].

INDV To assess sample specific SFL changes, first, a paired t-test (paired at 160 channels) between the average normal and abnormal SFL was conducted. In 8 of the samples, a consistent decrease in fluorescence lifetime between the average normal and average abnormal sample was observed. In 4 of the samples a consistent increase was observed, and in 2 no significant change

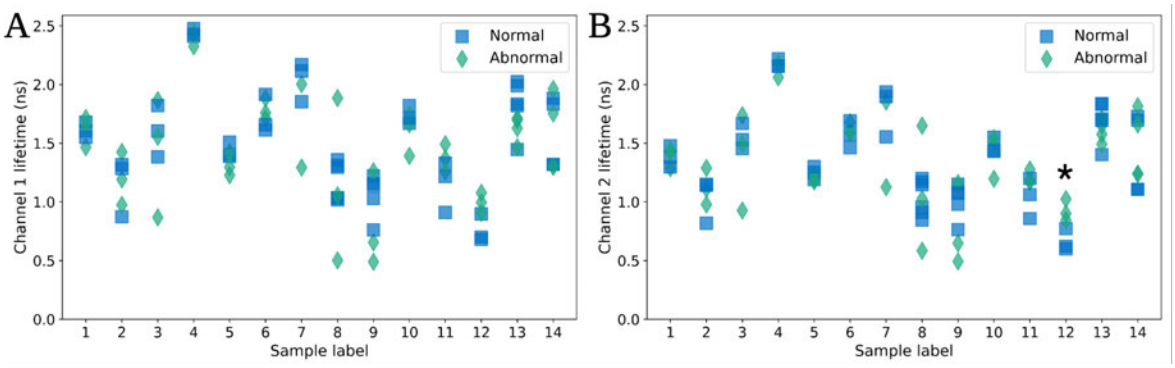

Fig. 5. The fluorescence lifetime, estimated using the least squares method, of all paired normal (blue square) and abnormal (green diamond) samples are shown. **A)** shows the lifetime measured from the first spectral channel (shorter wavelength channel: 557.13 nm-597.42 nm). **B)** shows the fluorescence lifetime measured from the second spectral (longer wavelength channel: 597.93 nm-638.22 nm). * denotes statistical significance, i.e., p-value of t-test is less than 0.05.

was observed, however, in these samples abnormal SFL is higher than normal SFL towards longer wavelengths (see Fig. 6 B). To present some sample specific SFL, three samples were visualised (see Fig. 6 C, D and E). These samples had the largest increase, largest decrease and no significant change between the SFL.

In all samples, overlap in the absolute lifetime value in at least one tissue location is observed (see supplementary Fig. S2, S3 & S4). Furthermore, the overlap in the lifetime values does not appear constant, with some wavelength ranges having a greater amount of overlap (i.e. in Fig. 6 F and in Fig. 6 H, one location overlaps in the lower wavelength range (560 nm - 570 nm) more prominently). Furthermore, in the sample which shows the greatest decrease in SFL (see Fig. 6 E and H), two of the abnormal locations appear lower than the normal range of between 1.2 ns and 0.7 ns, however, one of the abnormal locations appears in the higher region of the normal locations. T-tests assessed at each channel did not reveal significant change in lifetime except sample 12 where a p-value of less than 0.05 was observed in most wavelength ranges as also demonstrated by AFL.

3.3.3. SFL: Shape

POOL: To assess the SFL shape, independent of the absolute lifetime value, the Procrustes disparity between all samples was calculated. The median disparity between all normal SFL was 0.076, whereas the median disparity between all abnormal SFL was 0.159, suggesting a larger variety within the SFL shape in the abnormal than the normal. The pairwise distances (measured using the Procrustes distance metric) between all samples was assessed and plotted using tSNE dimensionality reduction (see supplementary Fig. S5). A slight difference between sample type can be observed (see supplementary Fig. S5 C), where, irrespective of the sample being normal or abnormal, the squamous cell samples and adenocarcinoma samples separate (see supplementary Fig. S5 C).

INDV: The median disparity between the sample specific normal and abnormal SFL was assessed (see Fig. 7). Two samples had noticeably higher median disparity within the normal, compared to the abnormal. However, the other samples either had a combined negligible median disparity suggesting very similar shapes (i.e. less than 0.1), or had a markedly higher disparity

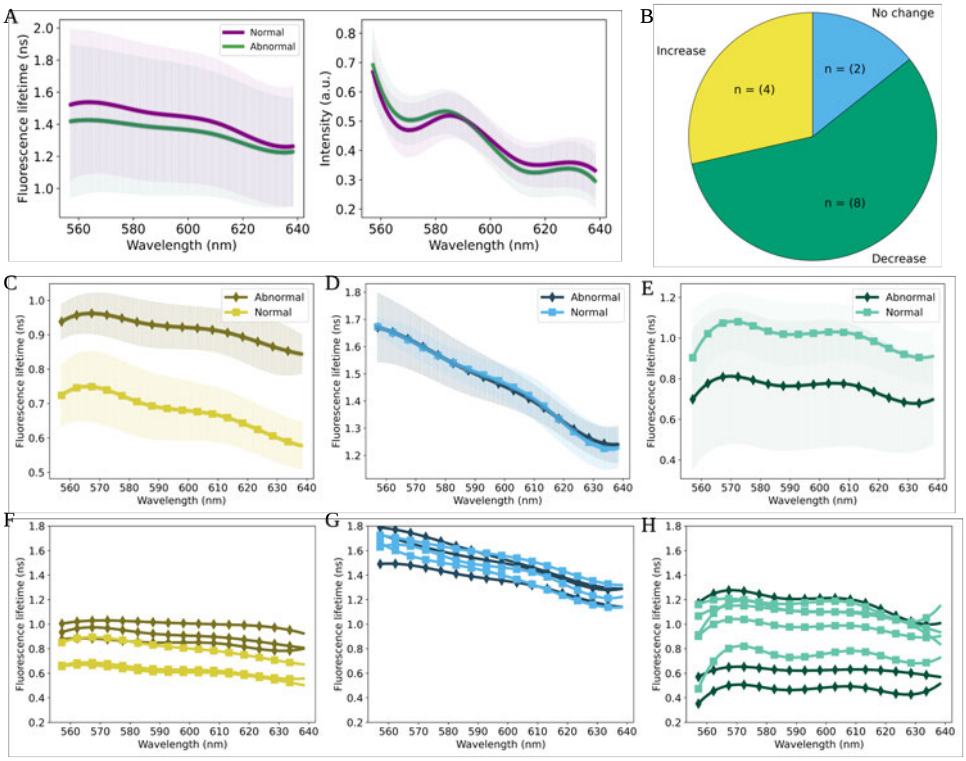

Fig. 6. Differences in the fluorescence profiles between paired normal and abnormal samples are shown. **A)** shows the average spectral profiles of all tissue samples labelled by histology as normal and abnormal. The left plot shows an overall decline in the average SFL of abnormal samples (green) compared to the paired normal samples (purple). The figure also shows a large amount of variance between the average normal and abnormal values. The right plot shows the average fluorescence intensity captured between the normal (purple) and abnormal (green). All tissue data has been analysed across the wavelength profile of between 557.13 nm-638.22 nm. **B)** shows a pie chart representing the proportion of all 14 samples where an increase, decrease or no change between the normal and the abnormal SFL was observed. **C)** shows the SFL between the sample that has the largest increase in lifetime in the abnormal tissue, compared to the normal tissue (sample label: 12). **D)** shows the SFL between the sample where no change between the normal and abnormal tissue was observed (sample label: 1). **E)** shows the SFL between the sample where the greatest decrease in the SFL was observed in the abnormal tissue compared to the normal paired sample (sample label: 9). **F), G) and H)** shows the absolute lifetime values of the different locations of the paired normal and abnormal samples from the above plots.

within the abnormal sample, compared to the normal sample. Most notable in samples number 2 and 8 which had a median disparity of 0.99 and 0.77 in their abnormal, compared to 0.122 and 0.058 in their normal (see Fig. 7).

4. Discussion

Previous systems used to measure tissue AF are limited in collecting fluorescence in low resolution spectral channels (i.e., [12]). Innovations into both high-resolution spectral devices,

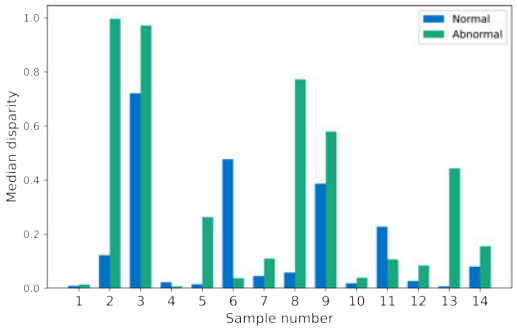

Fig. 7. Median disparity calculated from a Procrustes similarity test between the normal (blue) and abnormal (green), paired spectral fluorescence lifetime measurements of 14 paired, clinically defined normal and abnormal *ex vivo* lung cancer samples.

and analysis techniques to interrogate these signals allows the total temporal spectral histogram to be assessed in detail. The EP-TRFS device and MuFLE algorithm enable high resolution fluorescence intensity and SFL estimation spanning across an entire emission spectrum from 557.13 nm-638.22 nm providing unforeseen details of tissue AF [26].

We demonstrate that the magnitude and shape of SFL is influenced by the relative abundance of underlying fluorophores and their respective lifetimes (see Fig. 4). We observe this to occur while changing the relative abundance of both simulated fluorophores and endogenous fluorophores in samples matched to the expected fluorophores emitting in tissue with the same optical setup. We also observe that while changing the environment of the endogenous fluorophores, the SFL shape remains relatively similar. This provides a potential explanation to the variation we observe in the SFL tissue data where the magnitude and shape vary considerably. We might expect the magnitude and shape of SFL to not change if the relative abundance of the underlying fluorophores and their environment remain homogeneous e.g., in healthy, organised tissue. We might expect the magnitude to change, while shape remaining similar, if the lifetime of individual fluorophores changes without the respective emission spectra changing, and we might expect both magnitude and shape to vary if the relative abundance of the fluorophores change while the respective lifetimes remain fixed, or if both the relative abundance and lifetimes change, e.g., in heterogeneous, disorganised abnormal tissue, like cancer. We show that aggregating the spectral channels into channels with large bandwidths prevents these subtle spectral information between normal and abnormal tissue to be assessed. Although these observations align with our expectation and our results broadly align with results reported in existing studies, a complete validation of the hypothesis is beyond the scope of this paper. Nonetheless, we observe SFL to provide a detailed overview of tissue characteristics, which may provide potential for improved and informed diagnostics.

A limitation to the EP-TRFS device used in this study is that it produces fluorescence profiles alone. Therefore, specific structures observed within the sample which may account for a unique fluorescence profile, such as a fibrotic area, are not recorded alongside the fluorescence profile. So, without direct microscopic images of structure, intra-heterogenous data will arise from mixed tissue components. Furthermore, inter-heterogeneity may arise from differences in patient history i.e. exposure to smoking, pollution and other environmental factors which may alter the inflammatory state of the lung, limiting how normal the normal counterpart is. Additional limitations of our study include the limited patient sample numbers, and the assumption that every location of a tissue sample we take measurements from is biologically the same. Therefore,

the lack of significance can be attributed to both the smaller number of patients included in the study and smaller number of locations sampled for each tissue sample (resulting in a smaller number of point-based histogram samples accumulated per tissue area being assessed) as well as patient demographics and tissue environment.

Although the SFL magnitude and AFL do not show statistical significance in our analysis, the SFL shape show significant variability in abnormal (and often normal) lung tissue indicating the underlying complex molecular dynamics of the structure. Although the significance of the statistical test can be improved through additional data (assuming the difference of lifetime being 50 ps and the population standard deviation being 200 ps, 253 samples will lead to a significance test with level 0.5 and power 0.8), the underlying heterogeneity should be understood in more detail. E.g., if it is due to underlying physical-chemical processes that can both contribute to increase and decrease of lifetime [16], or due to patient demographics such as age or potentially smoking status, or due to the locality of the abnormality, e.g., if it is smaller than the field of view (i.e., $<32\,\mu m$). A better understanding will lead to more informed diagnosis in precision medicine with SFL providing more granular information than AFL.

A major limitation within the spectral range utilised in the analysis, due to the IRF measured, remains. Since we use a fibre-based EP-TRFS system, and our device contains bandpass filters, traditional methods for measuring the IRF remain ineffective. For example, shining light directly onto the sensor does not account for the time delay of the optical signal travelling back and forth through the fibre. Similarly, reflecting excitation light back through the fibre is not appropriate since a bandpass filter blocks light less than 520 nm from entering the detector. A proper alignment of IRF and the observed spectra remain crucial for the least squares fitting routine, and therefore, to measure the IRF, we opt for using a fluorophore that can be excited at 485 nm with as wide a spectral range as possible and with a decay rate shorter than the pulsed light source. Quenched Rose-Bengal has been used in this manner [35]. Variations of fluorescein sodium was also tested (data not shown) at various concentrations, however, we found that the decay rate of this modified fluorophore remained wider than the laser pulse.

An excitation of 485 nm in previous studies using OEM systems has been shown to discriminate normal from abnormal structures, therefore, as aforementioned, the same setup was applied with this method. However, the excitation of the specific endogenous fluorophores with this device, coupled with the IRF limitation prevent the emission peaks of either fluorophore to be measured. Therefore, the optical setup misses the emission peak of the endogenous fluorophores which are expected to be excited using a 485 nm excitation wavelength. However, we show, using both simulated data and data generated bench-side that, regardless of the presence of an emission peak, the ratio of the individual fluorescence compartments influence the SFL shape. A potential discrimination enhancement of this application is to alter the device setup. More specifically, to investigate this emission at a shorter excitation wavelength, i.e., 350 nm, so as to increase the amount of endogenous fluorophores being excited. However, this is beyond the scope of this paper.

5. Conclusion

Our study demonstrates that the relative concentration of individual fluorophores contributes significantly to the shape and magnitude of SFL, both in simulated data and reference data while this information is not visible in AFL. This emphasises the importance of utilising high-resolution spectral channel data when evaluating tissue AF. Specifically focusing on lung tissue, we observed that, in most cases, the SFL consistently drops in magnitude across all channels in abnormal tissue compared to normal *ex vivo* lung tissue, although this difference is not statistically significant. Additionally, we noted that the shape of the SFL, on average, displays greater variability in abnormal *ex vivo* lung tissue compared to normal tissue. Furthermore, our observations revealed significant inter- and intra-heterogeneity among the patient samples measured. While this limits

the immediate translation of this approach to tissue delineation, SFL provides unprecedented details on the tissue AF that can help better investigate the underlying tissue heterogeneity.

6. Backmatter

Funding. A. A. was supported by the Medical Research Council [grant number MR/N13 166/1].

Acknowledgments. We are grateful to the patients who consented to this study, and all the staff at the Department of Thoracic Surgery and Pathology at the Royal Infirmary of Edinburgh.

Disclosures. The authors declare no conflicts of interest.

Data availability. Data presented here is available upon request.

See Supplement 1 for supporting content.

References

1. J. Ferlay, I. Soerjomataram, R. Dikshit, S. Eser, C. Mathers, M. Rebelo, D. M. Parkin, D. Forman, and F. Bray, "Cancer incidence and mortality worldwide: sources, methods and major patterns in globocan 2012," Int. journal cancer **136**, E359–E386 (2015).
2. F. C. Detterbeck, D. J. Boffa, A. W. Kim, and L. T. Tanoue, "The eighth edition lung cancer stage classification," Chest **151**, 193–203 (2017).
3. Y. Ouyang, Y. Liu, Z. M. Wang, Z. Liu, and M. Wu, "Flim as a promising tool for cancer diagnosis and treatment monitoring," Nano-Micro Lett. **13**, 133 (2021).
4. W. Becker, "Fluorescence lifetime imaging–techniques and applications," J. microscopy **247**, 119–136 (2012).
5. L. Marcu, "Fluorescence Lifetime Techniques in Medical Applications," Ann Biomed Eng . **40**, 304–331 (2012).
6. D. S. Kittle, F. Vasefi, C. G. Patil, A. Mamelak, K. L. Black, and P. V. Butte, "Real time optical biopsy: Time-resolved fluorescence spectroscopy instrumentation and validation," Sci. reports **6**, 1–9 (2016).
7. J. R. Lakowicz, *Principles of fluorescence spectroscopy* (SSBM, 2013).
8. G. A. Wagnieres, W. M. Star, and B. C. Wilson, "In vivo fluorescence spectroscopy and imaging for oncological applications," Photochem. photobiology **68**, 603 (1998).
9. A. C. Croce and G. Bottiroli, "Autofluorescence spectroscopy and imaging: a tool for biomedical research and diagnosis," Eur. journal histochemistry: EJH **58** (2014).
10. M. Y. Berezin and S. Achilefu, "Fluorescence lifetime measurements and biological imaging," Chem. Rev. **110**, 2641–2684 (2010).
11. D. Chorvat Jr and A. Chorvatova, "Multi-wavelength fluorescence lifetime spectroscopy: a new approach to the study of endogenous fluorescence in living cells and tissues," Laser Phys. Lett. **6**, 175–193 (2009).
12. D. R. Yankelevich, D. Ma, J. Liu, Y. Sun, Y. Sun, J. Bec, D. S. Elson, and L. Marcu, "Design and evaluation of a device for fast multispectral time-resolved fluorescence spectroscopy and imaging," Rev. Sci. Instruments **85**, 034303 (2014).
13. M. Marsden, T. Fukazawa, Y. Deng *et al.*, "Flimbrush: dynamic visualization of intraoperative free-hand fiber-based fluorescence lifetime imaging," Biomed. Opt. Express **11**, 5166–5180 (2020).
14. G. Burgstaller, B. Oehrle, M. Gerckens, E. S. White, H. B. Schiller, and O. Eickelberg, "The instructive extracellular matrix of the lung: basic composition and alterations in chronic lung disease," Eur. Respir. J. **50** (2017).
15. P. Uehlinger, T. Gabrecht, T. Glanzmann, J.-P. Ballini, A. Radu, S. Andrejevic, P. Monnier, and G. Wagnières, "In vivo time-resolved spectroscopy of the human bronchial early cancer autofluorescence," J. biomedical optics **14**, 024011–024011 (2009).
16. M. Wang, F. Tang, X. Pan *et al.*, "Rapid diagnosis and intraoperative margin assessment of human lung cancer with fluorescence lifetime imaging microscopy," BBA clinical **8**, 7–13 (2017).
17. S. Fernandes, G. Williams, E. Williams, N. Finlayson, Q. Wang, D. Dorward, C. Dhaliwal, W. Wallace, A. Akram, and K. Dhaliwal, "Fluorescence-lifetime imaging: a novel diagnostic tool for suspected lung cancer," (2021).
18. M. W. Conklin, P. P. Provenzano, K. W. Eliceiri, R. Sullivan, and P. J. Keely, "Fluorescence lifetime imaging of endogenous fluorophores in histopathology sections reveals differences between normal and tumor epithelium in carcinoma in situ of the breast," Cell biochemistry biophysics **53**, 145–157 (2009).
19. P. J. Tadrous, J. Siegel, P. M. French, S. Shousha, E.-N. Lalani, and G. W. Stamp, "Fluorescence lifetime imaging of unstained tissues: early results in human breast cancer," The J. Pathol. A J. Pathol. Soc. Gt. Br. Irel. **199**, 309–317 (2003).
20. Y. Wang, C. Song, M. Wang, Y. Xie, L. Mi, and G. Wang, "Rapid, label-free, and highly sensitive detection of cervical cancer with fluorescence lifetime imaging microscopy," IEEE J. Sel. Top. Quantum Electron. **22**, 228–234 (2015).

21. M. Brandao, R. Iwakura, F. Basilio, K. Haleplian, A. Ito, L. C. C. de Freitas, and L. Bachmann, "Fluorescence lifetime of normal, benign, and malignant thyroid tissues," J. biomedical optics **20**, 067003–067003 (2015).
22. J. McGinty, N. P. Galletly, C. Dunsby, I. Munro, D. S. Elson, J. Requejo-Isidro, P. Cohen, R. Ahmad, A. Forsyth, A. V. Thillainayagam *et al.*, "Wide-field fluorescence lifetime imaging of cancer," Biomed. optics express **1**, 627–640 (2010).
23. P. De Beule, C. Dunsby, N. Galletly, G. Stamp, A. Chu, U. Anand, P. Anand, C. Benham, A. Naylor, and P. French, "A hyperspectral fluorescence lifetime probe for skin cancer diagnosis," Rev. scientific instruments **78**, 123101 (2007).
24. G. O. Williams, E. Williams, N. Finlayson *et al.*, "Full spectrum fluorescence lifetime imaging with 0.5 nm spectral and 50 ps temporal resolution," Nat. Commun. **12**, 1–9 (2021).
25. Q. Wang, S. Fernandes, G. O. Williams, N. Finlayson, A. R. Akram, K. Dhaliwal, J. R. Hopgood, and M. Vallejo, "Deep learning-assisted co-registration of full-spectral autofluorescence lifetime microscopic images with h&e-stained histology images," Commun. biology **5**, 1119 (2022).
26. A. Adams, A. Kufcsak, K. Ehrlich, K. Dhaliwal, and S. Seth, "Simultaneous spectral temporal modelling for a time-resolved fluorescence emission spectrum," IEEE Trans. on Biomed. Eng. (2023).
27. B. Valeur and M. N. Berberan-Santos, *Molecular fluorescence: principles and applications* (John Wiley & Sons, 2012).
28. W. Becker, A. Bergmann, and C. Biskup, "Multispectral fluorescence lifetime imaging by tcspc," Microsc. research technique **70**, 403–409 (2007).
29. J. M. Beechem and L. Brand, "Time-resolved fluorescence of proteins," Annu. review biochemistry **54**, 43–71 (1985).
30. L. Thiberville, S. Moreno-Swirc, T. Vercauteren, E. Peltier, C. Cavé, and G. Bourg Heckly, "In vivo imaging of the bronchial wall microstructure using fibered confocal fluorescence microscopy," Am. journal respiratory critical care medicine **175**, 22–31 (2007).
31. S. Tian, H. Huang, Y. Zhang, H. Shi, Y. Dong, W. Zhang, and C. Bai, "The role of confocal laser endomicroscopy in pulmonary medicine," Eur. Respir. Rev. **32** (2023).
32. L. Thiberville, M. Salaün, S. Lachkar, S. Dominique, S. Moreno-Swirc, C. Vever-Bizet, and G. Bourg-Heckly, "Human in vivo fluorescence microimaging of the alveolar ducts and sacs during bronchoscopy," Eur. Respir. J. **33**, 974–985 (2009).
33. Q. Wang, M. Vallejo, and J. Hopgood, "Fluorescence lifetime endomicroscopic image-based ex-vivo human lung cancer differentiation using machine learning," Pre-print (2020).
34. W. Becker, A. Bergmann, G. L. Biscotti, and A. Rueck, "Advanced time-correlated single photon counting techniques for spectroscopy and imaging in biomedical systems," in *Commercial and Biomedical Applications of Ultrafast Lasers IV,* vol. 5340 (SPIE, 2004), pp. 104–112.
35. M. Szabelski, R. Luchowski, Z. Gryczynski *et al.*, "Evaluation of instrument response functions for lifetime imaging detectors using quenched rose bengal solutions," Chem. Phys. Lett. **471**, 153–159 (2009).
36. T. M. Khan, M. Arshad, and M. A. Choudhry, "Modeling and control of cartesian robot manipulator," in *2005 Pakistan Section Multitopic Conference,* (IEEE, 2005), pp. 1–4.
37. L. Marcu, P. M. French, and D. S. Elson, *Fluorescence lifetime spectroscopy and imaging: principles and applications in biomedical diagnostics* (CRC Press, 2014).
38. Y. Sun, Y. Sun, D. Stephens *et al.*, "Dynamic tissue analysis using time-and wavelength-resolved fluorescence spectroscopy for atherosclerosis diagnosis," Opt. Express **19**, 3890–3901 (2011).

7. Supplementary Material

7.0.1. Endogenous Fluorophore Mixes

Table 3. Endogenous fluorophore mixes used in this study.

	Fluorophore concentration (uM)		
[redacted]	FAD	Riboflavin	Elastin
1	100	50	500
2	50	50	500
3	100	100	400

7.0.2. Marginalised Histogram

To compare high-resolution spectral lifetime against alternative methods from the literature, the histogram was aggregated into two distinct channels. This involved summing 80 fluorescence

decays across two different wavelength ranges, mimicking two broad spectral channels: one between 557.13 nm and 597.42 nm, which we label shorter wavelength channel, and the other between 597.93 nm and 638.22 nm, which we label longer wavelength channel. In addition, the IRF recorded across the histogram, as mentioned above, was aggregated in the same way (see supplementary Fig. 8).

Table 4. Lifetime value of normal and abnormal samples recorded on difference devices.

Cancer type	Excitation wavelength	Emission channel	Lifetime change	Device temporal resolution	Device channel width	Tissue preparation	Reference
Lung	485 nm	557.13 nm-638.22 nm	No significant difference	50 ps	0.5 nm	*ex vivo*	Current paper
Lung	405 nm	510 nm-550 nm & 600 nm-640 nm	No significant difference	No mention	40 nm	*in vivo*	[15]
Lung	405 nm	465 nm-495 nm & 545 nm-580 nm	Decrease (by 0.55 ns)	No mention	30 nm & 35 nm	Paraffin-embedded	[16]
Lung	488 nm	498 nm-570 nm	Decrease (by 0.36 ns)	1.6 ns	72 nm	*ex vivo*	[17]
Breast	780 nm & 890 nm	350 nm-720 nm 16 channels	Increase (by 229 ps)	0.2 ns	10 nm	Mouse model of human breast cancer fixed Paraffin-embedded	[18]
Breast	415 nm	No mention	Decrease (by 119 ps)	0.4 ns	No mention	paraffin wax by an alcohol only process	[19]
Cervical	405 nm	Above 430 nm, No mention of precise channel	Increase (by 1 ns)	No mention	No mention	fixed and paraffin-embedded	[20]
Thyroid	298 nm- 300 nm	340 nm & 450 nm	Increase (340 nm) No significant difference (450 nm)	0.012 ns per channel	No mention	*ex-vivo*, untreated	[21]
Colon	355 nm	375 nm	Increase (by 0.6 ns)	0.25 ns	No mention	formaldehyde fixation	[22]
Gastrointestinal	355 nm	375 nm	Increase (by 0.44 ns)	0.25 ns	No mention	formaldehyde fixation	[22]
Skin	435 nm	390 nm-600 nm 16 channels	Decrease (by 620 ps±340)	No mention	10 nm	*ex vivo* - untreated	[23]

Table 5. Average channel lifetime values, T statistic and P value results.

Sample label	Normal Shorter wavelength channel lifetime (ns)	Abnormal Shorter wavelength channel lifetime (ns)	Shorter wavelength channel p value	Normal Longer wavelength channel lifetime (ns)	Abnormal Longer wavelength channel lifetime (ns)	Longer wavelength channel p value
1	1.61	1.59	0.78	1.38	1.38	0.98
2	1.16	1.29	0.48	1.04	1.13	0.56
3	1.6	1.87	0.3	1.55	1.39	0.57
4	2.44	2.02	0.23	2.18	2.08	0.21
5	1.43	1.35	0.2	1.25	1.20	0.25
6	1.73	1.67	0.64	1.58	1.62	0.60
7	2.05	1.59	0.46	1.80	1.49	0.55
8	1.17	1.07	0.74	1.04	1.02	0.95
9	1.06	0.78	0.36	1.01	0.77	0.35
10	1.73	1.23	0.24	1.47	1.41	0.63
11	1.15	1.37	0.21	1.03	1.2	0.22
12	0.76	1.19	0.21	0.66	0.92	0.03
13	1.82	1.33	0.06	1.69	1.46	0.22
14	1.69	1.46	0.66	1.51	1.57	0.83

8. Supplementary Figures

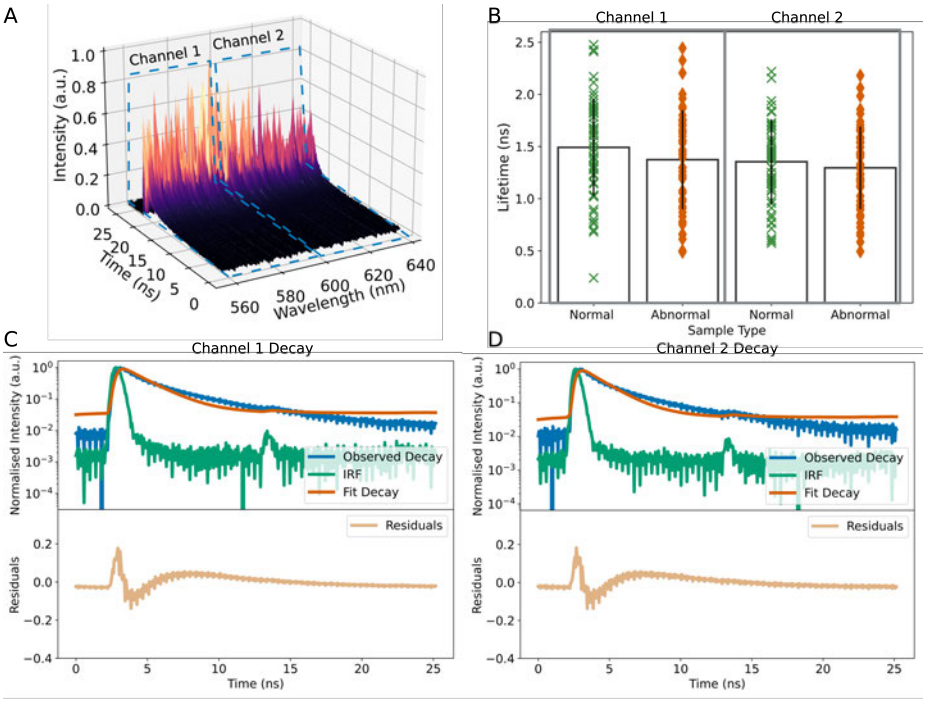

Fig. 8. The histogram and results of marginalising the histogram, splitting the observed decay traces into two spectrally distinct channels. The observed decay from the first channel is a product of summing all channels between 557.13 nm-597.42 nm across the time axis, the second channel is a product of summing all channels between 597.93 nm-638.22 nm across the time axis **A)**. The lifetime values between all normal (green crosses) and abnormal (orange diamonds) samples from both channel 1 and 2 is shown **B)**. The bar plots represent the average lifetime value from that sample type in the specified channel. The results from a sample following the least squares estimation of the fluorescence decay from the two channels is shown **C) and D)**. The blue decay represents the observed decay, the green represents the instrument response function and the orange decay represents the decay as a result of the fitted data. The subplot below the decay trace represent the residuals of between the observed and fitted data.

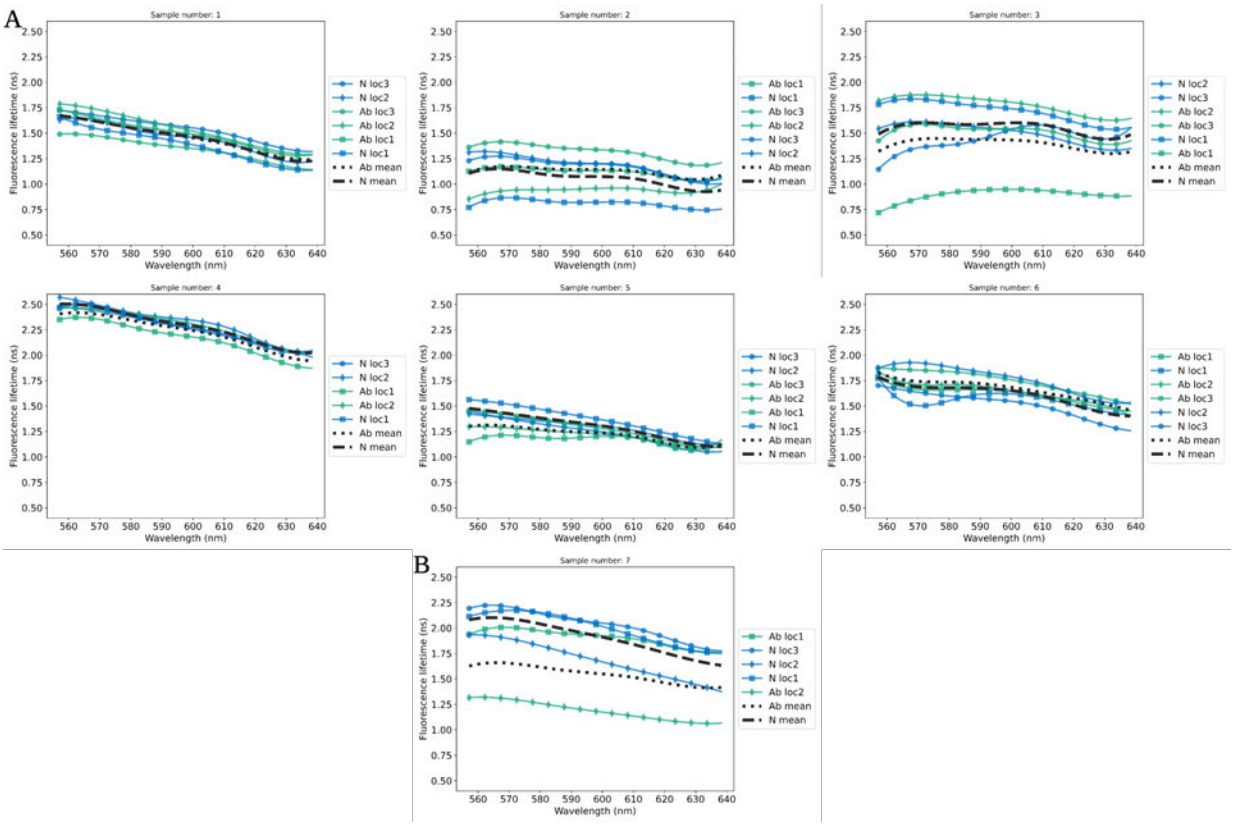

Fig. 9. Spectral fluorescence lifetime profiles of paired normal and cancer diagnosed as Adenocarcinoma. **A)** represent the 6 early stage samples and **B)** is a lung metastasis.

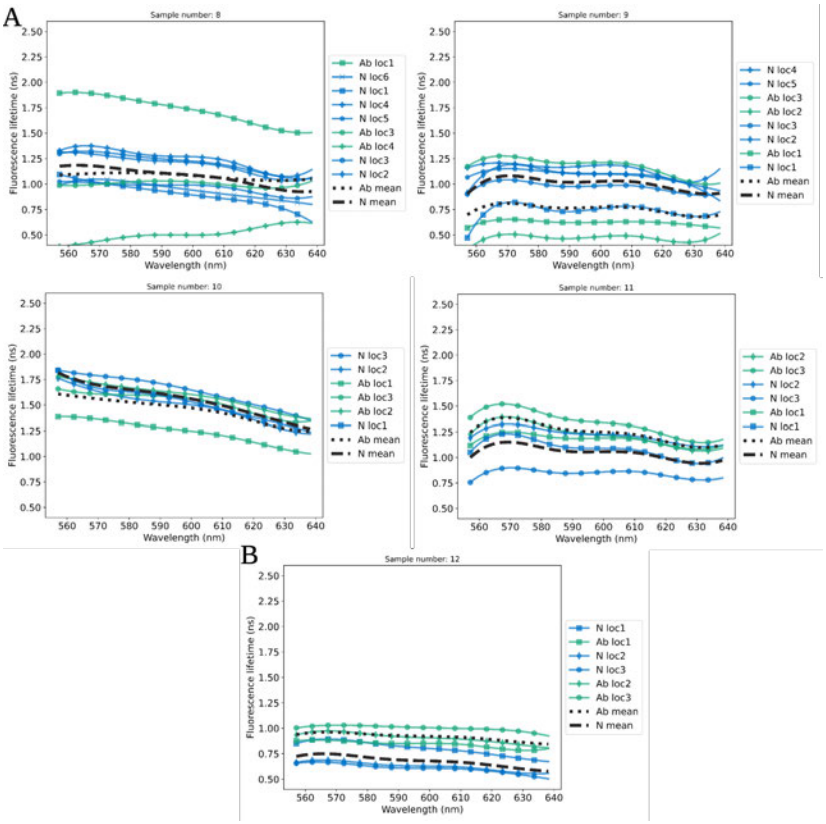

Fig. 10. Spectral fluorescence lifetime profiles of paired normal and cancer diagnosed as Squamous cell carcinoma. **A)** represent the 4 samples classified as stage 3A and **B)** is a sample classified as stage 2B.

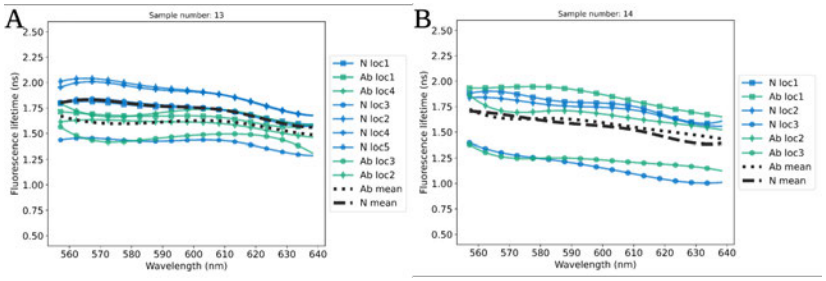

Fig. 11. Spectral fluorescence lifetime profiles of paired normal and cancer diagnosed as either large cell neuroendocrine carcinoma stage 3A **A)** or malignant melanoma **B)**

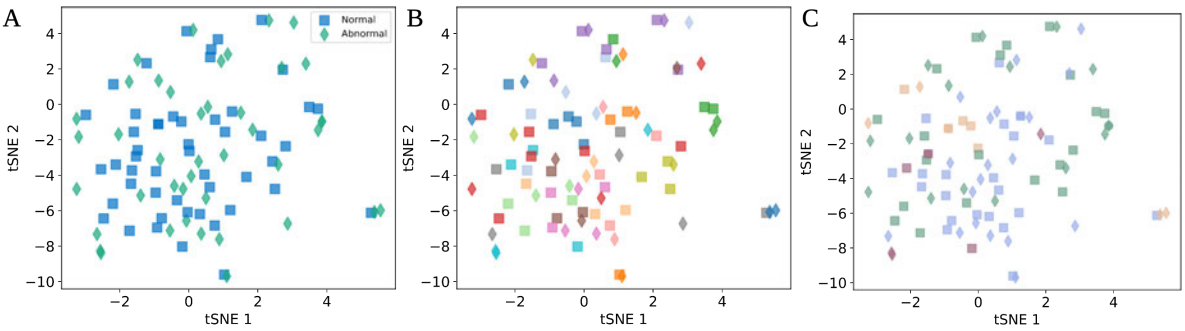

Fig. 12. tSNE plots representing the pairwise distance between the spectral fluorescence lifetime of 14 *ex vivo* clinically defined normal and abnormal samples. This distance was measured using the Procrustes similarity test. **A)** shows the difference between all normal samples (blue square) compared to the abnormal samples (green diamond). **B)** shows the difference between and within all samples, normal (square) and abnormal (diamond). **C)** shows the difference between samples clinically defined as Adenocarcinoma (blue), Squamous cell (green), Neuroendocrine (beige) and Melanoma (mauve).

Table 4.1: Sample information of the additional *ex vivo* lung tissue assessed in this thesis.

Sample label	Cancer type	Stage	Age	Sex
15	Adenocarcinoma	3	53	F
16	Squamous cell carcinoma	1	69	F
17	Mucinous Adenocarcinoma	3	73	F
18	Squamous cell carcinoma	3	79	M
19	Squamous cell carcinoma	2	82	M
20	Adenocarcinoma	3	67	M
21	Squamous cell carcinoma	2	72	M
22	Adenocarcinoma	3	75	F
23	Adenocarcinoma	3	72	M

4.2 Summary

As discussed in [41], the SFL may be influenced by the relative proportions, or concentrations, of underlying fluorophores excited in a system which is comprised of multiple fluorophores. This was explored using simulated data (see Fig. 4.1 & [41, Fig. 3]), and fluorophores when measured benchside (see [41, Fig. 4]). The SFL shape and magnitude was next explored in tissue, highlighting, on average a greater disparity in abnormal tissue SFL shape and magnitude compared to normal.

One of the main observations of [41], which limits the statistical significance of the results obtained from lung tissue, is the high inter- and intra-sample heterogeneity. The study's limitation lies in the number of point sampling measurements recorded per sample. Given the sensitivity of AF to numerous photo-physical factors, the low number of point sampling measurements may have contributed to the observed high levels of heterogeneity. Therefore, additional samples collected between January 2023 - June 2023, where feasible, were measured with a higher number of point sampling measurements. Specifically, 9 additional paired *ex vivo* lung samples were assessed, with each sample having between 1 and 22 point sampling EP-TRFS measurements collected (see Table.4.1).

4.3 Additional Samples Analysis

The additional samples were labeled samples number 15-23 (see Table.4.1). For one sample (number 16), due to its size, only 1 point sampling measurement was possible from both the normal and abnormal tissue collected (see Fig. 4.2).

First, the SFL of the additional samples are assessed (see Fig. 4.2). A Welch's t-test is applied to the SFL at each channel to assess whether a significant difference between the normal and abnormal samples is present. Statistical significance is determined if a p-value of < 0.05 is observed. In samples numbered 15, 19 20 and 21 a significant difference in

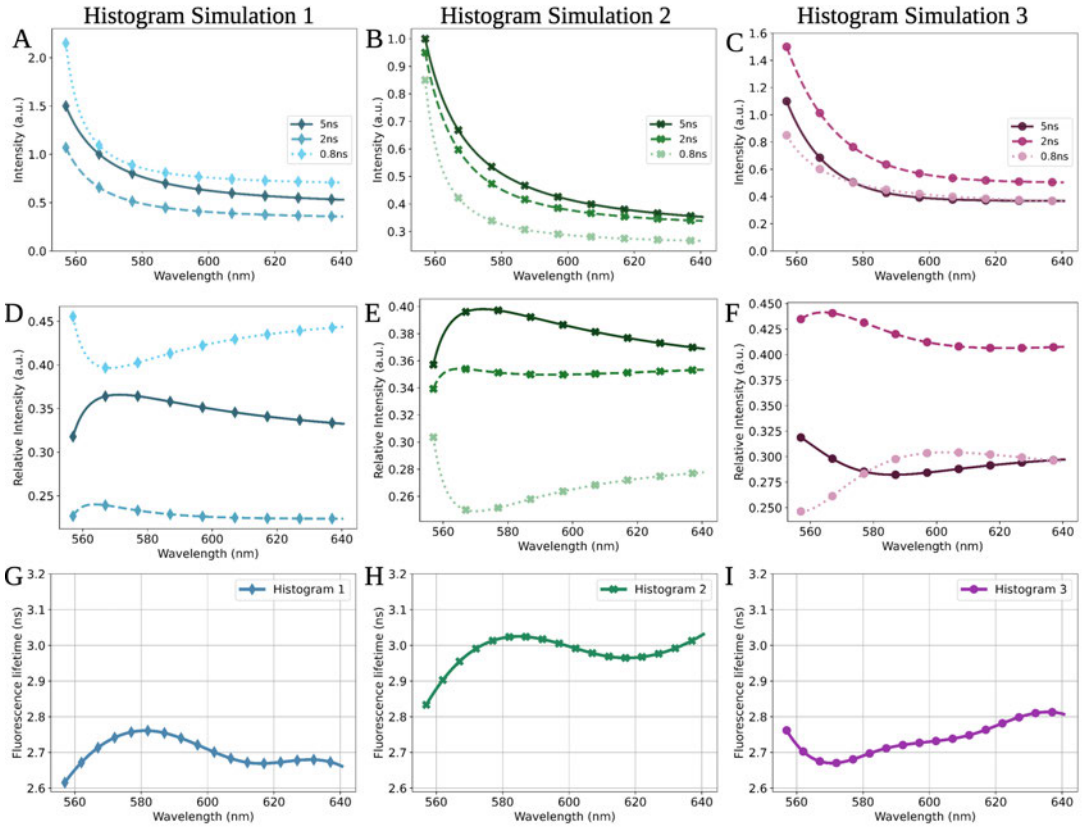

Figure 4.1: The underlying intensity (**A)**, **B)** & **C)**) from simulated histograms of individual fluorophores with varying relative intensities ((**D)**, **E)** & **F)**). Each histogram is generated from 3 individual fluorophores with fixed fluorescence lifetimes of 5 ns, 2 ns & 0.8 ns. The spectral fluorescence lifetime (SFL) (**G)**, **H)** & **I)**) of the simulated histograms was observed to vary, reflecting changes to the relative intensities of the individual fluorophores the histograms are simulated from. The SFL are estimated using the MuFLE model in single exponential mode. Figure adapted from [41, Fig. 3].

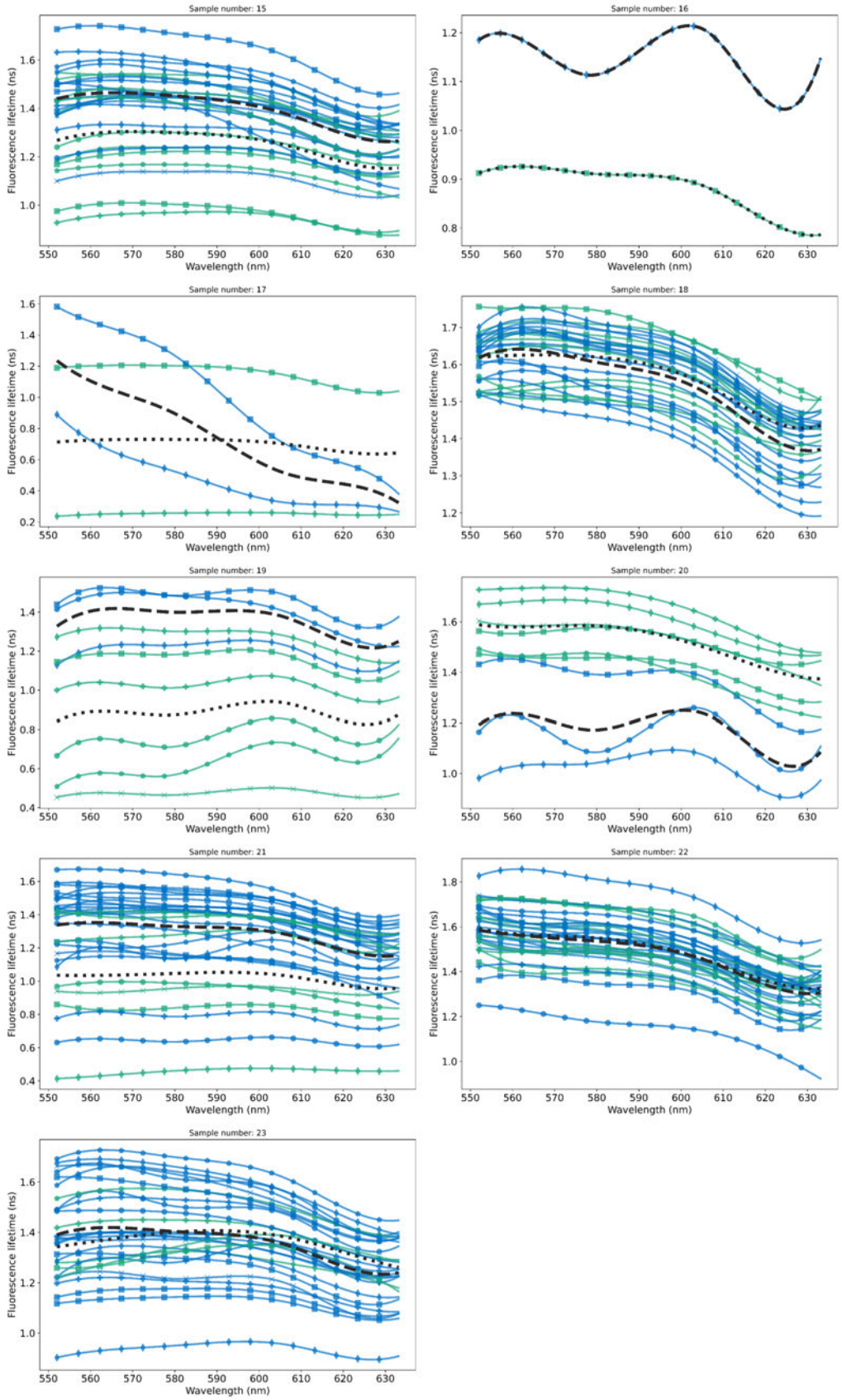

Figure 4.2: Samples paired clinically as *ex vivo* normal (green) and abnormal (blue) lung tissue. The black lines represent the mean spectral fluorescence lifetime of each sample type, dotted as the normal and dashed the abnormal. The data has been collected on the EP-TRFS device and analysed using the single exponential Multichannel Fluorescence Lifetime Estimation (MuFLE) model assessing the average spectral fluorescence lifetime trend across the emission spectrum.

all channels is observed (see Fig. 4.2). It is difficult to conclude, following the addition of 9 samples, if the larger number of point-sampling measurements contributed to a statistically significant difference between the normal and abnormal samples. Although 4 samples exhibit an overall significant difference, samples 18, 22 and 23, despite an increase in the number of point-sampling measurements collected, considerable overlap in their SFL is observed. Moreover, in sample 16, only two areas were sampled, however, a large difference ($>$ 0.5 ns SFL magnitude) between the two samples is observed.

A Procrustes disparity assessment is next conduced to determine differences in either the shape or magnitude of the SFL of the additional samples (see Fig. 4.3). In 7 of the 9 samples, an elevated median disparity in the abnormal sample, compared to the normal counterpart can be observed. There is one sample, however, sample 20, where a larger disparity in the normal tissue is observed. Therefore, variations in the significance of this metric for disseminating tissue remain. However, the additional samples complement the results observed in [41], showing overall, the SFL varies more in abnormal tissue compared to normal [41].

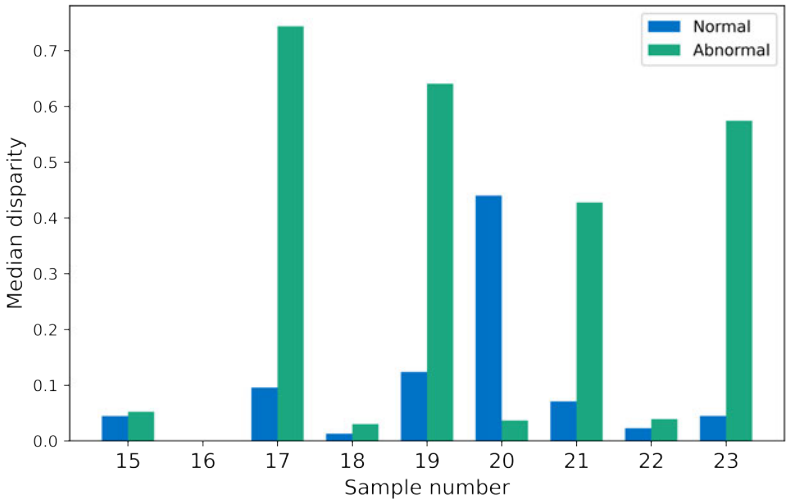

Figure 4.3: Samples paired clinically as *ex vivo* normal (green) and abnormal (blue) lung tissue. The data has been collected on the EP-TRFS device and analysed using the single exponential Multichannel Fluorescence Lifetime Estimation (MuFLE) model assessing the average spectral fluorescence lifetime (SFL) trend across the emission spectrum. Variation and magnitude of both the normal and abnormal SFL from the individual patients was analysed using a Procrustes similarity test, the median disparity from this test is shown.

4.3.1 Sample Type Assessments

In addition to inter-sample heterogeneity, variations in the FL change between normal and abnormal samples for different patient types are also observed [41, Fig 6 & 12]. An increase in the FL magnitude of the abnormal sample 20 is observed, however, a decrease in the FL magnitude from the abnormal sample in samples numbered 15, 19 and 21, compared to the normal counterpart is observed. Different photo-physical properties of the underlying fluorophores from individual patients may account for this difference. Including the metabolic profile of the tumour, and factors effecting the normal sample such as, patient smoking status, age and whether other comorbidities are also present within the lung, effecting how normal the normal sample is. From the entire patient cohort used in this study, a range of different patient types exist, such as, stage, age and gender, this may also account for the difference in the FL observed (see [41, Table 2] & Table 4.1).

To assess whether FL change is contributed to a patient sample type, independent to whether the sample was normal or abnormal, the FL of different sample types are analysed. A difference between the cancer type in both the normal and the abnormal counterpart can be observed. An increase in the Adenocarcinoma mean SFL is observed compared to the mean SFL of the Squamous cell carcinomas (see Fig. 4.4 A & B). Differences in the average SFL of patients presenting with tumours at difference stages can also be observed. The highest average SFL magnitude is observed from patients presenting with stage 2 disease. The lowest average SFL magnitude is observed from patients presenting with stage 1 disease. This can be observed in both the normal and the abnormal samples (see Fig. 4.4 C & D). No difference can be observed between the mean magnitude and shape of the SFL when samples are analysed based on their sex. Despite a difference in the mean values of patients with different cancer types and stage, large heterogeneity remains, preventing statistical significance. Therefore, additional samples and a further increase in the number of point sampling EP-TRFS measurements per sample are required to assess whether these results have clinical implications. Moreover, the samples were all measured *ex vivo*, therefore, their profiles may change when measured *in vivo* due to the presence of different environments, pH and vasculaculture surrounding the tumour in the body cavity.

4.4 Conclusion

This chapter shows the SFL shape and magnitude is influenced by the relative concentration of the underlying fluorophores in a sample. We show when applied to lung tissue samples that there is a greater variation of SFL shape within most of the abnormal samples, compared to the normal. This suggests that there is a larger amount of variation in the relative con-

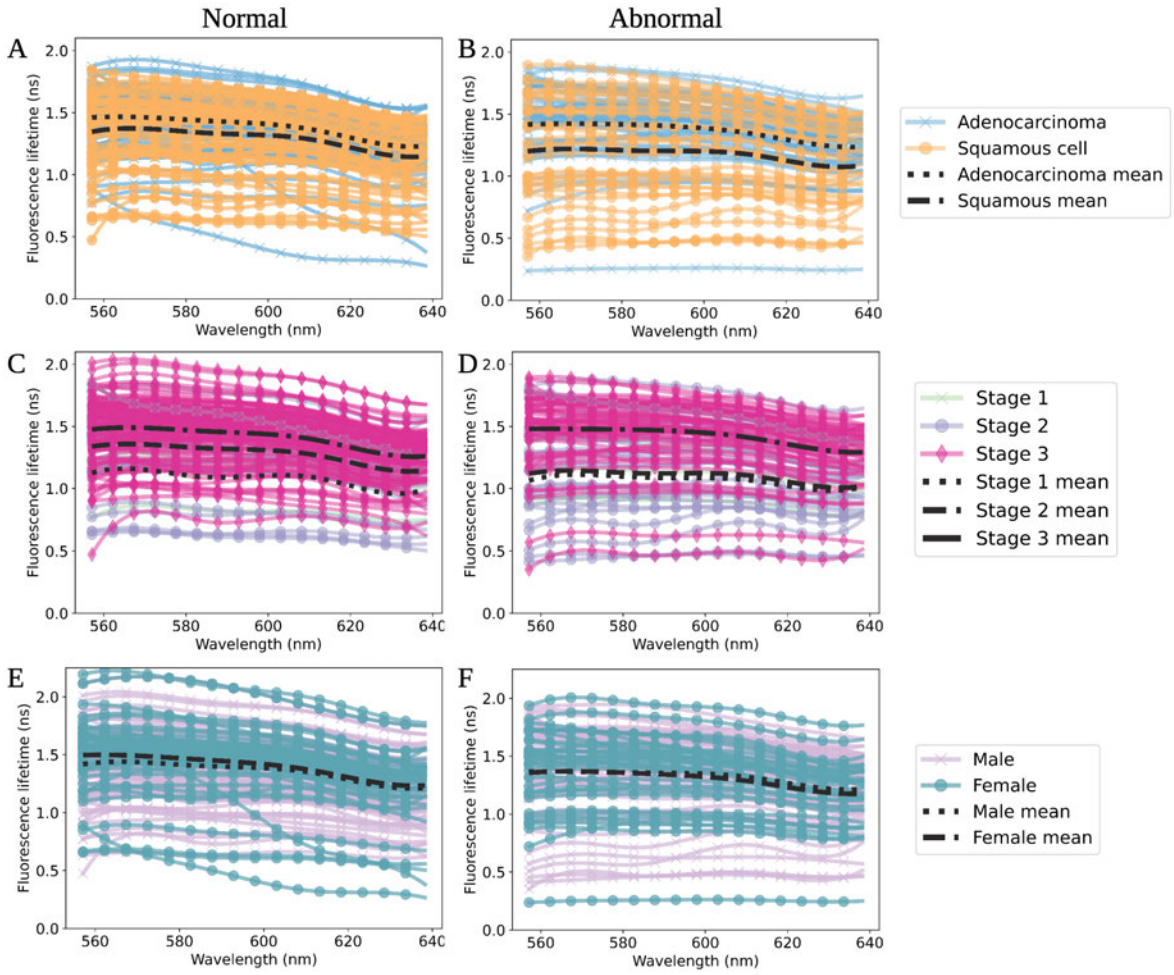

Figure 4.4: Spectral fluorescence lifetime (SFL) profiles measured on a time resolved fluorescence spectroscopy device (TRFS) and analysed using the Multichannel Fluorescence Lifetime Estimation (MuFLE) model of *ex vivo* clinically defined as non-cancerous (normal) and cancerous (abnormal) lung tissue. Samples from cancer cell types Adenocarcinoma and Squamous cell carcinomas from all normal **A)** are compared to all the abnormal **B)**. Samples from different stages are next displayed, comparing all the normal **C)** with all the abnormal samples **D)**. Finally, normal samples from patients of different genders **E)** and abnormal samples from patients of different genders **F)** are compared. The average SFL is included in each figure (black)

centration of endogenous fluorophores in cancerous tissue compared to the normal tissue. These results, however, were not consistent across all patients, or sample types. We also show changes in the the mean SFL values when compared to different tumours types and stages. However, heterogeneity also prevents this statistical significance.

A major limitation of this study is the limited number of patient samples, and of point sampling measurements conducted per sample. Therefore, future work involves both the collection of more lung samples, and a higher number of EP-TRFS point samples measured per lung tissue. In addition, these features are likely to change further when the tissue is analysed *in vivo*, therefore, future work to include assessing the SFL shape and magnitude of tissue *in vivo* is required. Furthermore, variation in the relative number of fluorophores has been shown, however, the single exponential model prevents the identification of which fluorophore(s) are changing. For a more in depth assessment of the individual fluorophores, a multi-exponential MuFLE model may be required.

Chapter 5

Towards Total Un-mixing

Advancements in high-resolution point-based TRFS devices, coupled with the development of computational models such as MuFLE, allow the concurrent spectral-temporal profile of individual fluorophores to be evaluated. When used in a multi-exponential mode, we demonstrate MuFLE to un-mix endogenous fluorophores simultaneously in both spectral and temporal domains of *ex vivo* lung samples from both cancerous and non-cancerous tissue, without relying on any *a priori* information (i.e., no previous reference to spectral or temporal information from the expected fluorophores).

We validate the presence of specific MuFLE un-mixed fluorescence components using a gold standard benchtop FLIM confocal microscope measurement of the same sample. Through a comparative analysis of the changes in FL between cancerous and non-cancerous profiles we finally show evidence of component specific changes responsible for the overall shift in tissue AF. The identification of the fluorescence components responsible for AF changes in *ex vivo* samples may, therefore, enable endogenous fluorophore specific label-free tracking.

Consequently, the integration of this device and MuFLE, when applied *in vivo* may facilitate the instantaneous measurement of specific molecular and environmental properties associated with individual endogenous fluorophores in tissue. This approach provides novel insights, offering a comprehensive understanding of the molecular dynamics in *ex vivo* tissue, label-free and in real-time.

5.1 Introduction

Novel optical technologies, such as FL devices (i.e., TRFS and FLIM) measure the photophysical characteristics of tissue samples [131]. The diagnostic advantages of these technologies over more traditional methods, such as PET scans, radiographs, and histology, include reduced exposure to ionizing radiation, lower cost, and localised real-time assessment of suspected diseased areas *in vivo* [8]. The sensitivity of FL devices has shown promise in early stage cancer discrimination, cancer margin detection, and differentiation between benign and

malignant tumors in various tissues [155, 154, 133]. Therefore, FL technologies may offer clinical advantages in diagnosing LC due to reduced radiation exposure and costs, enhanced local sensitivity, whilst also offering an immediate *in vivo* assessment. In doing so, these devices may also address LC specific complexities like late or uncertain diagnoses [3].

FL devices, when used in a label-free setting, measure the AF of tissue, encompassing both FI (the amount of photons detected) and the FL (the time the photons take to decay to $\frac{1}{e}$ of their initial value) of specific naturally occurring endogenous fluorophores (e.g., NAD(P)H, elastin, porphyrin) [117, Fig. 2]. Changes of the photo-physical properties of endogenous fluorophores in various disease states underpins the discriminating potential of these devices. The range of endogenous fluorophores responsible for different AF profiles between cancerous and non-cancerous samples depends also on the optical setup of the FS device (e.g., an excitation of 485 nm and emission setup of 500 nm-600 nm measures specifically elastin and flavins. Whilst an excitation of 400 nm and emission setup of 450 nm-550 nm measures elastin, collagen, lipopigments and flavins) [21, Fig.3.2]. Therefore, both the photo-physical properties of endogenous fluorophores and the optical setup of the device influence which fluorescence molecules are measured and in-turn, the overall discrimination potential.

Current devices assessing AF from *ex vivo* and/or *in vivo* samples typically use an excitation at 355 nm and measure the subsequent emission in distinct wavelength channels of 390$\pm$20 nm, 470$\pm$14 nm, 540$\pm$25 nm and 629$\pm$29.5 nm [132, 133, 134, 135, 126, 139]. Moreover, the analysis of the FL and FI in these studies typically involves a deconvolution method, either via the Laguerre expansion model (i.e., [126, 132, 139]) or a least squares fitting (i.e., [134]). These analysis tools then utilise either the average FL or a bi- and in one case a tri-exponential model (i.e., [120]) to estimate the FL within the channels (see Table 1.1).

These distinct emission channels are adjusted to collect photons from specific fluorophores: NAD(P)H, FAD, and porphyrins, by aligning with their expected emission peaks. Studies using an optical set-up optimised for FAD detection (i.e., an emission channel between 545–595 nm), observed metabolic specific FL alteration of BEAS-2B cells [120]. An increase in FL was observed when 3-bromopyruvate was administered (a glycolysis inhibitor), however, a decrease in FL was observed when $CoCl_2$ (an OXPHOS inhibitor) was administered compared to the control group [120].

Fluorophore specific channels also allow changes in multiple fluorophores to be assessed. In particular the ratio between metabolic fluorophores NAD(P)H and FAD, produces the redox ratio of the sample. Redox regulation and the disruption of this cellular process has implication in the downstream signalling resulting in changes to transcription factors such as NFκB [156]. This has implications in apoptosis, inflammation and cancer. The fluorescence lifetime redox ratio, FLIRR, provides a photo-physical assessment of this metric. Traditionally a bi-exponential decay fit within the channels allow the FI ratio of protein bound and un-bound NAD(P)H and FAD to be assessed. Comparing the protein bound ratio of both NAD(P)H and

FAD, produces the FLIRR. I.e.,

$$FLIRR = NAD(P)H_{\alpha^2}/FAD_{\alpha^1} \tag{5.1}$$

where the amplitude (α^2) from the longer FL in the NAD(P)H channel (i.e., an emission channel between 426-446 nm) is compared to the amplitude (α^1) from the shorter FL in the FAD channel (i.e., an emission channel between 542-582 nm) [110]. This indicates the redox status of the tissue, with an increase indicating an OXPHOS shift and a decrease indicating a glycolysis shift [124, 110].

More recent studies show the implication of fluorescence from bound and unbound FMN, also contributes to the FL within the FAD channel [110]. Due to the bi-exponential fit, the paper argues this fluorophore is not being accounted for in traditional FLIRR calculations. This particular paper redefined the FLIRR using a tri-exponential decay within the fitting routine of the FAD channel. Therefore, 3 different ratios were calculated:

$$FLIRR1 = NAD(P)H_{\alpha^2}/FAD_{\alpha^1} \tag{5.2}$$

$$FLIRR2 = NAD(P)H_{\alpha^2}/FAD_{\alpha^2} \tag{5.3}$$

$$FLIRR3 = NAD(P)H_{\alpha^2}/FAD_{\alpha^3} \tag{5.4}$$

where amplitudes α^1 α^2 and α^3 reflect the shortest to longest FL estimated from the FAD channel. From the analysis of cell lines, the study found FLIRR1 had the highest statistical significance between tumour and normal cells [110].

An alternative study, evaluating the FL of 111 brain tissue samples *in vivo*, classified the FL from a channel between 500-580 nm. In addition to the time domain assessment, the spectral emission between 430-740 nm was also assessed. Within the emission analysis, an increase in a peak at 495 nm was observed in correlation to increasing glycolysis. This was attributed to an increase in protein bound FMN which also has a higher quantum yield than FAD. Moreover, in the assessment of FL from the FL channel, an increase was also observed in correlation to increasing glycolysis. This FL increase was also attributed to protein bound FMN, which counter to FAD, increases in FL when bound to proteins [121](see Fig. 1.9). Both studies highlight the complex nature of characterising specific fluorophores in tissue. An additional component emitting within the FAD/flavins channel, and present in high levels in the brain amongst its ECM is elastin [157]. This fluorophore may also have additional implications in the redox calculation if un-described due to its FL similarities with protein un-bound FMN.

An alternative, fluorophore specific FL approach has been proposed [158]. This study shows that the average FL is indicative to the relative concentration of both mixed endogenous and exogenous fluorophores when measured in 6 individual wavelength channels, with a wavelength bandwidth resolution of 20 nm-70 nm. The authors argue that this technique can

be used to quantify and monitor the concentration of NAD(P)H and FAD *in vivo*. However, without an entire spectral reference, it is difficult to ascertain from the average FL alone whether alternative fluorophores or those present in different environmental states are responsible for the observed FL change [158]. This is particularly relevant in complex systems where the presence of specific fluorophores based on their decay rates alone are difficult to determine. E.g., the FL of FMN increases in glycolysis [121], however FAD FL decreases in glycolysis [120], potentially counteracting the overall FL values of these changes. Therefore, FL un-mixing without a spectral reference becomes difficult to interpret, limiting the specificity of these assessments.

The FL differences observed in cancerous tissues, whether increasing or decreasing compared to the non-cancerous counterpart, reflects a nuanced interplay of different photo-physical characteristics from the underlying endogenous fluorophores, emphasising the complexity of a FL diagnostic based interpretation. We argue that a system capable of simultaneously resolving endogenous fluorophores in both the spectral and temporal domains, across a broader wavelength range and at a higher wavelength bandwidth resolution, may enhance the certainty that the respective emission and FL compartments correlate to fluorophore specific alterations. We have previously shown that at an excitation of 485 nm, in a fibre-based system applicable for *in vivo* lung exploration, we can un-mix exogenous reference fluorophores accurately in both the spectral and temporal domain simultaneously with no information *a priori* (apart from the number of fluorophores present in the sample) [47]. We have also shown, in a separate study, the diversity and heterogeneity of FL differences between the average paired, early stage, cancerous and non-cancerous lung tissues; we have observed that in general the SFL shape in cancerous tissue is more varied than in non-cancerous tissue, suggesting an increase in the photo-physical complexity of the underlying endogenous fluorophores in a diseased state [41].

The EP-TRFS device, referred to as *Flamingo*, that is used in this study generates high resolution spectral-temporal histogram profiles of the underlying fluorescence. The histograms are analysed using multi-exponential variations of the MuFLE model (as detailed in [47]) to un-mix the spectral-temporal profile of the underlying endogenous fluorophores in paired *ex vivo*, clinically defined cancerous and non-cancerous early-stage lung tissue. We assess the spectral-temporal profiles of these fluorophores when measured benchside. In addition, we compare the relative concentration of these fluorophores from both cancerous and non-cancerous samples, and assess the MuFLE un-mixed compartments in differentiating LC from non-cancerous samples. We finally identify fluorophores in both the EP-TRFS device and in the FLIM confocal device, allowing the spatial location of these fluorophores to be assessed. This study shows, for the first time to the best of our knowledge, individual endogenous fluorophores, label free, may be assessed in both the spectral and temporal range, in a fibre

based system. This provides details into understanding which molecules are responsible for a fluorescence discrimination, and potentially enables us to understand why and how they are implicated in a disease setting, for a better, personalised diagnosis, which can be applied *in vivo* in the near future (see Fig.5.1 for the work flow overview).

5.2 Methods

5.2.1 Endogenous fluorophores

Three endogenous fluorophores known to be excited at 485 nm and be present in lung tissue were measured benchside: FAD (Sigma-Aldrich: F8384-100MG), riboflavin (Sigma-Aldrich: R9504-25G) and elastin (Sigma-Aldrich: E4527-1G). To standardise the measurements, these were all made up in $_{dd}H_2O$ to a pH of 7 and collected at room temperature. Both FAD and riboflavin were made up in a concentration of 100 µM, while elastin, due to its lower quantum yield was made up in a concentration of 250 µM.

5.2.2 *Ex vivo* lung resections

Upon initial assessment 14 paired *ex vivo* lobectomy specimens from patients between January 2022 - January 2023 were assessed, as also analysed in [41] (NHS Lothian BioResource, Scotland Research Ethics Service, reference 15/ES/0094). The paired samples were clinically defined as cancerous and non-cancerous samples and by type, stage and age (see Table. 2 [41]). The tissue area available to measure ranged from 50 mm-3 cm. Therefore, depending on the sample size available, between 3-6 locations were measured on the EP-TRFS device. In addition, as mentioned in [41], measurements were collected using a 3 axis Cartesian robot [159] (see Fig. 5.1 A). 3 repeated histograms were summed together, and histograms with a peak FI (i.e., photon counts) $<$300 were excluded from the analysis due to poor signal-to-noise. Following the initial tissue assessment 9 additional *ex vivo* lobectomy specimens from patients between January 2023 - June 2023 were also assessed. These samples were analysed using the same method detailed above. The details of all samples analysed in this chapter are presented in Table. 5.1. Following assessment on the EP-TRFS device samples numbered 11, 15 & 16 were assessed on a FLIM confocal microscope (see section. 5.2.4 for more detail). Note that only one location of cancerous and non-cancerous tissue from sample number 16 was collected due to the sample size.

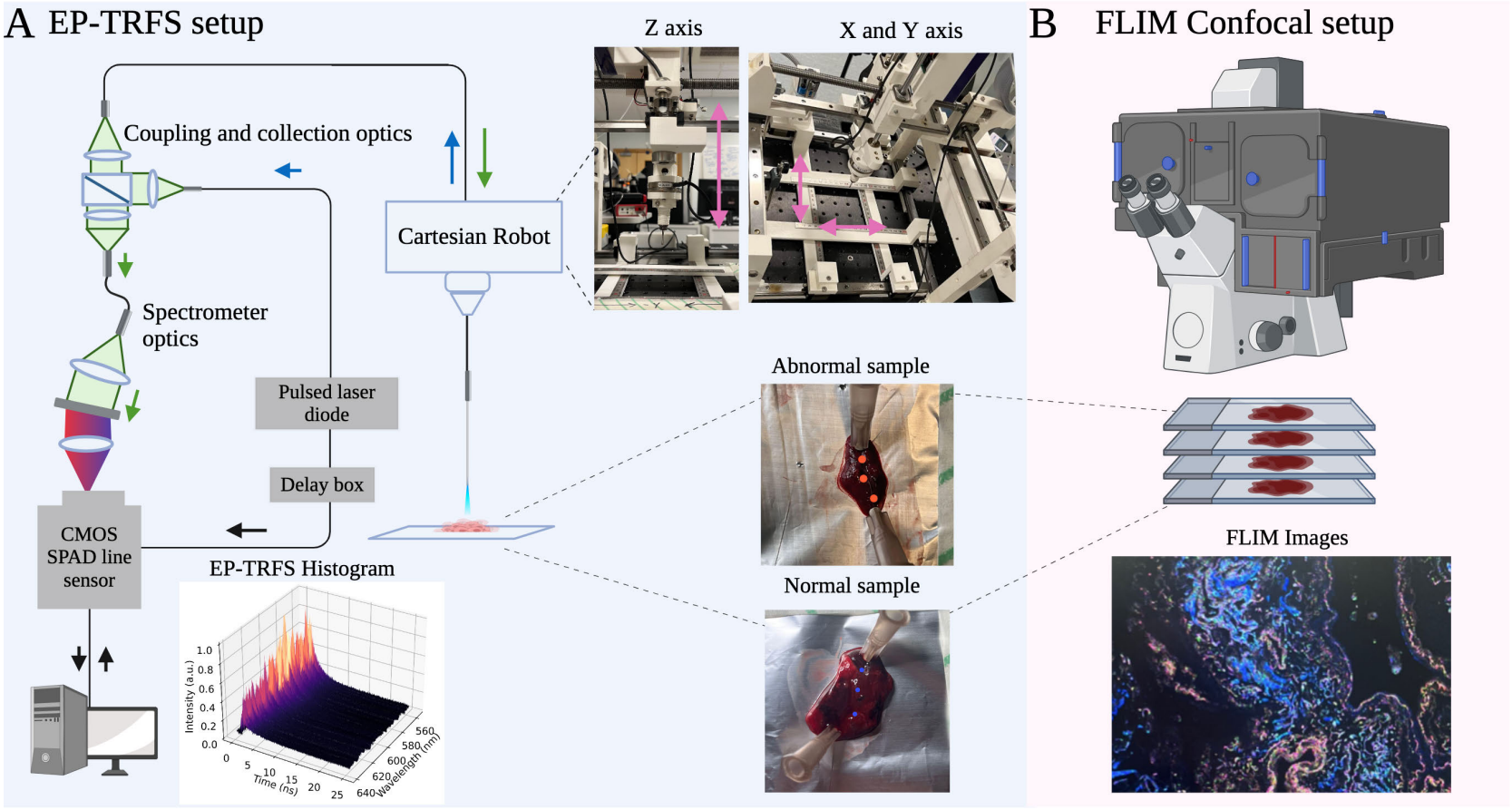

Figure 5.1: A schematic diagram of the workflow of the paper. **A)** *Ex vivo* lung samples are first assessed using the extensively parallel time resolved fluorescence spectroscopy setup. This setup produces high-resolution histograms. **B)** Samples are then paraffin embedded and sliced onto microscope slides before being analyzed on the fluorescence lifetime imaging microscope (FLIM) confocal device producing FLIM images.

Table 5.1: Tissue samples analysed alongside their respective features, with the number of components fitted using a multi-exponential MuFLE model displayed. Samples where t-tests were conducted are highlighted in blue.

Sample label	Cancer type	Stage	Age	Sex	Number of 3 components	Number of 2 components
1	Adenocarcinoma	1	63	F	n/a	2 AB, 3 N
2	Adenocarcinoma	1	63	M	3 AB, 3 N	n/a
3	Adenocarcinoma	2	73	F	n/a	3 AB, 3 N
4	Adenocarcinoma	1	74	F	n/a	2 AB, 3 N
5	Adenocarcinoma	2	77	M	1 AB	2 AB, 3 N
6	Adenocarcinoma	3	86	M	3 AB, 3 N	1 N
7	Adenocarcinoma	n/a	83	F	n/a	2 AB, 3 N
8	Squamous cell carcinoma	3	77	M	1 AB	1 AB
9	Squamous cell carcinoma	3	66	M	3 AB, 4 N	1 N
10	Squamous cell carcinoma	3	67	M	3 AB, 3 N	n/a
11	Squamous cell carcinoma	3	68	F	2 AB, 3 N	1 AB
12	Squamous cell carcinoma	2	77	F	n/a	1 AB
13	Large cell neuroendocrine	3	81	M	n/a	4 AB, 2 N
14	Malignant melanoma	n/a	83	M	n/a	3 AB, 2 N
15	Adenocarcinoma	3	53	F	8 AB	2 AB, 10 N
16	Squamous cell carcinoma	1	69	F	1 AB 1 N	1 AB
17	Adenocarcinoma	3	73	F	n/a	n/a
18	Squamous cell carcinoma	3	79	M	2 AB, 3 N	8 AB, 6 N
19	Squamous cell carcinoma	2	82	M	n/a	2 AB, 3 N
20	Adenocarcinoma	3	67	M	4 AB	1 AB, 3N
21	Squamous cell carcinoma	2	72	M	3 AB, 17 N	4 AB, 4N
22	Adenocarcinoma	3	75	F	17 N	10 AB, 3 N
23	Adenocarcinoma	3	72	M	3 AB, 6 N	2 AB, 13 N

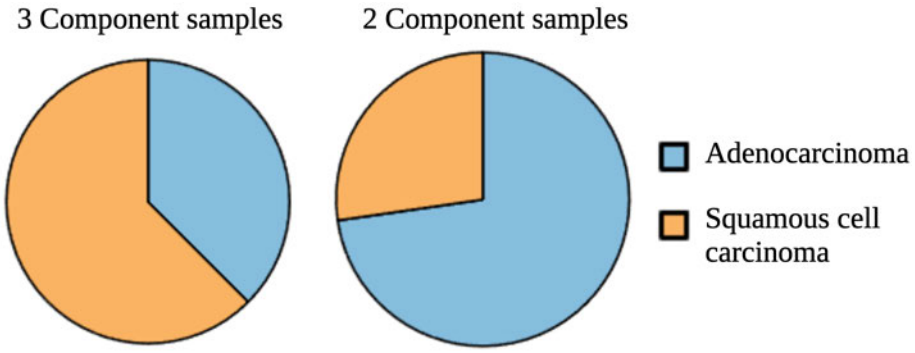

Figure 5.2: *Ex vivo* lung tissue samples were assessed using an extensively parallel time-resolved fluorescence spectroscopy device and analysed using the Multichannel Fluorescence Lifetime Estimation (MuFLE) model. Multi-exponential variations of MuFLE were applied, revealing tissue samples containing either 3 or 2 components. The tissue types, adenocarcinoma or squamous cell carcinoma, are shown to compare the number of components they exhibit.

5.2.3 EP-TRFS

The EP-TRFS device used in this study was used in TCSPC mode, the device has been characterised previously in [47] and [41]. A PicoQuant laser, with an excitation of 485 nm (laser diode head (LDH-P-C-485, PicoQuant, Germany) and laser driver (PDL 800-D, PicoQuant, Germany) used at a repetition rate of 20 MHz was used to excite the samples. This bespoke device has a highly integrated high-resolution line sensor which is able to measure 512 spectral channels of 0.5 nm resolution (or wavelength bandwidth resolution) and a total of 1200 time bins of 50 ps (temporal resolution). Histograms of photon arrival times measured at all channels in parallel using 1.5×10^6 exposures with a 5 µs exposure time and an optical laser output power of 175 µW. For the purpose of this study, a narrower spectral range was used for AF collection, 160 spectral channels between 552.03 nm-633.12 nm. We are limited to this spectral range due to the constraints of the IRF since an accurate measurement of the IRF is essential for the fitting routine used. In addition, due to both excitation filters and the dichroic beam splitter, following an excitation of 485 nm, we capture the emission tails of the 3 endogenous fluorophores anticipated to be present in the measured in tissue data as shown in [41, Fig. 2].

5.2.4 Fluorescence Lifetime Imaging Microscopy

A Leica STELLARIS Falcon FLIM confocal microscopy setup was used to assess the AF of paraffin embedded lung slides. To prepare the slides, a standard procedure was used, the tissue was fixed in formaldehyde 4 % in PBS overnight, then processed for embedding in paraffin on slides, 4 µm thick. The tissue was assessed on the FLIM device using two setups. The excitation and emission window of the device for both setups was 485 nm for excitation with an emission window of 550 nm-630 nm (so that the fluorescence collection matched the EP-TRFS). In the first setup a 20x objective lens was used, 512x512 spatial pixels were sampled, measuring images of 581.25 µm-581.25 µm, with a pixel size of 1.14 µmx1.14 µm. In the second setup zoom 4 was applied, such that images tiles of 145.31 µmx145.31 µm, with a pixel size of 0.284 µmx0.284 µm were collected. The analysis was performed using the multi-exponential precise fit method from the Leica X analysis software. The number of components was determined, in accordance to the FLIM Leica Handbook, when a chi-squared value close to 1 and smooth residuals was observed [45].

5.2.5 Analysis

The samples from the EP-TRFS device were analysed using a multi-exponential MuFLE model as detailed in [47]. Specifically MuFLE with 2 and 3 exponentials were assessed.

Multi-exponential MuFLE Analysis

In the multi-exponential MuFLE model, in addition to estimating the FI and FL simultaneously over all spectral channels, we assume the FL varying across the wavelength range is fixed, therefore, we used fixed FL values within the MuFLE model for each component where the number of exponentials are more than one, i.e., $L > 1$. The overall histogram can be described as

$$\begin{aligned} s[p,m] &= (f[p] * h[p])[m] + b[p] \text{ and} \\ f[p,m] &= \sum_{p=l}^{L} \gamma_l[m] \exp(-t_m/\tau_l[m]) \end{aligned} \tag{5.5}$$

where $\gamma_l[p]$ and $\tau_l[m]$ are spectral FI and FL for the individual components, $h[p][m]$ is the IRF and $b[p]$ is the dark count rate. $\gamma_l[m]$ is modelled using cubic B-splines (B_i) with equidistant knots as described in [47], i.e., $\gamma_l(\omega) = \sum_{i=1}^{I_\gamma} a_{li}^{\gamma} B_i(\omega)$, while $\tau_l[m]$ = τ_l is modelled to be fixed over channels. Given $y[p,m]$ is the observed signal at the m-th time bin and p-th spectral channel, the coefficients a_{li}^{γ} and τ_l are estimated by minimising the loss function (assuming $h[p,m]$ is known)

$$J_2 = \sum_{p=1}^{P} \sum_{m=1}^{M} (y[p,m] - s[p,m])^2. \tag{5.6}$$

The FI coefficients a_{li}^{γ} are initialised with randomly generated values uniformly distributed between (0, 1), and FL coefficients $\tau_l[m]$ are initialized with randomly generated values uniformly distributed between (0, 4). The solution with the lowest cost function from 10 different initialisations was chosen for further analysis.

Number of Exponentials

To determine the suitable number of components present in the tissue data, we fitted MuFLE with 2 and 3 exponentials since we expect at most three fluorophores to be excited in the tissue data from the excitation wavelength used. We choose the number of components with the least residual variance, referred to as ℓ. However, we prefer a smaller number of components, i.e., $\ell - 1$, if 1) one of the FLs in the best solution is less than 0.1 ns, as this is below the expected range of endogenous fluorophores found in tissue, and 2) if the difference between any two FLs is less than 0.5 ns, as these similar FLs might be a result of convergence issues due to inherently noisy measurements, and they might be originating from the same fluorophore.

Table 5.2: The average fluorescence lifetime of a tri-exponential MuFLE model applied to both cancerous and non-cancerous *ex vivo* lung tissue.

	Cancerous lifetime (ns)	Non-cancerous lifetime (ns)	p value
Lifetime 1	0.25 ± 0.099	0.19 ± 0.10	0.012
Lifetime 2	1.15 ± 0.37	1.017 ± 0.38	0.078
Lifetime 3	4.24 ± 1.52	4.13 ± 1.56	0.73

5.3 Results

5.3.1 Simulated Data

First, the accuracy of a multi-exponential MuFLE model on simulated data is assessed. The effectiveness in MuFLE un-mixing simulated fluorophores with overlapping emission spectra and similar FL compartments are explored (see appendix section 7.2 & Fig.7.2). In both the double and triple exponential mode, MuFLE accurately un-mixed spectral and temporal profiles of the underlying simulated fluorophores where the spectral regions overlap (as is expected with the fluorophores present in tissue following excitation at 485 nm). Moreover, where spectral emission peaks are present, MuFLE accurately un-mixed both the spectral and temporal profiles, showing if this model is to be extended to an excitation range assessing fluorophores with different peaks, MuFLE may be applied (see appendix Fig. 7.2).

5.3.2 Multi-Exponential Tissue and Endogenous Fluorophores

Next, we assess individual components within the *ex vivo* paired cancerous and non-cancerous tissue data. To determine how many components are present within each measurement a specific regime is applied, as aforementioned in section 5.2.5. From a total of 252 histograms (100 cancerous and 152 non-cancerous), a total of 102 histograms is observed to contain 3 components and 123 to contain 2 components (see Table 5.1). Within the histograms with 3 components, we observe 36 % as cancerous and 64 % as non-cancerous (see Fig. 5.3 A-D); within the 2 component data, we observe 41 % as cancerous and 59 % as non-cancerous (see Fig. 5.3 E-H). Furthermore, in assessing the number of components compared to the cancer type, a higher proportion of squamous cell carcinomas were found to contain 3 components, whereas more adenocarcinoma samples were found to contain 2 components (see Fig. 5.2 & Table 5.1).

Triple Component Assessment

Distinct average FL values can be observed from histograms containing 3 components, as presented in Table. 5.2. Furthermore, there is a decrease in the average FL across all compartments in the non-cancerous samples compared to the cancerous samples (see Table. 5.2).

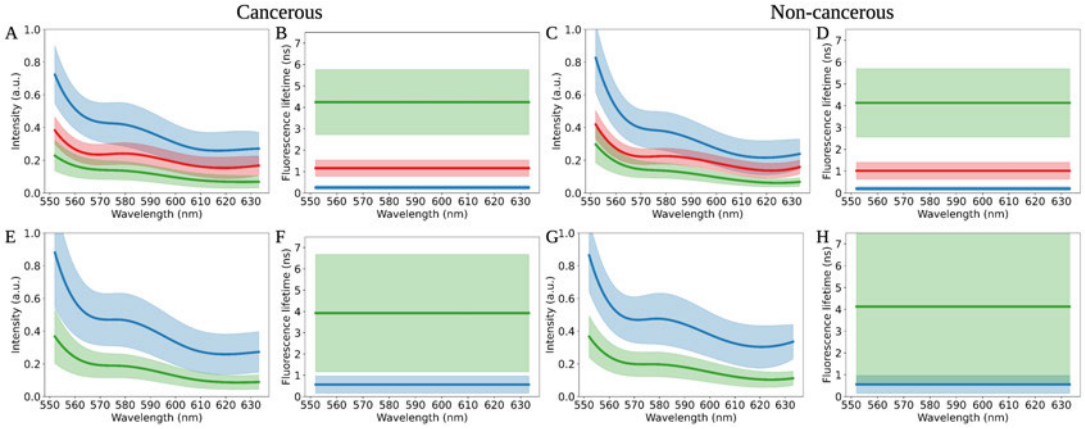

Figure 5.3: The average spectral-temporal profiles of *ex vivo* clinically defined cancerous and non-cancerous lung samples are shown. The samples were assessed using a multi-exponential Multichannel Fluorescence Lifetime Estimation (MuFLE) model. Two and three components are observed within the tissue data. The average spectral profiles from the tri-exponential cancerous samples are shown in **A)**, and the corresponding temporal (or fluorescence lifetime) profiles are shown in **B)**. The average spectral profiles from the bi-exponential cancerous samples are shown in **E)**, and the corresponding temporal profiles are shown in **F)**. In comparison, the average spectral profiles from the tri-exponential non-cancerous samples are shown in **C)**, and the corresponding temporal profiles are shown in **D)**. The average spectral profiles from the bi-exponential non-cancerous samples are shown in **G)**, and the corresponding temporal profiles are shown in **H)**.

When comparing the 3 FL values estimated within the tissue data to the FL of specific endogenous fluorophores anticipated to be excited at 485 nm and emit within the measured emission window of the EP-TRFS device, similarities are observed (see Fig. 5.4 and Table. 5.3). Specifically, the FL range of protein bound FAD, as reported in the literature, is anticipated to be between 0.1 ns-0.95 ns [160, 21]. A similarity between this FL range and the shortest FL value observed in the tissue data is observed (average cancerous 0.25 ns $\pm$ 0.099, average non-cancerous 0.19 ns $\pm$ 0.10) (see Fig. 5.4 D-F). Furthermore, a similarity is observed in the corresponding emission spectra in both shape and magnitude, between the spectra of FAD measured benchside and those corresponding to the short FL values (see Fig. 5.4 A-C).

The FL of elastin, as reported in the literature, is between 1.72-2.3 ns [89, 21] (see Table. 5.3). In addition, when elastin is measured benchside on the EP-TRFS device, a value of 1.13 ns is observed. An overlap between the FL range with the middle FL value estimated within the tissue data, and the elastin when measured benchside is observed (average cancerous 1.28 ns $\pm$ 0.56, average non-cancerous 1.09 ns $\pm$ 0.39) (see Fig. 5.4 D-F). A comparable shape and magnitude in the emission spectrum of the FL corresponding to the middle component in tissue, and the emission spectra of elastin measured benchside on the EP-TRFS device is also observed (see Fig. 5.4 A-C).

Table 5.3: Fluorescence lifetime values of the endogenous fluorophores excited at 485 nm as described in the literature.

Protein bound FAD lifetime (ns)	Elastin lifetime (ns)	FAD in PBS lifetime (ns)	FAD/FMN/Riboflavin lifetime (ns)
0.15-0.33 [21]	1.72-1.83 [89]	2.5[21]	3.13 [161]
0.3-0.4 [160]	$<$ 2.3[21]	2.8[21]	4.27-4.67 [21]
0.5-0.95[21]			4-12 [21]
			2.5-2.8 [160]

The 3rd FL component estimated from the tissue data exhibits the longest FL value among the unmixed components (average cancerous 4.40 ns $\pm$ 1.75, average non-cancerous 4.15 ns $\pm$ 1.41) (see Fig. 5.4 E & F). Notably, comparable FL values are observed between the FL of riboflavin measured on the EP-TRFS device (4.31 ns) and the longer FL values from the third component in tissue. Furthermore, similarities are also noted in the range of this FL measured in tissue compared to the anticipated FL values of both protein unbound FAD and protein bound FMN, as reported in the literature (3.13 ns-12 ns) [161, 21] (see Table. 5.3).

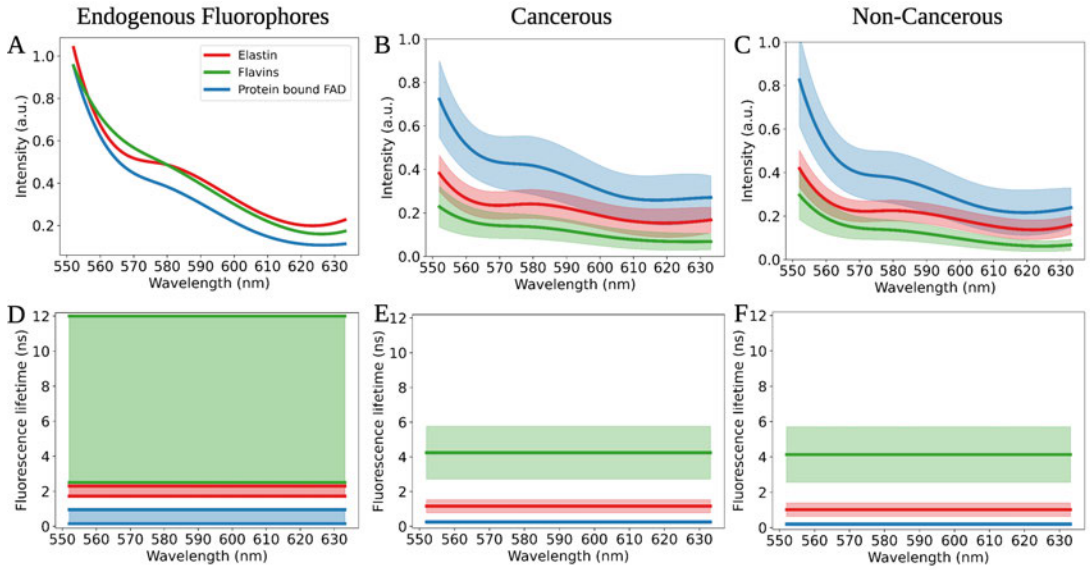

Figure 5.4: The spectral-temporal comparison of different samples measured on the extensively parallel time resolved fluorescence spectroscopy (EP-TRFS) device, coupled with the Multichannel Fluorescence Lifetime Estimation (MuFLE) model. The emission spectrum of MuFLE between endogenous fluorophores measured benchside **A)** is compared to *ex vivo* lung resections clinically defined as cancerous and non-cancerous **B)** & **C)**. The fluorescence lifetime (FL) values between endogenous fluorophores reported in the literature **D)** and the FL estimated using MuFLE on *ex vivo* lung resections **E)** & **F)** are also compared. The filled lines represent the average values and the shaded lines represents the standard deviation.

Table 5.4: The average fluorescence intensity of a tri-exponential MuFLE model applied to both cancerous and non-cancerous *ex vivo* lung tissue.

	Cancerous intensity (a.u.)	Non-cancerous intensity (a.u.)	p value
Intensity 1	0.37 $\pm$ 0.089	0.34 $\pm$ 0.085	0.15
Intensity 2	0.21 $\pm$ 0.052	0.20 $\pm$ 0.033	0.42
Intensity 3	0.11 $\pm$ 0.047	0.11 $\pm$ 0.038	0.58

When evaluating the relative FI of the 3 components using their corresponding FL and matching emission profiles in both cancerous and non-cancerous samples, the highest relative FI, on average, originating from the fluorophore with the shortest FL is consistently observed (average cancerous 0.37 $\pm$ 0.089, average non-cancerous 0.34 $\pm$ 0.085). Conversely, the lowest relative FI is observed to originate from the fluorophore with the longest FL (average cancerous 0.11 $\pm$ 0.047, average non-cancerous 0.11 $\pm$ 0.038) (see Table. 5.4). These findings are consistent with literature reports, where it was observed that over 70 % of the emission originated from a short FL compartment, with the longest FL compartment displaying the lowest FI 15 %-25 % [160, 110].

Double Component Assessment

When comparing the 2 component FL values estimated within the tissue data to the FL of specific endogenous fluorophores anticipated to be excited at 485 nm and emit within the measured emission window of the EP-TRFS device, similarities are also observed (see Fig. 5.3 E-H and Table. 5.3). Notably, similarities are observed with the component exhibiting the shortest FL value and the FL value of protein bound FAD (average cancerous 0.56 ns $\pm$ 0.40, average non-cancerous 0.55 ns $\pm$ 0.41). Although these values are marginally higher than those observed in samples where 3 components are estimated, there is overlap. Furthermore, this component also displays a higher FI (average cancerous 0.43 $\pm$ 0.10, average non-cancerous 0.40 $\pm$ 0.13).

Similarities are also observed with the longer FL and the FL corresponding to the group of flavins (including FMN, unbound FAD, and riboflavin) (average cancerous 4.12 ns, average non-cancerous 3.92 ns). However, the range of the FL from this compartment is notably broader than the range from the samples displaying 3 components (average cancerous 4.12 ns $\pm$ 3.48, average non-cancerous 3.92 ns $\pm$ 2.75) (see Fig. 5.3 F & H). The broad range of this longer FL component also aligns with both FL values of elastin reported in the literature and measured on the EP-TRFS device. Moreover, the FI with the long FL component exhibits the

Table 5.5: The average fluorescence lifetime of a bi-exponential MuFLE model applied to both cancerous and non-cancerous *ex vivo* lung tissue.

	Cancerous lifetime (ns)	Non-cancerous lifetime (ns)	p value
Lifetime 1	0.56 ± 0.40	0.55 ± 0.41	0.95
Lifetime 2	3.92 ± 2.75	4.12 ± 3.48	0.72

Table 5.6: The average fluorescence intensity of a bi-exponential MuFLE model applied to both cancerous and non-cancerous *ex vivo* lung tissue.

	Cancerous intensity (a.u.)	Non-cancerous intensity (a.u.)	p value
Intensity 1	0.40 ± 0.13	0.43 ± 0.10	0.26
Intensity 2	0.15 ± 0.059	0.17 ± 0.053	0.17

lowest relative FI (average cancerous 0.15 ± 0.059, average non-cancerous 0.17 ± 0.053) (see Table. 5.5 & Table. 5.6), aligning with the findings from the literature and with the 3 component samples. In addition, similarities in the emission profile in both elastin and the group of longer FL flavins can be observed (see Fig. 5.3 E & G).

In summary, the FL components from the tissue data using MuFLE, significantly overlap in both the spectral and temporal domain of the three distinct fluorophores anticipated to be present following an excitation of 485 nm. Note that a difference between FAD measured benchside (with an average FL of 2.65 ns $\pm$ 0.05) compared to the two anticipated lifetimes of FAD present within tissue is observed. A difference between FAD measured in PBS in the literature (2.5 ns-2.9 ns [21]), with FAD present in tissue is also observed (see Table. 5.3).

Cancerous vs Non-Cancerous Component Assessment

Next, under the assumption that the individual components reflect the photo-physical properties from the same/similar biological origin, sample specific changes of the components are investigated. Following the exponential regime (see section 5.2.5), 3 components are observed in 8 paired cancerous and non-cancerous samples, and 2 components are observed in 13 samples (see Table 5.1, blue highlights). A Welch's t-tests is calculated between the FL and average spectral FI of the components from samples where a suitable number of point-sampling measurements are collected. Differences with a p-value <0.05 are considered significant (see appendix Table 7.1, Table 7.3, Table 7.4 & Table 7.5).

A significant increase in one sample (sample 11) between the 2 longer FL components in the cancerous and non-cancerous tissue following a tri-exponential MuFLE assessment can be observed (p-value of 0.013 & 0.05)(see appendix Table 7.1). A significant difference between sample 18 can be observed between the cancerous and non-cancerous tissue in the average spectral FI of the two components corresponding to the longer FL components following a tri-exponential MuFLE assessment (p-value of $<$0.01 for both components is observed).

A significant increase in samples with 2 components, is observed between the FL of 3 cancerous and non-cancerous samples: samples numbered 1, 3 and 18 (see appendix Table 7.4). A significant decrease in sample number 15 and a significant increase in one component, however, decrease in another component is observed in sample number 19 (see appendix Table 7.4). In samples 1 and 3, the significant difference is observed from the component with the longest FL, however, in samples 15, 18 and 19 the significant difference is observed from both components. A significant difference is observed in the average spectral FI components between the cancerous and non-cancerous tissue from samples 18 and 19 (see appendix Table 7.5). A difference in both FI components is observed in sample 18, however, only a significant difference from the component with the longest FL is observed in sample number 19. In summary, based on this data measured with the EP-TRFS device and MuFLE, no single component contributes as definitively more significant in influencing the fluorescence properties of tissue. The wide range of significance observed across components, in both the FL and FI domains, emphasises the complementary roles these parameters play in detecting tissue changes.

Un-mixing of tissue types

To assess whether the spectral and/or temporal profile of the unmixed fluorophores provides greater insight into sample-specific changes, two histograms from two samples are compared (sample 2 and sample 23). An overall increase in FL in the cancerous sample compared to the non-cancerous sample is observed in sample 2 (average cancerous lifetime: 1.31 ns $\pm$ 0.07, average non-cancerous lifetime: 1.17 ns $\pm$ 0.07). Comparable FI magnitudes, in contrast is observed (average non-cancerous lifetime: 0.44 $\pm$ 0.08, average cancerous lifetime: 0.49 $\pm$ 0.07) (see Fig. 5.5 A). Furthermore, the shape of the SFL between the different sample types is similar (see Fig. 5.5, B). When assessing the samples using a multi-exponential model two specific alterations are observed, first, the relative concentration of the 3 components remains similar between both the cancerous and non-cancerous samples (see Fig. 5.5 C). Second, an increase by 0.34 ns between the 2nd component (red) and 0.30 ns of the 3rd component (green) in the cancerous sample, compared to the non-cancerous sample is observed (see Fig. 5.5 D). We hypothesise that the increase of these specific FLs is contributing to the overall

increase in the cancerous FL compared to the non-cancerous FL in this particular instance (see Fig. 5.5 B & D). In addition, the SFL shape of these samples in the single component model is comparable. We hypothesise that the similarity in the relative concentration of the individual FIs is contributing to the similarity of the SFL shape (see Fig. 5.5 B & C).

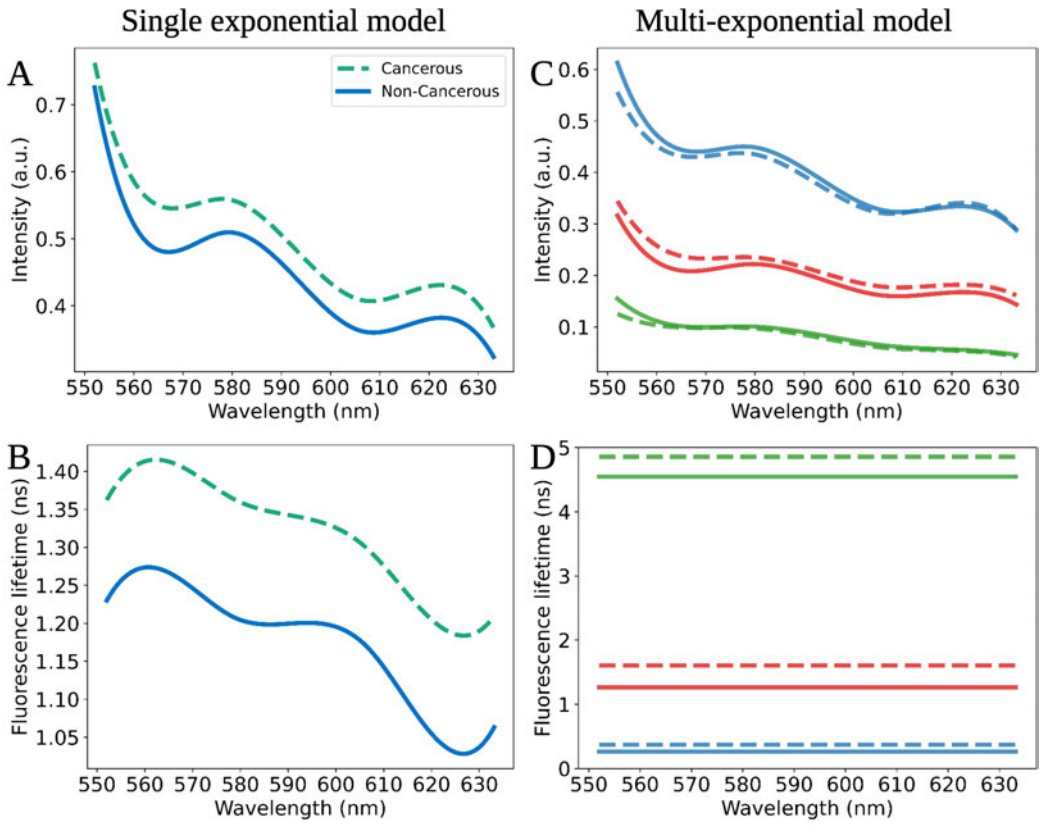

Figure 5.5: The fluorescence intensity (FI) and fluorescence lifetime (FL) of the same paired *ex vivo* clinically defined cancerous (dashed) and non-cancerous (solid line) samples, measured using component variations of the Multichannel Fluorescence Lifetime Estimation (MuFLE) model. The single exponential model extracts the average FI **A)** and the spectral fluorescence lifetime **B)**. The multi-exponential model estimate component specific FI **C)** and corresponding fluorescence lifetime **D)**.

Comparable FI magnitudes are observed in sample 23 (average cancerous FI: 0.29 $\pm$ 0.15, average non-cancerous FI: 0.38 $\pm$ 0.15) (see Fig. 5.5 A). In addition, comparable average FL values of the cancerous sample compared to the non-cancerous sample is also observed (average cancerous lifetime: 1.33 ns $\pm$ 0.05, average non-cancerous lifetime: 1.32 ns $\pm$ 0.04) (see Fig. 5.6 B). However, a different SFL shape in the cancerous sample compared to the non-cancerous sample can be observed. Most notably, a peak at 600.99 nm is observed in the cancerous sample and a peak at 552.03 nm observed in the non-cancerous sample (see Fig. 5.6 B). When assessing the samples using a multi-exponential MuFLE model two sample specific changes can be observed. First, the relative concentration of the 3 com-

ponents between the sample types differs. Most prominently, a change in the relative FI of the 1st component (blue) can be observed (the FI corresponding to the FL of 0.22 ns). Particularly, at 600 nm where it is observed to drop below the FI corresponding to elastin (the FI corresponding to the FL of 0.90 ns) (see Fig. 5.6 C). Second, the non-cancerous FL values were higher in the individual components, compared to the cancerous sample (see Fig. 5.6 D). We hypothesise that the changes in the relative concentration of the 3 components contributes to the lack of difference between the average FL of the two samples. Furthermore, we hypothesise that the peak in shape of the SFL of both samples is also influenced by the relative concentration. In the cancerous sample a peak in the SFL is observed at 600 nm. This is the spectral location where the FI of the shortest FL is lower than FL corresponding to the 2nd component (red), contributing to the peak in the SFL (see Fig. 5.6 C & D). The relative intensities of the 3 components in the non-cancerous sample are constant, therefore, the peak in the SFL reflects the peak of the intensities from all components (i.e., at 552 nm). These results align with the previous results from [41] and Chapter 4, highlighting the influence of the relative concentration of specific fluorophores to both the average and shape of the SFL.

In summary, we show that when un-mixing in both the spectral and temporal domain, we can potentially underpin the components effecting the overall fluorescence of a sample. We observed that in specific cases, despite a similar average FL between the cancerous and non-cancerous sample, a change in FLs between the specific components may still be present, and, these changes are better identifiable when both spectral and temporal properties are taken into consideration.

5.3.3 FLIM Data

Immediately following assessment on the EP-TRFS device, 3 paired *ex vivo* cancerous and non-cancerous samples numbered 11, 15 and 16 (6 tissue samples in total) are analysed using FLIM following formalin fixation and paraffin embedded onto 4 µm slides. 4 fluorescence components are observed from all but two tissue areas, where in these cases 3 components are observed when measured on the FLIM (see section 5.2.4 & appendix Fig 7.9-7.14). The shortest FL value of the components observed in the FLIM device is on average 0.41 ns $\pm$ 0.05 in the cancerous and 0.39 ns $\pm$ 0.05 in the non-cancerous sample. This value aligns with the FL measured on the EP-TRFS device of the same samples (see Fig. 5.7) and the FL of protein bound FAD (see Table. 5.3). The average 2nd component within the FLIM data is 1.62 ns $\pm$ 0.21 in the cancerous and 1.60 ns $\pm$ 0.25 in the non-cancerous. These values are also similar to the FL of the 2nd component measured on the EP-TRFS device and the anticipated FL of elastin (see Table. 5.3). The average 3rd component within the FLIM data is 4.47 ns $\pm$ 0.44 in the cancerous and 4.54 ns $\pm$ 0.72 in the non-cancerous. This value also aligns with the FL of the 3rd component measured on the EP-TRFS device and the FL of the flavins group (protein un-bound FAD/FMN/riboflavin) (see Table. 5.3). The average

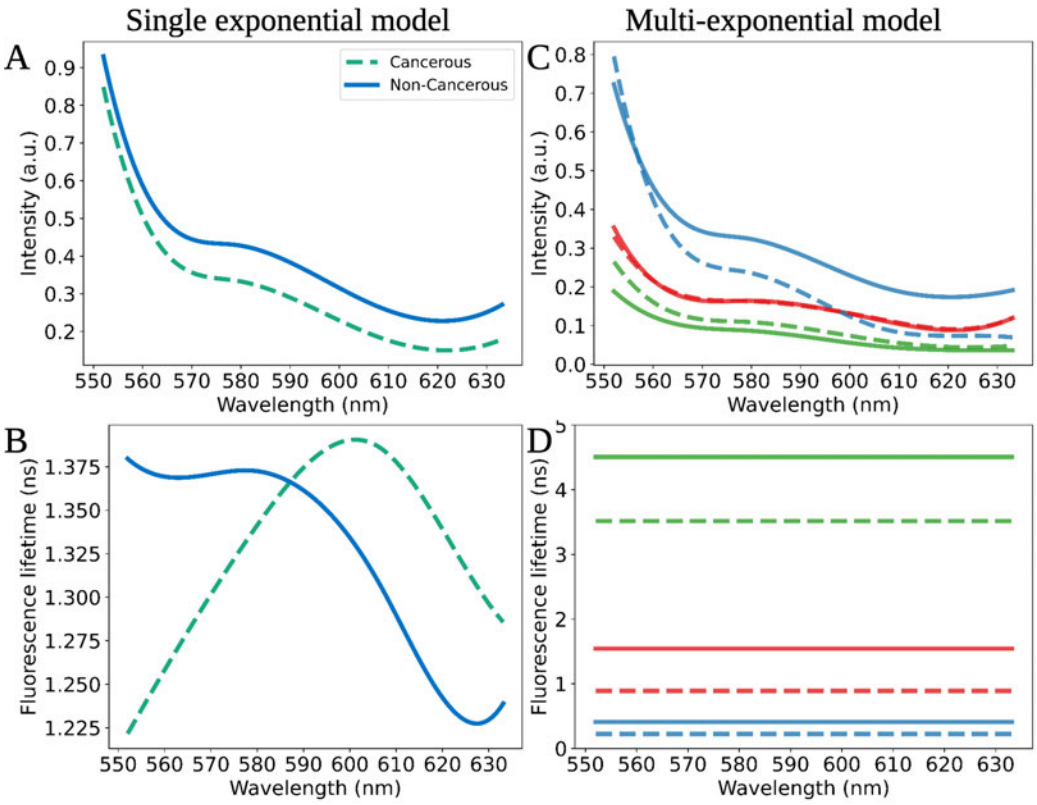

Figure 5.6: The fluorescence intensity (FI) and fluorescence lifetime (FL) of the same paired *ex vivo* clinically defined cancerous (dashed) and non-cancerous (filled) lung samples, measured using exponential variations of the Multichannel Fluorescence Lifetime Estimation (MuFLE) model. The average FI is shown **A)** alongside the corresponding average spectral fluorescence lifetime **B)**. The same measurements assessed on the multi-exponential MuFLE model are then compared. The FI of the individual components is shown **C)**, compared to the corresponding fluorescence lifetime values **D)**.

4th component within the FLIM data is the longest 12.16 ns $\pm$ 0.89 in the cancerous and 12.25 ns $\pm$ 1.76 in the non-cancerous sample. This value is not observed in the average FL of tissue when measured on the EP-TRFS device, however, these values are similar to the 3rd component in the cancerous sample number 11 (FL of 10.25 ns $\pm$ 0.71) (see Fig. 5.7 A). This value also falls within the upper range of the group of flavins (protein un-bound FAD/FMN/riboflavin), as estimated from the literature (see Table. 5.3).

When assessing sample specific FLIM compared to the EP-TRFS values, some discrepancy is observed. First, when measured on the EP-TRFS device, 2 components are estimated from all locations of sample 15. However, 4, and in two cases 3 components are estimated from the FLIM device (see appendix Fig 7.12). In both sample types measured on the EP-TRFS device, the highest FI is observed in the compartment with the lowest FL, this matches the FI from the components measured on the FLIM device. Moreover, in both tissue sample, the average FL values of the first component when measured on the FLIM align with the 1st average FL

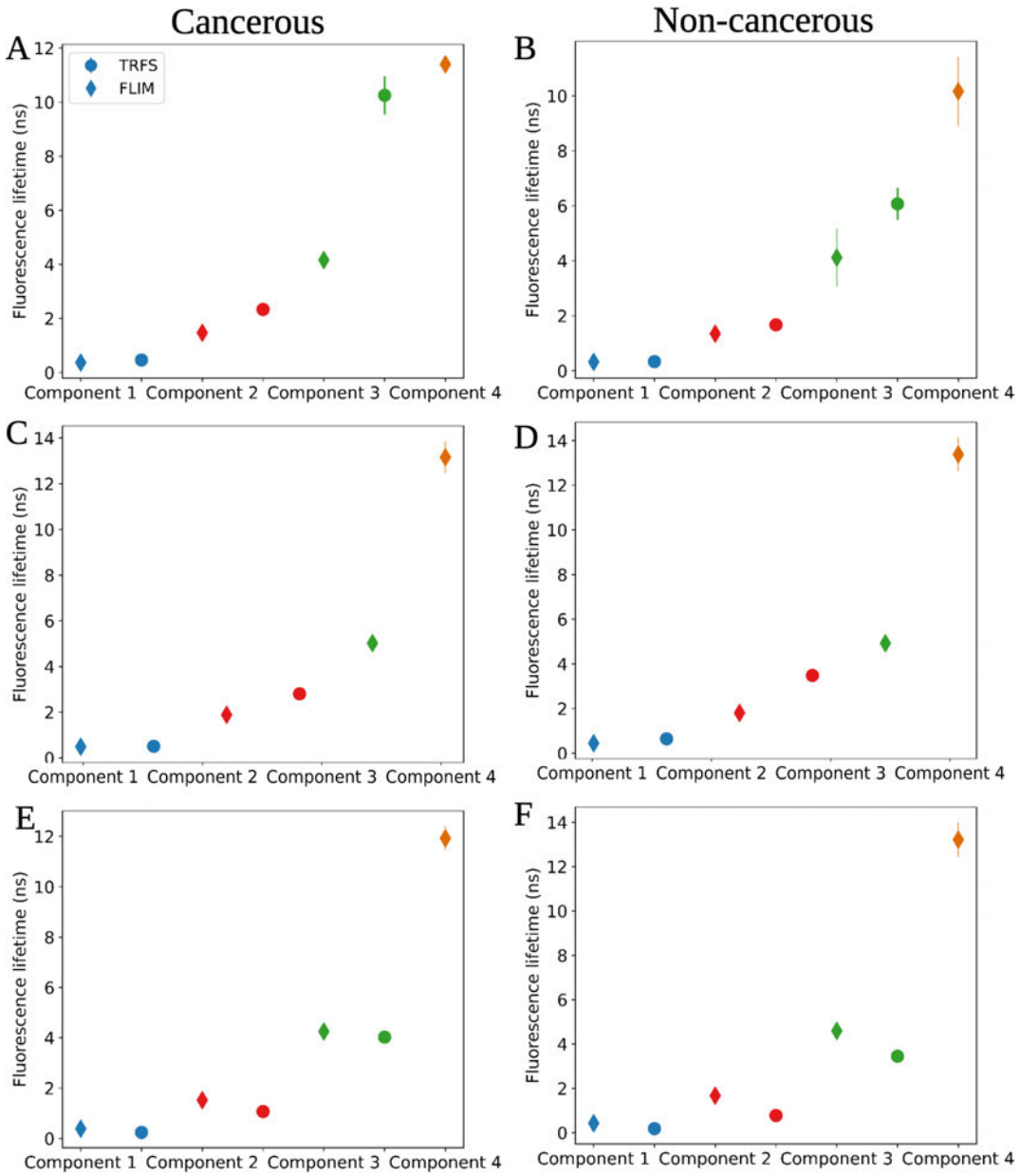

Figure 5.7: The fluorescence lifetime (FL) of *Ex vivo* lung samples clinically defined as cancerous and non-cancerous measured on either a time resolved fluorescence spectroscopy device (TRFS)(circles), and on a fluorescence lifetime imaging microscope (FLIM)(diamonds). Paired samples from sample number 11 are shown in figures **A)** & **B)**, paired samples from sample number 15 are shown in figures **C)** & **D)**, and paired samples from sample number 16 are shown in figures **E)** & **F)**.

value measured on the EP-TRFS device (Cancerous FL is 0.48 ns $\pm$ 0.03 in the FLIM device and 0.50 ns $\pm$ 0.02 in the EP-TRFS device. Non-cancerous FL is 0.44 ns $\pm$ 0.02 in the FLIM device and 0.64 ns $\pm$ 0.04 in the EP-TRFS device) (see Fig. 5.7 and Fig. 5.9). The FL from the 2nd component, when measured on the EP-TRFS in the non-cancerous sample is in between

the range of the 2nd and 3rd component measured on the FLIM device (FL of component 2 is 3.48 ns $\pm$ 0.16 on the EP-TRFS device. FL of component 2 is 1.80 ns $\pm$ 0.08 on the FLIM device & the FL of component 3 is 4.92 ns $\pm$ 0.23 on the FLIM device). In addition, due to limitations in the sample size, only 1 location was measured on sample 16 on the EP-TRFS device. Therefore, despite very similar FL values from both the cancerous and non-cancerous components between the EP-TRFS device and FLIM device (see Fig. 5.7 and Fig. 5.9), the sample size from the EP-TRFS device is limited.

The advantage of the FLIM analysis, although not applicable *in vivo* with this device, is the assessment of fluorescence images of tissue at a cellular level. The initial FLIM measurements had a larger pixel size and a lower spatial resolution (see appendix Figs. 7.3-7.8). Therefore, to assess the location of the FL components in more detail, paired cancerous and non-cancerous slides from sample 11 on the FLIM device with a smaller pixel size and a higher spatial resolution are investigated (FLIM pixel sizes of 145.31 µmx145.31 µm) (see section 5.2.4 for more detail) (see Fig. 5.8). A matching colour map is applied and the average FL is assessed. In both samples, the 1^{st} component with the shortest FL (estimated to be protein bound FAD) is the brightest and present in the most image pixels. This value appears to be present in cell like features (see Fig.5.8 non-cancerous sample's white arrows). Clear structural features from the 2nd component (estimated to be elastin) are also visible in both the cancerous and non-cancerous samples (see Fig.5.8 cancerous sample's white arrows).

In summary, we show the fluorescence component values assessed using the FLIM device on the same tissue, to be in agreement with some of the fluorescence components assessed on the EP-TRFS device un-mixed using MuFLE. We also observe spatial areas of tissue from both cancerous and non-cancerous samples to be dominant in either the 1st, shortest FL component, or the 2nd component which highlights clear structural features of tissue (see Fig.5.8 white arrows).

5.4 Discussion

Current devices with the potential to measure FL *in vivo* typically assess the average FL from channels with low wavelength bandwidth resolutions e.g., [126]. However, a comparative understanding of the origin of total fluorescence from individual endogenous fluorophores is complex and nuanced. Therefore, devices which measure fluorescence at a high-resolution coupled with bespoke analysis tools, in both the spectral-temporal domain may provide additional insights into the endogenous fluorophores. Our initial results show that using multi-exponential MuFLE un-mixing, FL from *ex vivo* lung tissue separates into two or three components in both the cancerous and non-cancerous paired tissue. When assessing the number of components present in the tissue compared to the cancer type, a higher proportion of

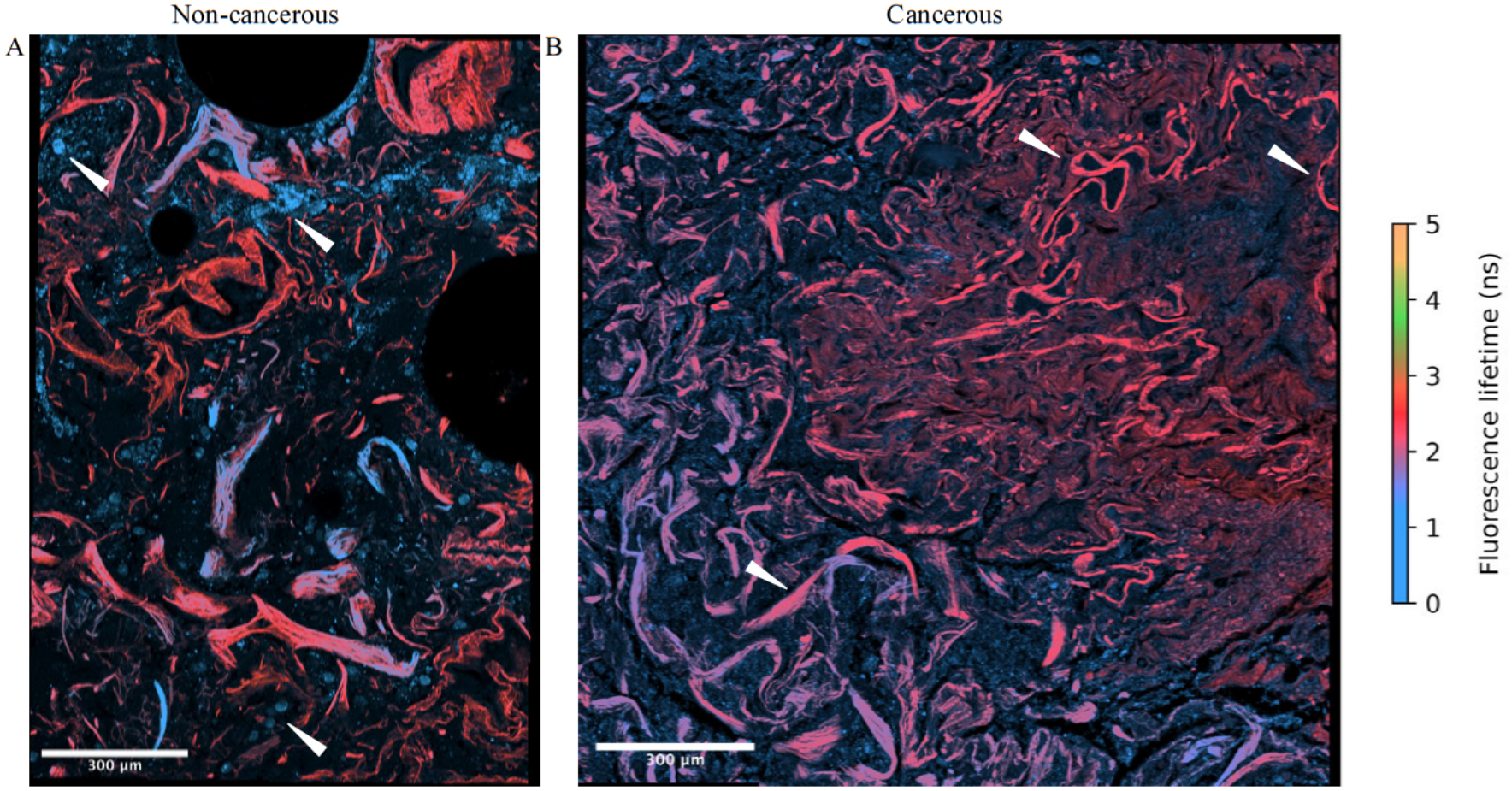

Figure 5.8: The average fluorescence lifetime (FL) measured of a fluorescence lifetime imaging microscope sample of a non-cancerous, paraffin embedded 10 µm thick lung slice **A)**, compared to the corresponding paraffin embedded cancerous slice **B)**. The colour map of the fluorescence lifetime values is displayed on the key, blue is chosen for short FL, red middle FL, green longer FL and orange the longest FL. Structural and cell like features are highlighted with the white arrows. The FL values were calculated using the Leica X precise fitting software. The images were processed using Python and FIJI.

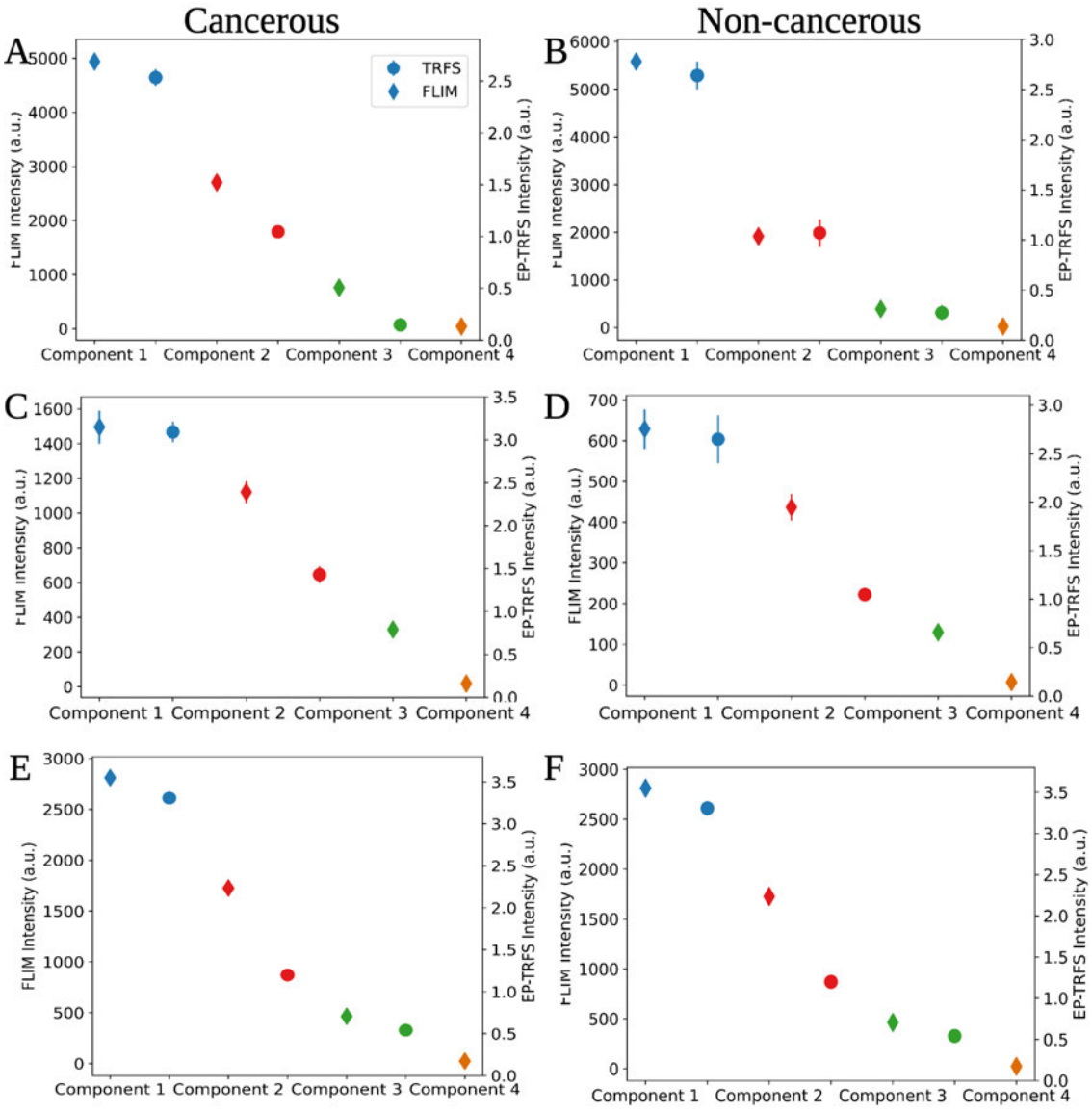

Figure 5.9: The fluorescence intensity (FI) of *ex vivo* lung samples clinically defined as cancerous and non-cancerous measured on either a time resolved fluorescence spectroscopy device (TRFS)(circles), and on a fluorescence lifetime imaging microscope (FLIM)(diamonds). Paired samples from sample number 11 are shown in figures **A)** & **B)**, paired samples from sample number 15 are shown in figures **C)** & **D)**, and paired samples from sample number 16 are shown in figures **E)** & **F)**.

squamous cell carcinomas were found to contain 3 components, whereas more adenocarcinoma samples were found to contain 2 components (see Fig. 5.2). This observation may be attributed to differences in the elastin compartment, often observed in adenocarcinoma, where elastin can become damaged and fragment [81]. However, further experiments are required to confirm this hypothesis. When assessing the ranges of the two and three components the samples are split into, we observe the respective FLs to overlap with FLs expected from

fluorophores that may be excited in tissue following an excitation wavelength of 485 nm. Specifically, FAD bound to protein, elastin and FAD unbound to protein/FNM/riboflavin. We also observe overlap in the spectral region of these fluorophores when measured benchside on the same device, and when measured on a plate reader (see Fig. 5.4).

Differences between the average FL and spectral FI of individual cancerous and non- cancerous samples are assessed. In both samples with 2 and 3 components identified, statistical significance is observed in some of either the FL and/or average spectral FI from the components. A significant difference in 2 samples (numbers 15 & 19) is observed between their cancerous and non-cancerous SFL values (see section 4.3), however, not observed in samples 1, 3, 11 or 18, suggesting the multi-exponential model may captures fluorophore specific changes better between the tissue types.

Specific SFL and multi-exponential component changes between cancerous and non- cancerous samples are next compared in more detail (see section 5.3.2). In the first sample, we observe a constant relative concentration of the 3 components, however, an increase in FL of the 2^{nd} and 3^{rd} components can be observed (which also match the FL of fluorophores identified as elastin and protein un-bound FAD/FMN/riboflavin). These components appear responsible for the overall average increase in the cancerous SFL compared to the non-cancerous SFL. In the second sample, we observe no change in the average FL between the non-cancerous and cancerous sample. However, we observe different SFL shapes between the two samples. Furthermore, when assessing the individual components, we observe an increase in FL between all components from the non-cancerous sample compared to the cancerous sample. Moreover, we observe a change in the relative concentration of the 1^{st} component (which match the FL of protein bound FAD) in the cancerous sample compared to the non-cancerous sample. This change, we observe, also influences the average FL, therefore, despite a constant drop in all FL values of the components in the cancerous sample, as the 1^{st} component (matching protein bound FAD) drops in relative concentration, the overall average FL is higher, counteracting a FL difference when only the averages are assessed (see section 5.3.2). These results highlight the insights into the fluorescence properties of a sample gained through high resolution assessments using models such as MuFLE. As the detailed fluorescence information is lost when the average FL from marginalised histograms is only considered.

We finally assess the same tissue when measured on the EP-TRFS and when measured on the Leica STELLARIS Falcon FLIM confocal microscope. We observe that the first 3 (in increasing order) FL components of the FLIM fall within a similar range of the components of MuFLE when measured with the EP-TRFS device from the same samples (see Fig. 5.7). However, a 4^{th} component with a FL value of around 12 ns measured on the FLIM device can also be observed. This has the lowest FI across the spatial sample. Therefore, given a non-uniformity of the FL ranges across the field of view, and the difference in sampling

size between the EP-TRFS and FLIM device, we rationalise this to be why a lifetime in the highest range is not present in the results from the EP-TRFS device (the EP-TRFS device has a smaller sampling area of $<100\,\mu m^2$ compared to the FLIM microscopic filed of view (see Fig.5.8)).

In addition, we observe spatial areas of these FL components when assessed on the FLIM device, particularly from the 2^{nd} (red) component, to define distinct structural areas of the lung (see Fig. 5.8). However, without further analysis, i.e., through additional biological techniques such as immunohistochemistry (IHC), determining if these structural features are elastin requires further analysis. Moreover, the FL particularly as estimated from protein bound FAD, although aligning with the value of this fluorophore within the literature, due to the sensitivity of FL to environmental features, also requires additional analysis, such as metabolic assessment of the same samples. Therefore, additional experiments are required to confirm the presence of individual fluorophores from the components which is something we save for future work.

There are several limitations in this study; a major limitation being the spectral width of the optical setup and the number of fluorophores expected to be excited from an excitation wavelength of 485 nm. An excitation within the UV range of 355 nm, for example, is likely to excite more endogenous fluorophores. In addition, the spectral range of the device could be enhanced to measure the emission peaks, this will allow a more comprehensive relative FI analysis to be made. Furthermore, the observed histograms generated from the EP-TRFS are particularly noisy, which we hypothesise is due to spectral sensitivity, that is the different sensitivity of detected photons within the individual SPADs [35]. These artefacts are not accounted for within the MuFLE model which may be limiting the number of components assessed reliably.

The final assumption within the device is that the components have a fixed spectral FL, while in the context of biological systems, coupled with the sensitivity of FL, ascertaining whether these signals are fixed and indeed originating from endogenous fluorophores alone is difficult. By jointly comparing the lifetime and spectral properties of the individual components from the sample, and of endogenous fluorophores when measured benchside, and of the same samples measured on a FLIM device, in addition to comparing the spatial location of these endogenous fluorophores using antibody staining (i.e., IHC which we save for future work), we can increase the confidence that what we see is of biological relevance. These results highlight the unprecedented biophysical detail between cancerous and non-cancerous samples which may be possible when high resolution devices, coupled with bespoke analysis models are applied to tissue data, improving both our understanding of AF, and of the diseased tissue.

5.5 Conclusion

In conclusion, we hypothesise that when using high resolution temporal-spectral EP-TRFS devices, coupled with a bespoke analysis model used to assess both the spectral and temporal components from the histograms, distinct endogenous fluorophores become recoverable label-free. The results of this study show that the fluorescence of *ex vivo* lung components when measured using a multi-exponential MuFLE model, match the fluorescence of specific individual fluorophores when measured benchside. The results between specific paired cancerous and non-cancerous samples show that the endogenous fluorophores and their photo-physical properties responsible for changes (or lack of) between average FL from different sample types is recoverable. Finally, the results also show these values are similar in the same samples when measured using a FLIM device, allowing the spatial location of individual fluorophores to be investigated. We show, for the first time, the temporal-spectral and spatial identification of specific components label free match specific endogenous fluorophores, un-mixing FAD bound to protein, elastin and FAD unbound to protein/FMN/riboflavin. We collect the results using a fibre based device which can be used *in vivo*. Therefore, as technology develops the certainty will continue to increase, whereby, the specific molecules, label free, may be assessed and tracked *in vivo*, potentially increasing instantaneous TRFS diagnostic certainty of the underlying tissue below.

Chapter 6

Outlook and Conclusion

LC is the leading cause of cancer related deaths world wide [3, 4], primarily attributed to a high prevalence of late-stage detection. LC diagnosis often commences with an image based assessment (i.e., a CT scan) followed by a biopsy, to excise tissue for histological and genetic analysis [1]. Details from histological and genetic assessments, e.g., the tumour mutational burden, act as biomarkers to identify patients suitable for targeted therapy [162]. However, these results are not available instantaneously, only a subset of the tumour is sampled, and can be indeterminate in early stage detection. Thus, there is a need for novel technologies which enhance tissue diagnostic certainty, provide real-time clinical insights, and enable an *in vivo* tissue assessment.

Fiber based TRFS devices, capable of simultaneously exciting multiple endogenous fluorophores, have the potential to enhance *in vivo* diagnostic accuracy. These devices not only measure a tissue's metabolic and structural composition but also assess its environmental changes. Therefore, the inherent sensitivity of tissue AF to metabolic, structural, and environmental change offers a label-free advantage. Coupled with innovative data analysis methods, these devices present an opportunity providing highly sensitive biological information instantaneously, improving clinical decision-making *in vivo*. Additionally, optical setups offer the advantage of characterising an entire tumor, including its vasculature and environment, a capability that traditional biopsies may lack.

Biologically, under the assumption that endogenous fluorophores excited in the visible light region predominate from structural (i.e., originating from the the extra cellular matrix) and metabolic proteins (specifically FAD and NAD(P)H), the deregulation of these functions, and alterations to their environment within cancer provide the photo-physical discrimination between cancerous and non-cancerous tissue [86]. FL provides a fluorophore-specific metric, enhancing the sensitivity of FI based assessments. This advantage becomes particularly evident in studies investigating tissue, where FL has been found to effectively discriminate between cancerous and non-cancerous tissue from *ex vivo* and *in vivo* samples (see Table 1.1). However, whilst these time-resolved devices are optimised for rapid data collection, they often either measure fluorescence in low wavelength bandwidth resolution channels (i.e., [139]) or, if multiple spectral decay channels are collected, decays are often amalgamated into one

(i.e., [141]). Consequently, detailed spectral information regarding the fluorescence decay properties of the underlying endogenous fluorophores is overlooked. Given the influence of individual endogenous fluorophores and environmental changes to tissue AF, this thesis aimed to develop computational tools for characterising fluorescence across numerous wavelength channels with high bandwidth resolution. This thesis then aimed to assess whether these computational tools improve our understanding of the photo-physical properties of tissue, thereby enhancing the differentiation between cancerous and non-cancerous *ex vivo* lung tissue.

6.1 Results and Key Findings

The key result of this thesis is the development of MuFLE, a computational tool capable of characterising both the FI and corresponding FL across the emission spectrum (see Chapter 3.1) [47]. This tool utilises non-parametric cubic B-splines in the spectral domain to estimate emission spectra and cubic B-splines, linear, or fixed values in the temporal domain to estimate (spectral) FL. The results underscore the ability of high-resolution devices to fully exploit spectral information, enabling the concurrent characterisation of an emission spectrum, typically estimated from a spectrometer, and corresponding FL, as well as FL changes across the spectrum, using the same device. This chapter highlights MuFLE when used in a single-exponential mode, provides insight into changes in the SFL of a sample [47, see Fig. 4 A-D]. Showing the SFL of mixed exogenous fluorophores captures the FL from both fluorophores, information which is not observed in the emission spectrum, thus providing additional fluorescence insight [47, see Fig. 4 A-D]. This chapter finally highlights MuFLE when used in a bi-exponential mode, to un-mix two fluorophores from a mixed sample simultaneously and accurately. The emission spectrum reference, including the spectral location of the emission peak, offers additional assurances that the subsequent FL from the mixed sample corresponds to that specific fluorophore [47, see Fig. 4 E-H].

Nuanced insights into fluorescence properties are next determined through analysis of the SFL of mixed samples [41]. Initially, simulated data was utilised to control fluorescence properties relating to the individual fluorophores (both the emission shape and FL value) and gauge the sensitivity of SFL. Modulating the proportion of simulated fluorophores revealed alterations in SFL shape, while the emission spectra remained relatively stable [41, see Fig. 3]. Extrapolating these findings to endogenous fluorophores measured benchside, independent of environmental influences, reveals that the SFL shape was modulated by the relative proportions of the individual fluorophores (i.e., when changing their molar concentrations), while the emission spectra remained largely unaffected [41, see Fig. 4]. These results highlight biologically relevant information provided by SFL pertaining to individual endogenous fluorophores within mixed samples. A feature not captured in the emission spectrum, or when FL data is aggregated into individual decays with large wavelength bandwidth resolutions.

The SFL was evaluated in paired *ex vivo* clinically labeled cancerous and non-cancerous lung samples. To statistically analyse both the magnitude and shape of the SFL across different tissue types, a Procrustes analysis was conducted on the cancerous and non-cancerous samples. A marginally larger median Procrustes disparity was observed among all cancerous samples (0.159) compared to the non-cancerous samples (0.076), suggesting greater variation in both magnitude and shape of the SFL in cancerous samples. Upon assessing the individual sample-specific SFL disparity, 2 samples exhibited a greater median disparity in the cancerous SFL (0.99 and 0.77) compared to their non-cancerous counterparts (0.122 and 0.058) [41, see Fig. 7]. However, when aggregating their FL values into two broad spectral channels, no significant difference was observed [41, see supplementary Table. 5]. These findings highlight the relevance of investigating changes to the FL across the emission spectrum in tissue samples. Taken together with SFL results on fluorophores measured benchside, this suggests that due to an increase in the deregulation of tissue in diseased settings, the relative proportion of endogenous fluorophores, and their environmental factors, may also contribute to the overall FL value. Moreover, the results suggest that with a larger sample size, the SFL metric may offer an alternative photo-physical assessment of the underlying fluorophores excited, and consequently, of the tissue's disease status.

While SFL allows the characterisation of FL variation spectrally, indicating changes to the relative proportion of the underlying endogenous fluorophores without requiring any *a priori* information, MuFLE can also be implemented in a multi-exponential mode to estimate the actual spectra and respective FL of individual components. Therefore, this multi-exponential mode was applied to tissue. First, results from the multi-component MuFLE matched the expected values in both spectral and temporal domains of fluorophores expected to be excited in tissue (see Fig. 5.4). To further validate these results matching samples measured on the EP-TRFS device were assessed using an alternative commercial FLIM confocal microscopy method. Both the relative concentration of un-mixed profiles and the FL values of the same samples measured on the FLIM system, matched the values estimated with MuFLE (see Fig. 5.7 & see Fig. 5.9). The preliminary results show similarities of the unmixed MuFLE components of tissue to individual endogenous fluorophores expected from the literature, in addition to the results of the same samples measured on the FLIM system, highlighting a robustness of the multi exponential MuFLE model when applied in tissue. Moreover, the FLIM confocal allows the spatial location of the FL values to be assessed, highlighting particular structural components of tissue with the FL which matches the expected value of elastin (see Fig. 5.8). Taken together these results show MuFLE un-mixing values matching specific endogenous fluorophores in tissue, providing the spectral emission value in addition to the corresponding FL values. Moreover, MuFLE is employed on a device which has *in vivo* capabilities, suggesting after further fluorophore specific characterisation of these un-mixed compartments, un-mixing endogenous fluorophores label free in tissue may be possible.

The final key finding from the results of this thesis highlight how optical changes observed in un-mixed compartments contributes to the overall average FL value. Un-mixing individual fluorophores/decay components within histograms from tissue reveals two distinct characteristics:

1. In samples where the shape of the SFL remains similar, but a difference in magnitude is observed, similar relative concentrations of the underlying components exist. However, changes in the overall FL of the individual components contributes to the change in the magnitude of the SFL (see Fig 5.5).
2. In samples where the magnitude of the SFL overlaps but the shape of the SFL differs, the multi-exponential assessment reveals that changes in the proportions of the components, influence the FL values, even when the FL of the underlying fluorophores are different (see Fig 5.6). These features are also something we observed when fluorophores were mixed benchside and the SFL shapes assessed [41].

In the former example, the average FL value aggregated across the emission spectrum differs between sample types. In the latter example, the average FL value aggregated across the emission spectrum overlaps in both sample types, despite changes in the FL of the un-mixed components. These results indicate that for diagnostic purposes, a quick contrast based FL assessment between tissue types may not provide sufficient information relating to the biological properties of a sample. However, given the range of biological and clinical implications specific endogenous fluorophores provide, these results demonstrate how high resolution TRFS has the potential to offer unprecedented clinical information *in vivo* and instantaneously.

6.2 Towards Clinical Translation

To realise the potential of this device and analytical methods for clinical translation, different research avenues may be explored further. The major disadvantage of an endogenous fluorophore based tissue assessment is the lack of specificity. For example, the FL of FAD bound or unbound to protein changes. FAD may however be bound to a number of different flavoproteins, e.g., Acyl-CoA oxidase or complex II, which have different functions in different cellular processes [163]. Understanding the origin of this fluorescence signal may not be possible from a global fluorescence analysis, or if the average fluorescence from tissue is assessed. This is clinically and biologically relevant due to complications with false positive diagnoses, as problematic with PET scans. Here PET signals indicating an increase in glycolysis suggesting the presence of a malignancy may actually originate from infection related inflammation [164, 165]. To enhance the specificity and potentially offer an optical alternative, a deeper understanding of the origin of the fluorescence signal may assist this. Therefore, the use of high-resolution fluorescence devices, and analysis tools optimised to extract a true reference profile of the underlying signal may enhance the specificity of fluorescence data.

As discussed in Section 1.6.11, current optical redox ratios primarily rely on the ratio of protein bound and unbound FAD and NAD(P)H to provide insights into tissue redox potential. Redox, which signifies the balance between oxidation and reduction processes within cells, provides valuable information regarding tissue oxidative stress [122]. Redox biology constitutes a comprehensive subfield, encompassing intricate interactions influenced by various factors such as the metabolic profile of the cell, levels of cellular apoptosis, genomic instability, and regulation of transcription factors like NFκB [156, 166, 123]. On the other hand, the expression and efficiency of antioxidant proteins such as superoxide dismutase also influences the redox balance of the cell [167]. In addition to the influence of the mitochondrial activity of cells, and therefore their metabolic profile (i.e., favouring glycolytic or OXPHOS), a fluorescence metric indicating levels of oxidative stress in tissue may, therefore, be very valuable. However, the calculation of the optical redox ratio has been challenged. Most recently for failing to consider alternative fluorophores (i.e., FMN) within its calculation [110]. Optical redox calculations typically originate from bi-exponential fluorescence analysis of channels with broad wavelength bandwidth resolutions. Yet, without considering environmental factors and other fluorophores emitting within the same emission channel, these calculations risk misinterpretation. The findings of this thesis suggest that analysing broad channels alone may oversimplify the photo-physical information provided by AF. Therefore, extending this research to the redox field could enhance confidence in accurately identifying the relevant fluorophores and their corresponding emission spectra in redox ratio assessments. Extending this research may also shed light into the complexity of both Redox and photo-physical properties of tissue, therefore, providing information that is even more biologically relevant than a general redox state current optical redox ratios allow.

The final clinical direction of time domain devices may stem from both the standardisation of these devices and the comparative assessment of measurements applied to various organs and tissue types. A recent study introduces a classification model that incorporates anatomical FL values in head and neck cancer identification, specifically the base of the tongue, the oral tongue and the palatine tonsil. The inclusion of these features was found to enhance tumour classification [168]. Moreover, as shown in [41, Table 1], The FL of different cancer types has been found to either increase, decrease, or both increase/decrease from cancer of different origins. Moreover, as discussed FL can be used as a metabolic and structural indicator. Complementary to this is an opinion within cancer biology that cancer diagnosis based on the tissue of origin, i.e., lung cancer vs cervical cancer, may limit the patients treatment options and stratification [169]. A diagnosis based on tumour metabolic/genetic deregulation may guide treatment selection, potentially improving survival outcomes. E.g., genetic alterations in neurotrophic tropomyosin receptor kinase have been targeted in clinical trials, showing efficacy irrespective of the tumour origin [169, 170]. Current research of FL assessed to examine cancerous compared to non-cancerous tissue assesses tumours/tissue

by site of origin. Therefore, analysing the photo-physical properties regardless of the site of origin, i.e., by pooling data from multiple different organ types, additional optical diagnostic features may be revealed. However, current FL assessments of tumours also use different optical setups. Therefore, to conduct these experiments device standardisation's are required.

6.3 Limitations and Future Work

6.3.1 Device Limitations

The optical setup of the device used in this thesis presents a significant limitation to its clinical readiness, primarily due to the speed of data collection. Currently, the TCSPC mode gathers data in approximately 0.2 s, depending on the exposure time and the number of line iterations recorded. However, HistMode, at the expense of temporal resolution, is optimised for higher-speed data collection. Therefore, investigations aimed at determining the optimal temporal and spectral resolutions to capture accurate TRES while improving data collection speeds are likely to be beneficial.

An additional optical limitation that, if addressed, holds the potential to enhance the diagnostic capabilities of the device is the modification of the excitation wavelength/optics. Currently, with the existing optical setup, the wavelength emission range of Ra-II spans from 470 nm to 720 nm. However, when a sample is excited at 485 nm to prevent excitation light from entering the detector, the available emission range is narrowed to 512 nm-720 nm. Furthermore, the spectral range used to assess samples in this thesis, limited by the choice of the IRF, is from 550 nm to 630 nm.

As demonstrated in this thesis, two key findings emerge: first, utilising photo-physical information from only 30 % of the available channels of the spectrometer enhances the photo-physical information of samples; second, an excitation wavelength that is not optimized to collect a large number of endogenous fluorophores still provides valuable photo-physical insights into the AF of tissue. Therefore, adjustments to this setup, such as exciting samples at 400 nm, along with alterations to the excitation and emission filters, lenses, and grating, to detect emission in all Ra-II channels from 470 nm-720 nm, would enable the detection of emission from NAD(P)H, collagen, and porphyrins, in addition to flavins and elastin (see Fig. 1.6).

The limitation of the spectral range analysed in this thesis is attributed to the exogenous fluorophore used to measure the IRF. This is a significant limitation, particularly in the assessment of the detection of flavins and other components extracted in the un-mixing section. The emission peaks of flavin and elastin differ, with the anticipated emission peak of flavins at

around 550 nm [64]. Thus, even with a shift in the IRF to accurately record decay from 520 nm, the distinction between the peaks of components originating from flavins compared to elastin may be discernible. Expanding the range of fluorophores to estimate the IRF across different spectral ranges would assist this.

Furthermore, if alterations are made to the optical setup, the issue of IRF measurement persists. Therefore, exploring alternative computational tools that allow for the estimation of fluorescence decays without requiring a measured IRF, such as inverse ML models, may be worthwhile [51]. Incorporating these approaches and utilising the total number of Ra-II channels in the analysis process could enable not only the assessment of fluorescence changes in collagen and porphyrins but also a multi-spectral redox calculation from NAD(P)H and FAD, guided by their total emission spectra and FL. This tool could be biologically and clinically powerful, given the implications discussed.

The features of MuFLE which estimate variations within the detector which do not originate from the fluorescence of a sample are limited to capture both the dark count rates present within the bias term, which in itself may be a limitation, and the IRF. A major component observed within the measured TRES histograms is the spectral sensitivity. This feature is anticipated to originate from different sensitivities of pixels in adjacent channels. When MuFLE is applied, spectral sensitivity is integrated into the spectral emission of MuFLE as a smooth feature attribute by the used of B-splines across the spectral range is determined, which includes the average spectral sensitivity of all channels. However, if spectral sensitivity is accounted for, the spectrum analysed from the model will theoretically originate only from the spectra of the underlying fluorophores. Although this aspect was addressed in an alternative model developed (results not shown), convergence issues prevented accurate results. An analytical tool that incorporates this feature may extend the number of possible fluorophores un-mixed by capturing the complete emission spectrum, thus facilitating FL convergence. Improvement to the spectral sensitivity incorporation within the analysis model is something we save for future work. Ultimately TRES from the in-house device is inherently noisy, particularly when tissue is measured. Therefore, computational work to address as many features of the noise as possible make accurate estimations of the underlying fluorescence possible.

6.3.2 Computational Limitations

Computational limitations to MuFLE also exist which can be improved upon. The underlying feature of MuFLE is the non-parametric B-splines estimating photo-physical changes across the spectrum. MuFLE is sensitive to initialisation parameters, due potentially to many local minima within the optimiser, therefore better optimisation tools should be explored. The spectral profile of endogenous fluorophores have been well characterised within the literature, therefore, functions more specific to these characteristics, such as a Gaussian or skewed Gaussian, may contribute to a more precise analysis. An additional, major limitation to the

computational model is in its inefficiency, in addition to a measured IRF required in the deconvolution element of the model further limiting its speed. This ultimately limits its clinical translation, preventing instantaneous analysis of the TRES. Alternative studies have shown inverse ML models are significantly quicker than curve fitting approaches [51]. These models have also been shown to estimate accurate FLs without the requirement of an IRF, this may be a further benefit if the device was adapted to collect emission from an excitation of 400 nm. However, this is also something we save for future work.

The final limitation of the results presented in this thesis exist in the application of the multi-exponential mode of MuFLE to tissue data. Using TRES alone to detect fluorophore-specific changes in unlabeled tissue is complex due to the ambiguity from components originating from various unknown sources. The sensitivity of FL and emission spectra to multiple factors, combined with the complexity of protein components and environmental variations in tissue, complicates the identification of specific fluorophores. Therefore, definitively attributing a component to a specific fluorophore remains a challenging task, presenting a significant limitation to the hypothesis of this final chapter. Limitations to the experimental design of the final chapter also arise from the assumption that only three groups of fluorophores are emitting within the TRES of tissue. It is assumed that the individual fluorophores within the longest FL component cannot be un-mixed due to their low brightness. Further experimental results, possibly including simulated data, are needed to determine the un-mixing computational limit of MuFLE on TRES. This aspect is saved for future work.

6.3.3 Data Collection Limitations

Despite the use of a high resolution spectral temporal device, the majority of the photophysical properties of clinically defined cancerous and non-cancerous tissue samples assessed in this thesis, following excitation at 485 nm was not found to be statistically significant due potentially to large heterogeneity. Paired cancerous and non-cancerous *ex vivo* samples following lobectomy examined in this thesis are examined using the fibre based EP-TRFS device exciting an area $\leq$100 µm^2 per point-based measurement. Characterising tumours based on such a small subset of tissue, especially considering the fluorescence sensitivity to various factors, may contribute to the substantial heterogeneity observed within the data. Moreover, the use of EP-TRFS alone captures no additional features of the tissue beyond this small field of view. Consequently, in the absence of an imaging parameter or an alternative reference tool *in vivo*, determining the cellular origin of the fluorescence and identifying tissue structural elements becomes challenging.

A significant assumption underlying the tissue analysis is that all samples clinically labeled as cancerous are cancerous, and conversely, all samples labeled as non-cancerous/normal are normal. However, this assumption introduces potential complexities into the outcomes. Firstly, cancerous samples may include tumor margins, which have been found to exhibit photo-physical differences from the tumour itself (e.g., [133]). Additionally, certain areas within cancerous tissue may possess more normal features than the tumour itself.

Furthermore, considering the tissue-level changes or even changes at the cellular level (assuming a cancer cell is approximately 10 µm wide), and accounting for the heterogeneity within tumors, both identifying a tumor-specific FAD change and discerning its origin (whether due to factors such as pH, known for its high sensitivity, or oxygenation) becomes a complex task that necessitates further investigation. Therefore, in addition to collecting an increased number of point samples of each tissue measured, the use of multi-modal technologies, including technologies with an imaging parameter may also enhance the specificity and reduce the heterogeneity. However, this is something we save for future work.

It is also essential to note that all samples assessed in this study were *ex vivo*. Some research suggests differences in fluorescence properties between *in vivo* and *ex vivo* samples [136, Fig. 3]. Factors such as temperature, oxygenation, pH, vascularization, and breathing patterns of the human lung are likely to influence photo-physical properties differently in *in vivo* conditions. Therefore, utilising systems that mimic *in vivo* conditions, such as the *Ex Vivo* Lung Perfusion system, may yield altered results. This aspect is something we save for future work.

None the less, to enhance confidence in identifying specific fluorophores, additional experiments are required. In addition to collecting more samples, one approach proposed involves correlating the expected structural components identified from MuFLE, anticipated to represent elastin, with IHC experiments. These experiments tag antibody specific epitopes of elastin followed by antibody specific staining, allowing the spatial location of these structural components to be compared to confirm whether they are elastin. Alternatively for the fluorophores anticipated to match bound or unbound FAD, it has been shown that either in OXPHOS or glycolysis, the ratios of protein bound to FAD changes. Therefore, an additional experiment to alter the metabolic processes of measured tissue may allow FAD specific changes to be detected by MuFLE. Subsequent adjustments to components expected to originate from FAD may suggest these are FAD. However, extrapolating both these experiments in *in vivo* tissue and avoiding false positives remains complex. Therefore, further additional structural and metabolic experiments may be required, these are something we save for future work. However, determining these features from these experiments may already improve on the specificity of the components.

6.4 Conclusion

This thesis first describes the high death rates of patients with LC and a lack of diagnostic devices that provide tissue specific certainty to LC *in vivo* detection. FS has potential to improve on the current diagnostic technologies, however, a lack of specificity may limit the clinical translation of the device.

The innovative potential of this thesis originates predominantly in the availability of the EP-TRFS device. Although currently limited in data collection speed, this device enables a comprehensive, high resolution, spectral-temporal assessment of a sample's fluorescence. Overcoming the resolution disadvantages of previous time-resolved fluorescence devices used to measure tissue fluorescence.

This thesis highlights the advantages of assessing AF at a higher resolution and across the wavelength spectrum, illustrating the importance of fluorophore specific analysis. A preliminary model capable of capturing high-resolution fluorescence data simultaneously is presented. Subsequently, the application of this model to evaluate both cancerous and non-cancerous samples is demonstrated, culminating in the spectral-temporal un-mixing of label-free fluorophores. This process potentially allows for the identification of fluorophore-specific alterations in cancerous tissue compared to non-cancerous tissue.

If MuFLE is adjusted to simultaneously un-mix a higher number of endogenous fluorophores in both the temporal and spectral range, it could further enhance specificity and deepen our understanding of the photo-physical changes observed between cancerous and non-cancerous lung tissue. Consequently, this may lead to precise tracking of their presence and environmental changes *ex vivo* and even *in vivo*, thereby facilitating better tissue classifications.

With further advancements these technologies hold the potential to offer instantaneous *in vivo* assessments of tissue akin to current histology methods. This unprecedented information may allow medical professionals to make better informed diagnostic and prognostic decisions, with the ultimate goal of improving survival rates of LC patients.

Chapter 7

Appendix

7.1 Exponential Criteria

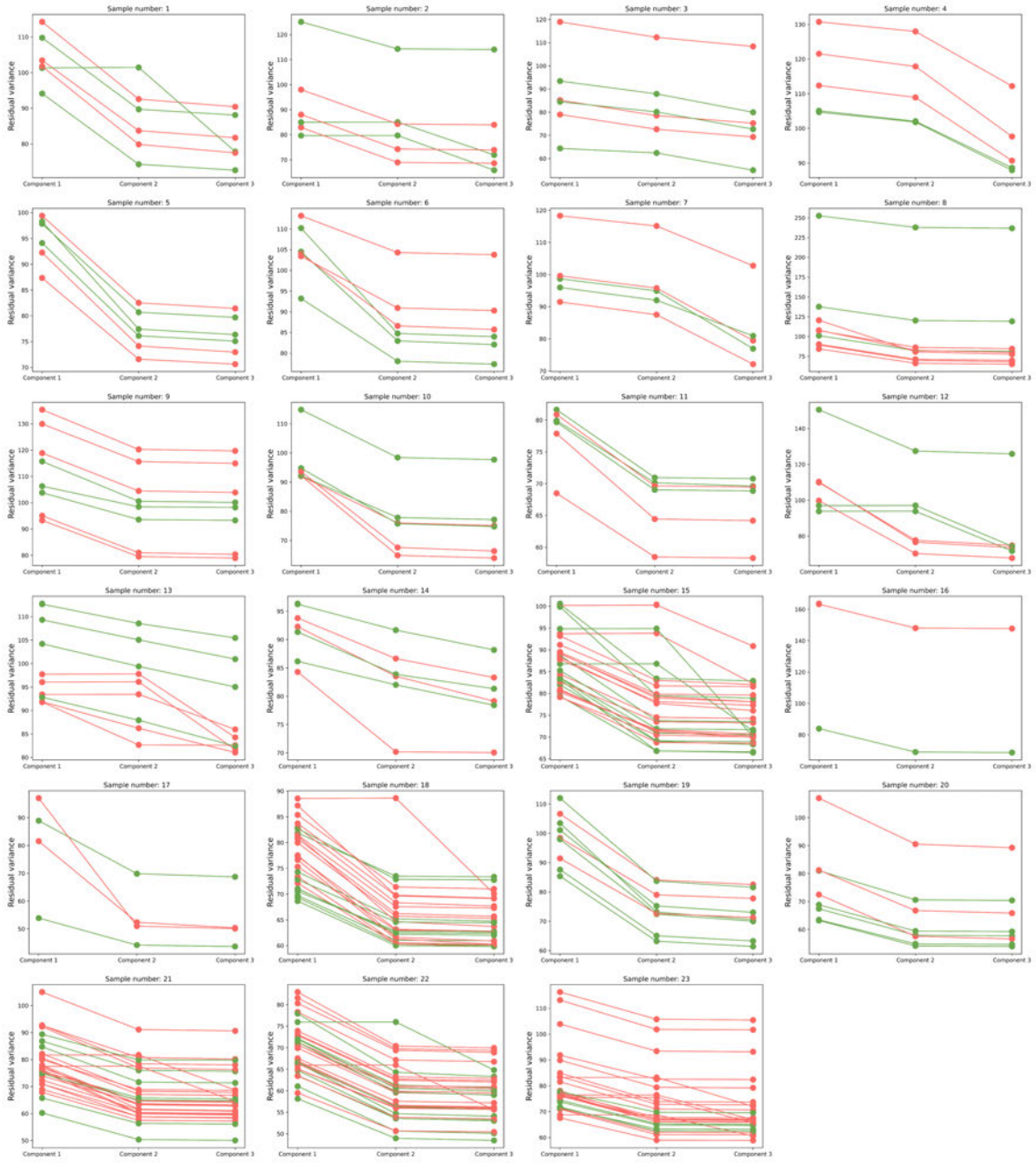

Figure 7.1: *Ex vivo* clinically defined as cancerous (red) and non-cancerous (green) samples are measured on the extensively parallel time-resolved fluorescence spectroscopy device and analysed using component (or exponential) variations of the Multichannel Fluorescence Lifetime Estimation made model. The residual variance is plotted of the different components used for analysis.

7.2 Simulated Data

Simulated data was used to assess whether MuFLE could resolve multi-component histograms. In the first instance we use a histogram with difference emission and lifetime values. In the second instance we used histograms matching the estimated spectral intensity and spectral fluorescence lifetime of endogenous fluorophores within tissue.

In previous studies (see Fig. 4 [47]), we show using reference exogenous fluorophores the MuFLE model is able to accurately un-mix in both the spectral and temporal domain two fluorophores. To validate the accuracy of un-mixing 3 fluorophores with varying spectral temporal ranges and assess the limitation of MuFLE, we first use simulated data, with a temporal resolution of 0.05 ns and in 160 spectral channels to match our experimental set up. A selection of hypothetical fluorophores were simulated using the model described in 5.5, from a range of both intensity and lifetime values. Hyperbolic, exponential and quadratic functions were used to model the emission i.e., $\gamma[p]$, of the underlying simulated fluorophores. The lifetime at each wavelength for the individual fluorophores was simulated to be fixed i.e., $\tau[m] = \tau$. The underlying fluorescence histograms were then summed together and convolved with a simulated instrument response function (IRF) to create the observed histogram. The IRF was simulated with a lifetime of 0.378 ns (matching the lifetime of the measured IRF). In addition, following convolution, the simulated intensity at each temporal channel was perturbed using Poisson noise.

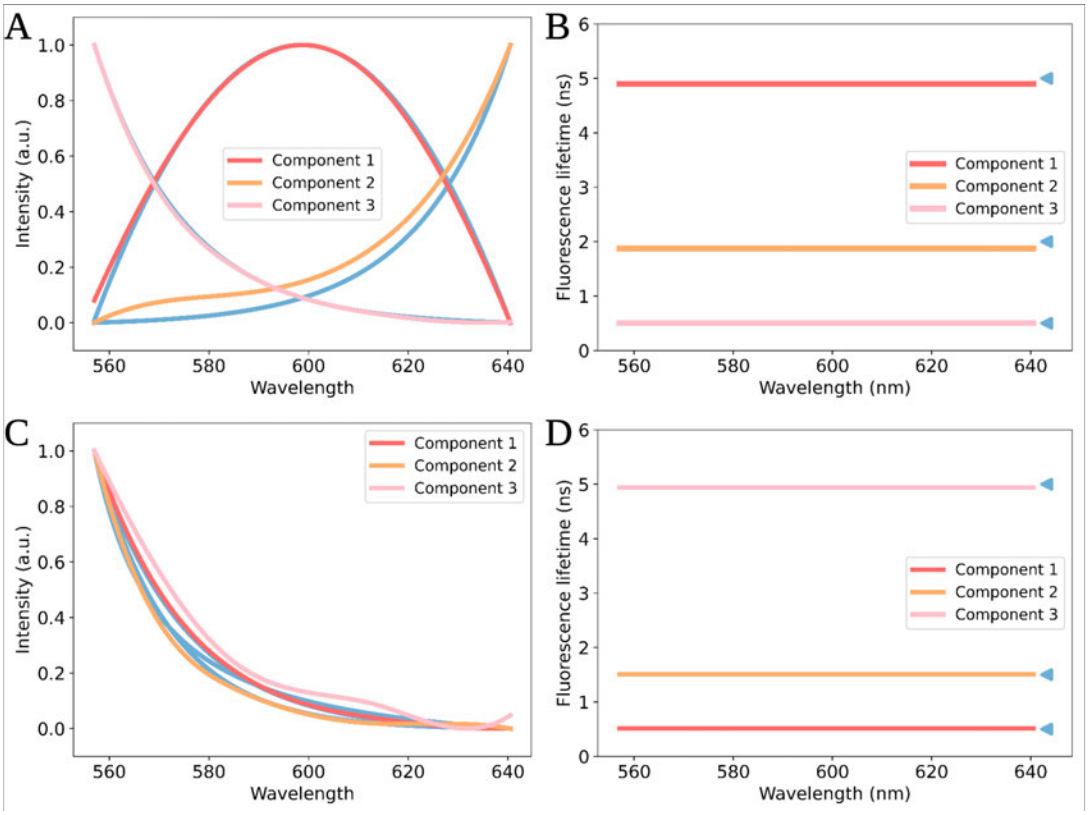

Figure 7.2: Simulated data showing using 2 different histograms, a multi-exponential MuFLE model un-mixing 3 individual fluorophores in both the spectral and temporal range. The ground truths of each fluorophore is depicted in the blue intensity and the blue ticks.

7.3 EP-TRFS Sample Specific Components

Table 7.1: Paired cancerous and non-cancerous *ex vivo* tissue samples with a tri-exponential MuFLE model fitted. T-tests conducted on the fluorescence lifetime values.

Sample label	Cancerous lifetime 1 (ns)	Non-cancerous lifetime 1 (ns)	p value	Cancerous lifetime 2 (ns)	Non-cancerous lifetime 2 (ns)	p value	Cancerous lifetime 3 (ns)	Non-cancerous lifetime 3 (ns)	p value
2	0.31 +/- 0.06	0.25 +/- 0.012	0.29	1.37 +/- 0.25	1.25 +/- 0.072	0.57	4.41 +/- 0.49	4.54 +/- 0.16	0.74
6	0.18 +/- 0.018	0.12 +/- 0.016	0.098	1.04 +/- 0.079	0.96 +/- 0.089	0.52	4.023 +/- 0.24	4.064 +/- 0.097	0.85
9	0.15 +/- 0.025	0.13 +/- 0.022	0.41	0.89 +/- 0.24	0.935 +/- 0.099	0.85	3.51 +/- 0.67	3.88 +/- 0.24	0.52
10	0.144 +/- 0.031	0.181 +/- 0.018	0.234	1.014 +/- 0.137	1.128 +/- 0.0438	0.363	4.302 +/- 0.3538	4.516 +/- 0.359	0.581
11	0.46 +/- 0.0018	0.33 +/- 0.043	0.054	2.33 +/- 0.020	1.67 +/- 0.12	0.013	10.25 +/- 0.71	6.071 +/- 0.58	0.05
18	0.410 +/- 0.057	0.16 +/- 0.043	0.12	1.62 +/- 0.14	0.86 +/- 0.099	0.10	4.60 +/- 0.18	3.61 +/- 0.15	0.09
21	0.213 +/- 0.0415	0.163 +/- 0.0333	0.227	0.894 +/- 0.1517	0.841 +/- 0.115	0.675	3.492 +/- 0.182	3.663 +/- 0.158	0.314
23	0.29 +/- 0.095	0.41 +/- 0.034	0.19	1.11 +/- 0.37	1.56 +/- 0.12	0.23	3.88 +/- 0.58	4.56 +/- 0.22	0.24

Table 7.2: EP-TRFS average lifetime components fitted using a bi-exponential model and compared using a t-test.

	Average lifetime 1 (ns)	Average lifetime 2 (ns)	Average lifetime 3 (ns)
Cancerous	0.27$\pm$0.11	1.23$\pm$0.42	4.40$\pm$1.77
Non-cancerous	0.23$\pm$0.11	1.09$\pm$0.39	4.15$\pm$1.41
p-value	0.03	0.07	0.41

Table 7.3: Paired cancerous and non-cancerous *ex vivo* tissue samples with a tri-exponential MuFLE model fitted. T-tests conducted on the fluorescence intensity values.

Sample label	Cancerous Intensity 1 (au)	Non-cancerous Intensity 1 (au)	p value	Cancerous Intensity 2 (au)	Non-cancerous Intensity 2 (au)	p value	Cancerous Intensity 3 (au)	Non-cancerous Intensity 3 (au)	p value
2	0.41 +/- 0.029	0.44 +/- 0.08	0.61	0.20 +/- 0.010	0.19 +/- 0.015	0.42	0.075 +/- 0.0036	0.075 +/- 0.0083	0.95
6	0.36 +/- 0.030	0.37 +/- 0.059	0.82	0.30 +/- 0.033	0.22 +/- 0.014	0.083	0.19 +/- 0.046	0.14 +/- 0.0015	0.29
9	0.49 +/- 0.039	0.45 +/- 0.024	0.32	0.16 +/- 0.018	0.20 +/- 0.0071	0.10	0.061 +/- 0.014	0.088 +/- 0.0095	0.097
10	0.40 +/- 0.066	0.41 +/- 0.039	0.87	0.23 +/- 0.0053	0.27 +/- 0.035	0.27	0.12 +/- 0.018	0.15 +/- 0.04	0.48
11	0.40 +/- 0.014	0.42 +/- 0.022	0.50	0.16 +/- 0.0064	0.17 +/- 0.020	0.74	0.024 +/- 0.0024	0.044 +/- 0.012	0.14
18	0.28 +/- 0.001	0.31 +/- 0.03	0.078	0.14 +/- 0.0067	0.24 +/- 0.026	$<$0.01	0.085 +/- 0.0057	0.17 +/- 0.028	$<$0.01
23	0.24 +/- 0.044	0.32 +/- 0.03	0.11	0.16 +/- 0.0097	0.15 +/- 0.0099	0.51	0.095 +/- 0.014	0.083 +/- 0.013	0.36

Table 7.4: Paired cancerous and non-cancerous *ex vivo* tissue samples with a bi-exponential MuFLE model fitted. T-tests conducted on the fluorescence lifetime values.

Sample label	Cancerous Lifetime 1 (ns)	Non-cancerous Lifetime 1 (ns)	p value	Cancerous Lifetime 2 (ns)	Non-cancerous Lifetime 2 (ns)	p value
1	0.23 +/- 0.0055	0.15 +/- 0.030	0.055	2.89 +/- 0.061	2.59 +/- 0.096	0.05
3	0.95 +/- 0.18	0.84 +/- 0.084	0.50	5.13 +/- 0.30	4.21 +/- 0.240	0.032
4	1.81 +/- 0.056	1.88 +/- 0.034	0.39	15.67 +/- 0.72	16.80 +/- 0.39	0.33
5	0.24 +/- 0.012	0.24 +/- 0.017	0.94	2.60 +/- 0.058	2.58 +/- 0.030	0.83
7	1.21 +/- 0.27	1.50 +/- 0.12	0.47	8.75 +/- 1.18	14.08 +/- 0.97	0.077
13	0.99 +/- 0.075	0.90 +/- 0.0096	0.11	4.82 +/- 0.40	4.52 +/- 0.24	0.44
14	0.90 +/- 0.18	0.93 +/- 0.014	0.85	4.18 +/- 0.36	4.36 +/- 0.091	0.57
15	0.50 +/- 0.025	0.64 +/- 0.048	0.064	2.80 +/- 0.042	3.46 +/- 0.175	$<$0.01
18	0.55 +/- 0.042	0.35 +/- 0.080	0.002	3.28 +/- 0.053	2.88 +/- 0.12	$<$0.01
19	0.12 +/- 0.005	0.22 +/- 0.024	0.02	2.29 +/- 0.037	2.67 +/- 0.092	0.017
21	0.264 +/- 0.0419	0.288 +/- 0.0178	0.426	2.343 +/- 0.339	2.765 +/- 0.094	0.117
22	0.26 +/- 0.039	0.30 +/- 0.031	0.19	2.75 +/- 0.11	2.85 +/- 0.097	0.31
23	0.52 +/- 0.061	0.50 +/- 0.061	0.79	3.082 +/- 0.12	3.13 +/- 0.22	0.77

Table 7.5: Paired cancerous and non-cancerous *ex vivo* tissue samples with a bi-exponential MuFLE model fitted. T-tests conducted on the fluorescence intensity values.

Sample label	Cancerous Intensity 1 (a.u.)	Non-cancerous Intensity 1 (a.u.)	p value	Cancerous Intensity 2 (a.u.)	Non-cancerous Intensity 2 (a.u.)	p value
1	0.50 +/- 0.0068	0.63 +/- 0.076	0.14	0.23 +/- 0.0037	0.25 +/- 0.0016	0.11
3	0.38 +/- 0.039	0.35 +/- 0.0058	0.45	0.069 +/- 0.022	0.11 +/- 0.0055	0.084
4	0.29 +/- 0.0093	0.33 +/- 0.024	0.12	0.044 +/- 0.001	0.049 +/- 0.0041	0.22
5	0.50 +/- 0.0060	0.48 +/- 0.021	0.39	0.20 +/- 0.010	0.21 +/- 0.0071	0.39
7	0.40 +/- 0.016	0.33 +/- 0.027	0.083	0.053 +/- 0.010	0.049 +/- 0.0031	0.75
13	0.32 +/- 0.028	0.38 +/- 0.013	0.058	0.085 +/- 0.0029	0.11 +/- 0.029	0.47
14	0.30 +/- 0.037	0.35 +/- 0.018	0.24	0.10 +/- 0.010	0.13 +/- 0.007	0.058
15	0.47 +/- 0.016	0.40 +/- 0.040	0.084	0.22 +/- 0.015	0.16 +/- 0.010	0.14
18	0.31 +/- 0.018	0.42 +/- 0.036	0.001	0.17 +/- 0.011	0.24 +/- 0.012	$<$0.01
19	0.82 +/- 0.018	0.55 +/- 0.053	0.01	0.24 +/- 0.026	0.23 +/- 0.0091	0.70
22	0.35 +/- 0.038	0.33 +/- 0.019	0.24	0.18 +/- 0.015	0.16 +/- 0.0097	0.074
23	0.34 +/- 0.019	0.39 +/- 0.051	0.18	0.16 +/- 0.023	0.16 +/- 0.014	0.96

7.4 EP-TRFS vs FLIM Plots

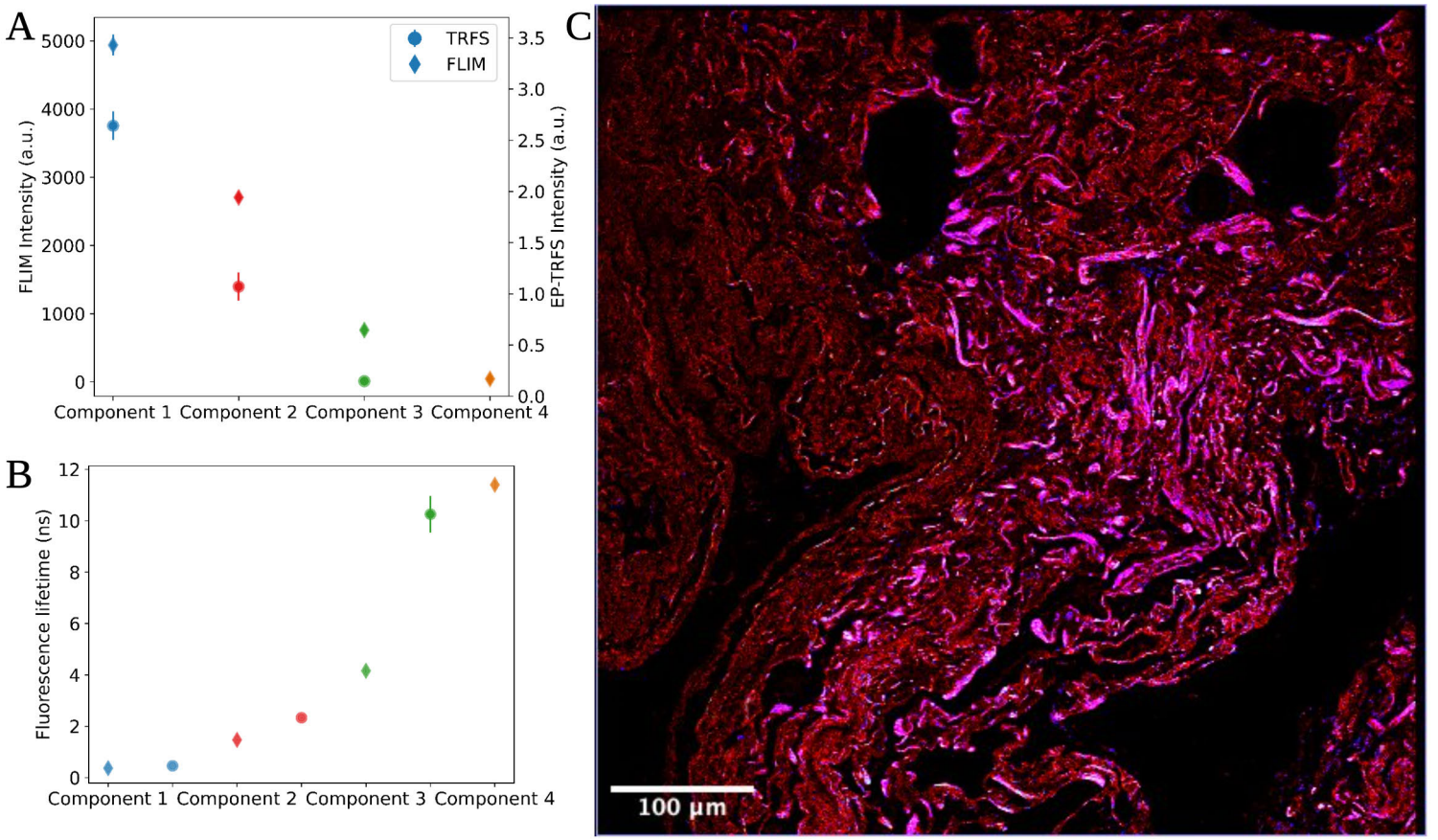

Figure 7.3: An *ex vivo* clinically defined as cancerous lung sample is measured on the extensively parallel time-resolved fluorescence spectroscopy device and on the fluorescence lifetime imaging microscope. The intensity of the sample measured on both devices is shown **A)**. The fluorescence lifetime of the same sample also measured on both devices is plotted **B)**. The corresponding image of the sample when measured on the FLIM device is shown **C)**.

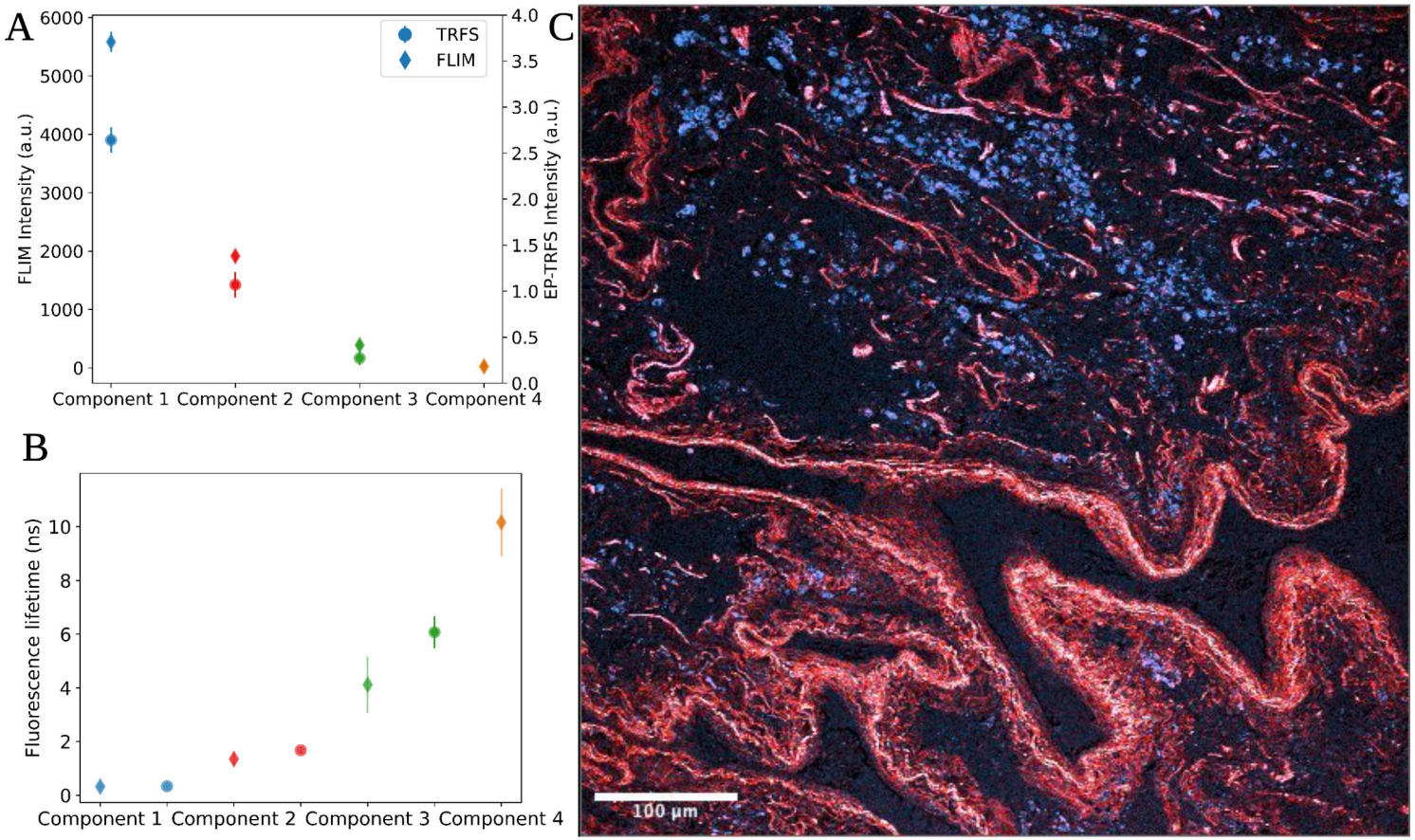

Figure 7.4: An *ex vivo* clinically defined as non-cancerous lung sample is measured on the extensively parallel time-resolved fluorescence spectroscopy device and on the fluorescence lifetime imaging microscope. The intensity of the sample measured on both devices is shown **A)**. The fluorescence lifetime of the same sample also measured on both devices is plotted **B)**. The corresponding image of the sample when measured on the FLIM device is shown **C)**.

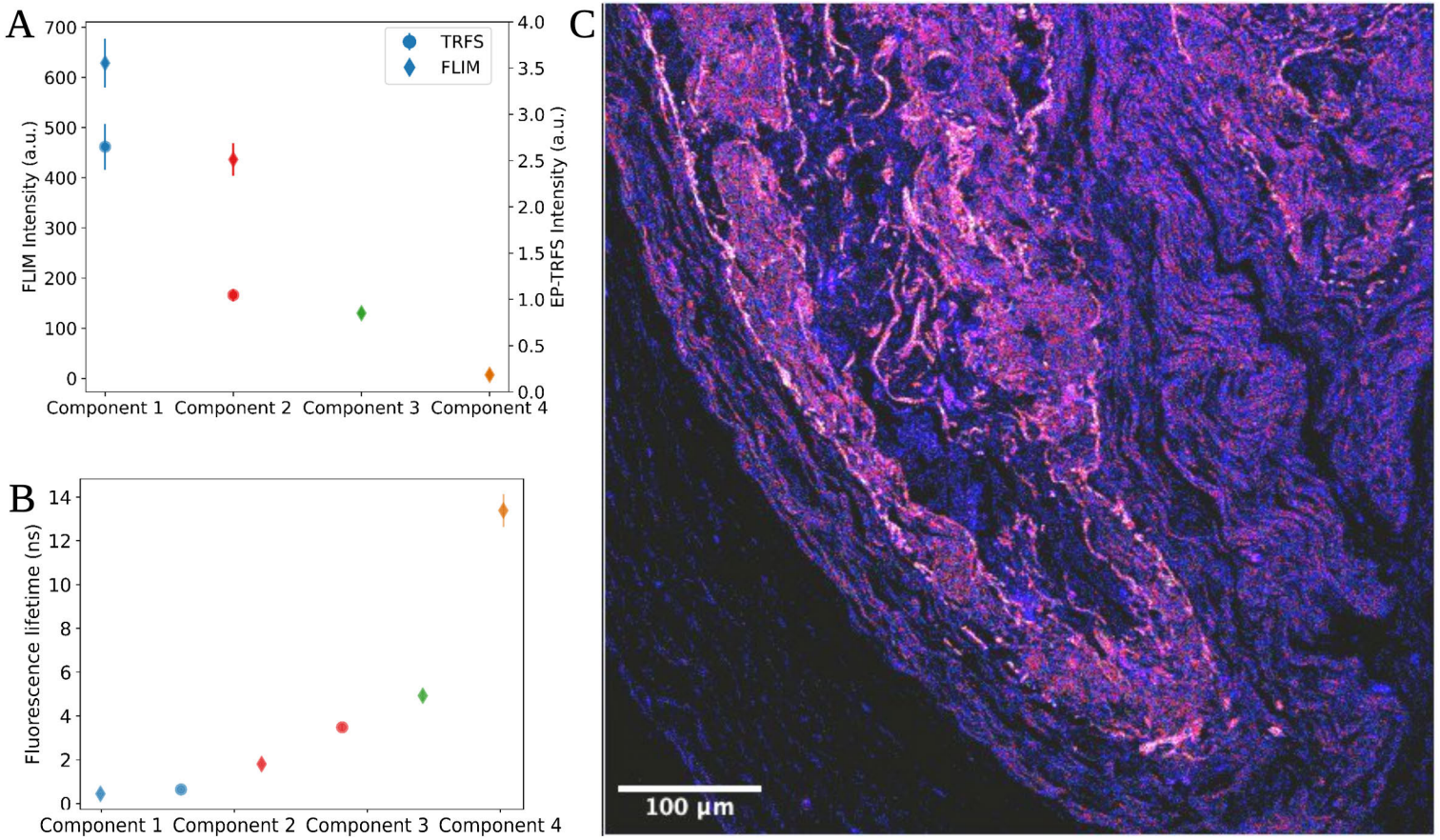

Figure 7.5: An *ex vivo* clinically defined as non-cancerous lung sample is measured on the extensively parallel time-resolved fluorescence spectroscopy device and on the fluorescence lifetime imaging microscope. The intensity of the sample measured on both devices is shown **A)**. The fluorescence lifetime of the same sample also measured on both devices is plotted **B)**. The corresponding image of the sample when measured on the FLIM device is shown **C)**.

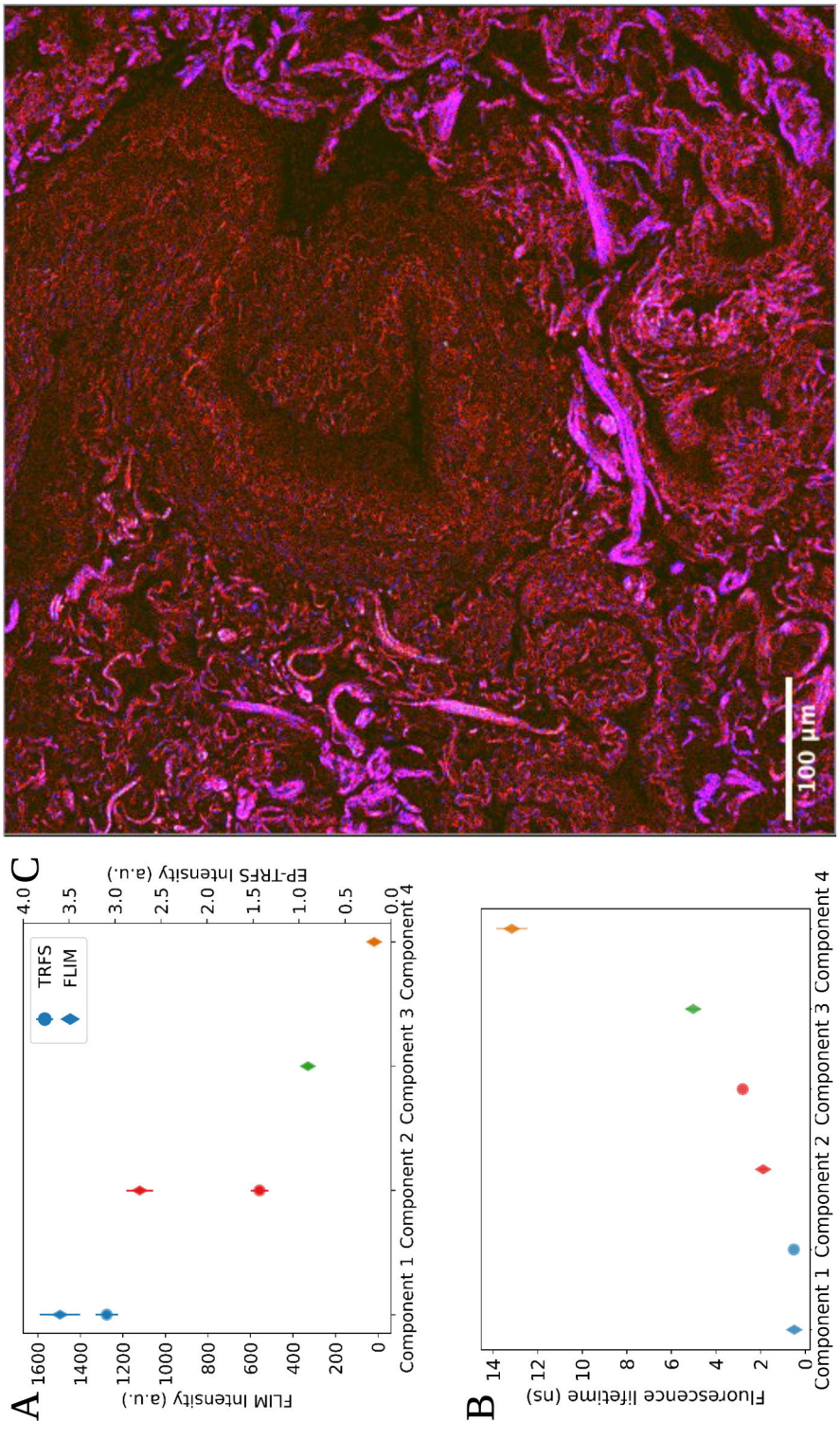

Figure 7.6: An *ex vivo* clinically defined as cancerous lung sample is measured on the extensively parallel time-resolved fluorescence spectroscopy device and on the fluorescence lifetime imaging microscope. The intensity of the sample measured on both devices is shown **A)**. The fluorescence lifetime of the same sample also measured on both devices is plotted **B)**. The corresponding image of the sample when measured on the FLIM device is shown **C)**.

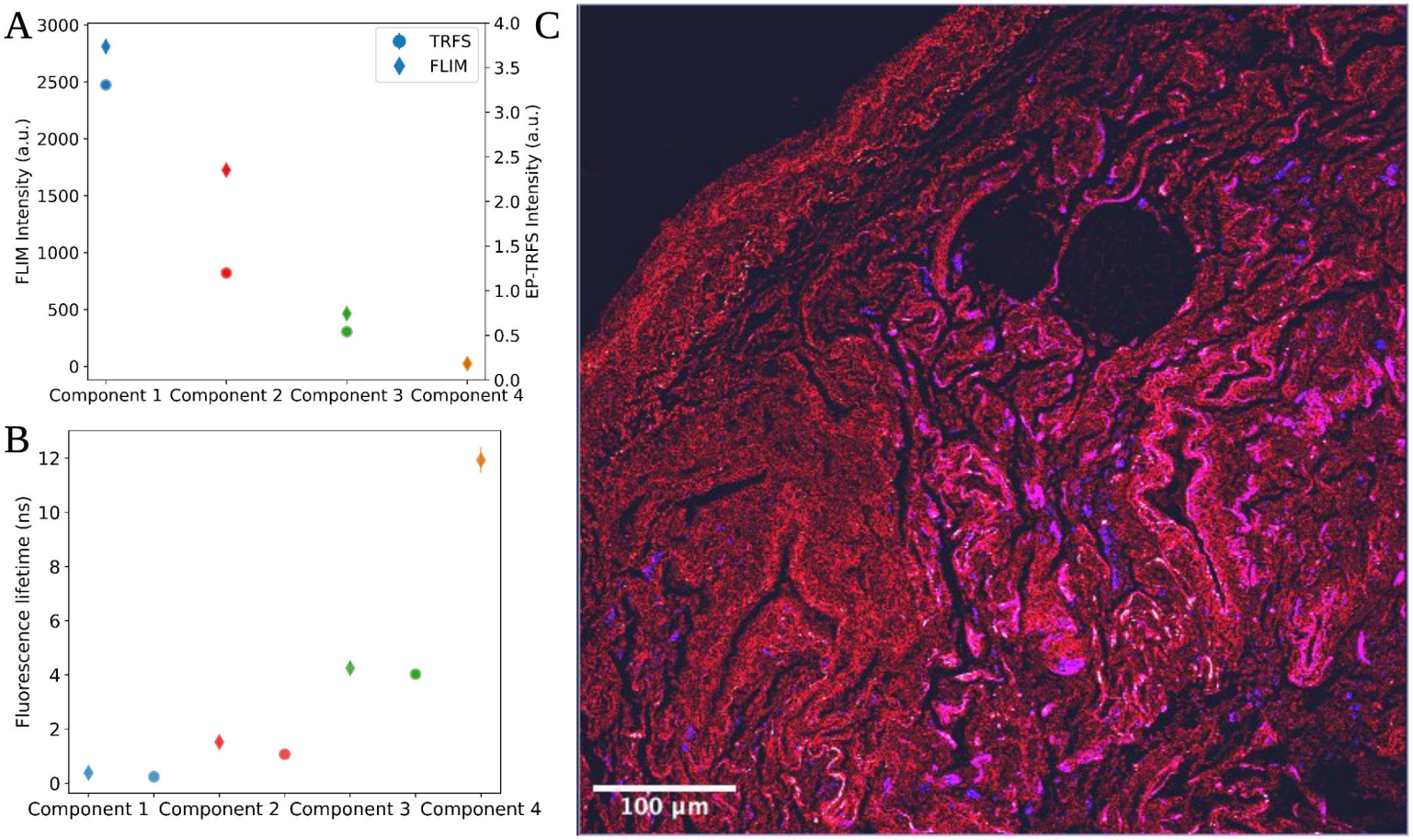

Figure 7.7: An *ex vivo* clinically defined as cancerous lung sample is measured on the extensively parallel time-resolved fluorescence spectroscopy device and on the fluorescence lifetime imaging microscope. The intensity of the sample measured on both devices is shown **A)**. The fluorescence lifetime of the same sample also measured on both devices is plotted **B)**. The corresponding image of the sample when measured on the FLIM device is shown **C)**.

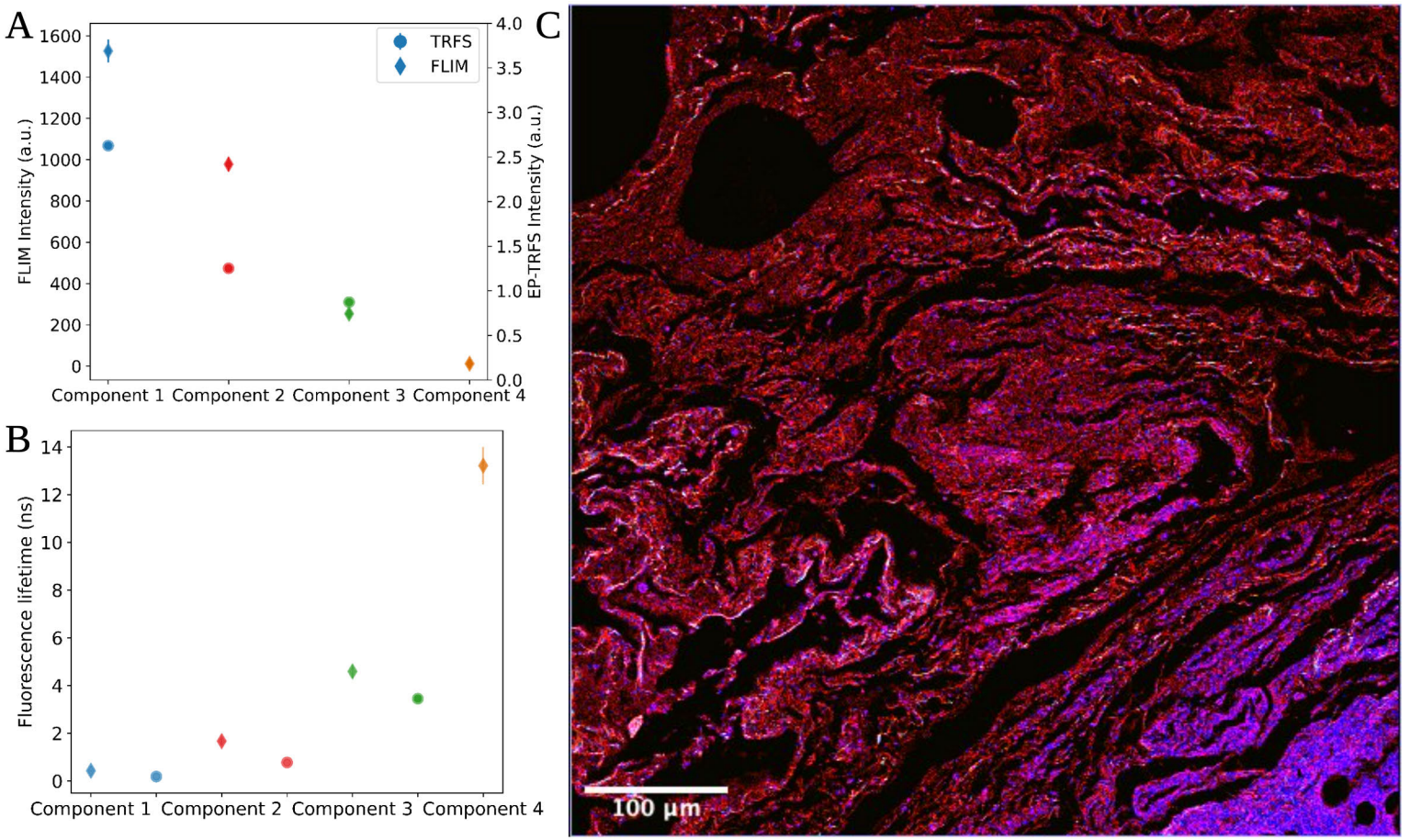

Figure 7.8: An *ex vivo* clinically defined as non-cancerous lung sample is measured on the extensively parallel time-resolved fluorescence spectroscopy device and on the fluorescence lifetime imaging microscope. The intensity of the sample measured on both devices is shown **A)**. The fluorescence lifetime of the same sample also measured on both devices is plotted **B)**. The corresponding image of the sample when measured on the FLIM device is shown **C)**.

Table 7.6: Fluorescence intensity of lung tissue analysed on a FLIM confocal microscope. Comparisons are drawn using a t-test.

Sample	Cancerous Amplitude 1 (a.u.)	Non-cancerous Amplitude 1 (a.u.)	p-value	Cancerous Amplitude 2 (a.u.)	Non-cancerous Amplitude 2 (a.u.)	p-value	Cancerous Amplitude 3 (a.u.)	Non-cancerous Amplitude 3 (a.u.)	p-value
30	186.934±95.2	78.575±48.78	0.018	140.075±63.54	54.548±32.52	0.007	41.235±17.6	16.253±10.06	0.006
31	351.422±63.97	190.797±55.92	0.000 19	215.691±44.09	122.247±32.85	0.001	57.967±13.16	31.718±9.12	0.001
32	617.369±152.9	697.953±173.9	0.373	338.069±71.15	239.454±33.72	0.005	94.969±20.81	48.753±12.7	0.0002

Table 7.7: Fluorescence lifetime of lung tissue analysed on a FLIM confocal microscope. Comparisons are drawn using a t-test.

Sample	Cancerous Lifetime 1 (ns)	Non-cancerous Lifetime 1 (ns)	p-value	Cancerous Lifetime 2 (ns)	Non-cancerous Lifetime 2 (ns)	p-value	Cancerous Lifetime 3 (ns)	Non-cancerous Lifetime 3 (ns)	p-value
30	0.487±0.031	0.448±0.022	0.017	1.885±0.138	1.804±0.09	0.216	5.021±0.308	4.925±0.233	0.521
31	0.387±0.03	0.426±0.029	0.025	1.522±0.108	1.667±0.121	0.033	4.25±0.234	4.589±0.281	0.028
32	0.368±0.014	0.322±0.028	0.002	1.469±0.04	1.349±0.244	0.22	4.16±0.074	4.116±1.056	0.914

7.5 FLIM Plots

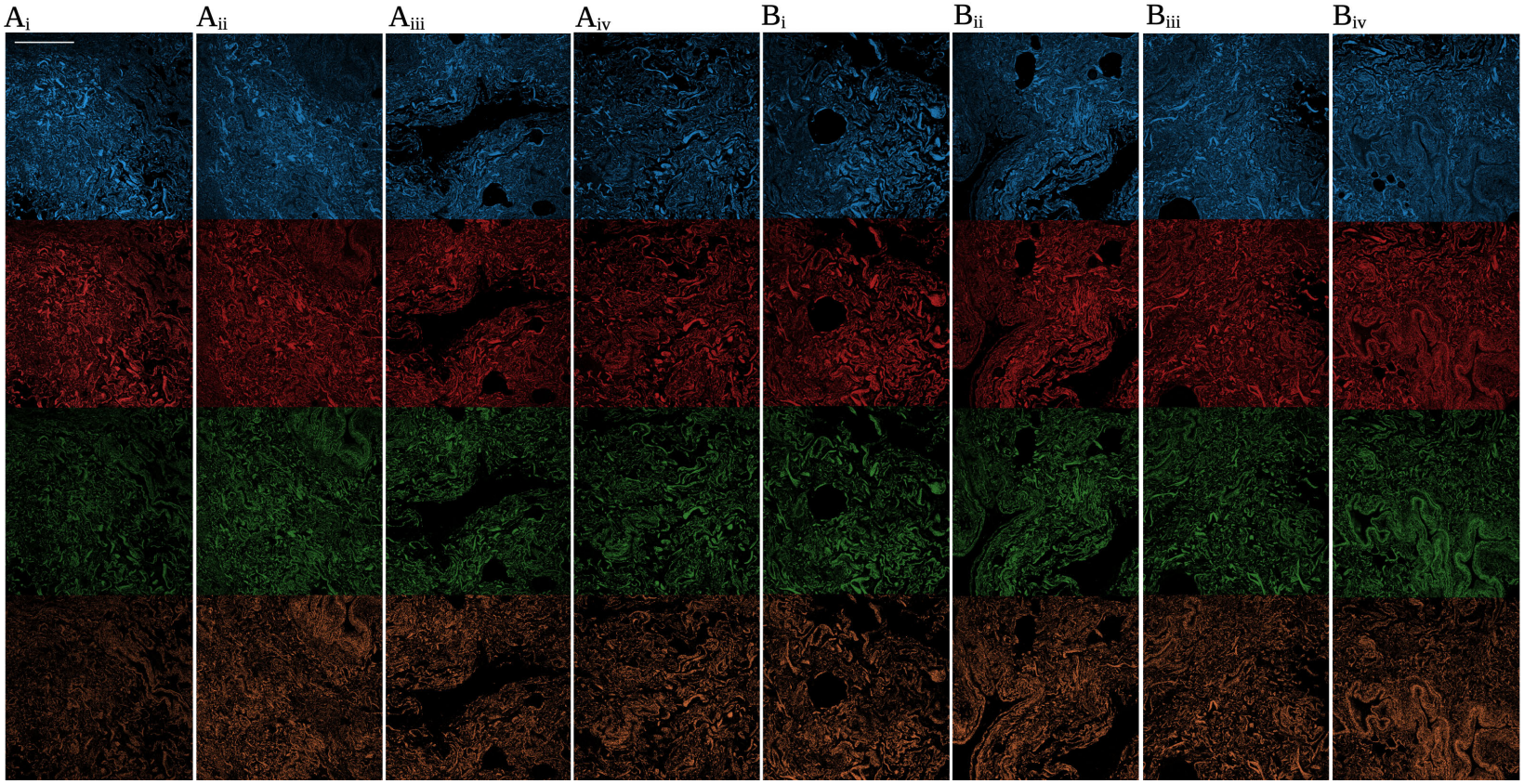

Figure 7.9: All FLIM images measured on a FLIM confocal microscope of cancerous sample number 11. The scale bar plotted in the top left is 500 µm wide. Each column contains the same image but colored for the corresponding fluorescence lifetime value. Blue represents the shortest fluorescence lifetime and orange represents the longest.

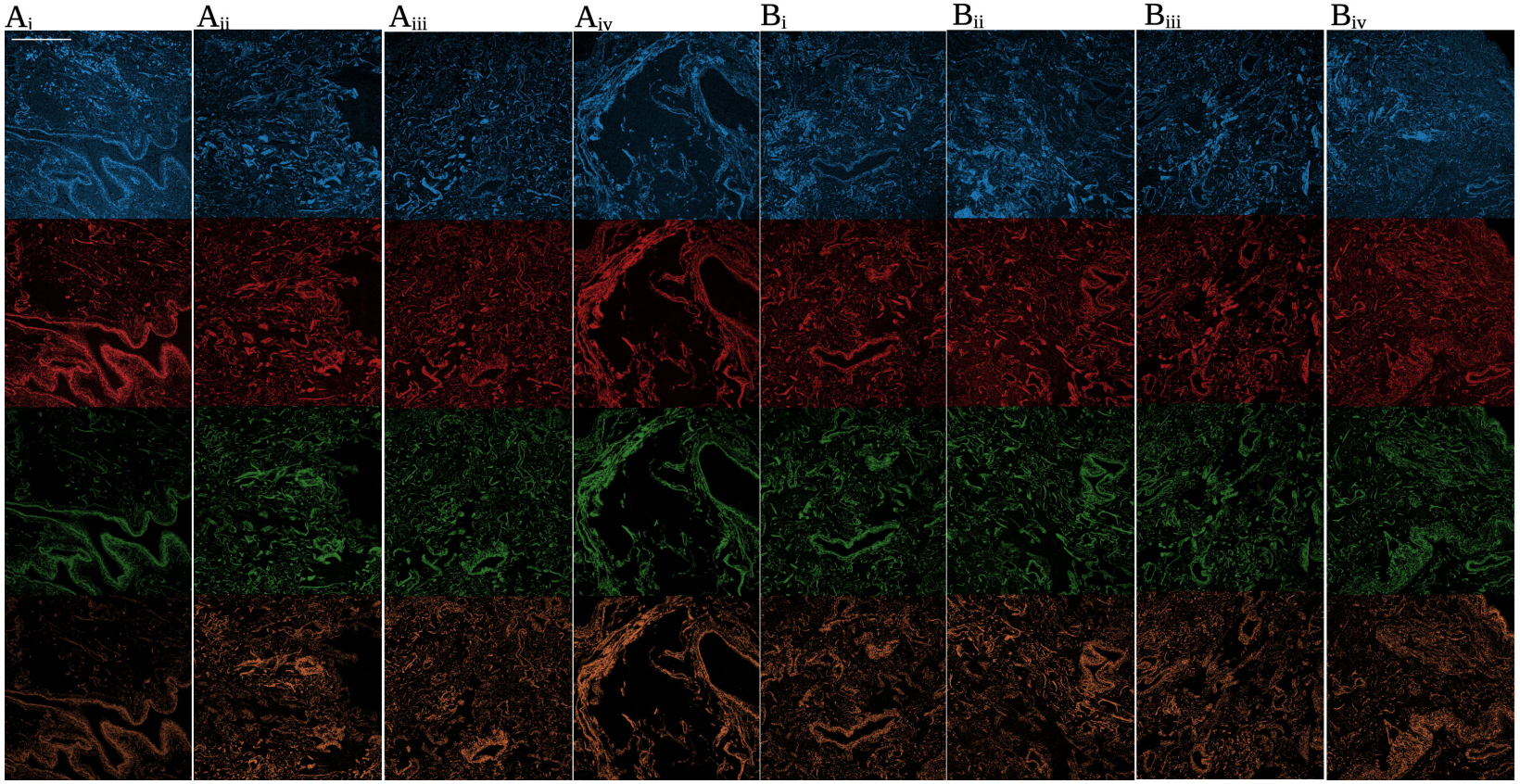

Figure 7.10: All FLIM images measured on a FLIM confocal microscope of non-cancerous sample number 11. The scale bar plotted in the top left is 500 µm wide. Each column contains the same image but colored for the corresponding fluorescence lifetime value. Blue represents the shortest fluorescence lifetime and orange represents the longest.

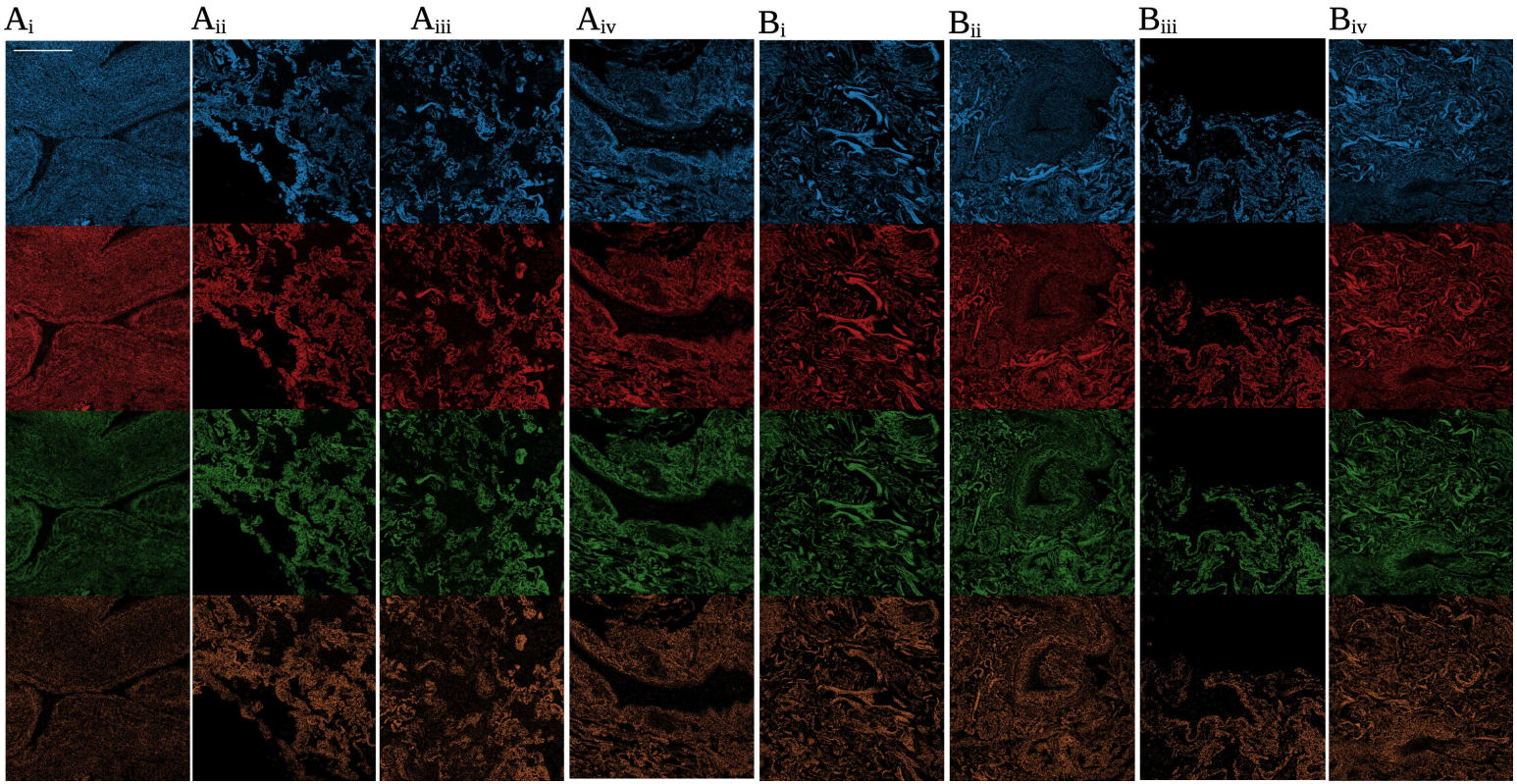

Figure 7.11: All FLIM images measured on a FLIM confocal microscope of cancerous sample number 15. The scale bar plotted in the top left is 500 µm wide. Each column contains the same image but colored for the corresponding fluorescence lifetime value. Blue represents the shortest fluorescence lifetime and orange represents the longest.

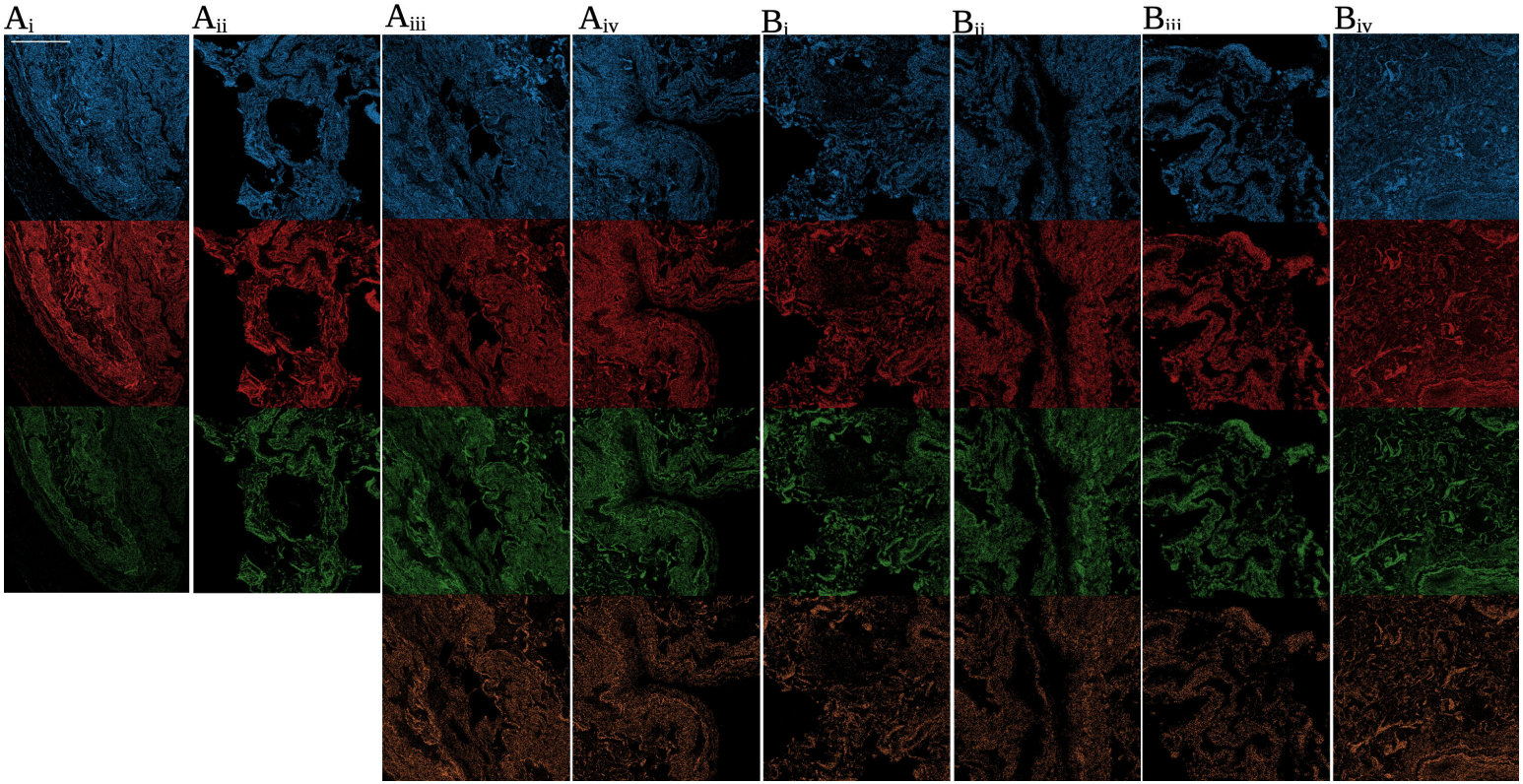

Figure 7.12: All FLIM images measured on a FLIM confocal microscope of non-cancerous sample number 15. The scale bar plotted in the top left is 500 µm wide. Each column contains the same image but colored for the corresponding fluorescence lifetime value. Blue represents the shortest fluorescence lifetime and orange represents the longest.

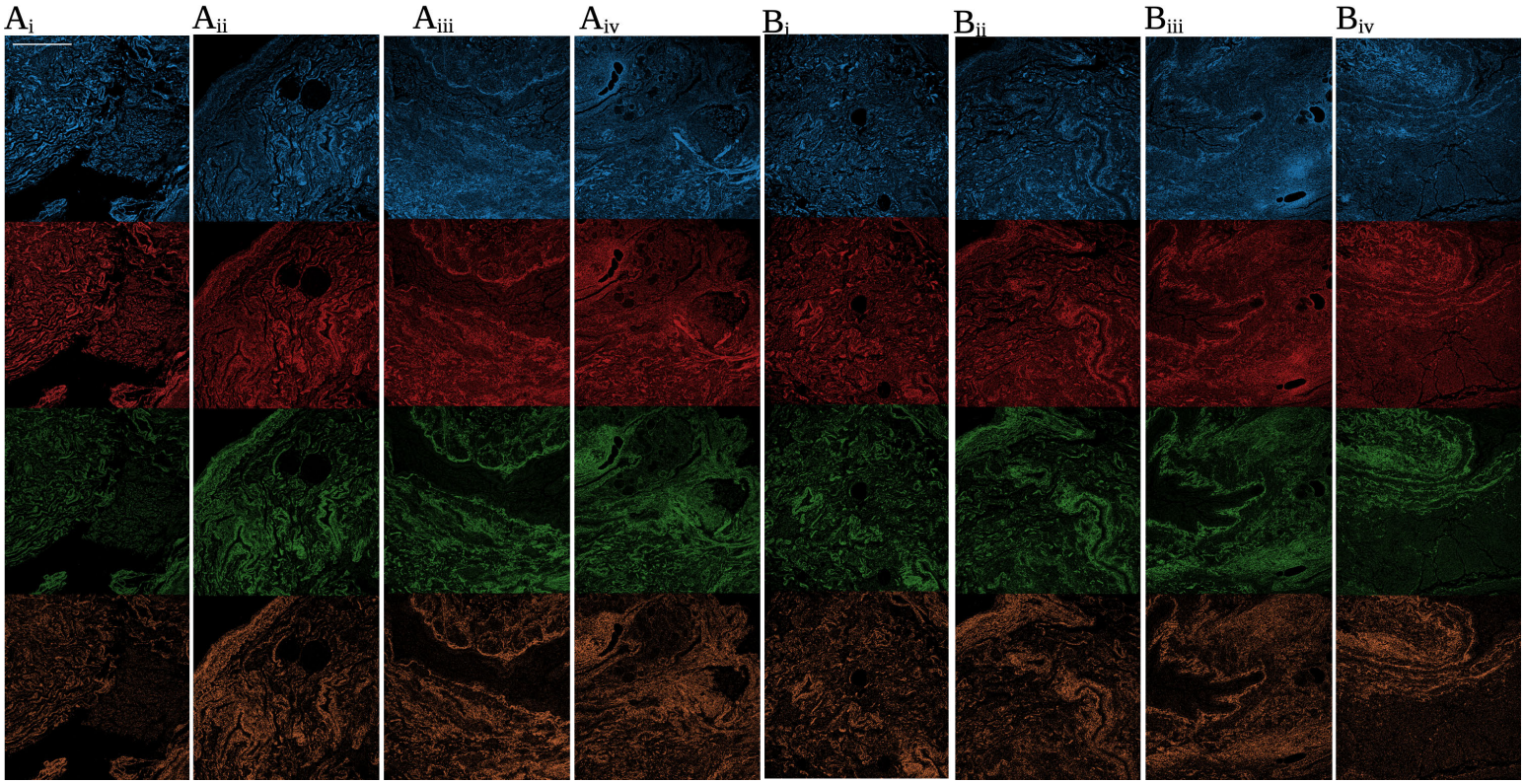

Figure 7.13: All FLIM images measured on a FLIM confocal microscope of cancerous sample number 16. The scale bar plotted in the top left is 500 µm wide. Each column contains the same image but colored for the corresponding fluorescence lifetime value. Blue represents the shortest fluorescence lifetime and orange represents the longest.

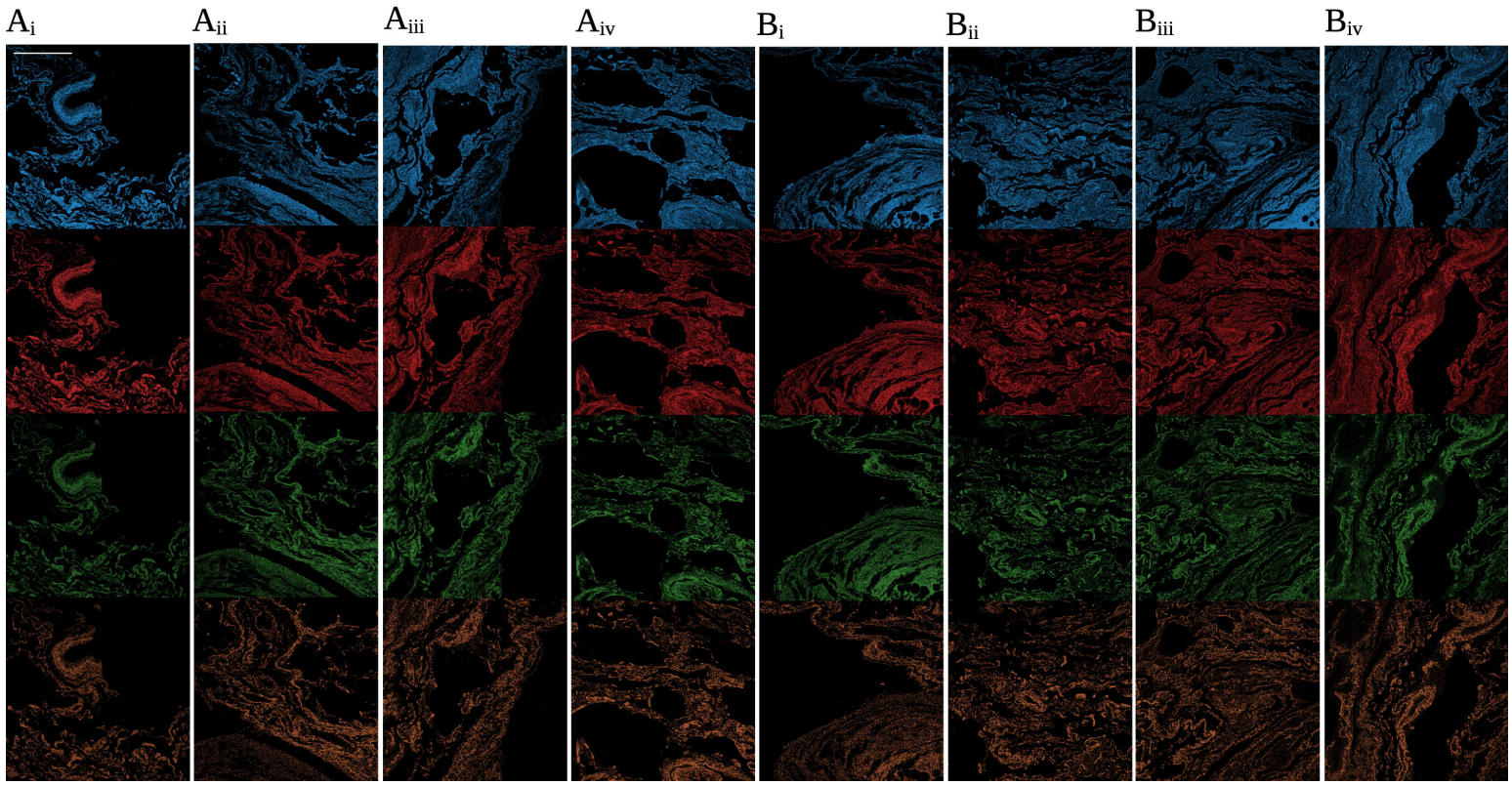

Figure 7.14: All FLIM images measured on a FLIM confocal microscope of non-cancerous sample number 16. The scale bar plotted in the top left is 500 µm wide. Each column contains the same image but coloured for the corresponding fluorescence lifetime value. The blue is the shortest FL and oragne is the longest.

Chapter 8

List of Publications

- Alexandra C Adams, András Kufcsák, Katjana Ehrlich, Kevin Dhaliwal, and Sohan Seth. Differentiating Individual Fluorophores from a Heterogenous Signature on a Fibre-based Time Resolved Fluorescence Spectroscopy (TRFS) System. **World Molecular Imaging Congress** (2022)
- Alexandra C Adams, András Kufcsák, Katjana Ehrlich, Kevin Dhaliwal, and Sohan Seth. Simultaneous spectral temporal modelling for a time-resolved fluorescence emission spectrum. **IEEE Transactions on Biomedical Engineering**, February 2023. ISSN 0018-9294.
- Alexandra C Adams, András Kufcsák, Charles Lochenie, Mohsen Khadem, Ahsan R Akram, Kevin Dhaliwal, and Sohan Seth. Fibre-optic based exploration of lung cancer autofluorescence using spectral fluorescence lifetime. **Biomedical Optics Express**, 15 (2):1132–1147, 2024

Bibliography

[1] Kelly M Latimer and Timothy F Mott. Lung cancer: diagnosis, treatment principles, and screening. *American family physician*, 91(4):250–256, 2015.

[2] Reem Nooreldeen and Horacio Bach. Current and future development in lung cancer diagnosis. *International journal of molecular sciences*, 22(16):8661, 2021.

[3] Hyuna Sung, Jacques Ferlay, Rebecca L Siegel, Mathieu Laversanne, Isabelle Soerjomataram, Ahmedin Jemal, and Freddie Bray. Global cancer statistics 2020: Globocan estimates of incidence and mortality worldwide for 36 cancers in 185 countries. *CA: a cancer journal for clinicians*, 71(3):209–249, 2021.

[4] Rebecca L Siegel, Kimberly D Miller, Hannah E Fuchs, and Ahmedin Jemal. Cancer statistics, 2022. *CA: a cancer journal for clinicians*, 72(1):7–33, 2022.

[5] Gavitt A Woodard, Kirk D Jones, and David M Jablons. Lung cancer staging and prognosis. *Lung Cancer*, pages 47–75, 2016.

[6] Frank C Detterbeck, Daniel J Boffa, Anthony W Kim, and Lynn T Tanoue. The eighth edition lung cancer stage classification. *Chest*, 151(1):193–203, 2017.

[7] Rachel E Gemine, Syedah Aleena Haider, Sofia Belo Ravara, and Keir E Lewis. Lung cancer patients. *Supporting Tobacco Cessation*, 90:165, 2021.

[8] Susan Fernandes, Gareth Williams, Elvira Williams, Katjana Ehrlich, James Stone, Neil Finlayson, Mark Bradley, Robert R Thomson, Ahsan R Akram, and Kevin Dhaliwal. Solitary pulmonary nodule imaging approaches and the role of optical fibre-based technologies. *European Respiratory Journal*, 57(3), 2021.

[9] William McNulty and David Baldwin. Management of pulmonary nodules. *BJR| Open*, 1(1):20180051, 2019.

[10] W Mazrani, K McHugh, and PJ Marsden. The radiation burden of radiological investigations. *Archives of disease in childhood*, 92(12):1127–1131, 2007.

[11] Stephen A Deppen, Jeffrey D Blume, Clark D Kensinger, Ashley M Morgan, Melinda C Aldrich, Pierre P Massion, Ronald C Walker, Melissa L McPheeters, Joe B Putnam, and Eric L Grogan. Accuracy of fdg-pet to diagnose lung cancer in areas with infectious lung disease: a meta-analysis. *Jama*, 312(12):1227–1236, 2014.

[12] Irving J Bigio and Judith R Mourant. Ultraviolet and visible spectroscopies for tissue diagnostics: fluorescence spectroscopy and elastic-scattering spectroscopy. *Physics in Medicine & Biology*, 42(5):803, 1997.

[13] George E Moore, William T Peyton, Lyle A French, and Walter W Walker. The clinical use of fluorescein in neurosurgery: the localization of brain tumors. *Journal of neurosurgery*, 5(4):392–398, 1948.

[14] Walter Stummer, Uwe Pichlmeier, Thomas Meinel, Otmar Dieter Wiestler, Friedhelm Zanella, and Hans-Jürgen Reulen. Fluorescence-guided surgery with 5-aminolevulinic acid for resection of malignant glioma: a randomised controlled multicentre phase iii trial. *The lancet oncology*, 7(5):392–401, 2006.

[15] J R Lakowicz. *Principles of fluorescence spectroscopy*. SSBM, 2013.

[16] Ulai Noomnarm and Robert M Clegg. Fluorescence lifetimes: fundamentals and interpretations. *Photosynthesis research*, 101(2):181–194, 2009.

[17] Peter W Atkins and Ronald S Friedman. *Molecular quantum mechanics*. Oxford university press, 2011.

[18] B Valeur and M N Berberan-Santos. *Molecular fluorescence: principles and applications*. John Wiley & Sons, 2012.

[19] Jonathan B Grimm and Luke D Lavis. Caveat fluorophore: an insiders' guide to small-molecule fluorescent labels. *Nature Methods*, 19(2):149–158, 2022.

[20] Robert Sjöback, Jan Nygren, and Mikael Kubista. Absorption and fluorescence properties of fluorescein. *Spectrochimica Acta Part A: Molecular and Biomolecular Spectroscopy*, 51(6):L7–L21, 1995.

[21] Laura Marcu, Paul MW French, and Daniel S Elson. *Fluorescence lifetime spectroscopy and imaging: principles and applications in biomedical diagnostics*. CRC Press, 2014.

[22] Edinburgh Instruments. Feature highlight: Micropl upgrade. `https://www.edinst.com/feature-highlight-micropl-upgrade/`, 2024. Last accessed on February 12, 2024.

[23] Mauna Kea Technologies. Cellvizio system. `https://www.maunakeatech.com/en/physicians/11-cellvizio-system`, 2024. Last accessed on February 12, 2024.

[24] Luc Thiberville, Mathieu Salaün, Samy Lachkar, Stéphane Dominique, Sophie Moreno-Swirc, Christine Vever-Bizet, and Geneviève Bourg-Heckly. In vivo confocal fluorescence endomicroscopy of lung cancer. In *13th world conference on lung cancer*, 2009.

[25] Rupsa Datta, Amani Gillette, Matthew Stefely, and Melissa C Skala. Recent innovations in fluorescence lifetime imaging microscopy for biology and medicine. *Journal of Biomedical Optics*, 26(7):070603, 2021.

[26] Hazel L Stewart and David JS Birch. Fluorescence guided surgery. *Methods and Applications in Fluorescence*, 9(4):042002, 2021.

[27] Donna J Webb and Claire M Brown. Epi-fluorescence microscopy. *Cell Imaging Techniques: Methods and Protocols*, pages 29–59, 2013.

[28] C Bruschini, H Homulle, I M Antolovic, et al. Single-photon avalanche diode imagers in biophotonics: review and outlook.

[29] Franco Zappa, Simone Tisa, Alberto Tosi, and Sergio Cova. Principles and features of single-photon avalanche diode arrays. *Sensors and Actuators A: Physical*, 140(1): 103–112, 2007.

[30] Claudio Bruschini, Harald Homulle, Ivan Michel Antolovic, Samuel Burri, and Edoardo Charbon. Single-photon avalanche diode imagers in biophotonics: review and outlook. *Light: Science Applications*, 8:87, 2019. ISSN 2047-7538. doi: 10.1038/s41377-019-0191-5. URL https://doi.org/10.1038/s41377-019-0191-5.

[31] David JS Birch and Robert E Imhof. Time-domain fluorescence spectroscopy using time-correlated single-photon counting. In *Topics in Fluorescence Spectroscopy: Techniques*, pages 1–95. Springer, 1991.

[32] D. V. O. O'Connor and D. Phillips. *Time-correlated Single Photon Counting*. Academic Press, London, 1984.

[33] Alexander P Demchenko. Photobleaching of organic fluorophores: quantitative characterization, mechanisms, protection. *Methods and Applications in Fluorescence*, 8: 022001, 2 2020. ISSN 2050-6120. doi: 10.1088/2050-6120/ab7365.

[34] R Datta, T M. Heaster, J T. Sharick, et al. Fluorescence lifetime imaging microscopy: fundamentals and advances in instrumentation, analysis, and applications. *J. Biomed. Opt*, 25(07). ISSN 1083-3668. doi: 10.1117/1.JBO.25.7.071203. URL https://www.spiedigitallibrary.org/journals/journal-of-biomedical-optics/volume-25/issue-07/071203/Fluorescence-lifetime-imaging-microscopy--fundamentals-and-advances-in-instrumentation/10.1117/1.JBO.25.7.071203.full.

[35] A T Erdogan, R Walker, N Finlayson, et al. A cmos spad line sensor with per-pixel histogramming tdc for time-resolved multispectral imaging.

[36] L Marcu. Fluorescence Lifetime Techniques in Medical Applications. *Ann Biomed Eng* ., 40(2):304–331, February 2012. ISSN 0090-6964, 1573-9686. doi: 10.1007/s10439-011-0495-y. URL http://link.springer.com/10.1007/s10439-011-0495-y.

[37] Sytsma, Vroom, De Grauw, and Gerritsen. Time-gated fluorescence lifetime imaging and microvolume spectroscopy using two-photon excitation. *Journal of Microscopy*, 191(1):39–51, 1998.

[38] Liping Wei, Wenrong Yan, and Derek Ho. Recent advances in fluorescence lifetime analytical microsystems: Contact optics and cmos time-resolved electronics. *Sensors*, 17(12):2800, 2017.

[39] OJ Steingraber and IB Berlman. Versatile technique for measuring fluorescence decay times in the nanosecond region. *Review of Scientific Instruments*, 34(5):524–529, 1963.

[40] G OS Williams, E Williams, N Finlayson, et al. Full spectrum fluorescence lifetime imaging with 0.5 nm spectral and 50 ps temporal resolution.

[41] Alexandra C Adams, András Kufcsák, Charles Lochenie, Mohsen Khadem, Ahsan R Akram, Kevin Dhaliwal, and Sohan Seth. Fibre-optic based exploration of lung cancer autofluorescence using spectral fluorescence lifetime. *Biomedical Optics Express*, 15 (2):1132–1147, 2024.

[42] N Periasamy. Analysis of fluorescence decay by the nonlinear least squares method. *Biophys. J.*, 54(5):961–967, 1988.

[43] J Kim and J Seok. Statistical properties of amplitude and decay parameter estimators for fluorescence lifetime imaging. *Opt. Express*, 21(5):6061–6075, 2013.

[44] Željko Bajzer, Terry M Therneau, Joseph C Sharp, and Franklin G Prendergast. Maximum likelihood method for the analysis of time-resolved fluorescence decay curves. *European biophysics journal*, 20:247–262, 1991.

[45] Becker & Hickl GmbH. Time-correlated single photon counting - Becker & Hickl GmbH - TCSPC Electronics - Photon Counting - FLIM, 2019. URL https://www.becker-hickl.com/literature/documents/flim/flim-for-leica-microscopes/.

[46] R M Ballew and JN Demas. An error analysis of the rapid lifetime determination method for the evaluation of single exponential decays. *Anal. Chem.*, 61(1):30–33, 1989.

[47] Alexandra Adams, Andras Kufcsak, Katjana Ehrlich, Kevin Dhaliwal, and Sohan Seth. Simultaneous spectral temporal modelling for a time-resolved fluorescence emission spectrum. *IEEE Transactions on Biomedical Engineering*, February 2023. ISSN 0018-9294.

[48] S P Poland, A T Erdogan, N Krstajić, et al. New high-speed centre of mass method incorporating background subtraction for accurate determination of fluorescence lifetime.

[49] D U Li, D Tyndall, R Walker, et al. Video-rate fluorescence lifetime imaging camera with cmos single-photon avalanche diode arrays and high-speed imaging algorithm.

[50] A S Dabir, C Trivedi, Y Ryu, et al. Fully automated deconvolution method for on-line analysis of time-resolved fluorescence spectroscopy data based on an iterative laguerre expansion technique.

[51] Mou Adhikari, Rola Houhou, Julian Hniopek, and Thomas Bocklitz. Review of fluorescence lifetime imaging microscopy (flim) data analysis using machine learning. *Journal of Experimental and Theoretical Analyses*, 1(1):44–63, 2023.

[52] Gang Wu, Thomas Nowotny, Yongliang Zhang, Hong-Qi Yu, and David Day-Uei Li. Artificial neural network approaches for fluorescence lifetime imaging techniques. *Optics letters*, 41(11):2561–2564, 2016.

[53] Shuxia Guo, Anja Silge, Hyeonsoo Bae, Tatiana Tolstik, Tobias Meyer, Georg Matziolis, Michael Schmitt, Jürgen Popp, and Thomas Bocklitz. Flim data analysis based on laguerre polynomial decomposition and machine-learning. *Journal of Biomedical Optics*, 26(2):022909–022909, 2021.

[54] Alexander Netaev, Nicolas Schierbaum, and Karsten Seidl. Artificial neural network (ann)-based determination of fractional contributions from mixed fluorophores using fluorescence lifetime measurements. *Journal of Fluorescence*, 34(1):305–311, 2024.

[55] Deborah Seah, Zhiming Cheng, and Marc Vendrell. Fluorescent probes for imaging in humans: Where are we now? *ACS nano*, 17(20):19478–19490, 2023.

[56] Hidde A Galema, Tessa M van Ginhoven, Gaston JH Franssen, Johannes Hofland, Claire GOT Bouman, Cornelis Verhoef, Alexander L Vahrmeijer, Merlijn Hutteman, Denise E Hilling, and Stijn Keereweer. Fluorescence-guided surgery using methylene blue to improve identification of metastatic small intestinal neuroendocrine tumours. *British Journal of Surgery*, 110(5):541–544, 2023.

[57] Victor G Prieto, Peter S Zhang, and Neil S Sadick. Evaluation of pulsed light and radiofrequency combined for the treatment of acne vulgaris with histologic analysis of facial skin biopsies. *Journal of cosmetic and laser therapy*, 7(2):63–68, 2005.

[58] Huihui Lu, Francesco Floris, Marc Rensing, and Stefan Andersson-Engels. Fluorescence spectroscopy study of protoporphyrin ix in optical tissue simulating liquid phantoms. *Materials*, 13(9):2105, 2020.

[59] Georg Widhalm, Jonathan Olson, Jonathan Weller, Jaime Bravo, Seunggu J Han, Joanna Phillips, Shawn L Hervey-Jumper, Susan M Chang, David W Roberts, and Mitchel S Berger. The value of visible 5-ala fluorescence and quantitative protoporphyrin ix analysis for improved surgery of suspected low-grade gliomas. *Journal of neurosurgery*, 133(1):79–88, 2019.

[60] Floris J Voskuil, Pieter J Steinkamp, Tian Zhao, Bert van der Vegt, Marjory Koller, Jan J Doff, Yalia Jayalakshmi, Jeffery P Hartung, Jinming Gao, Baran D Sumer, et al. Exploiting metabolic acidosis in solid cancers using a tumor-agnostic ph-activatable nanoprobe for fluorescence-guided surgery. *Nature communications*, 11(1):3257, 2020.

[61] Gregory T Kennedy, David E Holt, Feredun S Azari, Elizabeth Bernstein, Bilal Nadeem, Ashley Chang, Neil T Sullivan, Alix Segil, Charuhas Desphande, Eric Bensen, et al. A cathepsin-targeted quenched activity–based probe facilitates enhanced detection of human tumors during resection. *Clinical Cancer Research*, 28(17):3729–3741, 2022.

[62] María José García, Andrés Kamaid, and Leonel Malacrida. Label-free fluorescence microscopy: revisiting the opportunities with autofluorescent molecules and harmonic generations as biosensors and biomarkers for quantitative biology. *Biophysical Reviews*, pages 1–11, 2023.

[63] Ai Mochida, Fusa Ogata, Tadanobu Nagaya, Peter L Choyke, and Hisataka Kobayashi. Activatable fluorescent probes in fluorescence-guided surgery: Practical considerations. *Bioorganic & medicinal chemistry*, 26(4):925–930, 2018.

[64] Georges A Wagnieres, Willem M Star, and Brian C Wilson. In vivo fluorescence spectroscopy and imaging for oncological applications. *Photochemistry and photobiology*, 68(5):603, 1998.

[65] Dorian Gouzou, Ali Taimori, Tarek Haloubi, Neil Finlayson, Qiang Wang, James R Hopgood, and Marta Vallejo. Applications of machine learning in time-domain fluorescence lifetime imaging: a review. *Methods and Applications in Fluorescence*, 2023.

[66] Amar BT Ghisaidoobe and Sang J Chung. Intrinsic tryptophan fluorescence in the detection and analysis of proteins: a focus on förster resonance energy transfer techniques. *International journal of molecular sciences*, 15(12):22518–22538, 2014.

[67] Chenwei Li and Hui Zhao. Tryptophan and its metabolites in lung cancer: basic functions and clinical significance. *Frontiers in oncology*, 11:707277, 2021.

[68] Mateusz Kciuk, Beata Marciniak, Mariusz Mojzych, and Renata Kontek. Focus on uv-induced dna damage and repair—disease relevance and protective strategies. *International Journal of Molecular Sciences*, 21(19):7264, 2020.

[69] Christine Tara Peterson, Dmitry A Rodionov, Andrei L Osterman, and Scott N Peterson. B vitamins and their role in immune regulation and cancer. *Nutrients*, 12(11):3380, 2020.

[70] L Galluzzi, E Vacchelli, J Michels, P Garcia, O Kepp, L Senovilla, I Vitale, and G Kroemer. Effects of vitamin b6 metabolism on oncogenesis, tumor progression and therapeutic responses. *Oncogene*, 32(42):4995–5004, 2013.

[71] Claudio Bueno and María Victoria Encinas. Photophysical and photochemical studies of pyridoxamine. *Helvetica chimica acta*, 86(10):3363–3375, 2003.

[72] Barbara Young, Geraldine O'Dowd, and William Stewart. *Wheater's Basic Pathology: A Text, Atlas and Review of Histopathology E-Book*. Elsevier Health Sciences, 2009.

[73] Yasuhiro Mochizuki, Min Kyun Park, Takao Mori, and Seiichiro Kawashima. The difference in autofluorescence features of lipofuscin between brain and adrenal. *Zoological science*, 12(3):283–288, 1995.

[74] Madhav Sachar, Karl E Anderson, and Xiaochao Ma. Protoporphyrin ix: the good, the bad, and the ugly. *Journal of Pharmacology and Experimental Therapeutics*, 356(2): 267–275, 2016.

[75] Yoshinori Harada, Yasutoshi Murayama, Tetsuro Takamatsu, Eigo Otsuji, and Hideo Tanaka. 5-aminolevulinic acid-induced protoporphyrin ix fluorescence imaging for tumor detection: Recent advances and challenges. *International Journal of Molecular Sciences*, 23(12):6478, 2022.

[76] Jennifer A Russell, Kevin R Diamond, Tony J Collins, Henry F Tiedje, Joseph E Hayward, Thomas J Farrell, Michael S Patterson, and Qiyin Fang. Characterization of fluorescence lifetime of photofrin and delta-aminolevulinic acid induced protoporphyrin ix in living cells using single-and two-photon excitation. *IEEE Journal of Selected Topics in Quantum Electronics*, 14(1):158–166, 2008.

[77] Gerald Burgstaller, Bettina Oehrle, Michael Gerckens, Eric S White, Herbert B Schiller, and Oliver Eickelberg. The instructive extracellular matrix of the lung: basic composition and alterations in chronic lung disease. *European Respiratory Journal*, 50(1), 2017.

[78] Weiwei Shi, Bo Yang, Xiaoyan Li, Shengjie Sun, Lijie Wang, and Shunchang Jiao. The effect of lysyl oxidase polymorphism on susceptibility and prognosis of nonsmall cell lung cancer. *Tumor Biology*, 33:2379–2383, 2012.

[79] Z Deyl, K Macek, M Adam, et al. Studies on the chemical nature of elastin fluorescence. *Biochimica et Biophysica Acta (BBA)-Protein Structure*, 625(2):248–254, 1980.

[80] Mark G Jones, Orestis G Andriotis, James JW Roberts, Kerry Lunn, Victoria J Tear, Lucy Cao, Kjetil Ask, David E Smart, Alessandra Bonfanti, Peter Johnson, et al. Nanoscale dysregulation of collagen structure-function disrupts mechano-homeostasis and mediates pulmonary fibrosis. *Elife*, 7:e36354, 2018.

[81] SR Rønnow, JH Kristensen, J Thorlacius-Ussing, MA Karsdal, and A Heinz. Elastin. In *Biochemistry of Collagens, Laminins and Elastin*, pages 279–289. Elsevier, 2024.

[82] SM Partridge, DF Elsden, and J Thomas. Constitution of the cross-linkages in elastin. *Nature*, 197(4874):1297–1298, 1963.

[83] Erik Thunnissen, Noriko Motoi, Yuko Minami, Daisuke Matsubara, Wim Timens, Yukio Nakatani, Yuichi Ishikawa, Ximena Baez-Navarro, Teodora Radonic, Hans Blaauwgeers, et al. Elastin in pulmonary pathology: relevance in tumours with a lepidic or papillary appearance. a comprehensive understanding from a morphological viewpoint. *Histopathology*, 80(3):457–467, 2022.

[84] Yuzhen Ouyang, Yanping Liu, Zhiming M Wang, Zongwen Liu, and Minghua Wu. Flim as a promising tool for cancer diagnosis and treatment monitoring. *Nano-Micro Letters*, 13(1):133, 2021.

[85] Luc Thiberville, Sophie Moreno-Swirc, Tom Vercauteren, Eric Peltier, Charlotte Cavé, and Genevieve Bourg Heckly. In vivo imaging of the bronchial wall microstructure using fibered confocal fluorescence microscopy. *American journal of respiratory and critical care medicine*, 175(1):22–31, 2007.

[86] Matthew W Conklin, Paolo P Provenzano, Kevin W Eliceiri, Ruth Sullivan, and Patricia J Keely. Fluorescence lifetime imaging of endogenous fluorophores in histopathology sections reveals differences between normal and tumor epithelium in carcinoma in situ of the breast. *Cell biochemistry and biophysics*, 53(3):145–157, 2009.

[87] Kathleen M Daumer, Ahsan U Khan, and Marla J Steinbeck. Chlorination of pyridinium compounds: possible role of hypochlorite, n-chloramines, and chlorine in the oxidation of pyridinoline cross-links of articular cartilage collagen type ii during acute inflammation. *Journal of Biological Chemistry*, 275(44):34681–34692, 2000.

[88] SP Robins, A Duncan, N Wilson, and BJ Evans. Standardization of pyridinium crosslinks, pyridinoline and deoxypyridinoline, for use as biochemical markers of collagen degradation. *Clinical chemistry*, 42(10):1621–1626, 1996.

[89] Y Sun, Y Sun, D Stephens, et al. Dynamic tissue analysis using time-and wavelength-resolved fluorescence spectroscopy for atherosclerosis diagnosis.

[90] Yang Pu, Wubao Wang, Yuanlong Yang, and Robert R Alfano. Native fluorescence spectra of human cancerous and normal breast tissues analyzed with non-negative constraint methods. *Applied optics*, 52(6):1293–1301, 2013.

[91] Douglas Hanahan and Robert A Weinberg. Hallmarks of cancer: the next generation. *cell*, 144(5):646–674, 2011.

[92] Douglas Hanahan. Hallmarks of cancer: new dimensions. *Cancer discovery*, 12(1): 31–46, 2022.

[93] Otto Warburg, Franz Wind, and Erwin Negelein. The metabolism of tumors in the body. *The Journal of general physiology*, 8(6):519, 1927.

[94] Karolien Vanhove, Geert-Jan Graulus, Liesbet Mesotten, Michiel Thomeer, Elien Derveaux, Jean-Paul Noben, Wanda Guedens, and Peter Adriaensens. The metabolic landscape of lung cancer: new insights in a disturbed glucose metabolism. *Frontiers in oncology*, 9:1215, 2019.

[95] Matthew G Vander Heiden, Lewis C Cantley, and Craig B Thompson. Understanding the warburg effect: the metabolic requirements of cell proliferation. *science*, 324(5930): 1029–1033, 2009.

[96] Karen G de la Cruz-López, Leonardo Josué Castro-Muñoz, Diego O Reyes-Hernández, Alejandro García-Carrancá, and Joaquín Manzo-Merino. Lactate in the regulation of tumor microenvironment and therapeutic approaches. *Frontiers in oncology*, 9:1143, 2019.

[97] Iñigo San-Millán and George A Brooks. Reexamining cancer metabolism: lactate production for carcinogenesis could be the purpose and explanation of the warburg effect. *Carcinogenesis*, 38(2):119–133, 2017.

[98] Stephanos Pavlides, Diana Whitaker-Menezes, Remedios Castello-Cros, Neal Flomenberg, Agnieszka K Witkiewicz, Philippe G Frank, Mathew C Casimiro, Chenguang Wang, Paolo Fortina, Sankar Addya, et al. The reverse warburg effect: aerobic glycolysis in cancer associated fibroblasts and the tumor stroma. *Cell cycle*, 8(23): 3984–4001, 2009.

[99] Ralph J DeBerardinis and Navdeep S Chandel. We need to talk about the warburg effect. *Nature metabolism*, 2(2):127–129, 2020.

[100] Pierre Sonveaux, Frédérique Végran, Thies Schroeder, Melanie C Wergin, Julien Verrax, Zahid N Rabbani, Christophe J De Saedeleer, Kelly M Kennedy, Caroline Diepart, Bénédicte F Jordan, et al. Targeting lactate-fueled respiration selectively kills hypoxic tumor cells in mice. *The Journal of clinical investigation*, 118(12):3930–3942, 2008.

[101] Pei-Hsuan Chen, Ling Cai, Kenneth Huffman, Chendong Yang, Jiyeon Kim, Brandon Faubert, Lindsey Boroughs, Bookyung Ko, Jessica Sudderth, Elizabeth A McMillan, et al. Metabolic diversity in human non-small cell lung cancer cells. *Molecular cell*, 76 (5):838–851, 2019.

[102] Huai-Qiang Ju, Jin-Fei Lin, Tian Tian, Dan Xie, and Rui-Hua Xu. Nadph homeostasis in cancer: functions, mechanisms and therapeutic implications. *Signal transduction and targeted therapy*, 5(1):231, 2020.

[103] Patrick M Schaefer, Sviatlana Kalinina, Angelika Rueck, Christine AF von Arnim, and Bjoern von Einem. Nadh autofluorescence—a marker on its way to boost bioenergetic research. *Cytometry Part A*, 95(1):34–46, 2019.

[104] Taylor M Cannon, Joao L Lagarto, Benjamin T Dyer, Edwin Garcia, Douglas J Kelly, Nicholas S Peters, Alexander R Lyon, Paul MW French, and Chris Dunsby. Characterization of nadh fluorescence properties under one-photon excitation with respect to temperature, ph, and binding to lactate dehydrogenase. *OSA continuum*, 4(5):1610–1625, 2021.

[105] Thomas S Blacker, Zoe F Mann, Jonathan E Gale, Mathias Ziegler, Angus J Bain, Gyorgy Szabadkai, and Michael R Duchen. Separating nadh and nadph fluorescence in live cells and tissues using flim. *Nature communications*, 5(1):3936, 2014.

[106] Charles A Abbas and Andriy A Sibirny. Genetic control of biosynthesis and transport of riboflavin and flavin nucleotides and construction of robust biotechnological producers. *Microbiology and molecular biology reviews*, 75(2):321–360, 2011.

[107] Jia-Qi Xu, Yan-Li Fu, Jing Zhang, Kai-Yu Zhang, Jie Ma, Jing-Yi Tang, Zhi-Wei Zhang, and Zhong-Yan Zhou. Targeting glycolysis in non-small cell lung cancer: Promises and challenges. *Frontiers in Pharmacology*, 13, 2022.

[108] Jens Hühner, Álvaro Ingles-Prieto, Christian Neusüß, Michael Lämmerhofer, and Harald Janovjak. Quantification of riboflavin, flavin mononucleotide, and flavin adenine dinucleotide in mammalian model cells by ce with led-induced fluorescence detection. *Electrophoresis*, 36(4):518–525, 2015.

[109] PubChem. "pubchem compound summary for cid 643975, flavin adenine dinucleotide", 1 2024. URL `https://pubchem.ncbi.nlm.nih.gov/compound/Flavin-adenine-dinucleotide`.

[110] Sviatlana Kalinina, Christian Freymueller, Nilanjon Naskar, Bjoern von Einem, Kirsten Reess, Ronald Sroka, and Angelika Rueck. Bioenergetic alterations of metabolic redox coenzymes as nadh, fad and fmn by means of fluorescence lifetime imaging techniques. *International Journal of Molecular Sciences*, 22(11):5952, 2021.

[111] Kiran Thakur, Sudhir Kumar Tomar, Ashish Kumar Singh, Surajit Mandal, and Sumit Arora. Riboflavin and health: A review of recent human research. *Critical reviews in food science and nutrition*, 57(17):3650–3660, 2017.

[112] Hui-ting Yang, Pei-chun Chao, and Mei-chin Yin. Riboflavin at high doses enhances lung cancer cell proliferation, invasion, and migration. *Journal of food science*, 78(2): H343–H349, 2013.

[113] Javier Galbán, Isabel Sanz-Vicente, Jesús Navarro, and Susana De Marcos. The intrinsic fluorescence of fad and its application in analytical chemistry: a review. *Methods and Applications in Fluorescence*, 4(4):042005, 2016.

[114] Lucia Trisolini, Nicola Gambacorta, Ruggiero Gorgoglione, Michele Montaruli, Luna Laera, Francesco Colella, Mariateresa Volpicella, Anna De Grassi, and Ciro Leonardo Pierri. Fad/nadh dependent oxidoreductases: from different amino acid sequences to similar protein shapes for playing an ancient function. *Journal of Clinical Medicine*, 8 (12):2117, 2019.

[115] A King, MA Selak, , and E Gottlieb. Succinate dehydrogenase and fumarate hydratase: linking mitochondrial dysfunction and cancer. *Oncogene*, 25(34):4675–4682, 2006.

[116] P Drössler, W Holzer, Alfons Penzkofer, and PJCP Hegemann. ph dependence of the absorption and emission behaviour of riboflavin in aqueous solution. *Chemical Physics*, 282(3):429–439, 2002.

[117] Anna C Croce and Giovanni Bottiroli. Autofluorescence spectroscopy and imaging: a tool for biomedical research and diagnosis. *European journal of histochemistry: EJH*, 58(4), 2014.

[118] Olivia I Kolenc and Kyle P Quinn. Evaluating cell metabolism through autofluorescence imaging of nad (p) h and fad. *Antioxidants & redox signaling*, 30(6):875–889, 2019.

[119] Sandeep Chakraborty, Fang-Shin Nian, Jin-Wu Tsai, Artashes Karmenyan, and Arthur Chiou. Quantification of the metabolic state in cell-model of parkinson's disease by fluorescence lifetime imaging microscopy. *Scientific reports*, 6(1):19145, 2016.

[120] M Wang, F Tang, X Pan, L Yao, X Wang, Y Jing, J Ma, G Wang, and L Mi. Rapid diagnosis and intraoperative margin assessment of human lung cancer with fluorescence lifetime imaging microscopy. *BBA clinical*, 8:7–13, 2017.

[121] David Reichert, Lisa I Wadiura, Mikael T Erkkilae, Johanna Gesperger, Alexandra Lang, Thomas Roetzer-Pejrimovsky, Jessica Makolli, Adelheid Woehrer, Marco Wilzbach, Christoph Hauger, et al. Flavin fluorescence lifetime and autofluorescence optical redox ratio for improved visualization and classification of brain tumors. *Frontiers in Oncology*, 13:1105648, 2023.

[122] Helmut Sies. Oxidative stress: a concept in redox biology and medicine. *Redox biology*, 4:180–183, 2015.

[123] Asha Acharya, Ila Das, Des Chandhok, and Tapas Saha. Redox regulation in cancer: a double-edged sword with therapeutic potential. *Oxidative medicine and cellular longevity*, 3(1):23–34, 2010.

[124] Shagufta Rehman Alam, Horst Wallrabe, Zdenek Svindrych, Ajay K Chaudhary, Kathryn G Christopher, Dhyan Chandra, and Ammasi Periasamy. Investigation of mitochondrial metabolic response to doxorubicin in prostate cancer cells: an nadh, fad and tryptophan flim assay. *Scientific reports*, 7(1):10451, 2017.

[125] He N Xu and Lin Z Li. Quantitative redox imaging biomarkers for studying tissue metabolic state and its heterogeneity. *Journal of innovative optical health sciences*, 7(02):1430002, 2014.

[126] M Marsden, T Fukazawa, Y Deng, et al. Flimbrush: dynamic visualization of intraoperative free-hand fiber-based fluorescence lifetime imaging.

[127] A Alfonso-Garcia, J Bec, B Weyers, et al. Mesoscopic fluorescence lifetime imaging: Fundamental principles, clinical applications and future directions.

[128] L Marcu, R C Thompson, S Garde, et al. Time-resolved fluorescence spectroscopy of human brain tumors.

[129] Z Nie, S A Yeh, M LePalud, et al. Optical biopsy of the upper gi tract using fluorescence lifetime and spectra.

[130] Q Wang, M Vallejo, and J Hopgood. Fluorescence lifetime endomicroscopic image-based ex-vivo human lung cancer differentiation using machine learning. 2020.

[131] J A Kim, D J Wales, and G Yang. Optical spectroscopy for in vivo medical diagnosis—a review of the state of the art and future perspectives. *Prog. biomed. eng*, 2(4):042001, 2020.

[132] Jennifer E Phipps, Dimitris Gorpas, Jakob Unger, Morgan Darrow, Richard J Bold, and Laura Marcu. Automated detection of breast cancer in resected specimens with fluorescence lifetime imaging. *Physics in Medicine & Biology*, 63(1):015003, 2017.

[133] Jakob Unger, Christoph Hebisch, Jennifer E Phipps, João L Lagarto, Hanna Kim, Morgan A Darrow, Richard J Bold, and Laura Marcu. Real-time diagnosis and visualization of tumor margins in excised breast specimens using fluorescence lifetime imaging and machine learning. *Biomedical optics express*, 11(3):1216–1230, 2020.

[134] Elvis Duran-Sierra, Shuna Cheng, Rodrigo Cuenca, Beena Ahmed, Jim Ji, Vladislav V Yakovlev, Mathias Martinez, Moustafa Al-Khalil, Hussain Al-Enazi, Yi-Shing Lisa Cheng, et al. Machine-learning assisted discrimination of precancerous and cancerous from healthy oral tissue based on multispectral autofluorescence lifetime imaging endoscopy. *Cancers*, 13(19):4751, 2021.

[135] Javier A Jo, Shuna Cheng, Rodrigo Cuenca-Martinez, Elvis Duran-Sierra, Bilal Malik, Beena Ahmed, Kristen Maitland, Yi-Shing Lisa Cheng, John Wright, and Terry Reese. Endogenous fluorescence lifetime imaging (flim) endoscopy for early detection of oral cancer and dysplasia. In *2018 40th Annual International Conference of the IEEE Engineering in Medicine and Biology Society (EMBC)*, pages 3009–3012. IEEE, 2018.

[136] Mark Marsden, Brent W Weyers, Julien Bec, Tianchen Sun, Regina F Gandour-Edwards, Andrew C Birkeland, Marianne Abouyared, Arnaud F Bewley, D Gregory Farwell, and Laura Marcu. Intraoperative margin assessment in oral and oropharyngeal cancer using label-free fluorescence lifetime imaging and machine learning. *IEEE Transactions on Biomedical Engineering*, 68(3):857–868, 2020.

[137] Alessandro Cosci, Marcelo Saito Nogueira, Sebastião Pratavieira, Ademar Takahama, Rebeca de Souza Azevedo, and Cristina Kurachi. Time-resolved fluorescence spectroscopy for clinical diagnosis of actinic cheilitis. *Biomedical Optics Express*, 7(10): 4210–4219, 2016.

[138] Yulan Wang, Chuan Song, Mengyan Wang, Yonghui Xie, Lan Mi, and Guifang Wang. Rapid, label-free, and highly sensitive detection of cervical cancer with fluorescence lifetime imaging microscopy. *IEEE Journal of Selected Topics in Quantum Electronics*, 22(3):228–234, 2015.

[139] Alba Alfonso-Garcia, Silvia Noble Anbunesan, Julien Bec, Han Sung Lee, Lee-Way Jin, Orin Bloch, and Laura Marcu. In vivo characterization of the human glioblastoma infiltrative edge with label-free intraoperative fluorescence lifetime imaging. *Biomedical optics express*, 14(5):2196–2208, 2023.

[140] Pascal Uehlinger, Tanja Gabrecht, Thomas Glanzmann, Jean-Pierre Ballini, Alexandre Radu, Snezana Andrejevic, Philippe Monnier, and Georges Wagnières. In vivo time-resolved spectroscopy of the human bronchial early cancer autofluorescence. *Journal of biomedical optics*, 14(2):024011–024011, 2009.

[141] PAA De Beule, C Dunsby, NP Galletly, GW Stamp, AC Chu, U Anand, P Anand, CD Benham, A Naylor, and PMW French. A hyperspectral fluorescence lifetime probe for skin cancer diagnosis. *Review of scientific instruments*, 78(12):123101, 2007.

[142] D Ma, J Bec, D Gorpas, et al. Technique for real-time tissue characterization based on scanning multispectral fluorescence lifetime spectroscopy (ms-trfs).

[143] Sen Tian, Haidong Huang, Yifei Zhang, Hui Shi, Yuchao Dong, Wei Zhang, and Chong Bai. The role of confocal laser endomicroscopy in pulmonary medicine. *European Respiratory Review*, 32(167), 2023.

[144] M Szabelski, R Luchowski, Z Gryczynski, P Kapusta, U Ortmann, and I Gryczynski. Evaluation of instrument response functions for lifetime imaging detectors using quenched rose bengal solutions. *Chem. Phys. Lett.*, 471(1-3):153–159, 2009.

[145] Alexander P Demchenko. Photobleaching of organic fluorophores: quantitative characterization, mechanisms, protection. *Methods and Applications in Fluorescence*, 8(2): 022001, 2020.

[146] Matthias Klemm, Lydia Sauer, Sascha Klee, Dietmar Link, Sven Peters, Martin Hammer, Dietrich Schweitzer, and Jens Haueisen. Bleaching effects and fluorescence lifetime imaging ophthalmoscopy. *Biomedical Optics Express*, 10(3):1446–1461, 2019.

[147] Laura Marcu, Warren S Grundfest, and Jean-Michel I Maarek. Photobleaching of arterial fluorescent compounds: Characterization of elastin, collagen and cholesterol time-resolved spectra during prolonged ultraviolet irradiation. *Photochemistry and photobiology*, 69(6):713–721, 1999.

[148] Matthew Newville, Till Stensitzki, Daniel B. Allen, and Antonino Ingargiola. LMFIT: Non-Linear Least-Square Minimization and Curve-Fitting for Python, October 2015. URL `https://doi.org/10.5281/zenodo.11813`.

[149] M Hammer, D Schweitzer, S Richter, et al. Sodium fluorescein as a retinal ph indicator?

[150] A S Kristoffersen, S R Erga, B Hamre, et al. Testing fluorescence lifetime standards using two-photon excitation and time-domain instrumentation: rhodamine b, coumarin 6 and lucifer yellow.

[151] M Liu, M Jia, H Pan, et al. Instrument response standard in time-resolved fluorescence spectroscopy at visible wavelength: quenched fluorescein sodium.

[152] MA Rauf, John P Graham, Saeed B Bukallah, and Mariam AS Al-Saedi. Solvatochromic behavior on the absorption and fluorescence spectra of rose bengal dye in various solvents. *Spectrochimica Acta Part A: Molecular and Biomolecular Spectroscopy*, 72 (1):133–137, 2009.

[153] D Magde, E Rojas, and P G Seybold. Solvent dependence of the fluorescence lifetimes of xanthene dyes. *Photochem. Photobiol.*, 70(5):737–744, 1999.

[154] Mariana Brandao, Ricardo Iwakura, Fagne Basilio, Kaique Haleplian, Amando Ito, Luiz Carlos Conti de Freitas, and Luciano Bachmann. Fluorescence lifetime of normal, benign, and malignant thyroid tissues. *Journal of biomedical optics*, 20(6):067003–067003, 2015.

[155] Mingmei Ji, Jiahui Zhong, Runzhe Xue, Wenhua Su, Yawei Kong, Yiyan Fei, Jiong Ma, Yulan Wang, and Lan Mi. Early detection of cervical cancer by fluorescence lifetime imaging microscopy combined with unsupervised machine learning. *International Journal of Molecular Sciences*, 23(19):11476, 2022.

[156] Michael J Morgan and Zheng-gang Liu. Crosstalk of reactive oxygen species and nf-κb signaling. *Cell research*, 21(1):103–115, 2011.

[157] Alyssa Soles, Adem Selimovic, Kaelin Sbrocco, Ferris Ghannoum, Katherine Hamel, Emmanuel Labrada Moncada, Stephen Gilliat, and Marija Cvetanovic. Extracellular matrix regulation in physiology and in brain disease. *International journal of molecular sciences*, 24(8):7049, 2023.

[158] David S Kittle, Fartash Vasefi, Chirag G Patil, Adam Mamelak, Keith L Black, and Pramod V Butte. Real time optical biopsy: Time-resolved fluorescence spectroscopy instrumentation and validation. *Scientific reports*, 6(1):1–9, 2016.

[159] Taj Mohammad Khan, Muhammad Arshad, and Muhammad Ahmad Choudhry. Modeling and control of cartesian robot manipulator. In *2005 Pakistan Section Multitopic Conference*, pages 1–4. IEEE, 2005.

[160] Marina V Shirmanova, Vladislav I Shcheslavskiy, Maria M Lukina, Wolfgang Becker, and Elena V Zagaynova. Exploring tumor metabolism with time-resolved fluorescence methods: From single cells to a whole tumor. *Multimodal Optical Diagnostics of Cancer*, pages 133–155, 2020.

[161] Ahmed A Heikal. Intracellular coenzymes as natural biomarkers for metabolic activities and mitochondrial anomalies. *Biomarkers in medicine*, 4(2):241–263, 2010.

[162] Helen Sadik, Daryl Pritchard, Derry-Mae Keeling, Frank Policht, Peter Riccelli, Gretta Stone, Kira Finkel, Jeff Schreier, and Susanne Munksted. Impact of clinical practice gaps on the implementation of personalized medicine in advanced non–small-cell lung cancer. *JCO Precision Oncology*, 6:e2200246, 2022.

[163] Wolf-Dieter Lienhart, Venugopal Gudipati, and Peter Macheroux. The human flavoproteome. *Archives of biochemistry and biophysics*, 535(2):150–162, 2013.

[164] Febby Hutomo, Ryan Yudistiro, Ivana Dewi Mulyanto, and Hendra Budiawan. False positive finding from malignancy-like lesions on fdg pet/ct: case report of tuberculosis patients. *BMC Medical Imaging*, 20:1–5, 2020.

[165] Siema MB Bakheet, John Powe, Alaa Kandil, Adnan Ezzat, Assem Rostom, and John Amartey. F-18 fdg uptake in breast infection and inflammation. *Clinical nuclear medicine*, 25(2):100, 2000.

[166] Hideaki Kamata and Hajime Hirata. Redox regulation of cellular signalling. *Cellular signalling*, 11(1):1–14, 1999.

[167] Tohru Fukai and Masuko Ushio-Fukai. Superoxide dismutases: role in redox signaling, vascular function, and diseases. *Antioxidants & redox signaling*, 15(6):1583–1606, 2011.

[168] Mohamed Abul Hassan, Brent W Weyers, Julien Bec, Farzad Fereidouni, Jinyi Qi, Dorina Gui, Arnaud F Bewley, Marianne Abouyared, D Gregory Farwell, Andrew C Birkeland, et al. Anatomy-specific classification model using label-free flim to aid intraoperative surgical guidance of head and neck cancer. *IEEE Transactions on Biomedical Engineering*, 2023.

[169] Antonino Carbone. Cancer classification at the crossroads. *Cancers*, 12(4):980, 2020.

[170] Alessio Amatu, Andrea Sartore-Bianchi, and Salvatore Siena. Ntrk gene fusions as novel targets of cancer therapy across multiple tumour types. *ESMO open*, 1(2): e000023, 2016.